Dissertation

# Flux pinning in $Nb_3Sn$ containing artificial pinning centres: a systematic study

Ausgeführt zum Zwecke der Erlangung des akademischen Grades eines
Doktors der technischen Wissenchaften
eingereicht an der Technischen Universität Wien, Fakultät für Physik

von

**Mattia Ortino**, MSc

Matr.Nr.: 11726515

unter der Anleitung von

Privatdoz. Dipl.-Ing. Dr.techn. **Michael Eisterer**

Atominstitut
Technische Universität Wien
Stadionallee 2, 1020 Wien, Österreich

Wien, im February 2022

# Contents

# Abstract

Nowadays plans for next-generation particle accelerators demands for record-breaking high-field superconducting magnets, to be conceived based on state-of-the-art technologies from the base conductor to magnet design.
In particular, the CERN Future Circular Collider project (*FCC*) in its hadron-hadron version (*hh-FCC*) asks for high-field magnet dipoles. The latter are planned to bend the hadrons trajectory through the about 100 km long ring, so resulting in collision energies in the order of 100 TeV. The dipoles are required to produce a stable 16 T field at 4.2 K, with coils made from a conductor sustaining critical current densities $J_c$ of at least 1500 A mm$^{-2}$ at the same temperature and field.
In this respect, even though the high temperature superconductors (HTS) could represent a solid research investment towards the future, at present $Nb_3Sn$ is still considered the best candidate for matching hh-FCC tasks. Even considering $Nb_3Sn$ to be to-date industrially established, present market products do not reach yet those high-performance requirements, asking for a step forward in the material development towards its very best possible achievements. It is indeed well known that several aspects of $Nb_3Sn$ manufacturing can be improved, being it a hard challenge and often requiring for years of R&D.

As a possible solution to the problem, a new $Nb_3Sn$ manufacturing technology known as "artificial pinning centres (APC) $Nb_3Sn$" started to catch researchers' interest in 2014. The idea of introducing a wide scenario of small precipitates in the microstructure (A15) immediately showed great impact on the superconducting performances, resulting e.g. in $J_c$ exceeding the FCC specification by a factor 1.5 and more. Zr or Hf is alloyed in the starting recipe of these specimens, both elements forming oxides during the heat treatment by combining with oxygen. The oxides are nanometric precipitates, which contribute to the overall grain size refinement and eventually (individually) to flux pinning.
The idea of the artificial pinning centres is per se not new, while its successful application to multi-filamentary $Nb_3Sn$it is: finding a suited method for the internal oxygen supply and a reproducible good quality of wire drawing resulted in a great interest in this technology, which motivated the research contained in this thesis.

In this work, a systematic investigation of how the microstructure correlates with the main superconducting performance of several APC-$Nb_3Sn$ recipes is presented.
Starting from the mono-filamentary (binary) strands to the most advanced ternary versions of these prototype wires, an ad-hoc set of samples heat treated each at 675°C, 685°C, 700°C and 720°C (at *Fermilab*, US) with different percentages of Zr or Hf alloyed to the starting Nb- or Nb-Ta compound and characterized at the *Atominstitut* (Vienna, AT).
SQUID magnetometry was used to measure the specimens $J_c$ , $B_{irr}$ and $T_c$ at different temperatures/fields, coupled with resistive measurements at 4.2 K for several samples. This experimental technique was used also for pioneering a sensitive method for investigating the geometry of the A15 filaments, fundamental for the assessment of the layer-$J_c$.

In the magnetometry field range - 1 to 7 T- it is usually also possible to detect the maximum value of the pinning force $F_{p\text{-}max}$ at 4.2 K, which is an important parameter towards the understanding of the flux pinning at the operational temperature. This work shows how the most complete experimental datasets clearly indicate the $J_c$ standards of hh-FCC to be matched and even exceeded by the best samples.
The samples were also prepared for electron microscopy (SEM, TEM/STEM, EELS, EFTEM) through which it was possible to determine the grain sizes, the precipitate size and densities as well as Sn compositional gradients along the A15 radii. It was found that the content of Zr/Hf does influence the grain/particle size vs heat-treatment temperature, revealing also a consistent grain refinement against the no-oxygen version of the same recipe.

Several aspects of the mixed flux pinning in this wires were investigated through the collected data. Critical temperature distributions were either magnetically probed by using SQUID (bulk) and scanning Hall probe microscopy (locally) or mapped by correlating to the Sn content by using EDX. These data were useful to simulate the local currents, finding that it is possible to assess through them both the co-existing grain-boundary and point-particle pinning contributions. It was found from these analyses and from $J_c$ measurements that point particles play a significant role in the overall pinning, motivating additional modelling work to deepen the understanding of such complex systems.

Starting from Dew-Hughes models, fits of the experimental data by using different combinations of summation were produced and discussed. The role of $B_{irr}$, of the actively pinning grain-boundary surfaces and the elasticity degrees of the fluxon lattice are discussed. A focus on the efficiencies of the individual pinning mechanisms led eventually to a proposal for modelling the point particle one, which was found to decrease hyperbolically once exceeding the coherence length $\xi$.

# Chapter 1

# Introduction

This introductory chapter serves as a foundation for the study conducted in this work. The aim of this thesis was to characterize and understand the physics governing the new $Nb_3Sn$ wires doped with artificial pinning centers (APC-$Nb_3Sn$), comparing their performances with the commercial strands and deepening the understanding of their flux pinning by means of several experimental techniques. APC-$Nb_3Sn$ strands are being considered among the best candidates as base conductor for the future hadronic accelerator dipole magnets at *CERN*. Indeed, this work found its room within a collaboration between TU Wien, *CERN* and other academic/industrial partners.
The motivation and goals behind this project are described in Section 1.1, where only the technology/application frame of the main existing superconductors is discussed. A concise but fundamental-physics oriented description of the phenomenon of superconductivity is given in Section 1.2, while the details of $Nb_3Sn$ and, more specifically, of the APC-$Nb_3Sn$ manufacturing technology are discussed in Section 1.3. Finally, the experimental and theoretical background of flux pinning in type II superconductors is described in Section 1.4.

## 1.1 The hadron-hadron Future Circular Collider (FCC-hh): new frontiers for applied superconductivity

### 1.1.1 Particle colliders and superconducting magnets

High-energy physics projects, especially grand international collaborations as particle accelerators or fusion reactors, had always fuelled the research and development of new technologies. Among them, R&D in material science is surely one of the most exploited.
As being an example of upcoming "technologies booster" infrastructure, the future circular collider (FCC) is part of the newly designed accelerator complex to be built at *CERN*, in Geneva (CH).

The FCC study started in 2014, with the aim of exploring physics at energy levels higher than the nowadays *Large Hadron Collider (LHC)* operational levels. In fact, the discovery of the Higgs boson (2012) at the LHC unveiled a new path for research, as this particle could shed light into a whole new physics. Experimental evidence requires physics beyond the Standard Model to account for observations such as dark matter and the domination of matter over antimatter. Therefore, detailed studies of the Higgs properties are considered a priority for any future high-energy physics accelerator [184]. This clearly follows the European Strategy for particle physics, which aimed to "propose an ambitious post-LHC accelerator project at *CERN* by the time of the next strategy update" [57].
In the last years, the conceptual design of a new collider involved several academic institutions and companies, ending in 2019 with a final report indicating three viable machines to be implemented

in the *CERN* complex [31]. The main goal of the new machines is to increase the collision *energy* (as a sum of the two colliding particle beams, also called "center of mass energy") and/or the *luminosity*, which is the measure of the number of potential collisions per surface unit over a given period of time, essentially an accelerator's performance indicator.
The study presented three viable solutions: a leptonic machine ("FCC-ee"), a hadronic machine ("FCC-hh") and a possible upgrade of the existing 27 km LHC machine ("he-LHC"). The first two proposals conceive the realization of a whole new synchrotron, which would profit from the nowadays existing chain of accelerators at *CERN* as beam injectors. This eventually means, as a consequence, that *LHC* itself will become an injector of the future machine. The last one is instead the "higher energy" version of the nowadays 27 km long collider, foreseeing for the hadron beams an energy doubling ( ca. 27 TeV collision energy) and an integrated luminosity of at least a factor of 5 larger than *LHC*.

The final choice on these scientific (and also strategic) decision is bonded mainly by the center of mass energy $E_{c.m.}$ target, which results into a technological burden. For a synchrotron in fact, $E_{c.m.}$ scales as:

$$E_{c.m.} \propto \rho \cdot B \tag{1.1}$$

where B is the maximum magnetic field produced by the dipole bending magnets and $\rho$ is the bending radius [222]. At the present day in LHC, this product results in a center of mass energy $E_{c.m.}$ of about 14 TeV, with $\rho \simeq 4.3$ km and a dipole field of $B = 8.3$ T [44].
If the target $E_{c.m.}$ is 100 TeV as for the FCC-hh project, this means approximately a 8 times higher product, to be achieved either with a bigger machine and/or much powerful dipole magnets. Once again at CERN, the choice fell on superconducting high-field magnets (at least for FCC-hh), with the collider length scaling to $\sim$ 100 km (4 times higher than LHC) and the dipoles magnets to produce 16 T bending field (2 times the LHC strength). A schematic of the project (top view) is shown in Fig. 1.1, while a more detailed representation of the path the accelerator will follow beneath the ground level is shown in Fig. 1.2.

None of the two extreme solutions (increasing only $\rho$ or B) would have been feasible alone: the first because the new synchrotron machine would be more than 200 km long, which is morphologically unrealisable in the existing CERN area. Even if the technology for building such an infrastructure is somehow already mature [150], that tunnel would nevertheless be difficult to handle during operations.

In the second case, the technological problem is even tighter.
As of today, building electromagnets (for applications) able to produce magnetic field strength above 20 T is an extremely difficult challenge [86]. Using resistive conductors for these devices is sometimes still considered, as for the Chinese *Circular Electron Positron Collider (CEPC)*: this future accelerator complex is designed to be an other Higgs-boson factory, with most of the physics goals being the same as for FCC [83].
On the other side, as the 1970s turned into the 1980s, *Fermilab*'s first upgrade of the Main Ring collider (Batavia, US) made superconducting dipoles mass-production become a reality. Based on 800 superconducting dipole magnets with a field higher than 4 T, the nowadays known as *Tevatron* machine represented the first circular accelerator been built to work at a higher energy without increasing its radius [162]. Right after it, superconducting magnet production scaled to

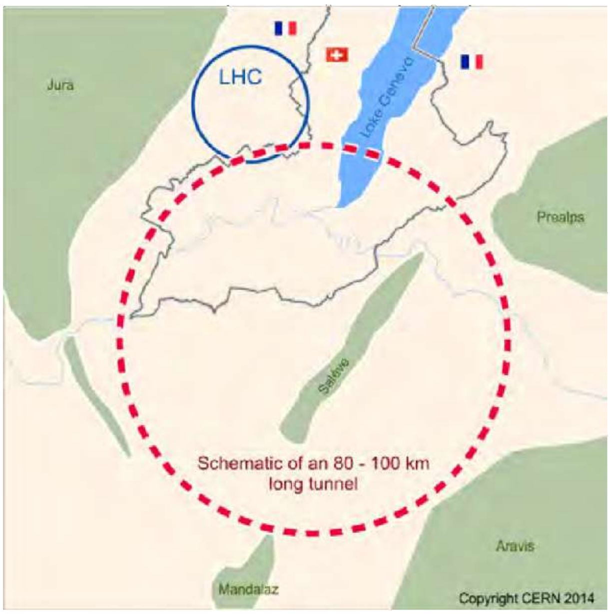

**Fig. 1.1:** Schematics of the ∼100-km-long tunnel of the next future circular collider (FCC) to be built in the CERN accelerator complex (Geneva,CH). The ring would be about 100 km-long (red dashed line), almost four times larger than the nowadays operating LHC (blue solid line).

the industrial level, with the 6 km long collider *HERA* (Hamburg, DE) to implement 5 T dipoles produced for the first time by external companies.
On the same route, LHC and its approaching upgrade *High-Luminosity LHC* (HiLumi-LHC) are showing how effective can be superconductors for making the different coils used in an accelerator: dipoles for bending the charged particle trajectories, current links [6], quadrupoles and sextupoles for focussing the beam just before the collisions happen [157, 163, 178, 192, 195].

With resistive coils there is heat generation caused by the intrinsic resistivity of the conductors, resulting in power losses; with superconductors there is instead no heat generation, allowing for loading higher currents resulting in a more compact magnet.
Summarizing, using superconductors considerably reduces the power requirements at the cost of using more or less expensive coolants.
The latter is one of the weakest point of these materials, all of them needing low operational temperatures (at room pressure) to "activate" their superconducting phase. The latter is known as the "critical temperature" $T_c$, which is the point below which the electrical resistance of the material drops to zero, making it a perfect conductor. $T_c$, together with the upper critical field $B_{c2}$ (the magnetic flux density that completely suppresses superconductivity in a type-II superconductor) and critical current $I_c$ (the maximum current that a superconductor can carry with zero resistance) represent the main performance indicators of a technical superconductor.
A more detailed description of these quantities, and how they are related to the selection of the conductor for applications, is presented in the next sections.

### 1.1.2 Superconductors: what for what

Based on their $T_c$, one can divide technical superconductors in three categories as follows:

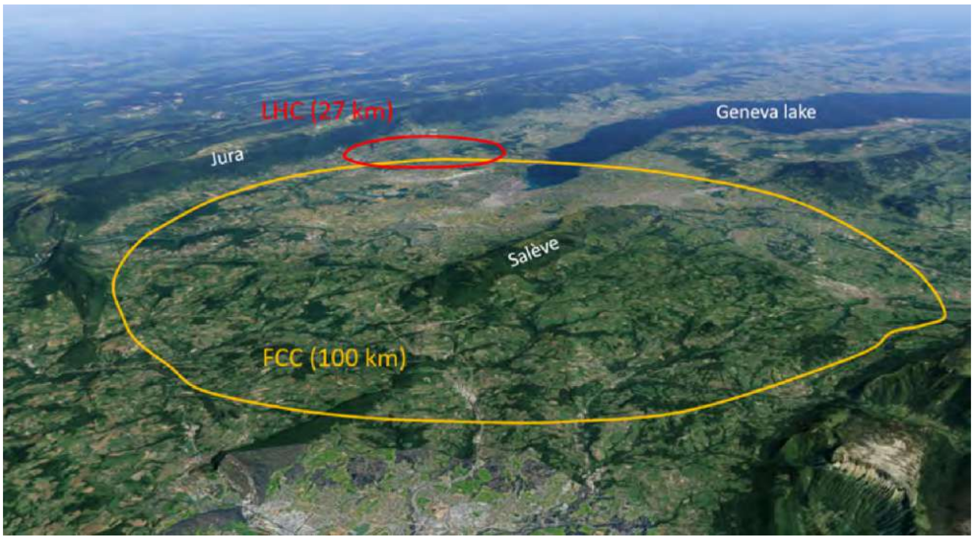

**Fig. 1.2:** Satellite image of the Swiss-French area planned to host the FCC infrastructure beneath the ground level. Great care has been reserved on avoiding the mountain ranges (*Jura* and *Salève*) where the rock workability is much more difficult than the surrounding areas [85, 102].

- Materials operated in liquid-He baths (4.2 K), known as "low temperature superconductors" (LTS). These are the oldest and highly industrialized conductors, being alloys as NbTi or inter-metallic compounds as for $Nb_3Sn$.
- Materials that can be operated in liquid-N baths (77 K), known as "high temperature superconductors" (HTS). First discovered about 35 years ago, the majority of the HTS are ceramic materials, having usually better superconducting performances than the LTSs.
- Materials that can be operated in liquid-$H_2$ (boiling temperature at ca. 20 K) or cryo-coolers, known also as "medium temperature superconductors" (MTS). This category is not as established as the other two, since most of the time these superconductors - e.g. $MgB_2$ or Fe-based compounds - are operated in liquid-He baths anyway [169].

Room-temperature superconductivity is still considered the "holy grail" for applications, but so far the research in this respect produced good results only at very high pressures [87, 175]. The different refrigeration media play therefore a key role in deciding which conductor to deploy for a specific application: nowadays the cost of liquid-He ranges between 5 $ and 35 $ per litre [109], while liquid nitrogen has an average price of 0.37 $/litre [59].

Besides the performances, the cost of the raw materials and the industrialisation level of a certain manufacturing technology are also important factors for selecting the proper conductor for building a magnet.
Low temperature superconductors can be ductile metallic compounds, well known since the 1960s to be mouldable in round wires as well as in films/tapes [103]. Nowadays, the most widespread technical superconductor is indeed NbTi, being manufactured in its optimized version since at least 20 years and representing the workhorse for more than 90% of all superconducting magnets in the world [159]. This material (superconducting at ∼9 K in zero field) is the cheapest and most

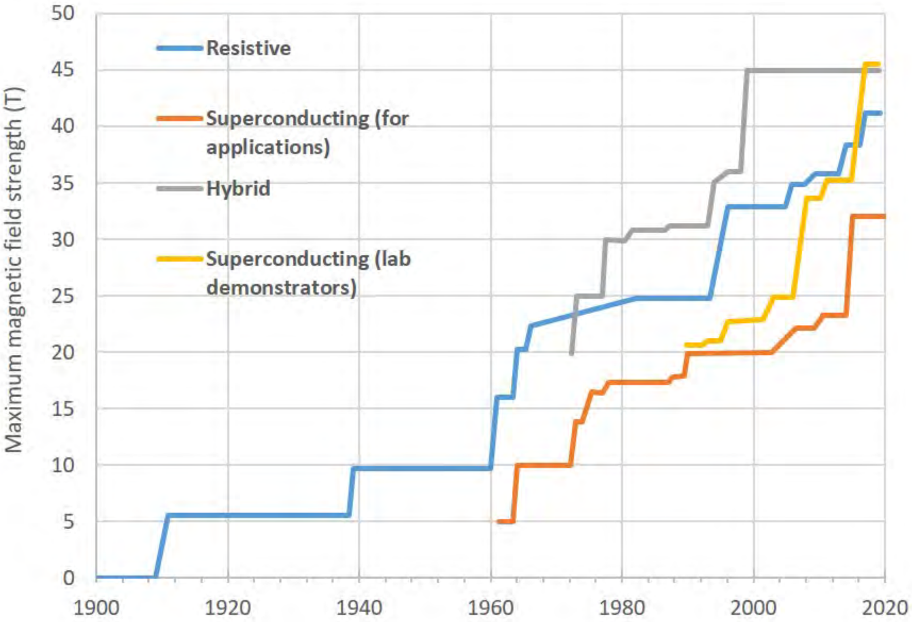

**Fig. 1.3:** Advancements in the worldwide production of record-breaking magnet, from the very first electromagnet.
Source: *Mark Bird, National Magnetic Field Laboratory (NHMFL)*

reliable superconductor on the market, being e.g. the first choice for magnetic resonance imaging (MRI) magnets: these devices developed together with the advancements on the manufacturing of NbTi conductors, first focusing on the best achievable performance and then refining the industrial production costs through the last 40 years [201].
All considered, the main advantage of NbTi over the other superconductors still remains its mechanical flexibility under different temperature/pressure conditions [172]. This results in a unique drawability (the property of a rod/wire to be reduced in cross section by *drawing* through successive dies), allowing for producing NbTi "single-piece" wires more than 1 km long [41]. These brilliant mechanical properties allowed for the diffusion of the *Rutherford cables*, the first type of cable composed of superconducting wire used for high-field coils applications [48]. Rutherford cables and single-piece long NbTi wires (Fig. 1.4) were the technological base for the production of the LHC superconducting magnets, raising the bar of the worldwide industrial superconductors production and giving birth to whole new high-field magnets applications [72].

If NbTi represents the best example of low-cost/high efficiency manufacturing (at the cost of a liquid-He supplying plant for achieving the operational conditions), the much newer high temperature superconductors take place at the opposite end of the spectrum.
As having been first discovered in 1986 in Ba-La-Cu-O systems [19], these materials are almost all united by the presence of Cu in their complex structures (therefore they are called *cuprates*). As mentioned, their main advantage is their critical temperature $T_c$ to be higher than the liquid nitrogen boiling point (77 K), allowing for using this relatively cheap cooling medium. Moreover, these compounds show always higher superconducting performances (higher $I_c$, higher $B_{c2}$) making them the first choice - in principle - for building high-field magnets with the same (or higher) characteristics of the LTS-based but in much more compact shapes.

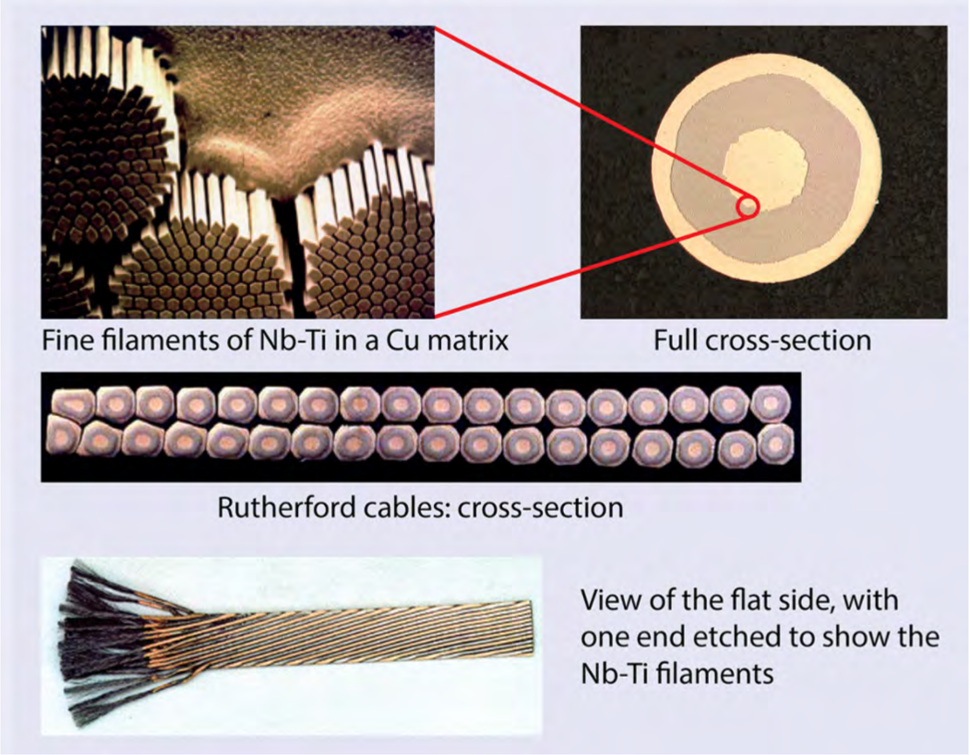

**Fig. 1.4:** Structure of the superconducting cable used in the LHC: from NbTi filament to the final cable.
Credits: *CERN*

Over the last decades there has been a steady increase in the quality of commercially available products, with the best representative conductors being the rare-earth (RE)-Ba-Cu-O (also known as "REBCO") and Bi-Sr-Ca-Cu-O (also known as "BSCCO") compounds [7].
Fig. 1.5 shows the gap between LTSs (left side) and HTSs (right side) in terms of upper critical field $H_{c2}$ and irreversibility field $H_{irr}$ (the field at which electrical resistivity starts to appear). Considering today's (growing) needing of magnetic fields above 15 T [135, 194], it appears clear from Fig. 1.5 how NbTi is slowly becoming an obsolescent resource with its relatively low $H_{irr}$ ($\simeq$ 15 T at 0 K). In the same way, also the critical current densities $J_c$ can be considerably higher in HTSs, as it is depicted in Fig. 1.6.
The true downside of these materials is their difficult workability, as being complex anisotropic compounds, extremely brittle and often not shapeable in round wires. These problems made their manufacturing very delicate so far, resulting in a significantly higher conductor cost and overall lower reliability if compared with the established LTS "competitors" [33].

All in all, HTS are extremely good candidates for being selected as the base conductor of the next generation magnets dipoles for FCC, but their state-of-the-art high costs and still industrial "niche" scale make the investment not reliable [138].

Between the two extremes, the long time discovered $Nb_3Sn$ was the very first material demonstrating superconductors applicative potential (even before NbTi), by showing that superconductivity could exist at very high fields [112].

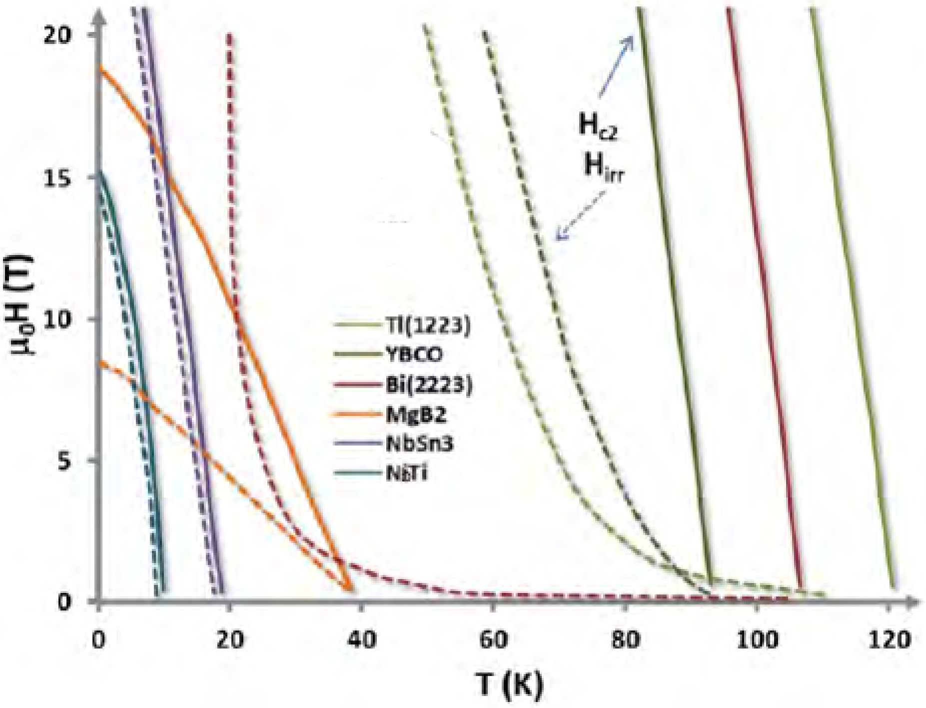

**Fig. 1.5:** Magnetic field (T) vs temperature (K) for several superconductors involved in the conceptual design study of the FCC project. For each conductor both the upper critical field ($H_{c2}$) and the irreversibility field $H_{irr}$ are displayed, stressing out the considerable difference between these two values in HTS materials (right side of the plot). Source: *Johannes Gutleber*

First discovered in 1954 [132], this compound is part of the "$A_3B$" superconductors family (where A is a transition metal and B can be any element), which is also known as the "A15" group [23, 91]. The latter also includes other superconductors as $V_3Si$, $V_3Ga$, $Nb_3Ti$ and $Nb_3Al$ [130, 200]. $Nb_3Sn$ has a critical temperature $T_c$ of 18.3 K, with better $I_c$ and $B_{c2}$ if compared to other LTSs as for example NbTi [68, 74]. Due to its not negligible mechanical fragility, $Nb_3Sn$ did not establish itself immediately on the market: as almost all the "$A_3B$"s, this intermetallic conductor is granular, strain senstive (its critical parameters depend on the applied strain, reversible for small strains) and of limited ductility: these are nightmarish properties for producing the necessary wires and coils for high field magnets (if one considers the giant electromagnetic forces - therefore stresses/strains - taking place at high fields on the conductors) .

For $Nb_3Sn$, the first technological relevant step towards applications was the development of a deposition technique (chemical vapour deposition, "CVD"), producing a thin enough layer of $Nb_3Sn$ on a wire or tape that was flexible enough to wind magnets [26]. Nevertheless, tape-conductor based magnets suffered from flux jumps (instabilities of the critical state in a superconductor [137]) that made them slow to charge currents and sometimes irregular in performance [185].

Later on, the work done on realizing mono-core wires of NbTi and $V_3Ga$ threw the doors open to $Nb_3Sn$ filamentary (mono- and multi-) wire production. Even considering the fragility of $Nb_3Sn$ in its final form, Nb, Sn and Cu have a favourable workability at room temperature, allowing multifilamentary composites to be assembled at larger size, co-drawn to final wire

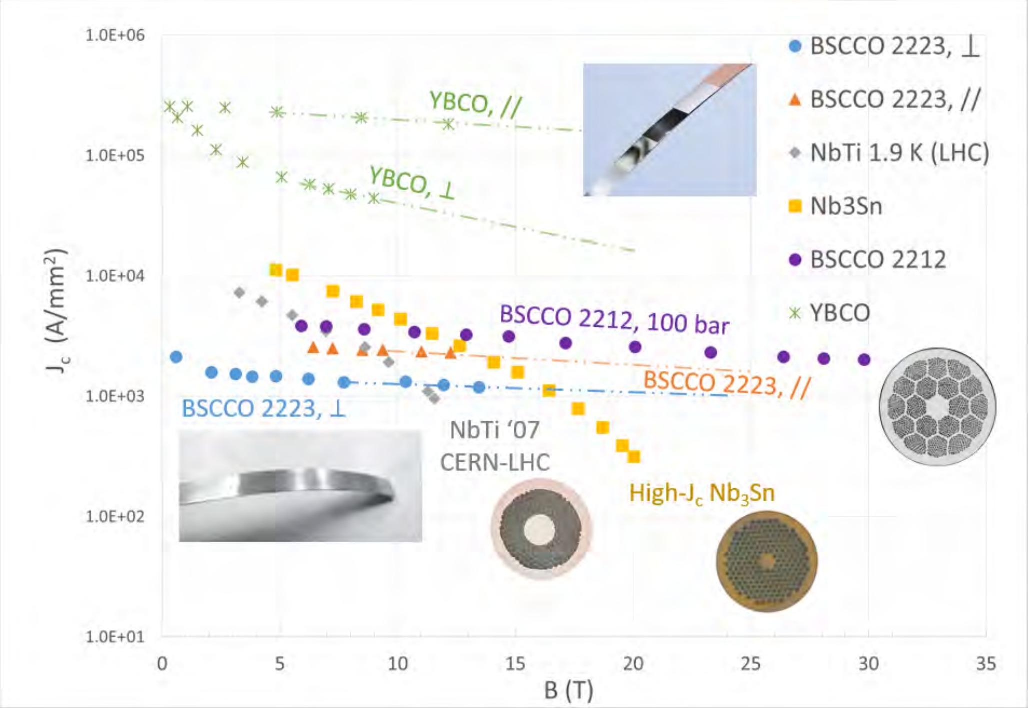

**Fig. 1.6:** Critical current density $J_c$(B) vs field for the main technical superconductors used for winding high-field magnets. For wires (NbTi, $Nb_3Sn$, BSCCO-2212) $J_c$(B) is intended as the *layer*-$J_c$, the critical current $I_c$ flowing through the superconducting cross section only (A/mm$^2$.

dimensions and reacted to form the phase of interest in the filament structure.
As for NbTi, the choice of producing a multi-filamentary wire responds to technical issues. For accelerator magnets for example, each superconductor should be designed as follows:

- Subdivided in filaments of small diameter, for reducing flux jumps and minimize field distortions due to superconductors' magnetization [70, 113, 217, 223];
- Twisted together, for reducing interfilament coupling and AC losses [36, 58, 125, 203]. When subjected to time varying fields, straight filaments can in fact generate large current loops eventually superimposing on the transport currents, which flow through the resistive wire matrix generating ohmic losses; with twisted filaments instead, the magnetic flux embraced by the induced current loops changes sign every half-twist pitch, not leaving enough space for significant transverse currents to build up through the matrix between sign reversals;
- Embedded in a Cu matrix (as purest as possible), for protecting the superconductor after a "quench" (the sudden loss of superconductivity due a temperature increase) and reduce as well flux jumps [11, 118, 161, 202, 214].

$Nb_3Sn$ wire are therefore produced following these specifications, even though the limited extrusion capacity of the A15 materials does not allow to reduce the filament size to few microns as for the NbTi case.

Forty-seven years have passed from the very first $Nb_3Sn$ multifilamentary wires produced with the *internal tin* (IT) [218] and *bronze route* processes [119] (both using Nb-rods inserted in a

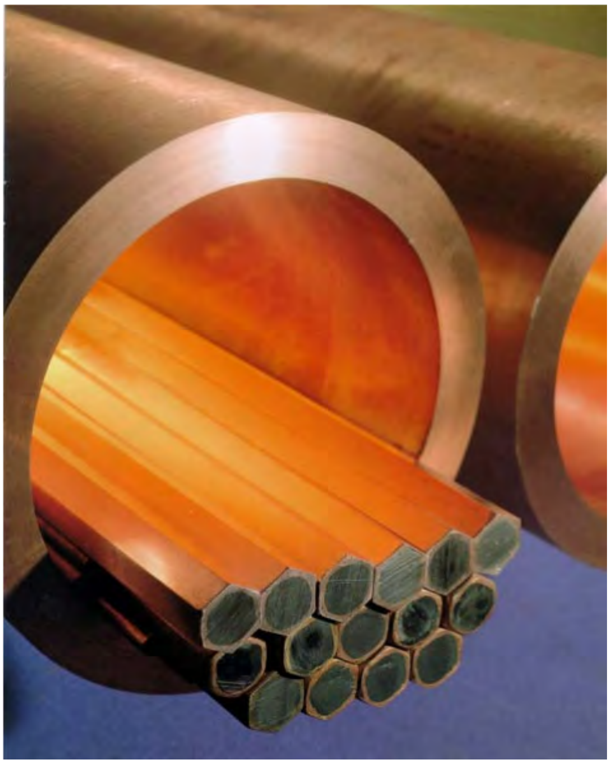

**Fig. 1.7:** Assembly of a multi-filament billet by stacking of mono-filament rods.
Credits: *Furukawa Electric Company*

Sn-Cu matrix, then reacted) to the nowadays state-of-the-art commercial products.
The best $Nb_3Sn$ manufacturing technologies today are the following (each information refers to pre-heat treatment and drawing phases, where the wires are still in their billet shape as it is shown in Fig. 1.8):

- *Powder in tube* (PIT), where for each filament a powder (e.g. $NbSn_2$ plus additional elements) is put into Nb hollow tubes, surrounded by high purity Cu matrix;
- *Rod restack process* (RRP), where in each filament a Sn core is surrounded by Cu-embedded Nb rods (a newer version of the internal tin process) [54]. If the number of filaments is very high, the multi-filamentary rods can be re-stacked once again (from this double stacking process comes the "restack" name).

The listed manufacturing have the best superconducting performances as well as the most optimized industrial processes among the production technologies so far. Considering as a key parameter, for example, the "non-Cu" critical current density $J_c$ (the critical current $I_c$ flowing through the non-Cu cross section of the superconducting wire), the performance of the two best commercial products on May 2017 can be summarized as in Tab. 1.1.

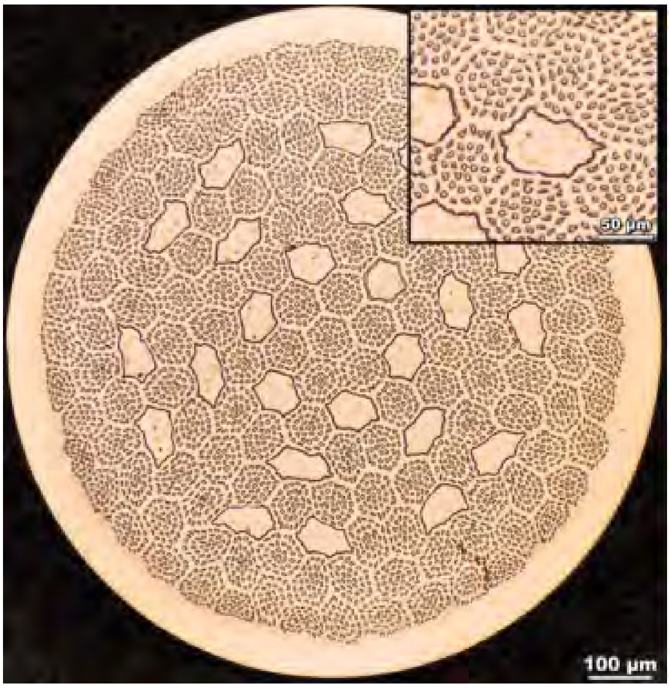

**Fig. 1.8:** More than 5000-filament bronze-process strand manufactured by the UK Atomic Energy Research Establishment group in early 1974 (Harwell, UK). The application of a diffusion barrier is shown protecting internal stabilizer elements of Cu.
Credits: *P.J. Lee*

**Tab. 1.1:** Selected manufacturing and performance indicators of the best commercial RRP and PIT wires as being used for winding the upgraded High-Luminosity LHC (HiLumi-LHC) magnets.

| | Filaments /*Stack | Filament size | $J_c$ (12 T) , *RMS* (A/mm$^2$) | $J_c$ (15 T) , *RMS* (A/mm$^2$) | $J_c$ (16 T) , *RMS* (A/mm$^2$) | $J_c$ (18 T) , *RMS* (A/mm$^2$) | $H_{c2}$(4.3 K) , *RMS* (T) |
|---|---|---|---|---|---|---|---|
| RRP ($\phi$=0.7 mm) | 108/127 | 46 $\mu$m | 2676, 68 | 1410, 58 | 1098, 55 | 610, 47 | 24.5, 0.4 |
| RRP ($\phi$=0.84 mm) | 108/127 | 55 $\mu$m | 2835, 44 | 1601, 33 | 1289, 10 | 785, 25 | 25.9, 0,2 |
| PIT ($\phi$=0.84 mm) | 192 | 39 $\mu$m | 2323, 83 | 1342, 49 | 1093, 40 | 688, 26 | 26.7, 0.1 |

[*] The "stack number" refers to the number of hexagonal centred elements, the total amount of hexagons in the wire (sub-elements), some of which are made of Cu only (central ones).

[*] $J_c$ values expressed as non-Cu $J_c$ (A/mm$^2$).

In both manufacturing, a Sn solid state diffusion takes place, since the latter is placed always far from Nb in the billet (Fig. 1.9). Therefore, Sn needs to "travel" some microns during the heat treatment in order to form the A15 phase, meaning eventually 10 $\mu$m in the largest PIT filaments. This process results always into some Sn gradients along the filaments' radial direction which, for example in PIT wires, stands between 0.1 and 0.4 at.%/$\mu$m [93, 94].

As it will be described in Subsections 3.5.5 and 3.5.6, the critical temperature and the upper critical field are parameters sensitive to compositional gradients, therefore Sn gradients impact on the conductor performance.
Sn gradients are considered among the remaining optimization issues for $Nb_3Sn$ manufacturing, eventually preventing to exploit the full potential of this superconductor for applications.

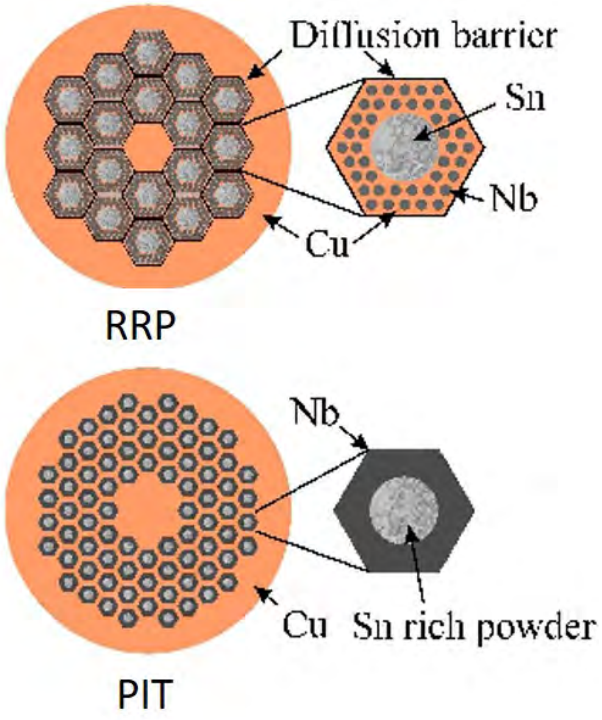

**Fig. 1.9:** Differences in the base-layout between powder-in-tube (PIT) and restack-rod-process (RRP) manufactured $Nb_3Sn$ wires. In the RRP case, the A15 to Cu matrix barrier (usually Nb) can be single or distributed (each filament has its own barrier). Adapted from: *A.Godeke, PhD Thesis*

For FCC-hh, both HTS and $Nb_3Sn$ have been considered as good conductor candidates. If the almost ready-to-go HiLumi-LHC specification for $Nb_3Sn$ are already fulfilled by commercial products (e.g. non-Cu $J_c$(12 T, 4.2 K) $>$ 2450 A/mm$^2$, Tab. 1.1), for FCC-hh the required performance scaled to a not yet exploited potential for $Nb_3Sn$. The key word is "high currents": a non-Cu $J_c$ target of at least 1500 A/mm$^2$ at 16 T (4.2 K) is required, with the same strand diameter and amount of Cu (thermal stabilizer) as for the HiLumi project [9, 193].

This ambitious requirements stimulated a "renaissance" of the research on $Nb_3Sn$ in the last 7 years, aiming to develop the already existing technologies to their limit, but keeping the costs down within a higher threshold of 5 EUR / kA·m. From these clear ground, several research initiatives for improving the base manufacturing started around the world, as it is the case for the "cluster layout" wire produced by TVEL (Bochvar Institut, RU) or the distributed Sn-Ti (with common Ta barrier) strand produced by Kiswire Advanced Technology (KAT) [101, 140]. Fig. 1.10a shows a wire sample from TVEL manufacturing, from which Cu has been chemically etched away in order to better investigate the Sn inhomogeneities along the radial direction as being the main performance limiters.

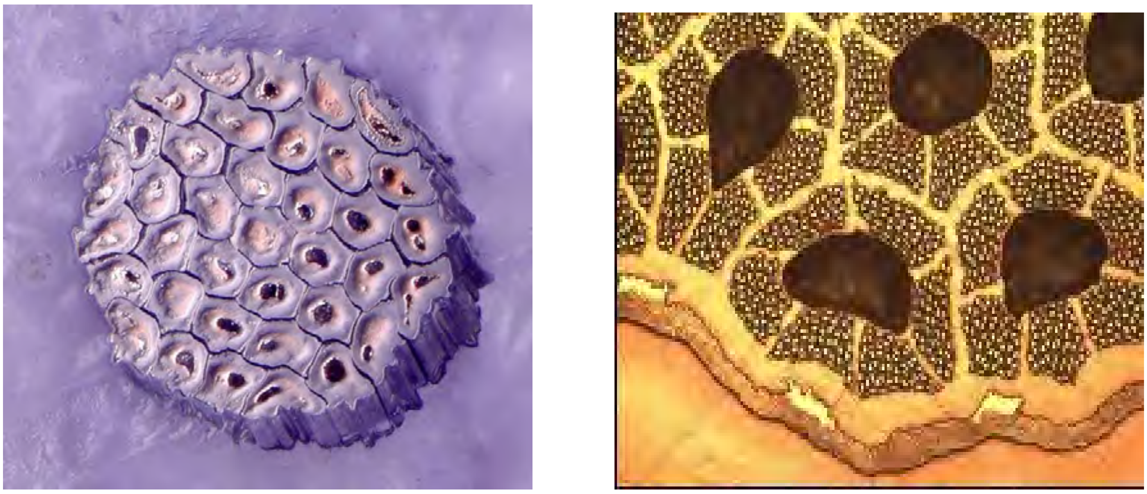

(a) (b)

**Fig. 1.10:** a): Cu-etched 3-D image of a $Nb_3Sn$ sample from 2017 TVEL (Bochvar Institut, RU) manufacturing, used for accurate compositional gradients measurements.
b): "cluster layout" sample produced by TVEL. The filaments are sub-divided into clusters, each separated in turn by Cu or Cu-Mb corridors, eventually facilitating the Sn diffusion toward the peripheral areas of the filament.

In the same way, also the study of possible new doping elements, to be added to the A15 phase, started in 2014.
At the Ohio State University (Columbus, US) in fact, initial attempts of including point-particle precipitates in the superconducting phase took place by alloying Zr in the starting Nb-matrix. The study showed from the very beginning the wires to have superior $J_c$ compared to the best wires on the market, advancing to the point where several other academies/industries are now giving their own attempt on optimizing this manufacturing, nowadays known as "artificial pinning centres (APC) - $Nb_3Sn$".
The characterization and deep understanding of flux pinning in the new $Nb_3Sn$ samples produced by means of this technology were the key motivations for this Thesis, as it will be discussed in Section 1.3 and deepened in Chapters 3 and 4.

## 1.2 Superconductivity: a briefing

The following Section serves as a succinct introduction to the main notions regarding superconductivity and the distinction between type I and type II superconductors, with a final focus on $Nb_3Sn$ as being part of the $2^{nd}$ category.

Perfect electrical conductivity (resistivity $\rho$ dropping suddenly to zero) was the first macroscopic phenomena recorded by *H. Kamerlingh Onnes* in 1911 while investigating the properties of Hg at cryogenic temperatures [107]. It was indeed thanks to the discovery of liquid He, from the same Kamerlingh Onnes 3 years before, that these new experiments took place: by using pre-cooling stages and the Hampson-Linde cycle, he lowered the He temperature down to its boiling point (ca. 4.2 K), eventually lowering it further to ∼1.5 K by reducing the bath pressure.

As it is displayed in Fig.1.11, the 1913 Nobel laureate noticed that, at about 4.17 K, an abrupt disappearing of electrical (DC) resistance occurred reproducibly in Hg, which was categorized as the first "superconductor".

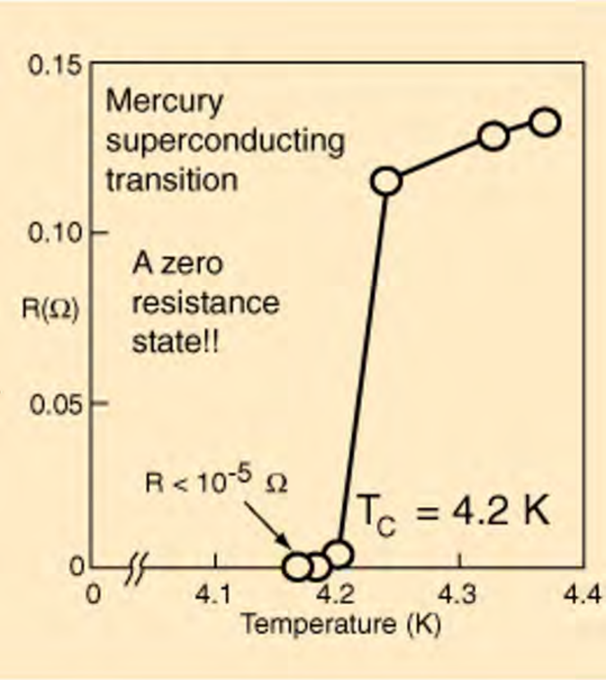

**Fig. 1.11:** Resistance vs temperature plot of the first superconductor ever measured (1911, H.Kamerlingh Onnes): elemental Hg.
Source: *Wikidot*

After it, other pure elements as lead and tin were found to show the same behaviour at different temperatures. It was on these materials that, in 1933, new experiments by *Meissner* showed the complete ejection of magnetic fields lines from the sample interior, occurring - simultaneously - once cooled in constant magnetic field at the same temperature where the resistance disappears [134]. This will be referred, from that moment on, as the "Meissner" effect.

The two evidences together indicated already that these phenomena could not be entirely described by classical electro-dynamics (no "perfect conductor" would have shown also perfect diamagnetism, which is a change of thermodynamic state) but by means of something else: the newborn quantum mechanics.

Right after the experimental discovery of the Meissner effect, the *London* brothers formulated the very first theory of superconductivity in 1934 [126]. They conceived a set of equations that accounted for the observed properties of zero resistance and perfect diamagnetism. They contain the essence of a collection of experimental facts and reduce them to a deeper set of questions, thus being the first (even though phenomenological) theory describing superconductivity. The London's first and second equations are here summarized:

$$\frac{\mathrm{d}\vec{J}}{\mathrm{d}t} = \frac{\vec{E}}{\mu_0 \lambda_L^2} \qquad \text{with} \qquad \lambda_L = \sqrt{\frac{m_e}{\mu_0 n_s e^2}} \tag{1.2}$$

$$\nabla \times \vec{J} = -\frac{\vec{H}}{\lambda_L^2} \tag{1.3}$$

where $m_e$ is the electron mass, $e$ is the elementary electron charge and $n_s$ is a phenomenological parameter representing the density of super-carriers. $\lambda_L$ is called "London's penetration depth", a first explicit formulation of the magnetic penetration depth, the length (m) a magnetic field is able to penetrate into a superconductor to the point where it equals $1/e$ times its value at the surface of the superconductor [108]. Eventually the London theory was extended to include the two-fluid concept, namely the idea that a superconductor consists of two interpenetrating fluids, a normal one exhibiting resistance and a superconducting one obeying the London equations.

After the Londons, also *Ginzburg* and *Landau* introduced their famous phenomenological theory [117]. They postulated the existence of a macroscopic wave function (or order parameter) to describe the behaviour of the superconducting electrons, thus postulating in more fundamental terms the intuition had by London when referring to $n_s$ as:

$$\psi = |\psi| e^{i\phi} \qquad , \qquad n_s^* = |\psi|^2 \tag{1.4}$$

Rather than just deepening the Londons theory, they provided a set of equations through which the superconducting macroscopic wave function could be calculated under many circumstances: in particular in the presence of applied currents and magnetic fields, accounting of course for the zero resistance and the Meissner effect, but also for the second order (or continuous) nature of the superconducting phase transition in zero magnetic field.
Among the outputs of the "GL" theory, there are two new characteristic lengths:

$$\xi = \sqrt{\frac{\hbar^2}{2m|\alpha|}} \qquad , \qquad \lambda = \sqrt{\frac{m\beta}{4\mu_0 e^2 |\alpha|}} \tag{1.5}$$

where $\alpha$ and $\beta$ are two phenomenological parameters that, below the superconducting transition temperature, take the form $|\psi|^2 = -\alpha/\beta$ (with $\alpha = \alpha_0(T - T_c)$ and $\alpha_0/\beta > 0$).
$\xi$ is called "coherence length", interpreted as being the distance over which small perturbations of density of "superelectrons" (the superconducting electrons) recover their equilibrium value $\psi_0$. The penetration depth $\lambda$ has instead a similar meaning to $\lambda_L$, as it sets the exponential law according to which an external magnetic field decays inside a superconductor.
Oddly, in 1957 Abrikosov found a solution for the GL in which the magnetic induction inside the superconductor was not zero [1]. He noticed that, if a sufficiently large magnetic field was present, vortices (regions of circulating currents around a singularity) started to appear (as displayed in Fig. 1.12), together with a peak in the magnetic field that decayed from the center over a length scale given by the magnetic penetration depth.
This was the first time someone started to talk about "type-I" and "type-II" superconductors.

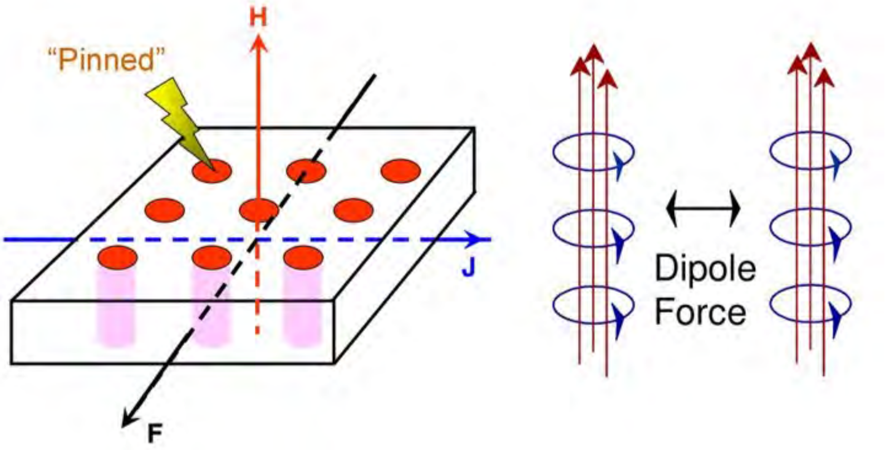

**Fig. 1.12:** Schematics of the vortex state in a type-II superconductor: on the left the lattice, where the tubes of magnetic flux (fluxons) form with a regular pattern, eventually pinned in the sample; on the right, the shape of the flux tubes and the supercurrents, the latter causing the repulsive force occurring between them.
Adapted from: *EPRI Workshop on SCDC Cables, P.Grant 2005*

For type-I superconductors, it is intended a material in which superconductivity is abruptly destroyed when the strength of the applied field rises above a critical value $H_c$, as it is visible in Fig. 1.13a. For type-II superconductors instead, there is no more a single critical field, but two different ones: the first is called "lower critical field" $H_{c1}$ and it delimits the Meissner-effect region, while the second is the "upper critical field" $H_{c2}$ (Fig. 1.13b). Above the latter, the sample is again normal conducting, while between the two fields takes place the so called "vortex phase" or "mixed state": magnetic field vortices form if an external magnetic field is applied, eventually increasing their density with increasing external field strength. The vortices are also called "fluxons", small tubes of normal phase surrounded by supercurrents circulating around the normal core.

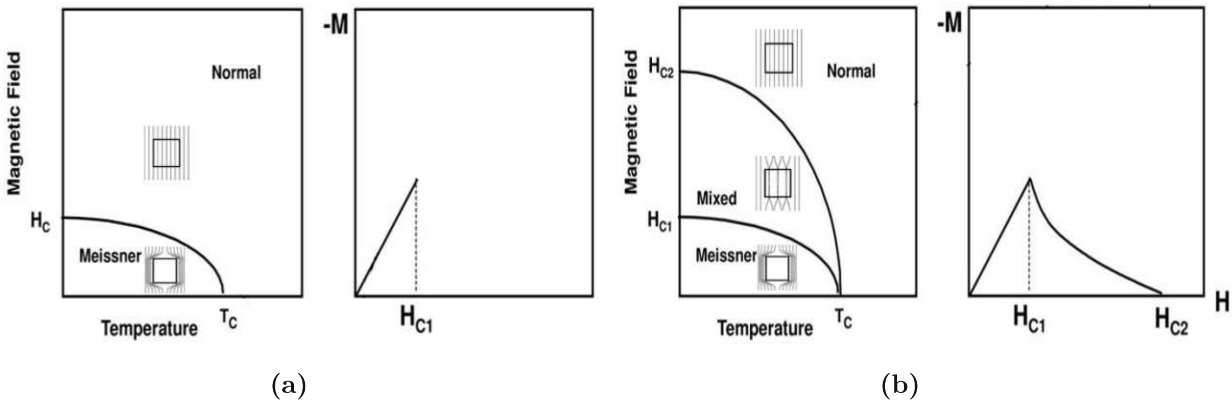

**Fig. 1.13:** a) Magnetic phase diagrams for a type-I superconductor: the Meissner region coincides with the superconducting state.
b) Magnetic phase diagrams for a type-II superconductor: the Meissner state gives way to Abrikosov's vortex state as the field is increased above $H_{c1}$.

Fig. 1.12 shows how a type II superconductor, that carries a transport current, will experience a Lorentz force acting on the flux-line lattice (also known as "FLL"). A free movement of the flux-line lattice would result in dissipation, thus destroying zero resistivity.
But Fig. 1.12 shows also the appearance of another phenomenon: flux pinning. The latter refers literally to the "trapping" occurring to the field penetrating the superconductor bulk as it would happen - figuratively- by "pinning" a brooch on a texture. Magnetic flux pinning, in type-II superconductors, occurs on the fluxons, which form in quantized packets (to be thought as tubes arranged in a fix-shaped lattice, mostly triangular).
Fluxons have therefore fixed density, diameter and length, the former being determined (per unit volume) as:

$$L_{fl} = \frac{B}{\phi_0} \qquad (1/m^2) \tag{1.6}$$

where B is the magnetic field and $\phi_0$ is the magnetic flux quantum.
Flux quantization was indeed one of the most important outcomes of the research on superconductivity, being experimentally confirmed in 1961 by Deaver and Fairbanks [37], Doll and Näbauer [47]. Flux quantization is also the key idea behind the superconducting quantum interference devices (SQUID), which is one of the most sensitive magnetometers available nowadays [104, 116].
Including Abrikosov's work, the first proposing a way to distinguish type-I from type-II superconductors - still at a phenomenological level - was the same Landau in the late 50's.
According to GL theory, in a type-II superconductor the ratio $\kappa = \lambda/\xi$ - known as "Ginzburg-Landau parameter" - is $> 1/\sqrt{2}$, while for type-I superconductors stays $<1/\sqrt{2}$. Most of the materials belonging to the last category are elemental superconductors, as it is the case for the very first discovered Hg, down to Pb with its record $T_c$ value (among type-I) of 7.2 K.
All the alloys, some pure elements (Nb, V, etc. ) and every oxide ceramic compound (HTS family) are instead type-II superconductors, being their impurities a key reason for their flux pinning: fluxons are in fact pinned mostly by heterogeneities/defects of the crystalline lattice.

The discovery of the *isotopic effect* [133] - by which the transition temperature of a superconductor was found to go up as the inverse square root of its isotopic mass of the element - suggested the vibrations of the ionic lattice (or phonons) to be playing a key role in the involved physics, thus preparing the table for a first, microscopic, understanding of the mechanism involved in superconductivity.
In 1957, as an incredible achievement in many-body physics, John Bardeen, Leon Cooper and J Robert Schrieffer, at the University of Illinois, presented a microscopic theory of superconductivity known as the Bardeen–Cooper–Schrieffer (BCS) theory [10].
Cooper already showed one year before, that in the presence of an attractive interaction (whatever small) two independent electrons above a filled Fermi sphere are unstable toward the formation of a so-called "bound Cooper pair" [35]. The subsequent year, the three scientists demonstrated that this evidence accounts for all the conduction electrons in a solid.
Two negatively charged electrons experience a repulsive Coulombian interaction, but the formation of a bound pair requires an attractive interaction between the electrons. Understanding the origin of the latter was clearly the stroke of genius: this net attractive interaction results from interactions involving the crystalline lattice, being sufficient to overcome the repulsive forces. As

a conduction electron travels through the lattice, it experiences an attraction to the positively charged ions on the lattice sites.
This interaction can displace the ions from their equilibrium lattice positions, resulting in a region of increased positive charge density constituting an attractive potential for other electrons. The attraction is mediated by the lattice phonons (quanta of lattice vibrations), which act on the 2-electrons interaction over a characteristic distance called "coherence length" $\xi_0$.

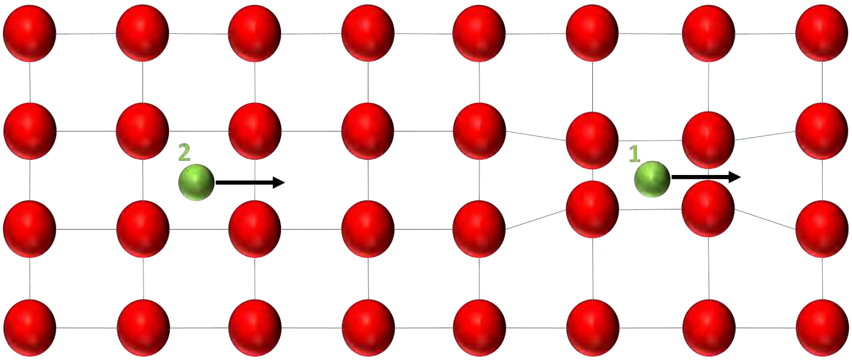

**Fig. 1.14:** Representation (2-D) of a superconductor crystalline lattice: the red spheres are the ions, the green ones the electrons. When the first electron moves through the lattice, the ions will slightly displace, so creating a potential attracting the second electron.

Fig. 1.14 illustrates how a second electron can be attracted towards the electron that caused the ion displacement, therefore forming a bound Cooper pair. Since there is a lot of such electron pairs in a superconductor, these pairs overlap very strongly and form a highly collective condensate. Cooper pairs have some bosonic properties, which at sufficiently low temperature are exactly the ones of a Bose-Einstein condensate [24, 49]: Pauli's exclusion principle would in fact not allow electrons (which are fermions) to condense in the same energy level, so they have to behave as bosons. Moreover, the BCS wave function is expressed in the form of a product of creation operators for Cooper pairs, with its coefficients $u$'s and $v$'s being complex numbers: they have each, in principle, a phase [18].
The striking feature of superconductivity is that there is a phase ordering of all the Cooper pairs, resulting in each phase locking to the same value: as Gor'kov made clear in 1959, the overall phase of the BCS wave functions is exactly the phase of the Ginzburg-Landau wave function [80].

As an other consequence, BCS theory demonstrated the existence of an energy gap $\Delta$ for single-particle excitation. The latter, differently from *semiconductors*, is not a band gap, which would arise due to the interaction with the periodic lattice. In superconductors instead, this energy difference lies between the Cooper pairs-occupied ground state and the lowest available state (fermionic), thus defining the energy required to break a Cooper pair and form normal electrons [73].
This gap was first measured by Giaever in 1960: he confirmed that below $T_c$, the available thermal energy is less than the energy gap and hence Cooper pairs contribute for conductivity with zero resistivity. The energy value of $\Delta$ depends on $T_c$ as follows:

$$\begin{cases} \Delta = 1.764\kappa_B T_c & (T = 0) \\ \Delta \approx 3.06\ \kappa_B\ T_c\ \sqrt{1-(T/T_c)} & (T \to T_c) \end{cases} \tag{1.7}$$

where $\kappa_B$ is the Boltzmann constant. As being one of the main achievements of the BCS theory, the critical temperature $T_c$ is predicted in terms of the electron-phonon coupling potential V and the Debye frequency $\omega_D$, being the latter a "cut-off" frequency since it separates the collective thermal lattice vibration from the independent thermal lattice vibration [69].
The electron-phonon coupling can thus be expressed through a dimensionless parameter $\lambda_{ep} = N(E_F)V$, where V represents the (weak) attractive potential ruled by the Debye cut-off energy $E_D = \hbar\omega_D$ and $N(E_F)$ is the so called "DOS" (electron density of states) at the Fermi energy level $E_F$.
The expression for $T_c$ is the following:

$$\kappa_B T_c = 1.134\ \frac{\hbar\omega_D}{\kappa_B}\ e^{-\frac{1}{N(E_F)V}} \tag{1.8}$$

The main limitation of the BCS theory was nevertheless the assumption of electron-phonon weak coupling, in other words not accounting for the lattice vibrations. The latter, was eventually called "weak-coupling approximation" (occurring for $\lambda_{ep} \ll 1$).
Few years later, Eliashberg solved the problem by generalizing the BCS theory to the whole spectrum of lattice vibrations (strong coupling) [55].
Eventually in 1959, Gor'kov understood that the overall phase of the BCS wave functions was just the phase of the Ginzburg-Landau wave function. He showed that one could derive the Ginzburg-Landau theory from the BCS, defining the GL theory as a limiting case of the BCS [80]. Profiting also from the work of Abrikosov, Gor'kov finally extended the phenomenological approach to what we now know as being the "GLAG" (Ginzburg-Landau-Abrikosov-Gor'kov) theory.

Simultaneously but independently of BCS and the other developing theories, the research on manufacturing of superconducting materials, aiming for demonstrating their applicative potential, continued tirelessly.
By studying the properties of the $Nb_3Sn$ compound, J.Kunzler experimentally demonstrated once for all the validity of Abrikosov's intuitions: superconductors do exist in which flux penetrates in the form of quantized flux lines. He not only measured a very high (for that time) critical temperature in $Nb_3Sn$, but also noticed that this material was able to sustain superconductivity at very high magnetic fields and/or high current densities [111, 112].
From his work came the nowadays famous "critical surface plot", a diagram in which the main interconnected values of a type-II superconductor - namely $T_c$, $B_{c2}$ and $J_c$ - are displayed together, showing how one parameter modifies the others.
The last one -$J_c$ - as mentioned in Sec. 1.1 is called "critical current density". It can be defined when the Lorentz force, acting on the FLL, becomes larger than the bulk pinning force $F_p$ that prevents the flux-lines from moving. The absolute value of $F_p$ is thus equal to the Lorenz force per volume $\vec{J} \times \vec{B}$ for $|\vec{J}| = J_c$, to be practically expressed as:

$$F_p = J_c B \tag{1.9}$$

$F_p$, therefore $J_c$, depends on the applied field and temperature. The function $J_c$(B,T) thus represents a critical surface, below which the material can carry a loss free current.

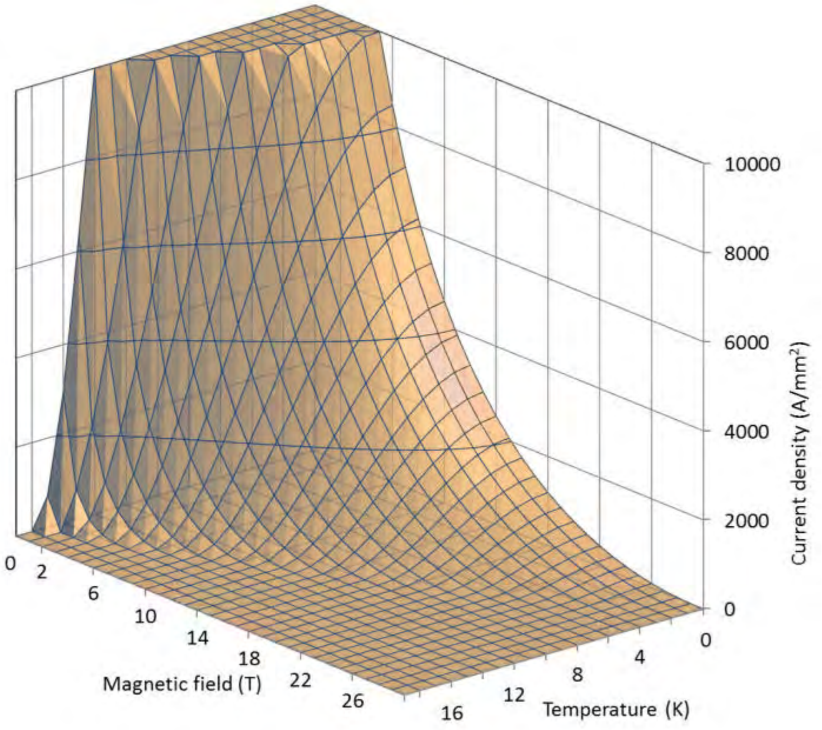

**Fig. 1.15:** Critical surface $J_c$(H,T) of a commercial $Nb_3Sn$ multifilamentary strand. Adapted from: *S.Prestemon and P.Ferracin, "Practical superconductors for accelerator magnets", 2015*

Figure 1.15 displays the critical surface for $Nb_3Sn$ as for the most updated values present in literature. During the last 60 years, this plot was periodically modified, according always to most updated performance of the further and further optimized $Nb_3Sn$. Pushing the superconductors performance to its physical limits, by shaping them in a feasible applicative form (wire/tapes/etc.) was the goal for both manufacturers and scientists in the last decades.

Speaking about $Nb_3Sn$, this thesis aims to shed light on the reasons for the pinning force improvement occurring in one of the last manufacturing technologies of this type-II superconductor (APC-$Nb_3Sn$), by understanding how different types of microstructure impact on retaining the fluxons, thus increasing $J_c$.

A description of $Nb_3Sn$ and the APC manufacturing is given in Sec. 1.3, while the models used for describing the flux pinning in this superconductor are presented in Sec. 1.4.

## 1.3 Artificial pinning centres (APC) $Nb_3Sn$

As mentioned, in Section 1.1, $Nb_3Sn$ is a LTS part of the $A_3B$ (also known as A15) family.

It exists in a thermodynamically stable condition if the Sn content ranges from 17 at.% to $\sim$ 25 at.% [62]. In fact, even though A15 compounds have the nominal composition ratio of $A_3B$ (and their stoichiometric $A_3B$ composition is obtained by diffusion), actually all possible compositions that are stable also form, thus producing a range of superconducting properties. The phase diagram of $Nb_3Sn$ is presented in Fig. 1.16.

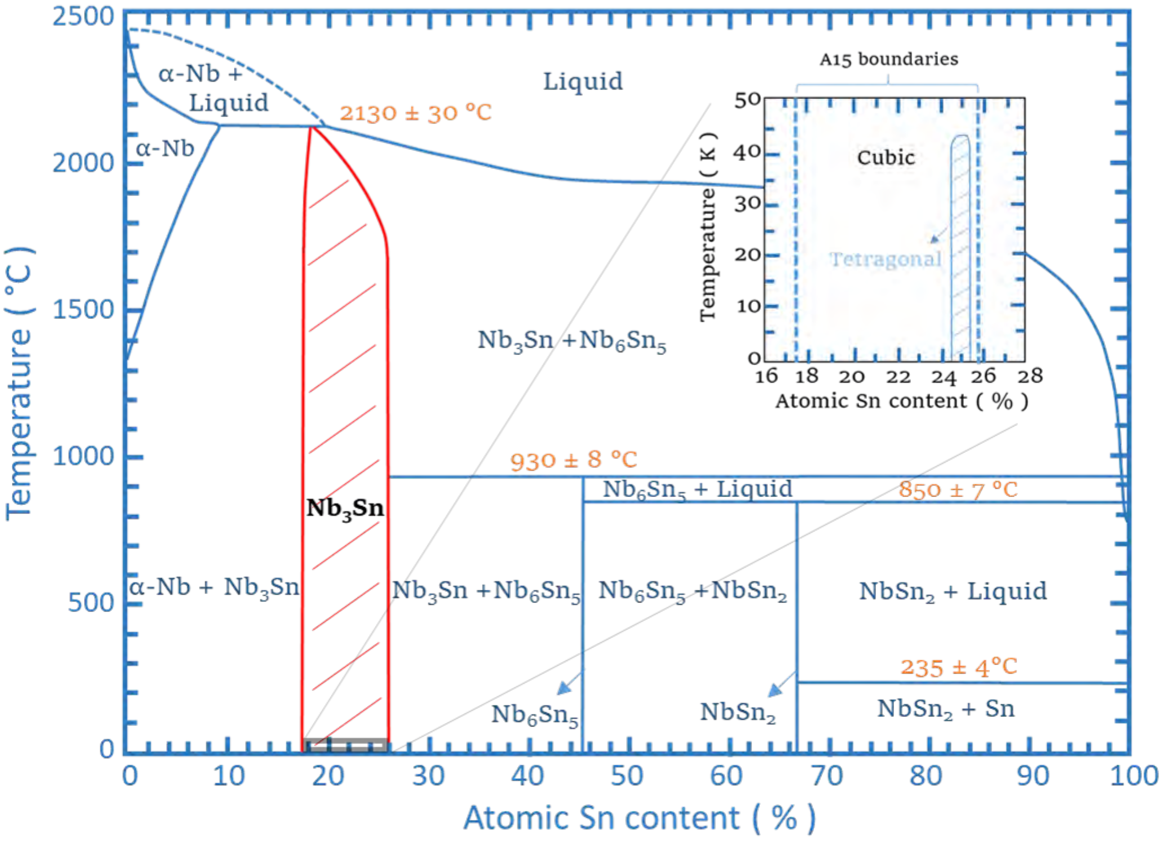

**Fig. 1.16:** Phase diagram of the Nb-Sn binary system. The red dashed area is the region where $Nb_3Sn$ is formed. Within the latter, the zoom inset shows the martensitic transformation that $Nb_3Sn$ undergoes below the temperature $T_m$ = 43 K: the cubic A15 lattice gets distorted into a tetragonal lattice for Sn content above 24.5 at.% (up to 25.2 ± 0.2. at.%) [62].

The phase diagram shows a variety of possible compounds of Nb and Sn, with the formation of the A15 phase being between 17 and about 25.2 ± 0.2. at.% in Sn content. As mentioned in Section 1.1, the latter is the superconducting phase of interest, having normally a cubic structure but undergoing to a tetragonal distortion - displayed in Fig.1.17 - if the Sn content (also called "$\beta$" ) is between 24.5 and 25.2 Sn at.%, and only if $T < 43$ K.
The latter is called *martensitic* temperature $T_m$ and the lattice transformation occurring below it modifies significantly the performance of the superconductor, e.g. $T_c$: a lattice softening occurs, implying a decrease in the lattice stiffness that results in a $T_c$ reduction according to *McMillan*'s $T_c$ equation [2].

The highest recorded $T_c$ for $Nb_3Sn$ (without doping additions) is 18.3 K [90], which together with the upper critical field $H_{c2}$ and the electron-phonon interaction constant $\lambda_{ep}$ constitutes the main set of fundamental parameters for applications. Moreover, $Nb_3Sn$ wires are often doped with ternary specimens as Ti, Ta and Cu, which change the properties significantly e.g. by

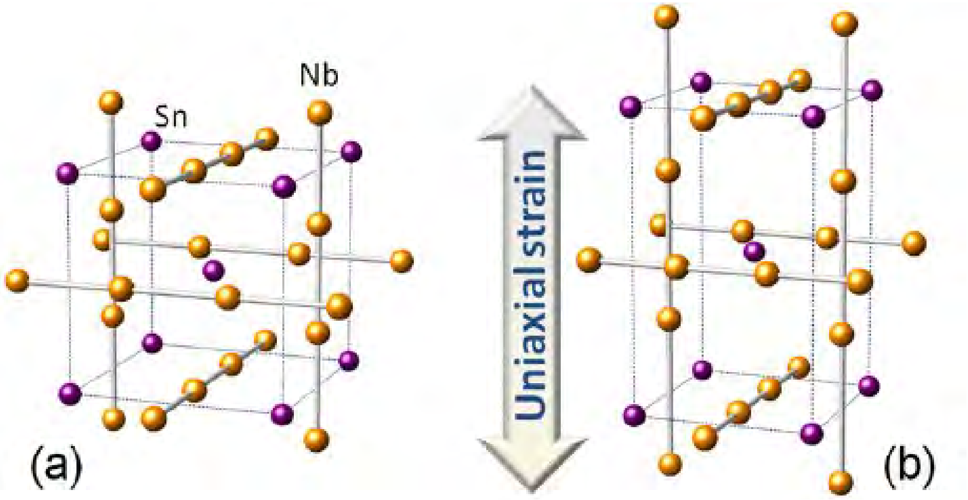

**Fig. 1.17:** Differences in atomic arrangement between cubic and tetragonal $Nb_3Sn$ A15 phases. On the left, Fig.(a) shows the *bcc* structured $Nb_3Sn$ unit cell, with the orange balls being the Nb sites, while the violet ones refer to Sn atoms. Fig.(b) shows the tetragonal distortion occurring for T < 43 K.
Credits: *M.Buongiorno*.

substituting to Nb or Sn sites [95] or catalysing the formation of intermediate phases during the diffusion process [63].
Table 1.2 summarizes the main properties for technical $Nb_3Sn$ wires, considering their best ever recorded values.

In Table 1.2, the upper critical field value is indicated as a threshold, since it refers to the best ternary/quaternary optimized samples. In fact, their value can vary significantly (e.g. by 2-3 T for $\mu_0 H_{c2}$) by alloying ternary/quaternary elements such as Ta, Zr or Ti.
Actually, when it comes to wires fabrication, the $Nb_3Sn$ A15 formation already involves three elements, since also Cu is present in every manufacturing as mentioned in Sec. 1.1. Therefore, ternary phase diagrams should be used, but at the present day literature data often disagree from each other, resulting in a general lack of exact knowledge on the Cu-Nb-Sn ternary system. The absence of information on this respect is nevertheless not dramatic as Cu does not modify much the superconductor behaviour, except for a certain suppression of $\mu_0 H_{c2}$ [106].

Ta and/or Ti additions are instead historically used for improving the performance of the A15 phase. As mentioned in Sec. 1.1, one of the remaining optimization issues to be solved in $Nb_3Sn$ manufacturing is the wide compositional range of Sn along the diffusion direction, which results for example in a continuum of $T_c$ values rather than a single one (referred as "$T_c$ distribution"). Moreover, also the individual grains themselves are different from each other in composition, resulting in a broader transition when measuring $T_c$ or $B_{c2}$ [155].
By the way, optimizing Sn homogeneity is not the only way for improving the superconducting relevant parameters for applications.
Substituting elements as Ti and Ta to Sn or Nb sites (recent study demonstrated the interchangeability of both dopants substituting both elemental sites [188]) slightly modifies the cubic lattice, impacting e.g. on the normal state resistivity $\rho_n$ (the resistivity measured at a temperature slightly above $T_c$). As a first clear effect, these two elements are able to suppress the tetragonal

Tab. 1.2: Selected best parameters of $Nb_3Sn$ for applications as in [77, 84, 106, 139, 146, 147].

| Parameter | Symbol | Value |
|---|---|---|
| Highest critical temperature | $T_c$ | 18.3 K |
| Martensitic transformation temperature | $T_m$ | 43 K |
| Lower critical field* | $\mu_0 H_{c1}$ | $< 0.05$ T |
| Upper critical field* | $\mu_0 H_{c2}$ | $> 30$ T |
| Lattice parameter** | $a$ | 5.293 Å |
| Ginzburg-Landau coherence length* | $\xi$ | 3.6 nm |
| Ginzburg-Landau penetration depth* | $\lambda$ | 124 nm |
| Superconducting energy gap | $\Delta$ | 3.4 meV |
| Electron-phonon interaction constant | $\lambda_{ep}$ | 1.8 |

* At zero temperature.
** At room temperature.

distortion at low temperatures, at contents above 2.8 at.% for Ta and 1.3 at.% for Ti, thus allowing profiting from the higher critical field values of the cubic phase (up to 4 T at zero temperature) [21, 67, 76].

Moreover, the upper critical field $B_{c2}$ can even be increased, as a consequence of an increased disorder. In fact, $\rho_n$ depends on $\kappa$ as explained by Gor'kov [81] - in the framework of the GLAG theory - with the following equation:

$$\kappa = \kappa_0 + C\sqrt{\gamma}\rho_n \quad \text{for } l << \xi_0 \qquad \text{with} \quad C = 2.37 \cdot 10^6 \, \frac{\text{kg}^{3/2}\ \text{m}^{5/2}}{\text{K A}^2\ \text{s}^4} \tag{1.10}$$

Equation 1.10 is called the "Gor'kov-Goodman" relation, where $\kappa_0$ is the Ginzburg-landau parameter of pure $Nb_3Sn$, $\gamma$ the Sommerfeld's electronic specific heat coefficient, $l$ is the electronic mean free path and $\xi_0$ is the (BCS) coherence length.

The condition $l << \xi_0$ is what is called "dirty limit" of a type II superconductor [1, 123, 127], meaning that the short electron free path results from more scattering, macroscopically manifesting in a resistivity increase.

If we then consider the relationship from Abrikosov's work [1]:

$$B_{c2} = \kappa\sqrt{2}B_c \tag{1.11}$$

it is possible to understand how a more disordered ("dirtier") compound results in a higher $B_{c2}$. The thermodynamic critical field $B_c$ is in fact expected to change only slightly considering that also $T_c$, at the same time, is expected to be slightly lowered due to increase disorder ($B_c = N(E_f) \cdot \Delta^2$, with $\Delta \propto T_c$ as shown in Eq. 1.7).

In terms of highest sustainable $J_c$(B), no doping additions - thus no additionally triggered mechanism - is known to date to contribute "per se" on increasing the bulk pinning force $F_p$ (therefore $J_c$, as in Eq. 1.9). Rather, the current transport properties are determined by the pinning scenario, as it is typical of a type-II superconductor, and none of the additives so far listed is acknowledged to act as additional pinning centres in $Nb_3Sn$.
Despite the great investments and efforts made for improving the non-Cu $J_c$(B) of the most optimized wires, no relevant achievements have been reached in the last two decades in this respect, resulting in a plateau of the highest achievable current density since ∼ 2003 [152]. Solving once for all the Sn-diffusion problem is still considered an insurmountable issue, and lighter solutions - as further optimization of the heat treatments [165] - do not bridge the gap on carrying $Nb_3Sn$ to the high current levels required nowadays (e.g. hh-FCC target).
Despite the general conclusion for $Nb_3Sn$ to have reached its maximum exploitable potential [60, 208], in 2014 X.Xu and M.Sumption at The Ohio State University (US) proposed an interesting, new, manufacturing method promising great results.
Based on the idea that in $Nb_3Sn$ flux pinning is historically known to occur mainly alongside the grains surfaces (also called "grain boundary pinning"), this research group - in collaboration with Hyper Tech Research, Inc. (Columbus, US) - studied a possible way to let the $Nb_3Sn$ grains growing smaller, therefore increasing the number of grain boundaries, thus the flux pinning potential [217].

Fig. 1.18 shows how, through about 30 years, a lowering of the average (representative) grain size GS (expressed as average diameter) in $Nb_3Sn$ samples has led to an increase in $F_p$, accordingly. The relationship $J_c \propto 1/GS$ is valid independently from the selected wire manufacturing process (indeed a mix of several manufacturing, at different levels of optimization, is collected in Fig. 1.18). For the current normalized by the A15 layer only ("layer $J_c$"), the single line on the semi-logarithmic plot of in Fig. 1.18 has the following expression:

$$F_{p-max} = 39.2\ ln(\frac{1}{GS}) - 10 \qquad (\mathrm{GN/m^3}) \tag{1.12}$$

For $Nb_3Sn$, an average grain size of less than 50 nm were so far reached only in film production [174] or with two-stage (often not reproducible) reactions in multifilamentary wire [167], but still never brought to the industrial level, therefore never optimized.
Several other research groups have chased the same goal with a number of techniques, but none was able to both refine GS and produce high-$J_c$ strands at the same time [64, 141, 158, 220, 221]. Present day average GS in $Nb_3Sn$ strands is about 100-200 nm [76, 120], considering each fabrication technology to aim at using only the grain boundary (GB) pinning mechanism potential. The latter is even not fully exploited, since ideally the optimum grain size should be tailored on the expected spacing between the fluxons (with the assumption of 1 boundary

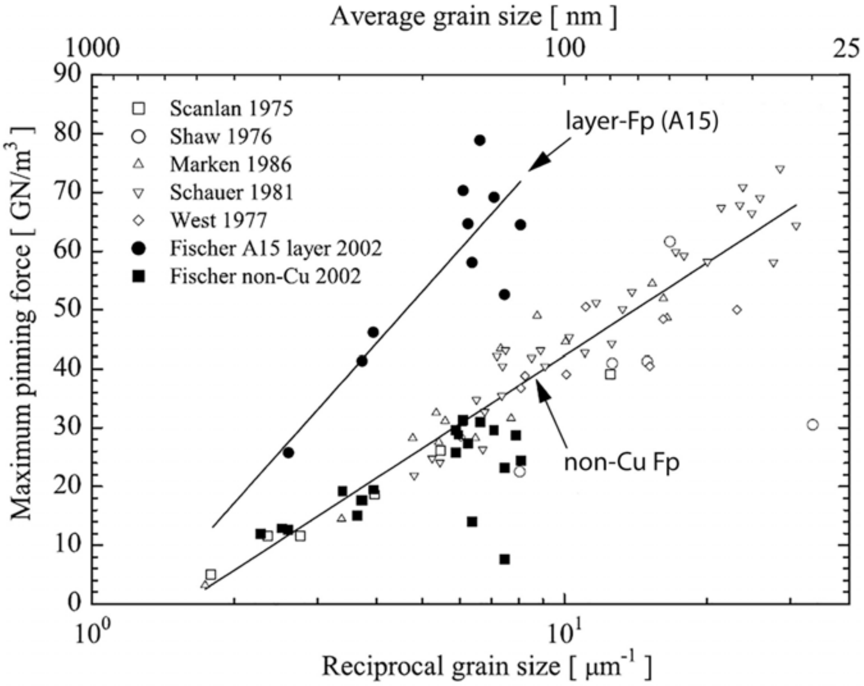

**Fig. 1.18:** Maximum pinning force $F_{p\text{-}max}$ vs 1/grain size for different type of $Nb_3Sn$ samples from different manufacturing through about 30 years. Both the layer- and non-Cu-$J_c$ trendlines are shown.
Adapted from: *A.Godeke, PhD Thesis.*

pinning 1 fluxon). In fact, if we assume a triangular flux line lattice, it is possible to calculate the spacing between each flux line at a specific field as follows [191]:

$$FLS_{\Delta}(H) = \left(\frac{4}{3}\right)^{1/4} \left(\frac{\phi}{\mu_0 H}\right)^{1/2} \tag{1.13}$$

where $\phi$ is the magnetic flux quantum and $FLS_{\Delta}$ is the flux line spacing (for a triangle), which results in $\sim$ 11 nm at 16 T (e.g. the operational field for hh-FCC).
Based on these improvement margins, the Ohio State group conceived a technique for refining the grain size by deploying the internal oxidation method in strands [217]. The key idea behind internal oxidation is that using a less noble solute than the solvent can specifically attract oxygen to the solute, in a solid solution. The oxygen partial pressure is high enough to oxidize *selectively* the solute only, eventually producing oxided particles which may precipitate in the matrix (solvent) [3]. The real applicative news for strands, in this respect, were the way and aim why this technique was deployed: using a specific oxygen source and pointing to refine the surrounding matrix (A15 grains), respectively.
In a naive but efficient way, the idea was to create a finer microstructure as the grains are forced to grow smaller by the presence of oxide precipitates all around them.

Trying Zr as being the solute was almost a straight decision, since its affinity to oxygen is well above the Nb level [38, 164] and the Nb-Zr alloy is relatively common on the market.

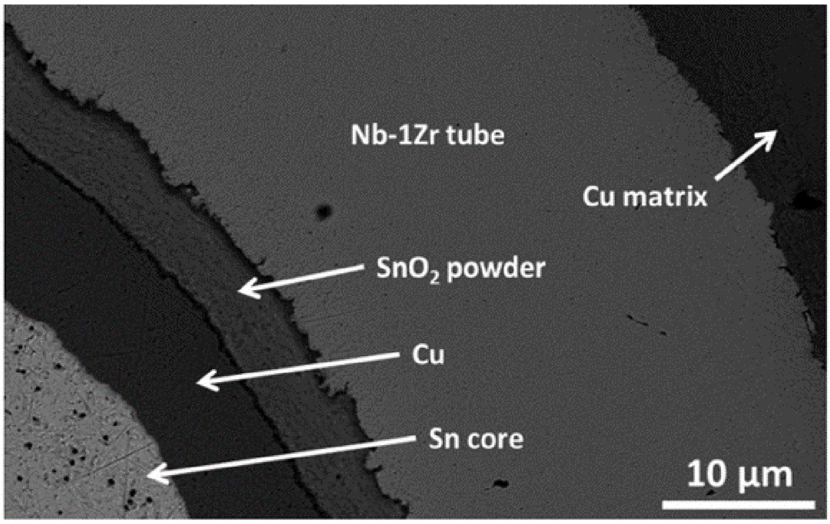

**Fig. 1.19:** Back scattered electrons (BSE) image taken with scanning electron microscope (SEM) of one of the first mono-filamentary wires (cross section), before reaction. The $SnO_2$ source is placed between the Cu-tube and the Nb-Zr alloy.
Credits: *X.Xu*.

Particular attention was given instead to the oxygen source choice.
Addressing the latter was the main problem, among the mentioned attempts during the 80s and 90s, preventing from producing refined grain $Nb_3Sn$ strands because:

- Oxygen cannot be pre-dissolved in the Nb-Zr matrix since the billet has to be drawn to its final filamentary shape. Drawing-related issues are the main problem when trying to alloy new elements, considering how dangerous would mean enriching the $Nb_3Sn$ precursors with hard compounds (especially oxides), resulting in possible cracks/breakages during the extrusive process [220];
- Oxygen cannot be supplied from the exterior, since transporting it towards the core would be blocked by the outer Cu sheath [213];
- Metal-oxide powders can be a solution but selection of the metal is critical: it should be more affine to O than Nb, for being easily reduced during the heat treatment thus freeing O. On the other side, it must not be too noble, thus preventing from releasing too much O that would oxidise both Nb and Zr [207].

For this reason, oxygen was introduced as $SnO_2$ powder and placed between the Sn-Cu core and Nb-Zr alloy, as it is shown in Fig. 1.19. This layout granted O not to be blocked by Cu and the specific $SnO_2$ powder (other powders were tried out, as ZnO or $Nb_2O_5$) to supply enough O ($> 2$ at.%), eventually oxidizing all the Zr atoms.
The final output is a refined A15 microstructure, with grains reproducibly growing at about GS = 20-90 nm. Moreover, the formation of $ZrO_2$ nanoparticles was clearly confirmed by transmission electron microscopy measurements, as it is shown in Fig. 1.20.

This manufacturing, which fall into the "tube type" category [182], showed record $J_c$ values from the very first mono-filamentary sample.

**Fig. 1.20:** Transmission electron microscope (TEM) picture of the A15 microstructure in a monofilamentray APC-$Nb_3Sn$ sample. $ZrO_2$ nano-precipitates are visible both between and within the grains.
Adapted from *X.Xu, APL 2014*.

This evidence was explained by a two-fold pinning gain: on one side, the GB pinning mechanism was optimized, since as explained a finer grain structure allows to more fluxons to get pinned; at the same time, a different - simultaneous -pinning mechanism takes place.
The $ZrO_2$ particles, ranging between 1 and 20 nm in diameter from the first evaluations, could act as *point pinning centres*, each being able, in principle, to pin a fluxon. Their active role was confirmed by pinning force measurements, showing the peak $F_{p\text{-}max}$ to shift towards higher field ranges. As it will be better explained in the next section, this is a clear indication of point particle pinning, a second pinning mechanism eventually occurring in these samples together with GB pinning [42, 110, 166], explaining the name assigned to this new product: artificial pinning centres (APC)-$Nb_3Sn$.

The success obtained with these first mono and (right after) 48-filament binary wires revitalized a general interest in material science research on $Nb_3Sn$, enhancing other scientists in the world to try the same or slightly different approaches [5, 27, 28]. Eventually, also Hf was tried in place of Zr, with promising results, as well as ternary-APC strands (Nb-Zr/Hf-Ta starting alloy). Powder-in-tube approaches (similar to tube-type) started to be applied to the manufacturing (Fig. 1.21, further shortening the path towards APC-$Nb_3Sn$ final optimization steps: thermal/magnetic stability in the 10-20 T range, drawability in long lengths, good mechanical features under typical magnet layout stress conditions, etc. [8].

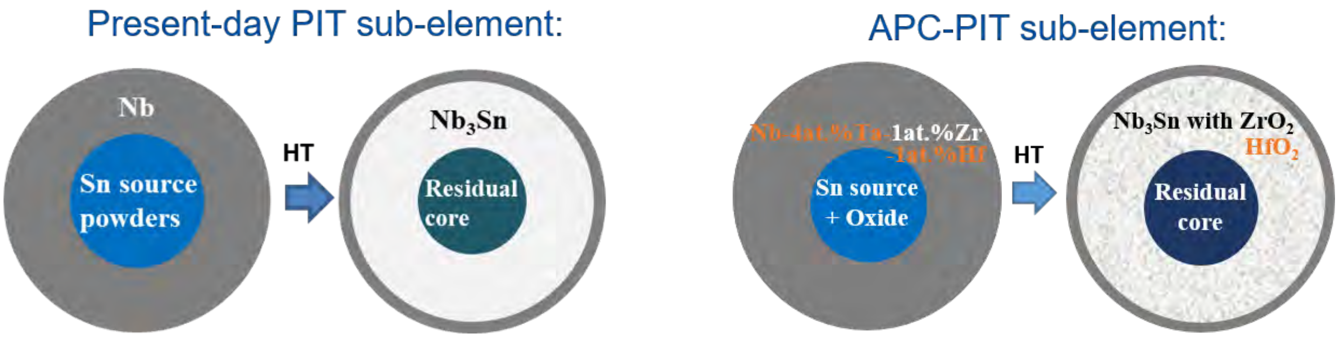

**Fig. 1.21:** Differences between starting/final layout for standard PIT (left) and APC-PIT (right) $Nb_3Sn$ manufacturing technologies.

The evolution of the superconducting properties, as well as the identification of the microstructual features and understanding of the complex flux pinning scenario involved in the APC-$Nb_3Sn$ samples was the core of this Thesis.
Details on the flux pinning models correlating the bulk pinning force to the microstructural features are discussed in Sec. 1.4, while details on the studied samples are given in Chapter 2.

## 1.4 Flux pinning: a new perspective

In this section, some of today's main models for predicting the bulk pinning force $F_p$(B) are showed and briefly discussed. Moreover, the most interesting parameters - to date not yet fully understood- are highlighted and considered for a new interpretation.

As mentioned in Sections 1.2 and 1.3, flux pinning is the true applicative feature of superconductors (type-II). The importance of flux pinning is seen more and more often also in every day's life, through implementations such as lifts, frictionless joints, and transportation.
The key feature of flux pinning are the pinning centres, which can manifest in several ways always as a microstructural characteristic of the sample. As mentioned, defects in the superconductor crystal are able to retain the fluxons to move from the their high density region to the low density region (driven by the repulsive interaction between them), schematically picturable as in Fig. 1.22.

Pinning centres interact with fluxons because of the different superconducting properties of the former compared to the latter. This gap can be small, as e.g. differences in $\kappa$ due to changes in $\rho_n$, compositional gradients of the superconducting phase or even by martensitic transformation of the lattice structure. The difference can be instead relevant if the pinning centres are non-superconducting particles, typically being insulators, other metals or even voids. Therefore, if we divide the pinning centres in these two categories, we can refer to their role as "$\Delta\kappa$" or "normal" pinning centres, respectively.
This was the distinction upon which the pinning mechanisms of type-II superconductors were first classified, in 1974 by D. Dew-Hughes [42]. The latter, together with Fietz, Webb and Kramer [61, 110] set the formalism of the magnetic field dependence of the bulk pinning force $F_p$(B), still valid and in use nowadays. In this thesis, the focus is on the practical set of equations published

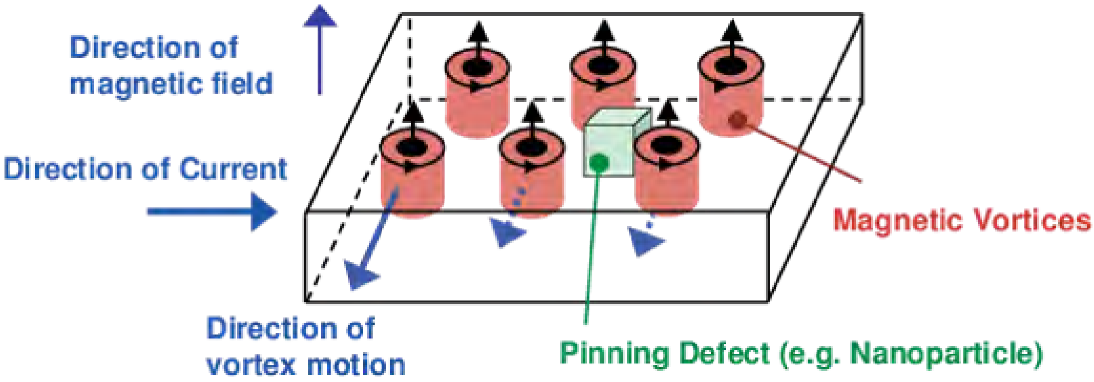

**Fig. 1.22:** Schematics of a flux-line lattice FLL. The possible presence of defects as nanoparticles is portrayed as being preventing the vortexes to drift in the direction of the Lorentz force.

by Dew Hughes, as it contains all the key elements - in common with the other authors - of a rigorous derivation of $F_p$(B).
The formulation of the pinning force per unit volume is given as:

$$F_p = \eta L f_p = -\eta L \Delta W / x \tag{1.14}$$

where $f_p$ (N/m) is the pinning force per unit length of pinned flux-line (referred often as "elementary pinning force"), being equivalent to the work done in moving a unit length of flux-line from a pinning centre to the nearest position where it gets unpinned, divided by the range $x$ (transversal to the fluxon) over which the pinning occurs. $L$ (m/m$^3$) is the effectively pinned length of the flux-line (per unit volume) and $\eta$ is considered an "efficiency factor", so far not thoroughly explained in literature but indicated to be related with the elasticity of the flux line lattice FLL.
For many Nb-based superconductors, Fietz and Webb found out that, if $F_p$ is plotted as a function of the reduced field h=H/$H_{c2}$, the pinning force obeys a scaling law having the form:

$$F_p(h,T) \propto H^n_{c2}(T) f(h) \tag{1.15}$$

where the exponent $n$ and the function *f(h)* depend both on the characteristic pinning mechanism operating in the given superconductor. The striking feature of *f(h)* is the position $h_{peak}$ of its maximum, which clearly identifies the undergoing pinning mechanism [30].

An important role is also played by the magnetic penetration depth $\lambda$. In 1972 in fact, Hampshire and Taylor pointed out how the microstructure, if compared to $\lambda$, gives room for two different type of possible interactions: "magnetic" and "core" [88].
The first occurs if the size $a$ and spacing $l$ of the pinning centres are greater than $\lambda$: the magnetic field induction B will be able to adjust everywhere to its equilibrium value, being it different in

the pins from that in the matrix. This $\Delta B$ results in a Bean-Livingston barrier blocking the flux motion, thus pinning the fluxons.
Core interactions occur instead if $\lambda$ is greater than $a$ or $l$. The local modification of the order parameter by the presence of defects has an incidence on the electronic structure and the diameter of the vortex core. These give rise e.g. to a local change in $T_c$ and hence of the condensation energy $E_c = \frac{1}{2}\mu_o H_c^2$ – the energy gain due to the formation of a paired sate [191] - which may range from a minor, secondary effect (due to local strain, for example) to the complete suppression of superconductivity in or around the defect. In more generic terms, core pinning is provided when there is a gain in the Gibb's function of unit length of flux-line as it moves from the matrix to the pinning centre.

Besides the type of interaction, the shape and size of the pinning centre, compared to the inter-flux-line spacing $FLS_\Delta(H)$ (cf. Eq. 1.13), defines also the magnitude and the field dependence of $F_p$. "Point pins" are microstructural features as precipitates or voids, with each dimension being smaller than $FLS_\Delta(H)$. They usually interact with only one flux line over their length. "Surface pins" are considered instead grain-, twin- and martensitic boundaries. These planar defects have two dimensions bigger than $FLS_\Delta(H)$, exploiting their full pinning potential once oriented perpendicular to the direction of the Lorentz force. Finally, features as large precipitates or thick dislocations cell-structures are considered as "volume pins", having all their dimensions larger than $FLS_\Delta(H)$. They interact with the fluxons through their surface, being the projection of the latter (in the direction of the Lorentz force) the relevant parameter for calculations.
All in all, core volume pinning is preferably expected to occur at high field as $FLS_\Delta$ decreases, resulting in a set of pinning functions (rather than a single one) for describing the full field-range pinning spectrum.
Equation 1.14 shows how the bulk pinning force $F_p$ functions are based on thermodynamic arguments. A schematic interpretation of 1-3 D types of pinning mechanism is shown instead in Fig. 1.23.

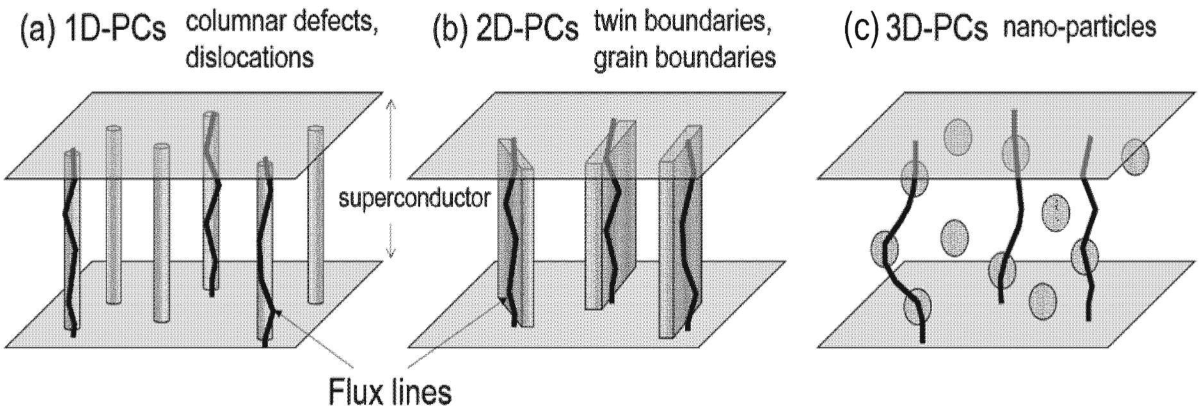

**Fig. 1.23:** Different type of pinning mechanisms grouped by shape. Adapted from *Sueyoshi, IEEE 2021.*

For magnetic pinning for example, pinning strength is based on the work done in moving a quantity of flux $\phi_0$ through a boundary separating two regions of different induction $\phi_0 \Delta M(B)_{rev}$, where $\Delta M(B)_{rev}$ is the difference in reversible magnetization [29]. For each type of the aforementioned pinning mechanism, the practical series of equation collected by Dew Hughes is listed in Tables 1.3 and 1.4, these containing the ingredients useful to calculate the bulk pinning force (N/m$^3$) for each specific pinning interaction.

**Tab. 1.3:** Parameters to be used for calculating $F_p$(B) as in Eq. 1.14.

| Interaction | Pin geometry | L | $x$ | Type of centre | $\Delta W(H)^*$ | $F_p(H)^*$ | $h_{peak}$ position |
|---|---|---|---|---|---|---|---|
| Magnetic | Volume | $\frac{S_v}{d}$ | $\lambda$ | Normal | 1 | 1 | h=0.33 |
| | | | | $\Delta\kappa$ | 2 | 2 | h=0.17, 1 |
| Core | Volume | $\frac{S_v}{d}$ | $d$ | Normal | 3 | 3 | - |
| | | | | $\Delta\kappa$ | 4 | 4 | h=0.5 |
| | Surface | $\frac{S_v}{d}$ | $\xi$ | Normal | 5 | 5 | h=2 |
| | | | | $\Delta\kappa$ | 6 | 6 | h=0.6 |
| | Point | $\frac{BV_f}{\phi_0}$ | $\frac{a}{2}$ | Normal | 7 | 7 | h=0.33 |
| | | | | $\Delta\kappa$ | 8 | 8 | h=0.67 |

$^*$ $\Delta W(H)$ and $F_p(H)$ functions are indicated by a number referring to the respective equation in Tab. 1.4.

In the first of the two tables, the interaction type, the pin shape, the length of interacting flux line $L$ and position $h_{peak}$ corresponding to the maximum of $F_p$(H) are shown. The second table contains instead the $\Delta W(H)$ functions for each mechanism to be plugged in Eq. 1.9 and the respective $F_p$(H) to be used for directly calculating the bulk pinning force (N/m$^3$).
The length of interacting flux-line $L$ is a particularly interesting parameter, since it is related both to the type of pinning centre and the *rigidity* of the FLL.
According to [42], if we consider in fact a pinned flux-line to be perfectly rigid, it will have (averagely) a volume fraction $V_f = (a/l)^3$ of its length inside the pinning centre, where $l$ (m) is the average distance between the centres. As pointed out also by Petermann [154], the apex of this ratio should be indicating the degree of flexibility of the FLL, being $V_f = (a/l)$ the volume fraction in case of perfectly flexible fluxon. The actual value lies most probably between the two extremes, as it was also suggested by Labusch: the FLL experiences indeed elastic distortion under the action of pinning forces [114]. His calculation of the elastic constants of the fluxoid lattice were derived for point pins (called "point obstacles"), with the formulation for linear (dislocations)/surface/volume pins needing only adjustments from the latter [115]. Further discussion and a deepening of this term will be present in Sec. 4.2.

**Tab. 1.4:** $\Delta W(H)$ and pinning functions $F_p(H)$ as in Eq. 1.14.

| Eq. number | $\Delta W(H)$ | $F_p(H)$ |
|---|---|---|
| 1 | $\frac{-\phi_0(H_{c2}-H)}{2.32\kappa^2}$ | $\frac{\mu_0 S_v H_{c2}^2 h^{1/2}(1-h)}{\kappa^3}$ |
| 2 | $\frac{-\phi_0(H_{c2}-2H)\Delta\kappa}{2.32\kappa^3}$ | $\frac{\mu_0 S_v H_{c2}^2 h^{1/2}(1-2h)\Delta\kappa}{\kappa^4}$ |
| 3 | $\frac{-\mu_0\phi_0(H_{c2}-H)^2}{4.64B\kappa^2}$ | $\frac{\mu_0 S_v H_{c2}^2(1-h)^2}{5.34\kappa^2}$ |
| 4 | $\frac{-\phi_0(H_{c2}-H)\Delta\kappa}{2.32\kappa^3}$ | $\frac{\mu_0 S_v H_{c2}^2 h(1-h)\Delta\kappa}{2.67\kappa^3}$ |
| 5 | $\frac{-\pi\xi^2\mu_0(H_{c2}-H)^2}{4.64\kappa^2}$ | $\frac{\mu_0 S_v H_{c2}^2 h^{1/2}(1-h)^2}{4\kappa^2}$ |
| 6 | $\frac{-\pi\xi^2\mu_0 H(H_{c2}-H)\Delta\kappa}{2{,}32\kappa^3}$ | $\frac{\mu_0 S_v H_{c2}^2 h^{3/2}(1-h)\Delta\kappa}{2\kappa^3}$ |
| 7 | $\frac{-\pi\xi^2\mu_0(H_{c2}-H)^2}{4.64\kappa^2}$ | $\frac{\mu_0 V_f H_{c2}^2 h(1-h)^2}{4.64a\kappa^2}$ |
| 8 | $\frac{-\pi\xi^2\mu_0(H_{c2}-H)\Delta\kappa}{2.32\kappa^3}$ | $\frac{\mu_0 V_f H_{c2}^2 h^2(1-h)\Delta\kappa}{2.32a\kappa^3}$ |

Still in Tab. 1.3, also the pinning interaction distance $x$ is listed. For magnetic pinning for example, this distance over the matrix plane is simply $\lambda$, since the latter is the length over which the magnetic induction changes. For core surface or point pins, since the active dimension of the pins (whatever amount of their size $a$ parallel to the Lorentz force) is always $< FLS_\Delta$, therefore $x = \xi$ is appropriate.

Table 1.3 also shows a characteristic feature of the different pinning mechanism: the characteristic position of $h_{peak}$. Once identified the roots of the different interactions, evaluating $h_{peak}$ has always been the first experimental indication of the operating pinning mechanism: each functional dependence manifests always with the same shape and same peak position, as it is depicted in Fig. 1.24. A different shape from the ones illustrated is therefore a clear indication of mixed-pinning scenario.

If we consider $Nb_3Sn$, grain boundary GB pinning was acknowledged since the 60s to be the main occurring pinning mechanism [61, 166]. This evidence came experimentally by producing samples (mainly by chemical deposition) with grains of different sizes resulting reproducibly in different $J_c$, always $\propto 1/GS$.

A full explanation of this mechanism in $Nb_3Sn$ is to date not available. One interpretation was given by Campbell [30], who stated that grain boundaries provide pinning in just the same way as secondary phases if adjacent grains have different superconducting properties. Following studies addressed these planar defects to be source of flux pinning due to the alteration of the electrons mean free path caused by the electron scattering off the (pinning) plane [197, 219]. This type of pinning is nevertheless clearly dominant in materials showing anisotropy or compositional gradients, eventually suggesting a combination of factors ruling grain boundary pinning.

As an example, if there is a difference of 1% in $H_c$ between grains of $Nb_3Sn$, this results in a drop in field induction across the boundary of about 0.2 mT at 8 T. At the same field, for a

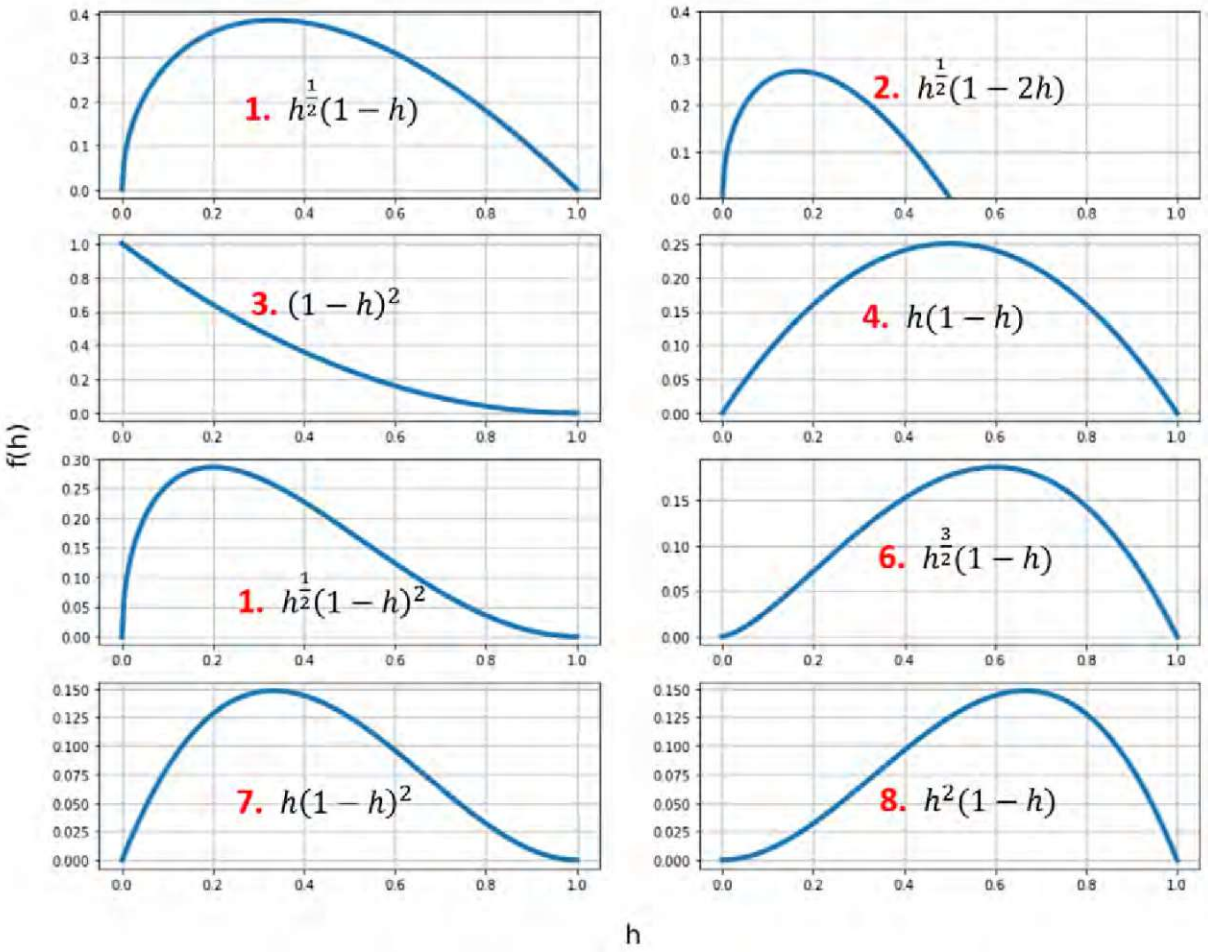

**Fig. 1.24:** Functional dependences f(h) for each listed pinning mechanism as enumerated in Tab. 1.3 and 1.4.

grain size of 40 nm, this gives a current density of about $5 \cdot 10^7$ A/mm$^2$, which was the value measured by Hanak and Enstrom (1966) [89]. After decades of optimization, in commercial $Nb_3Sn$ anisotropies in all the parameters are still likely to be considerably larger than 1 % and *f(h)* continues to peak at about 0.2, further confirming GB to be the leading pinning mechanism in $Nb_3Sn$ A15.
Nevertheless, strong indications of combined pinning mechanism is present in APC-$Nb_3Sn$.
As the oxide precipitates first showed to be forming in nanometric particles ($ZrO_2$ , $HfO_2$ ) distributing everywhere in the A15 matrix, the simultaneous occurrence of point particle PP pinning can be possible.
The impact of a parallel/competitive pinning mechanism occurring together with GB in $Nb_3Sn$ was shown, for example, by proton or neutron irradiation on reacted $Nb_3Sn$ sample [13, 16, 176, 177]. A significantly improved non-Cu $J_c$ by introducing point pinning centres was demonstrated, even though the practical application of radiation damage on present $Nb_3Sn$ winding technology is difficult to foresee. If for the latter addressing the PP contribution is possible as the reacted samples performance can be measured before and after irradiation, for the APC-$Nb_3Sn$ case this assessment is much more difficult. As mentioned, in these samples the nanoparticles formation acts also on the grains refinement, eventually heading to the "holy grail" target of grain sizes comparable to $FLS_\Delta$ (meaning highest GB exploitable potential).

This phenomenon can lead to misinterpretations of the operating pinning scenario. Fig. 1.23 shows the the reduced pinning curves (where f=F/$F_{p\text{-}max}$ and b=B/$B_{irr}$ are plotted) of the first manufactured (monofilamentary) APC-$Nb_3Sn$ samples.

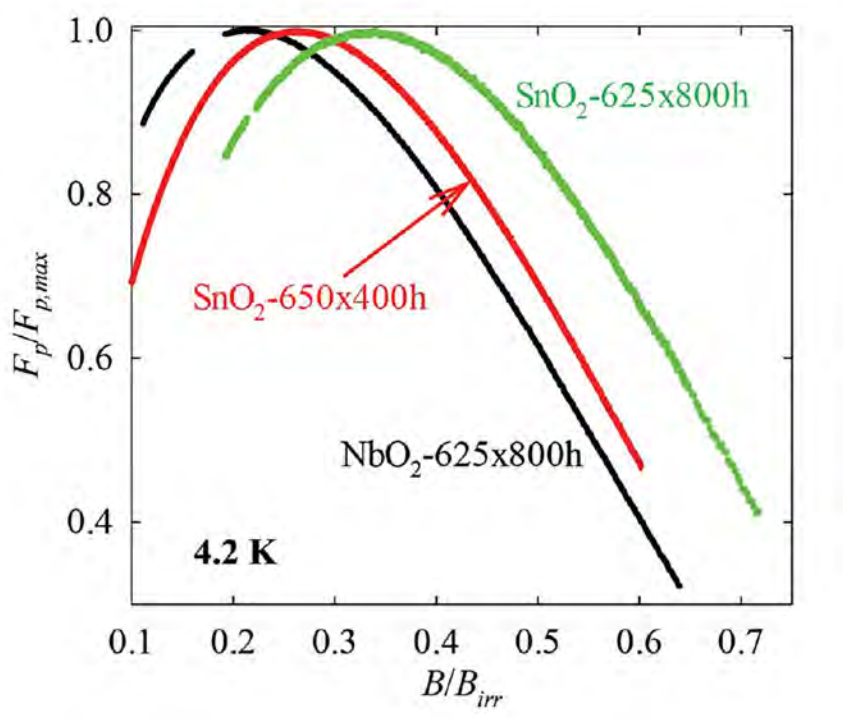

**Fig. 1.25:** Reduced pinning force plot of the first APC-$Nb_3Sn$ samples produced in 2014 by Hyper Tech Research Inc. On the y axis there is $f = F/F_{p-max}$ while on the x axis $b = B/B_{irr}$.
Adapted from *X.Xu, Advanced Materials 2015.*

In this plot three attempts of different oxygen supplying sources/heat treatment parameters are shown, and for the best selection a clear shift towards higher $h_{peak}$ positions is evident.
How was this achieved?
Does this only depend on the - eventually - introduced PP mechanism, or to the GS refinement, or a combination of the two? If one looks to present day literature, it is impossible to find an answer to this questions: in 1998 e.g., Dietrich's experiment on $Nb_3Sn$ films showed that with a grain size refined to 15–30 nm and different size/density/shape inclusions, the peak of the $F_p$-B curve could be shifted from $0.2B_{irr}$ even up to $0.5B_{irr}$, resulting in a $J_c$(12 T) improvement by a factor of three [45, 46].
Still, how the two (or more, as the field changes) contributions sum up together, is a mystery. The latter, in the more generic frame of addressing the origin of the macroscopic bulk pinning force, is called "summation problem". If two acknowledged pinning mechanisms are operating in type-II superconductor, how should be Eq. 1.9 treated? A straight forward solution would be a direct summation as in the following equation:

$$F_p(H) = \frac{\mu_0 S_v H_{c2}^2 h^{1/2}(1-h)^2}{4\kappa^2} + \frac{\mu_0 V_f H_{c2}^2 h(1-h)^2}{4.64 a\kappa^2} \tag{1.16}$$

where the left side is the one referring to GB pinning ($h_{peak}$=0.2) and the right one to PP pinning ($h_{peak}$=0.33). The validity of this assumption or the possible appearance of a "mixed-interactions" term will be discussed in Chapter 4, in Sections 4.2 and 4.3.
From Dew Hughes '70s models also compositional gradients - tipycal of $Nb_3Sn$- are not taken into account. As we now know, they can deeply affect $T_c$,$H_{c2}$ and therefore $J_c$.
$H_{c2}$ itself, since the difference between $H_{irr}$ and $H_{c2}$ was clarified, doesn't appear to be any more valid: most of the $F_p$(H) fits (using Eq. 1.9) are not matching the experimental data at the field range end.
As J.Ekin said in one his famous collection of papers on $Nb_3Sn$: "The tail does not scale" [51].

The last interesting question to answer, as mentioned, is about the role of $\eta$, the pinning efficiency. This factor, according to Dew-Hughes, is determined by the extent to which its neighbours in the flux-lattice allow a flux-line to relax toward a position of maximum pinning. This could mean that the different efficiencies of a pinning mechanism should be ascribed only to different conditions of elasticity of the flux lattice, which looks to be only a *partial* answer to the problem. Essentially, this factor was not discussed any more and left =1. A possible new interpretation of $\eta$, which includes also the shape and type of pin, is proposed and verified by means of experimental data in Chapter 4.

# Chapter 2

# Samples

In this work seven different recipes of multifilamentary ternary APC $Nb_3Sn$ wires were analysed. These strands were in their prototyping phase, being none of them already optimized for cabling and/or industrial production.
The wires were fabricated by Hyper Tech Inc. (Columbus, US) and heat treated at Fermilab (Batavia, US) before being shipped to the Atominstitut. The sample specifications are listed in Section 2.1, describing their basic manufacturing information. All the specimen underwent standardized heat treatments, meaning that each wire sample was reproducibly heat treated at the same temperatures, allowing for comparison between the recipes. The manufacturing details are described in Subsection 2.1.1.
Finally, the different preparation methods to which the samples were subjected are explained in Section 2.2.

## 2.1 Sample specifications

All the samples investigated in this work were manufactured following the powder-in-tube (PIT) process. As already mentioned in Chapter 1, this manufacturing technology implies a starting hollow Nb-based tube with a Sn-based powder placed in its center. During the heat treatment ("HT" from now on), the Sn diffuses through the surrounding metallic matrix forming the superconducting $Nb_3Sn$.
In particular, the wires studied in this work are all belonging to the mentioned APC-$Nb_3Sn$ technology: each billet sub-element (usually called "filament" once drawn and reacted) is a Nb-Zr or Nb-Hf alloyed hollow tube filled with Sn-Cu-$SnO_2$ powder. During the last few years, also ternary additions (to the starting alloy) were deployed. Since Ta was identified to be the most suited element [212], it was added to each starting alloy at different concentrations.
Through all this thesis, the designations assigned to the wire types indicates the compound type ("T" stay for ternary, "B for binary), the alloyed element (Zr or Hf) and the order of manufacturing. As an example, all the T-Hf2 are ternary samples reacted from a Nb-Ta-Hf starting billet, being manufactured later than the previous generation of T-Hf1.
Table 2.1 describes in detail the samples specifications, with their code, starting alloy and powder compositions, number of filaments and type of expected inclusions (the precipitates formed from the reaction of Zr or Hf with oxygen) after the reaction.

**Tab. 2.1:** Specifications of the analysed samples.

| Recipe | starting alloy | starting powder | filaments | inclusion type |
|---|---|---|---|---|
| T-Zr1 | Nb-4 at.%Ta-1 at.%Zr | $Sn/Cu/SnO_2$ | 48/61 | $ZrO_2$ |
| T-Hf1 | Nb-4at. %Ta-1 at.%Hf | $Sn/Cu/SnO_2$ | 48/61 | $HfO_2$ |
| T-Zr2 | Nb-4 at.%Ta-1 at.%Zr | $Sn/Cu/SnO_2$ | 48/61 | $ZrO_2$ |
| T-Hf2 | Nb-4 at.%Ta-0.7 at.%Hf | $Sn/Cu/SnO_2$ | 48/61 | $HfO_2$ |
| T-Hf3 | Nb-4 at.%Ta-1 at.%Hf | Sn/Cu | 48/61 | / |
| B-Zr1[1] | Nb-1 at.%Zr | $Sn/Cu/SnO_2$ | 48/61 | $ZrO_2$ |
| B-Zr2[1] | Nb-1 at.%Zr | $Sn/Cu/SnO_2$ | 48/61 | $ZrO_2$ |
| PIT-R* | Nb-4 at.%Ta | Sn/Cu | 192/207 | / |

[1] Old generation binary APC sample
[2] Old generation binary APC sample
* Commercial PIT sample used as a reference.

### 2.1.1 Heat Treatments

The samples were reacted at Fermilab after having been drawn to their final form. The latter is an essential step considering how brittle is the superconducting A15 region formed during the reaction. The furnaces have an actively controlled temperature length of about 15 cm, so only short lengths of the wires were shipped to the Atominstitut.
For each ternary sample, a systematic set of heat-treatments at specific reaction temperatures has been performed: 675 °C, 685 °C, 700 °C and 720 °C. Depending on the wire diameter, the heat treatment time was carefully tuned in order to obtain always full phase reactions at the selected temperature. For the binary samples, only lower temperatures (640° C and 650° C) were considered for the heat treatments.
The heat treatments performed on each type of wire are listed in Table 2.2, where "A" and "B" represent the wire diameters $\phi$= 0.71 mm $\phi$= 0.84 mm, respectively.

## 2.2 Preparation

In the following paragraphs the preparation methods used for different measurement purposes are listed. In Subsection 2.2.1 it is described how the samples were prepared for bulk magnetization measurements, in Subsection 2.2.2 for transport measurements and in Subsection 2.2.3 for both Hall probe microscopy and electron microscopy.

**Tab. 2.2:** Samples specifications: heat treatment temperature and duration for each wire recipes. The prefix "A" means $\phi = 0.71$ mm while "B" means $\phi = 0.84$ mm .

| Recipe | 650 (°C) | 675(°C) | 685 (°C) | 700 (°C) | 720 (°C) |
|---|---|---|---|---|---|
| T-Zr1 | / | A-317 h | B-195 h, B-236 h | A-71 h | A-45 h |
| T-Hf1 | / | B-317 h | A-228 h | A-91 h, B-120 h | A-45 h |
| T-Zr2 | / | B-380 h | B-225 h | A-69 h | A-45 h |
| T-Hf2 | / | A-252 h | A-198 h | B-110 h | A-45 h |
| T-Hf3 | A-126 h | A-43 h, A-70 h | / | B-80 h | B-45 h |
| B-Zr1 | A-250 h / | / | / | / | / |
| B-Zr2* | A-300 h | / | / | / | |
| PIT-R | / | B-250 h | / | / | / |

* The exact heat treatment temperature of this sample was 640 °C.

### 2.2.1 SQUID measurements

After having been shipped to the Atominstitut, the wires were carefully checked and classified as being not damaged. The first step, as it is described in Section 3.1, was to prepare them for magnetic measurements in a SQUID magnetometer.

The wires were cut in pieces of 3.3 mm to 4 mm deploying a low speed diamond saw at approximately 80 rpm (Figure 2.1a), using water as a coolant. Fixing the sample for cutting was done by using wax on a warm solid plate (warmed up for melting the wax around the wire, no more than 150° C).

The cut was always performed perpendicular to the wire axis and eventually repeated on adjacent pieces in order to investigate possible inhomogeneities along the sample length (cf. Sec. 3.4). After the samples were cut, their length was measured with a *KEYENCE VHX-7000* digital microscope as it is shown in Figure 2.1b.

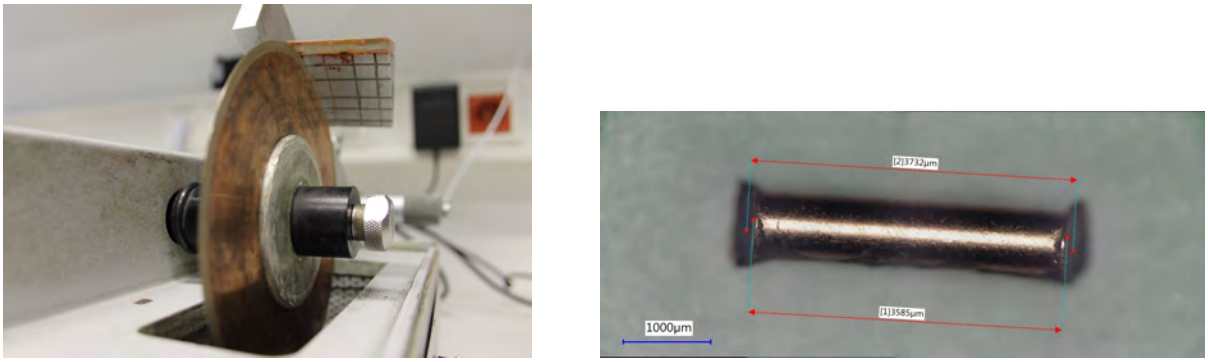

(a)

(b)

**Fig. 2.1:** Sample preparation for bulk magnetometry measurements. (a): low speed diamond saw used for transversal cut of wire samples; (b) approximately 3.7 mm long wire sample cut with the diamond saw.

Every sample showed no sign of fracture after these preparations. Therefore, each wire described in Table 2.2 was prepared for SQUID measurements.

### 2.2.2 Resistive measurements

The wires were also prepared for resistive measurements, one of the oldest characterization techniques deployed in superconductivity. These relatively simple measurements are often used to assess $J_c$ and $H_{c2}$ of a sample, as described in detail in Section 3.2. Only few samples were here prepared for this purpose, due to the limited amount of available reacted wires. Table 2.3 shows the samples prepared for $J_c/H_{c2}$ measurements.

**Tab. 2.3:** Samples for resistive measurements: the ones with round markers were prepared and measured, while the crossed and slashed ones were not prepared or not available, respectively.

| Location | 650 (°C) | 675(°C) | 685 (°C) | 700 (°C) | 720 (°C) |
|---|---|---|---|---|---|
| T-Zr1 | / | ○ | ○ | × | × |
| T-Hf1 | / | × | × | ○ | × |
| T-Zr2 | / | × | ○ | ○ | × |
| T-Hf2 | / | × | × | ○ | ○ |
| T-Hf3 | ○ | × | / | × | × |
| B-Zr1 | ○ | / | / | / | / |
| B-Zr2 | ○ | / | / | / | / |

For current transport measurements, the samples were cut (using a wire cutter) in pieces of 35 mm-37 mm, as described in Section 3.2. The specimen is placed perpendicular to the insert rod as showed in Fig. 2.2, where a schematic of the used sample holders is presented.

A longer sample would be in principle safer for high current measurements, since the local heat near the transition to resistive would be better distributed and the quench would eventually come later, so preserving the wire and diminishing the noise. The limitation on this is caused by the bore (maximum available rod-insert diameter) of the two croystats exploited, with the largest being 50 mm (*NHFML* 31 T resistive magnet).

A similar holder was used for $H_{c2}$ measurements, but with a shorter sample length: approximately 20 mm.

### 2.2.3 Scanning Hall probe and Electron microscopy

The sample preparation adopted for Hall probe measurements was unified with the one used for electron microscopy. Deploying a single technique is efficient, since preparing the samples for these experiments is time consuming and often the final quality can be unacceptable, so the entire procedure has to be repeated.

The samples hereby prepared are first cut in 15-20 mm pieces, then clamped in a ©*Ted Pella "MultiClips"* holder used to keep 3-5 wires upright during the embedding phase. The samples are

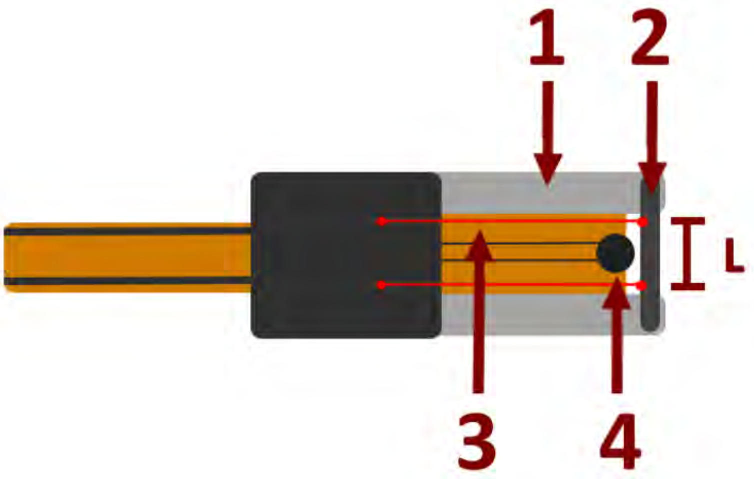

**Fig. 2.2:** Schematic of the sample holder as being the bottom of the rod inserted in the cryostat. 1: current contacts, 2: sample, 3: voltage contacts, 4: temperature sensor.

then soaked in a cylindrical plastic mould, so filled with an epoxy resin mixture (40% resin - 60% hardener) by *Buehler*. The mould is then put in an oven at 70 °C for 1 hour, till it fully solidifies.

**(a)** **(b)**

**Fig. 2.3:** Accessories used for sample embedding for Hall probing and scanning electron microscopy; (a) shows the plastic clamps for holding the wires; (b) the mould to be filled with the clamp in (a) and the epoxy-hardener mixture . *Credits: Buehler.com*

Alternatively, the liquid compound can be left drying at room temperature and, at the same time, pumped down in a chamber with low vacuum for removing the air bubbles trapped in, being the latter often source of mechanical fragility towards the subsequent polishing phase. Figure 2.3 shows the clamp and the mould where the former (clamping usually 5 samples altogether) is set in with epoxy. After drying, the embedded unit - from now on referred as "e-unit" only - is detached from the mould and looks as shown in Fig. 2.4.

As a last step before the effective polishing, the e-unit is cut - transversally to the wire axes - using a diamond-coated wire, which separates the most of the (unuseful) embedded volume from the last 0.5 mm -1 mm of the embedded samples cross sections. While this procedure is relatively straightforward, the subsequent polishing phase is more sensitive.

**Fig. 2.4:** Example of e-unit containing five samples after the embedding process. In this form, the samples are ready to be polished.

Mechanical polishing of $Nb_3Sn$ e-units was done using an *Allied Multiprep™* polishing machine, as it is shown in Fig. 2.5a. The latter is an automatic disk-rotating device, which can be equipped with polishing disks (aluminium or silicon dioxide) of different grain sizes. It is also provided with a sensor indicating the thickness-removal level, programmable in order to roughly (± 5 $\mu$m) polish away the desired thickness.
The e-unit is mounted on a holder made of glass, polished itself before each operation with a coarse diamond disk for achieving an even surface. The e-unit is mounted on the holder by using acetone-soluble wax. The polishing starts by exploiting disks with grains of $\sim$10 $\mu$m and high rpm (100-150), getting down to fine-grained disks (0.5 $\mu$m and 0.1$\mu$m) by using 10-30 rpm. Cooling is provided by water or soap, while the polishing leftovers are constantly removed by the user by cleaning the polishing disk during operations (Fig. 2.5b).

Maximum care has to be given during the last steps of this process, since below 150 $\mu$m in thickness the shear stress becomes relevant and the samples could start to fracture. In this regard, several quality checks were done during polishing, by removing the e-unit at subsequently thinner stages and measuring the thickness with a *Leica Digital Microscope*, as it is shown in Fig. 2.6.
These pictures display how sharper gets the image after polishing from circa 230 $\mu$m down to 10 $\mu$m: the black lines, often present over the cross sections, are Sn smeared from the filaments cores. This is not strange nor dangerous, since Sn in the core represents only a leftover of the diffusion process, not dedicated to any mechanical or superconducting purpose. The details of the surface get clearer and clearer by polishing the specimen to the thinnest achievable thickness. The latter was discovered to be between 10 and 15 $\mu$m, with the Zr-doped sample to be slightly more ductile (therefore resistant to stresses coming from polishing friction) than the Hf doped ones. Below this threshold, the slices start to break apart, to crack inside or even exfoliate away from the e-unit. In Fig. 2.7 this process is displayed, with a comparison between a damaged and

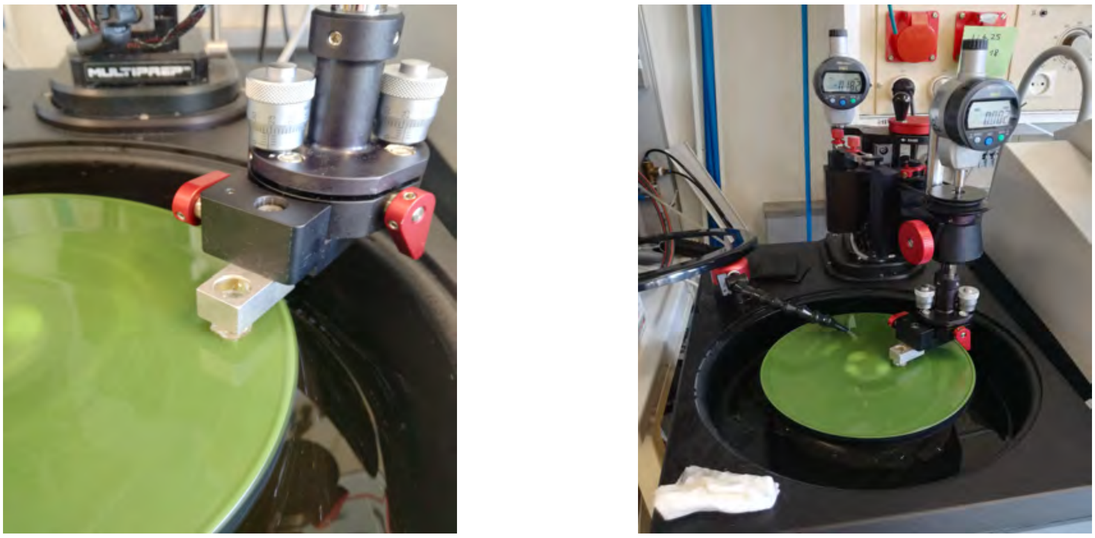
(a) (b)

**Fig. 2.5:** *Multiprep™* polishing machine: in (a) the sample holder with the e-unit during operations is shown ; in (b) the entire device, with thickness sensors, cooling system and polishing disk (in green) is presented.

a well prepared sample.

The integrity of the polished slices depends on the quality of the embedding and on the care expressed by the user in the last polishing phases, where a slightly higher pressure can compromise the entire procedure. The reason for this extreme polishing answers to the needing of almost "two-dimensional" samples, from which the analysis of remanent magnetization profiles can lead to precious local information. The evaluation methods of the Hall scans will be described in detail in Section 3.4 and Subsection 3.5.7.

Wire samples were embedded also along their length (longitudinal e-unit), repeating the same procedure hereby described but without aiming for the thinnest achievable thickness. This preparation was done only on few samples (mainly first ones), in order to check eventual longitudinal manufacturing problems, so the development of the layout quality during the prototyping phase (Section 3.4).

### 2.2.4 Electron microscopy

The sample preparation for electron microscopy followed basically two distinct paths:

- SEM: samples for electron microscopy imaging and energy dispersive x-rays spectroscopy (EDX);
- STEM/TEM : samples for transmission electron microscopy and transmission Kikuchi diffraction (TKD);

For the first type of experiments, the sample preparation followed slavishly the procedure described in Subsection 2.2.3, eventually finalized by a last cleaning of the e-unit using the plasma cleaner for removing any residual contamination. The e-unit is then connected with silver paste to the the stage (so making the samples conductive) and directly mounted in the SEM sample holder, with no need of further treatments.

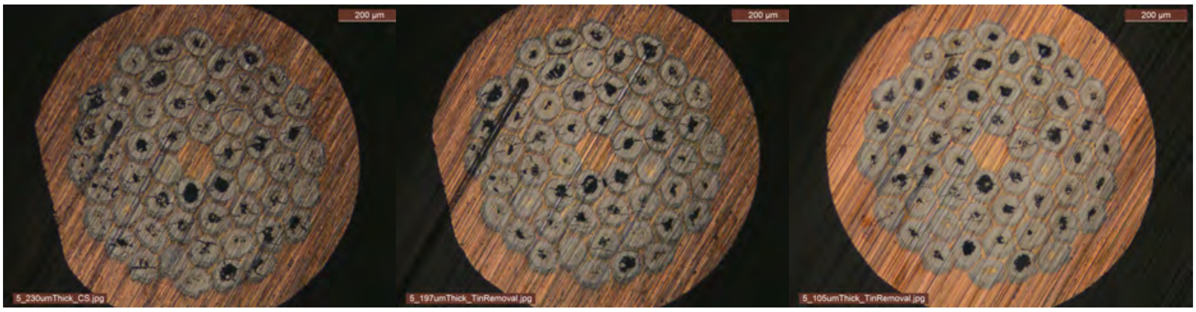

**(a)** 230 $\mu$m **(b)** 197 $\mu$m **(c)** 105 $\mu$m

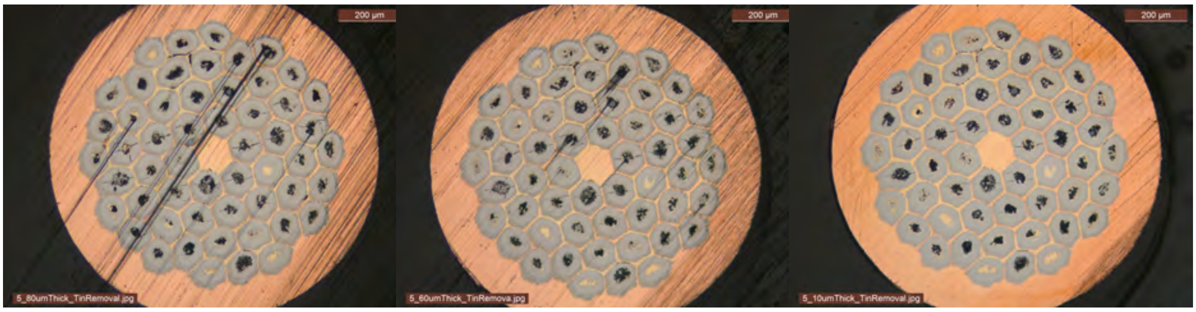

**(d)** 80 $\mu$m **(e)** 60 $\mu$m **(f)** 10 $\mu$m

**Fig. 2.6:** Phases of the polishing process of a T-Zr1 sample: from (a) to (f) the sample is polished down to the thinnest achievable slice. The thickness is measured by using the microscope focusing, each time as a difference between the focus at the base plane and at sample surface.

In the second case, even if not prepared by the author, a description of the different preparation process used is needed. STEM/TEM samples were prepared at USTEM (TU Wien, AT) using the focused ion beam (FIB) for cutting out the desired "lamella". The latter is the name for a micrometric piece of the sample, to be removed (from the A15 region) and thinned enough to match the transmission requirements. In fact, since electrons cannot readily penetrate sections thicker than 200 nm, STEM/TEM cannot image through thick samples [123]: the usual sample thickness to reach is below 100-150 nm. This was done with the FIB in different steps:

1. a layer of Pt is deposited on the SHPM/SEM-prepared sample for protecting it from beam damage;
2. the lamella's contours are cut using a high beam accelerating voltage and a current of approximately 20 nA; a first thinning is also performed, reducing the sample thickness down to $\simeq$ 2-3 $\mu$m;
3. the lamella is removed and connected to a needle using a micro-manipulator, then lifted out and mounted on a dedicated Mo-based holder (the needle is therefore dismounted);
4. further thinning with FIB: once the thickness is about 200-300 nm, a final sensitive step is needed;
5. last thinning to 30-90 nm is achieved by using the $^{TM}$ *Gatan* precision ion polishing system ("PIPS"). This is an ion milling machine, a device similar to FIB which fires ions at the surface of the sample.

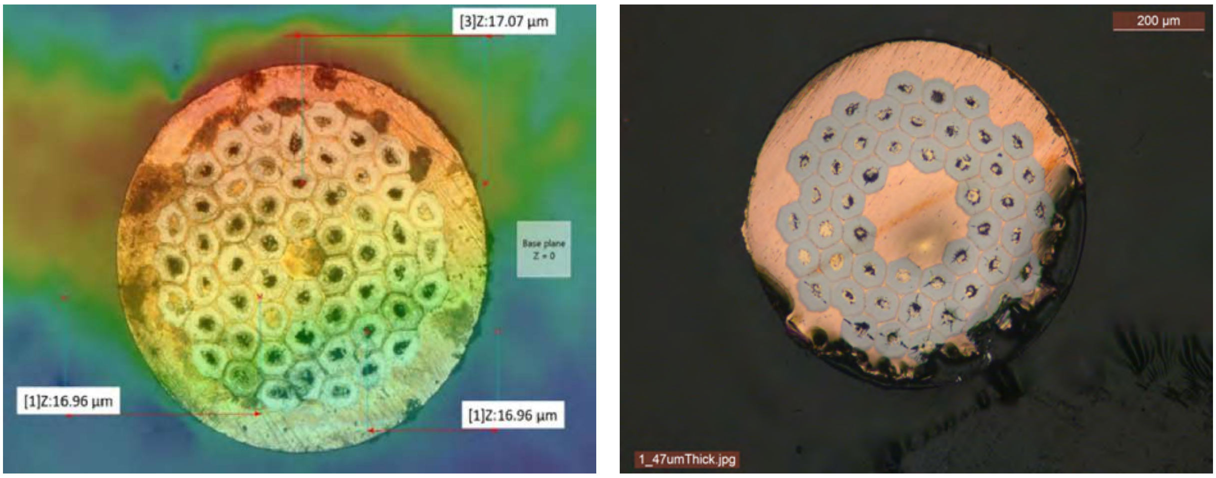

**(a)** **(b)**

**Fig. 2.7:** (a) A well prepared thin slice (averagely 17 $\mu$m thick): the darker areas refer to the deepest points (base plane), the lighter ones to the thickest; (b) the sample is damaged after polishing down to 45 $\mu$m: the left-souther side exfoliates (bending on its own) and other cracks start to appear as well.

Even though the last step could be achieved with FIB as well, the ion mill was preferred since the low energy Ar+ ions used by the latter are gentler than the Ga+ used with FIB, so further preserving the lamella even for deeper thinning. Figure 2.8 shows the different position over the sample cross section where the lamellae are usually extracted from, with a focus on the cut out using the micro manipulator.

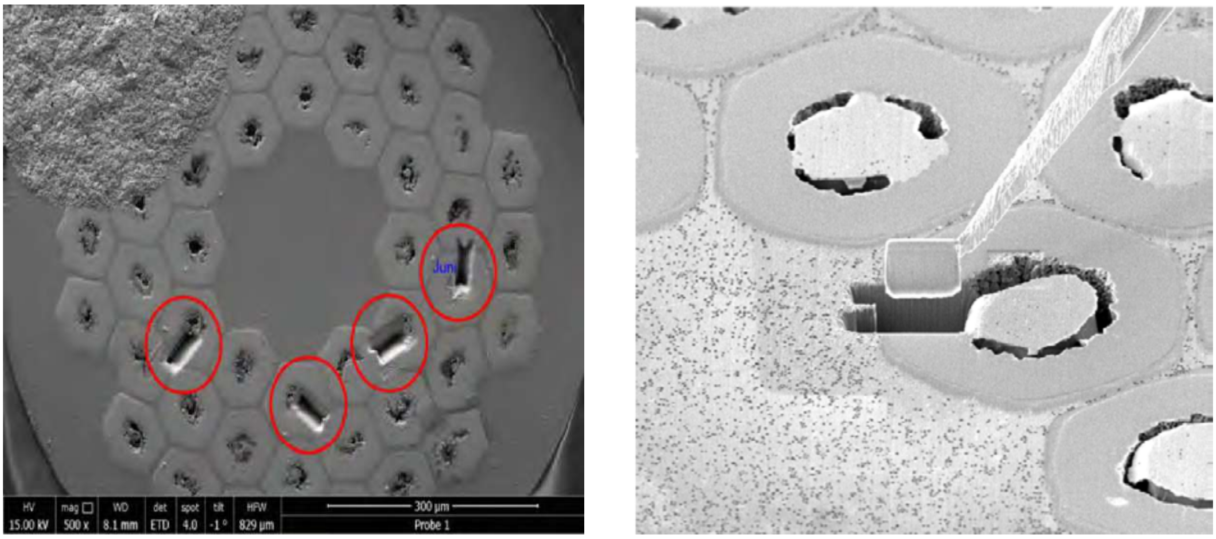

**(a)** **(b)**

**Fig. 2.8:** (a) 4 different extraction sites for lamellae on a T-Zr2 sample. On the top left a conductive paste was applied;
(b): lamella removal from the A15 region by using a micro manipulator.
*Courtesy of S.Schwarz and S.Pfeiffer.*

Completing with success the just described procedure is not easy, requiring for lot of training and experience. It is in fact not uncommon to ruin a long sample preparation only at the very last stage, when it comes to the final thinning. For further detailed information about the procedures adopted for $Nb_3Sn$ transmission electron spectroscopy, the author followed the work of *Pfeiffer* in [155]

The experiments conducted with these samples are described in Subsection 3.3.3. The analyses are discussed in Subsections 3.5.8 and 3.5.9, while the results are presented in Chapter 4.

# Chapter 3

# Experimental

In this chapter the experimental work done during the project is widely described, ranging from the measurements set up to the data analysis procedures. In Section 3.1 it is given a description of the bulk magnetization (SQUID) experiments, while in section 3.4 the local magnetometry measurements (SHPM) are discussed. Resistive measurements, provided only on few samples, are described in Section 3.2. The electron microscopy experiments, investigating the microstructural features to be correlated with the superconducting properties, are presented in Section 3.3. Finally, the evaluation praxis deployed to understand and correlate the experimental results is described in Section 3.5.

## 3.1 SQUID measurements

Magnetometry devices offer fast, precise and safe characterization possibilities for superconductors. In particular, the superconducting quantum interference devices (SQUID) are exceptionally sensitive and used to detect a vast range of different physical parameters, with a maximum sensitivity in the range of $10^{-11}$ Am$^2$.

First of all, SQUID magnetometry has been used to assess the critical current density $J_c$ of the samples by measuring the magnetic moment, $m$, as a function of temperature and field H ("$m$-H loops"). In fact, differently from current transport measurements (Section 3.2) - where a direct assessment of the ultimate sustainable current is possible - SQUID magnetomtery allows for an indirect evaluation of $J_c$. The model relating the measured $m$ to the critical current density is well established and based on the Bean critical state [16] together with some geometric assumptions, thoroughly described in Section 3.5.

As one of the main advantages, using SQUID magnetometry allows to measure the maximum pinning force values $F_{p\text{-}max}$ also in the 4.2 K-10 K range. This temperature range is usually not reachable with transport measurements, since the currents would be too high and the wires would easily quench. Moreover, SQUID measurements were always the less time consuming among all the experiments performed, allowing for redundant measurements on the same wire and for a low helium consumption.

Secondly, the same loops were used to assess the irreversibility field line $H_{irr}$ (the field at which there is no more apparent pinning, therefore no more hysteresis) between 10 K and 15 K measurements.

Furthermore, as being able to detect both AC and DC signals, the system allows also for AC susceptibility measurements, used for assessing the critical temperature $T_c$. The samples do not need a different preparation, therefore these measurements were always performed right after the $m$-H loops.

As a final purpose, the same samples prepared for the $m$-H loops were used for a new experimental technique based on magnetometry models (*Bean*), aiming to indirectly assess some local geometrical features of the wire sub elements, as it will be explained in detail in Subsection 3.1.3

Each measurement was performed with a *Quantum Design MPMS®XL*, which is shown in Figure 3.1a. This device allows measurements in the temperature range from 1.9 K to 400 K, together with an applicable magnetic field up to 7 T. The core of the measurement system is a second order gradiometer pick-up coil assembly: the samples move through the coils length as depicted in Figure 3.1b. The sample can be moved step-by-step (standard sample transport option) or periodically (reciprocating sample option) through the assembly.

The experimental procedure for measuring magnetic moments is described in Subsection 3.1.1, while AC susceptibility measurements are described in Subsection 3.1.2 and the magnetometry based technique in Subsection 3.1.3 .

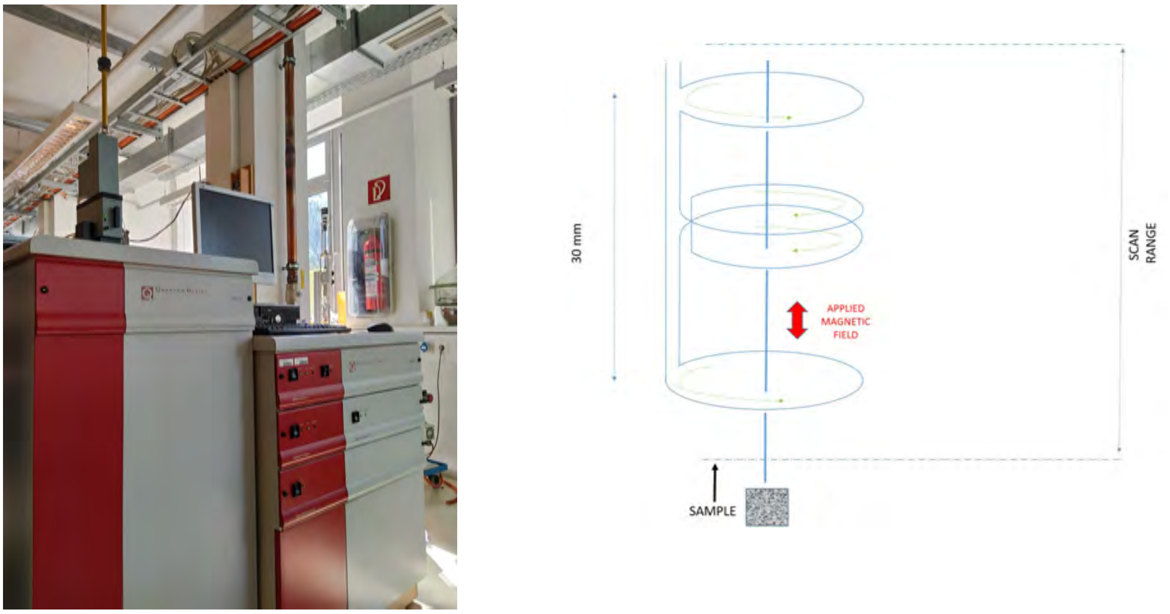

**(a)** MPMS Quantum Design XL used in this work

**(b)** Second order gradiometer used in the Quantum Design MPM XL SQUID.

**Fig. 3.1:** SQUID device and its core measuring device (gradiometer) used at the Atominstitut, TU Wien.

### 3.1.1 m-H loops

The measurement of the magnetic moment $m$ at different fields and temperatures was performed consistently on all the samples. There are two main options for operating the SQUID:

- Standard sample transport: the sample is moved through the pick-up coils in small steps, measuring the SQUID response voltage as a function of the sample position $z$.
- Reciprocating Sample Option (RSO): the sample is moved cyclically through the pick-up coils as it would be the case in a vibrating sample magnetometer (VSM). This essentially turns the entire system in a VSM with a SQUID sensor.

In the first case, the sample rod is a stainless steel tube with a phosphor-bronze ending. This connects the transport unit to the the sample holder, which is self made in order to match the

user's needing. The second option consists instead of brass tube sealed on one extremity (so becoming an airlock), comprising of a plastic sample rod to which end the sample holder is rigidly attached.
Both options are depicted in Figure 3.2, allowing either for measuring the same quantity $m$. In particular, for the $J_c$ assessment it is used:

$$m_{irr}(H_a) = \frac{1}{2}(m_-(H_a) - m_+(H_a)) \tag{3.1}$$

where $m_{irr}(H_a)$ is the "irreversible" magnetic moment, with $m_-(H_a)$ and $m_+(H_a)$ being the moments measured in decreasing and increasing applied field, respectively. A reliable detection of these quantities is possible only by providing the following experimental conditions:

- Sample size $\ll$ coils assembly size, so that the their reciprocal interaction can be considered as a magnetic dipole ;
- Signal/(background +noise) $\gg 1$ ;
- Magnetic moment $m$ to be constant through the measurement;

The first condition is easily matchable by preparing the sample to be much smaller than the pickup coils assembly (Figure 3.1b), as it is described to be the case in Section 2.2.1. Provided the entire SQUID sample space to be not magnetic (removal of noise sources), the second point also asks for the signal coming from the sample to be much higher than whatever other source of $m$ (mainly coming from the sample holder). This is usually granted while dealing with $Nb_3Sn$ high-$J_c$wires, at least if the applied field and temperature do not approach $H_{c2}$ and $T_c$, respectively.
The third and last point has been granted thanks to the studies of *Baumgartner* [16], who first tracked the limits and advantages of both standard sample transport and RSO options in DC magnetization measurements. As being clearly more precise and reliable, the RSO option was ultimately chosen to be used for each measurement of $m$.
The wire samples were mounted orthogonal to the applied field, as this would be their operational configuration in a dipole magnet. The exact placement of the specimen is shown in Figure 3.2b: the sample holder is made of a transparent straw (as suggested by *Quantum Design*, with the sample placed on a non magnetic silica plate by using a thin layer of *Dow Corning® High Vacuum Grease* (perfectly holding the sample at low temperatures, where it freezes).
The system is set for automatically measure two-quadrants cycles of $m$, with $H_a$ steps of 0.1/0.2 T depending on the accuracy required for the evaluations, as it is described in Subsection 3.5. The settings used for the RSO measurements, freely adjustable by the user, are summarized in Table 3.1.

**Tab. 3.1:** RSO experimental parameters

| Parameter | Experimental setting |
|---|---|
| Frequency | 4 Hz |
| Amplitude | 2 mm |
| Number of cycles | 20 |
| Number of measurements | 3 |

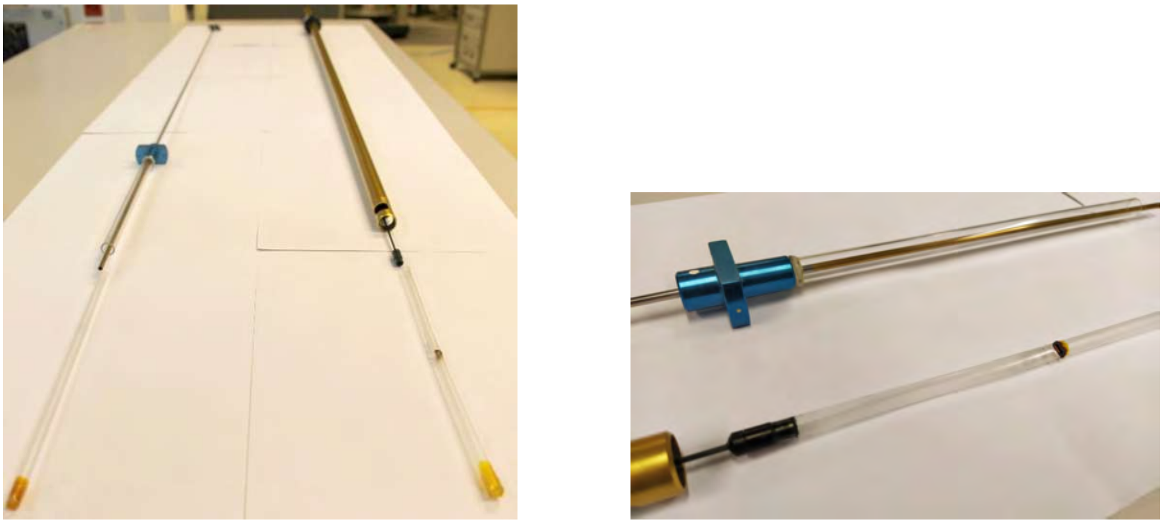

**(a)** SQUID options: on the left the standard sample transport holder and on the right the RSO rod;

**(b)** Standard sample transport (up) and RSO (down) sample holders: the latter is rigidly connected to the rod; the first is left free (floating), being connected to the rod by means of a non magnetic lanyard

**Fig. 3.2:** Experimental equipment used for magnetization measurements in the MPMS XL Quantum Design SQUID.

During operations, the RSO moves the sample periodically around the point corresponding to the maximum slope of the SQUID response function, between the central and upper pick-up coils. The magnetic moment $m$ is obtained by the SQUID software after computing a linear fit through the data points measured for each cycle. The result is then averaged over three measurements, after which a new measurement at new applied field/temperature begins. A typical example of $m$-H loops measured at different temperatures is shown in Figure 3.3. The magnetic moments measured in increasing and decreasing applied field are $m_+$ and $m_-$ respectively, as they are formulated in Eq. 3.1. The arrows indicate the outmost loop to be referred to 4.2 K: the higher the temperature, the less intense gets the magnetic moment, resulting in an always smaller loop.

The analyses of the m-H loops and how to extract different useful information out of these data is explained in Section 3.5, while the results and their correlations are discussed in Sections 4.1, 4.2 and 4.3.

### 3.1.2 AC susceptibility

AC susceptibility is a useful and simple technique for investigating the critical temperature of the wire samples. The idea is based on the relationship between the susceptibility $\chi$ and the critical temperature $T_c$ in a superconductor, sensing the response of the sample to a small AC magnetic field.

Applying AC fields allows the user to freely choose between the two measuring options described in Subsection 3.1.1, since the eventual differences arise only in DC magnetization measurements. The magnetic susceptibility is defined as:

$$\chi = \frac{dM}{dB} \tag{3.2}$$

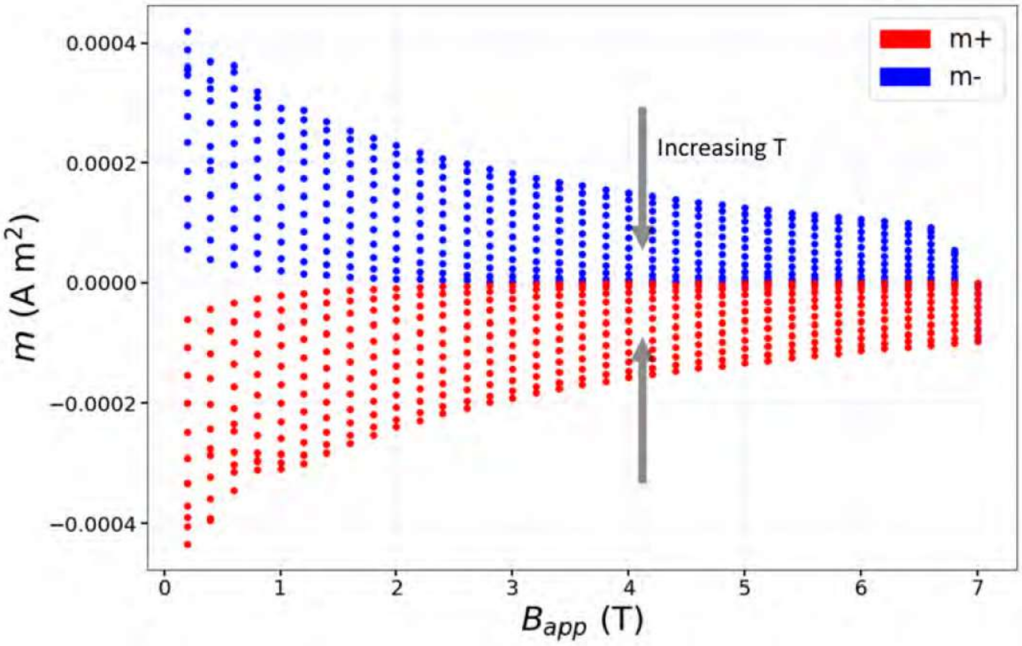

**Fig. 3.3:** m-H loops of a T-Zr1 sample between 4.2 K and 15 K. In red the magnetic moment $m_+$ recorded in raising field, in blue the one recorded in decreasing field $m_-$.

The system measures, with respect to applied AC magnetic field, the in phase (real) $m$' and out of phase (imaginary) $m$" components of the magnetic moment. Therefore, the susceptibility can expressed as following:

$$\begin{aligned}\chi' &= \frac{\mu_o}{VH_{AC}}m' \\ \chi'' &= \frac{\mu_o}{VH_{AC}}m''\end{aligned} \tag{3.3}$$

where V is the volume of the superconducting region of the sample and $H_{AC}$ is the applied AC field. If the latter is smaller (absolute value) than $B_{c1}/\mu_0$ (while $T < T_c$), one will measure the magnetic response of a perfect diamagnet, so $\chi' = -1$ and $\chi'' = 0$. Raising the temperature in small steps (always waiting for stabilization) up to $T_c$ produces a variation in $\chi$, therefore in $m$': the sample enters in the vortex phase, $\chi' \neq -1$ (but still $\ll -1$) and $\chi'' \neq 0$, the latter showing small positive values reflecting AC losses.

Recording $m'(T)$ is therefore an effective method to measure $T_c$ together with its whole transition from superconducting to normal state ($\Delta T_c$).

The measurements are composed of "blocks" comprising each of two sine wave cycles. The user defines how many blocks will be contained in one measurement, as well as how many measurements are needed for extracting an average result value (as a trade-off between measuring time and statistical precision). The settings used in this work are summarized in Table 3.2.

**Tab. 3.2:** AC susceptibility experimental parameters

| Parameter | Experimental setting |
|---|---|
| Frequency | 33 Hz |
| Amplitude | 30 $\mu$T |
| Number of blocks | 3 |
| Measurements per data point | 3 |

An example of an AC susceptibility measurement is shown in Figure 3.4 for sample T-Zr1 A-314. In-phase magnetic moment $m'$ (only $m$ in the plot) is normalized to its minimum value and plotted against temperature, the latter ranging from 5 K to 19 K. The first step depicts the transition to the normal state of pure Nb present in the sample, while the second and main one occurs smoothly between 9 K and 18.2 K, with an evident two-fold final step between 16 K and 18.2 K. For better investigating these last $\sim$ 2 K, the temperature step size was often reduced on purpose aiming for a better accuracy (100 to 50 mK).

The reason for this two-component transition was identified within the microstructural features of the PIT manufacturing: two sharply different population of grains are present, a "coarse" (diameter $> 150$ $nm$) and a "fine" one, also called "CG" (coarse grains) and "FG" (fine grains) population, respectively. They have each a slightly different $T_c$, represented by a different susceptibility and therefore $m'$. In a pure $Nb_3Sn$ crystal, the transition would look steep and the magnetic moment between them constant. The reason for the differences to the scenario depicted in Fig. 3.4 is related to the ternary additions together with the presence of the initial solute (Zr/Hf), chosen to be form the inclusions during the heat treatments [211].

The evaluation of the $T_c$ curves, the correlated microstructural inhomogeneities and their effect on the critical current density $J_c$ are discussed in Subsection 3.1.3, Section 3.5 and in Chapter 4.

### 3.1.3 Radii probing

The evaluation of the layer $J_c$, the critical current flowing through the effective superconducting cross-section of a wire/tape, has always been crucial for the determination of the pinning characteristics of technical superconductors. The relations between the microstructure and the volume pinning force are essential to predict the final superconducting parameters directly from a proper manufacturing control, tuning the heat-treatment and precursor parameters in order to get the desired layer $J_c$.

Nevertheless, the calculation of this current density always passes through an indirect step, whatever the measurement technique (transport current or magnetometry): one has to know the exact cross-section of the superconducting elements, often affected by inhomogeneities throughout the length and the radius of the specimen. The effective single-filament A15 area (cross-section) will be called "$A_{eff}$" and the number of filaments "$N$" in the following.

In the specific case of multi-filamentary $Nb_3Sn$ wires, especially at their prototype stage, the right identification of the effective superconducting phase ("A15 phase") borders turns out to be sometimes ambiguous, possibly leading to non-negligible discrepancies between independent measurements. This is usually due to:

- Morphological differences among the filaments through the cross-section, especially in non-optimized wires (sub-elements bigger than 50 $\mu$m);
- Longitudinal inhomogeneities: "sausaging" of the filaments along the wire length can lead to discrepancies when evaluating the cross sections;

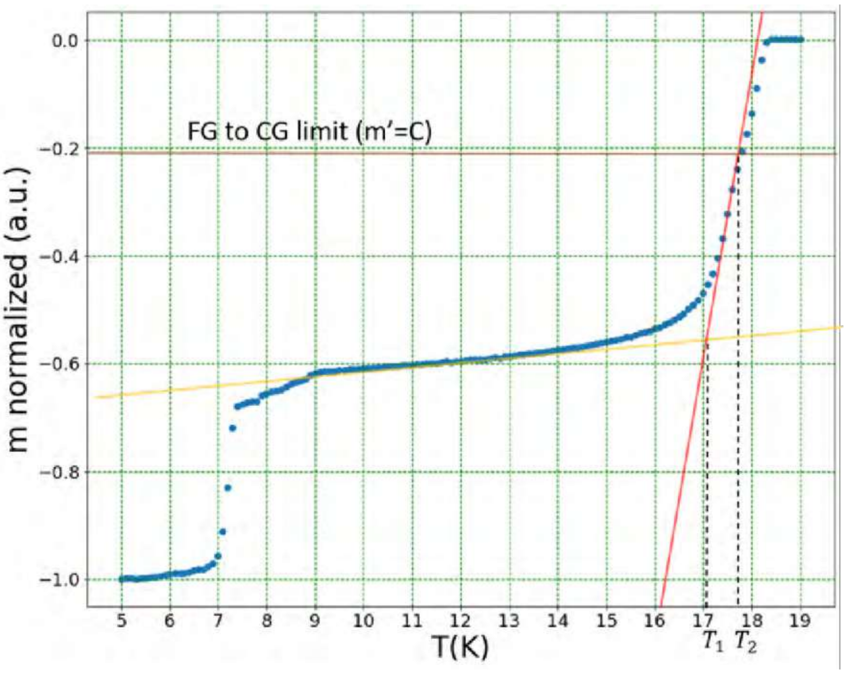

**Fig. 3.4:** AC susceptibility measurement for $T_c$ evaluation: the blue experimental points are fitted with linear functions (solid lines) for the $T_c$ evaluation only in the FG region. The solid red, yellow and brown lines are used for extracting the critical temperature $T_c$, as it is explained in Subsection 3.1.2

- Definition of the "current-carrying element". As mentioned before, there is an acknowledged classification of "coarse grain" (CG) and "fine grain" (FG) population in literature, respectively $> 1$ $\mu$m and $\leq 150$ nm [93, 171], with the first not significantly contributing to transport current. Still, the current density contributions arising from this continuum of sizes is still not fully assessed: how much does a volume of connected 800 nm large grains influence the $J_c$? Should this "zone" be ascribed to the A15 region?

The last point of this list generates most of the ambiguities when coming to SEM-image evaluation of polished surfaces of $Nb_3Sn$ wires cross-sections. As already mentioned in Subsection 3.1.2, there is e.g. in PIT wires always a transition between CG and FG, stemming from the decomposition of the $Nb_6Sn_5(Cu_x)$ layer preceding the A15 reaction, which leaves traces of a broad distribution of semi-refined grains, as is clear by looking at two adjacent filaments in Fig. 3.5.

In this picture, two adjacent filaments show different A15 geometry and phase/brightness boundaries (brightest part surrounding the dark central leftover Sn-Cu). While the outer contours can be easily evaluated (differences between the Nb-barrier and $Nb_3Sn$ are evident) the inner ones are more subjective and rely on the experience of the operator.

A new experimental method is proposed in this work to cross-check the outer and inner average radii of the filament's A15 areas ($r_o$ and $r_i$, respectively) from magnetometry based models.

For assessing the filament geometry, the samples were prepared as for the $m$-H loops but mounted with the wire axis parallel to the applied magnetic field and field-cooled to 4.2 K at 6.5 T. The latter was the base-field, $H_0$, upon which a measurement cycle was performed, chosen because it is above the Nb upper critical field $H_{c2}$, in the field range of interest and ensuring a negligible variation of $J_c$. This sequence (field increased - RSO measurement - back to $H_0$ - RSO

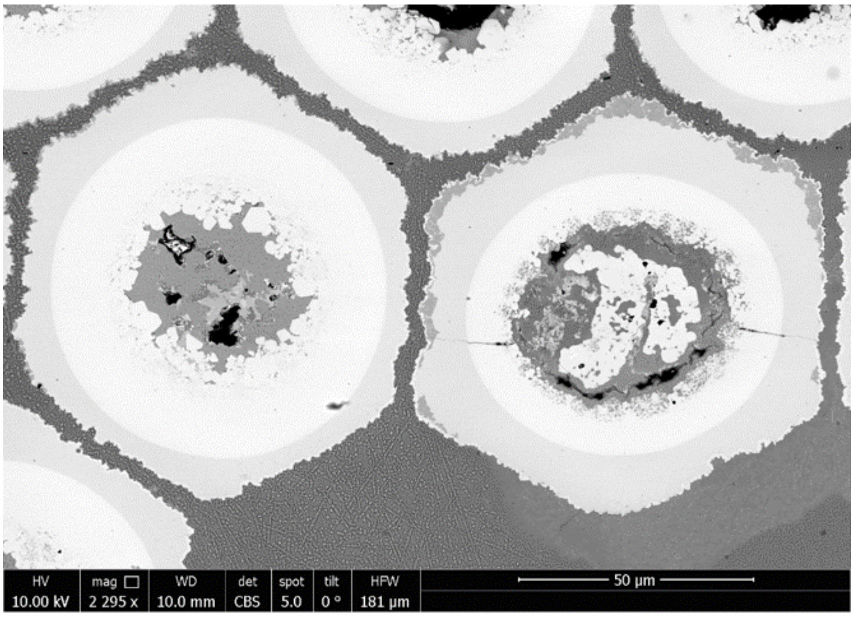

**Fig. 3.5:** Two filaments of a 48 sub-elements $Nb_3Sn$ wire. For the filament on the right, the CG region is much more evident than on the one on the left, allowing a more direct evaluation of the A15 contours.

measurement) had 30 steps, measuring each time at a higher applied field $H_n$ up to 6.95 T as depicted in Fig. 3.6.

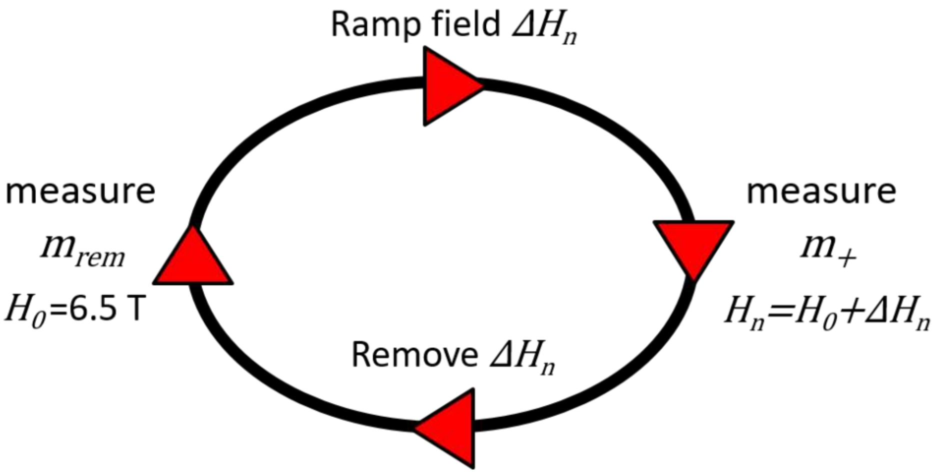

**Fig. 3.6:** Measurement sequence: the magnetic moment is measured at $H_0$, the field is then ramped to $H_n$ and $m$ is measured again, finally back to $H_0$ where another measurement is performed.

The field at the n$^{th}$ step, starting from $H_0$, was imposed by always adding a field step of 0.01 T as follows:

$$\begin{aligned} H_n &= H_0 + \Delta H_n, \\ \Delta H_n &= n \cdot 0.01 \text{ T} \end{aligned} \tag{3.4}$$

The magnetic moment measured at the field $H_n$ is called "$m_+$", while the one we measure subsequently at $H_0$ is "$m_{rem}$", since it is the remaining magnetic moment in the sample.
The results of the experiments and the validity of the method are discussed in Section 4.1.1.

## 3.2 Resistive measurements

Resistive measurements are among the most common and old characterization techniques in applied superconductivity. These techniques rely on measuring the change in resistivity $\rho$ when the sample passes from the superconducting to the resistive state. As the latter can be achieved by increasing the applied field, the transport current or the sample temperature, this technique is used to primarily measure respectively $H_{c2}$, $J_c$ and $T_c$ of a type-II superconductor.

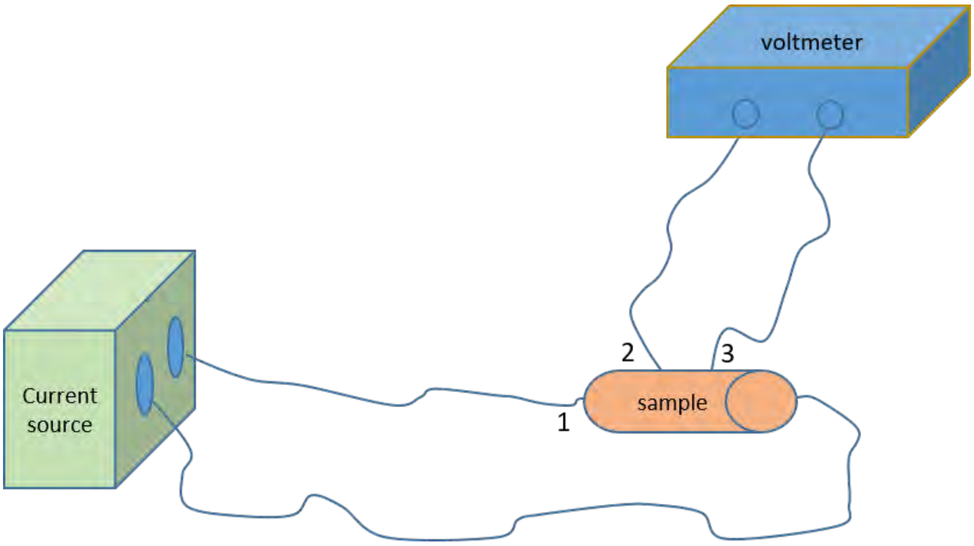

**Fig. 3.7:** Schematics of the 4-point resistance method.

Low resistance samples are difficult to measure using an ohmmeter (2-point connections). For this reason, to measure the resistance of the sample only, it is necessary to use the 4-point resistance technique. As it is shown in Fig. 3.7, with the 4-point method, one sends a current through the ends and measures the voltage across two points of the sample, determining the resistance using Ohm's law. In this case, the resistance is measured between the two points on the sample where the voltage contacts are located. For this purpose, the samples are prepared as described in Subsection 2.2.2 with a length of approximately 3.5 cm for transport measurements and 2 cm for the $H_{c2}$ ones. They are mounted perpendicular to the applied field and soldered to the four-terminal sensing. For the transport measurements, particular attention is given on well polishing the current contacts before each measurement, removing any impurity that could lead to bad contacting, so to undesired Joule effects/measurement offsets.

In this work, only few $H_{c2}$ and $J_c$ measurements were performed, mainly because of the short samples length and constraints related to the experimental set-up. Some of the $H_{c2}$ measurements were taken at the Atominstitut in a cryostat equipped with a 17 T (maximum reachable applied field) superconducting magnet. The latter is supplied with a current generator of max 120 A and can produce up to 17 T when the bath temperature is lowered enough (by pumping). For this reason, only measurements where $H_{c2}(T) < 17$ T were possible, accomplished by measuring the critical temperature at constant applied field by applying $I$=100 mA and lowering the temperature from above $T_c$ while measuring the voltage drop across the sample. The resulting output are voltage vs. temperature curves, measured at different values of constant applied field.

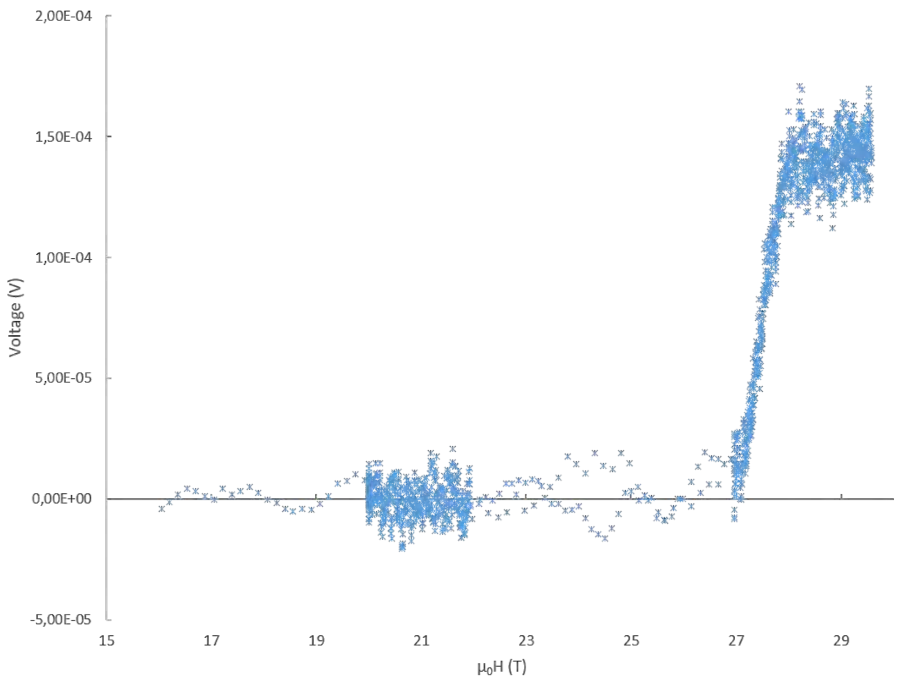

**Fig. 3.8:** Raw data of a $H_{c2}$ measurement performed on sample T-Hf1-700x91: the steep change between 27 and 28.5 T indicates the transition from superconducting to normal state resistivity.

Transport current and few remaining $H_{c2}$ measurements were instead taken at the National High Magnetic Field Lab (NHMFL) in Tallahassee (US), where a resistive 31 T magnet is particularly useful for assessing the $H_{c2}$ of the $Nb_3Sn$ samples at low temperatures (particularly valuable is 4.2 K, as being often the operational temperature of the magnet dipoles). With this set-up, the $I_c$ is measured both in increasing and decreasing current, each time at a constant magnetic field with a maximum available current of 700 A. The elementary current step as well as the estimated transport current rate were adjustable by the user according to the expected heat load (increasing with decreasing applied field).

Both systems were equipped with several peripheral devices such as nanovoltmeters, a temperature controller and a PC which controls all components of the system via GPIB. Both systems are displayed in Figure 3.9.

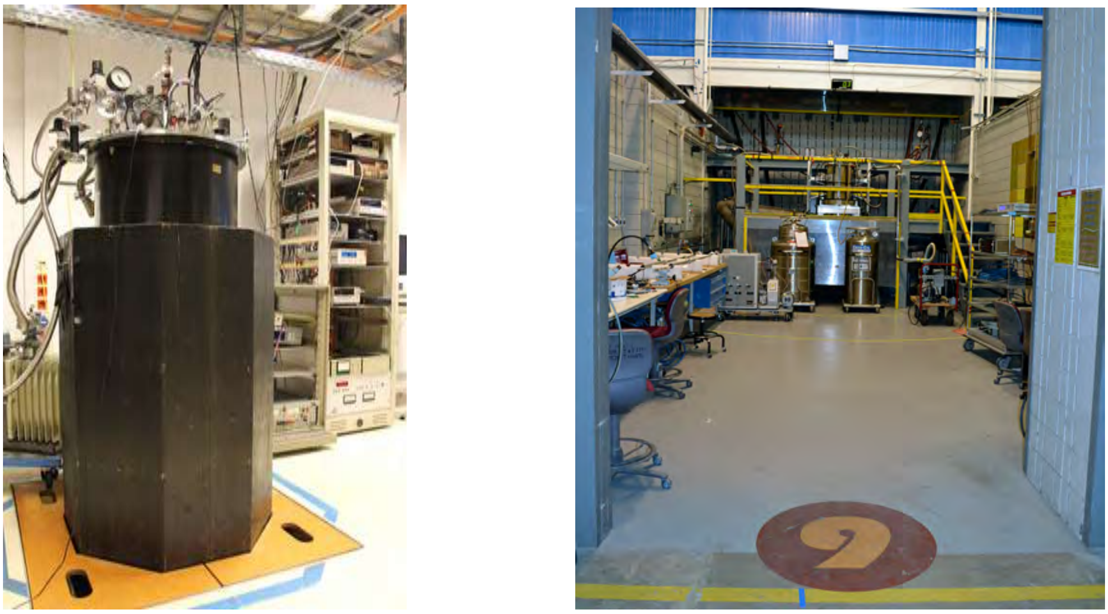

**(a)** 17 T superconducting cryostat at the Atominstitut, TU Wien

**(b)** 31 T resistive cryostat at the NHFML, Tallahassee

**Fig. 3.9:** Resistive measurements cryostats used in this work.

Fig. 3.8 shows the output of an R-H measurement taken in a 31 T magnet on a $Nb_3Sn$ wire sample: the voltage across the contacts stays constant at around 0 V, rapidly increasing during the transition to normal state between 27 and 29 T.

## 3.3 SEM and TEM

Scanning Electron Microscopy (SEM) - as being part of a generalized need for magnification of microstructural details - has been historically a key for material science development, so of course also for R&D in superconductivity . Without high resolution microscopy, scientists would have encountered several problems on interpreting the outputs of, for example, magnetization or heat capacity measurements. In this way, the assessment of nowadays established phenomena as flux pinning or secondary phases would have definitely been difficult or at least delayed.
This applies also for quality assessment purposes. As for an example: prototyping of a new wire/cable/coil often needs feedbacks from microstructural imaging, as a consequence of eventually new heat treatment parameters, new stress/strain levels or fatigue. Sn leakages, cracks and micro fractures are among the possible consequences of these last mentioned phenomena, being easily detectable by means of electron microscopy.
Coupling these experiments with new image analysis techniques (free-to-use software as *ImageJ* or *FIJI*, machine learning, etc.) completes the possibilities for the user, allowing for quick pixel counting, phase recognitions, layout identification, etc. All considered, electron microscopy and, in particular, the nowadays user friendly SEMs, are an essential tool for a systematic characterization study as the one performed in this work.
The SEM investigations were carried out using a FEI Quanta 250 FEG device. The latter is also equipped with an energy-dispersive X-ray (EDX) detector and with an electron backscatter diffraction (EBSD) camera, allowing as well for transmission Kikuchi diffraction (TKD). The latter is an important technique for identifying the morphology of the granular structure, so

mapping the grain sizes: these measurements were also provided for the systematic study in this work, but not performed by the author.

### 3.3.1 Imaging

The two main detectors, namely the backscattered electron (BSE) and the secondary electron (SE) were both used in this work for taking high quality pictures of the wire samples cross sections.

The different principles behind these two modes are depicted in Fig. 3.10. Excluding the Auger emission, the electrons coming from the outmost surface or near-surface layers are the secondary electrons. These last are very useful for the inspection of the topography of the sample's surface, as being a result of inelastic interactions between the beam and the sample, so having lower energy than the backscattered electrons.

The latter are instead a result of elastic collisions deeper in the sample bulk: the number of them reaching the detector is proportional to their Z number, so to the atomic number of the collided compounds. This dependence is useful for differentiating between different phases, providing images carrying information on the sample's composition.

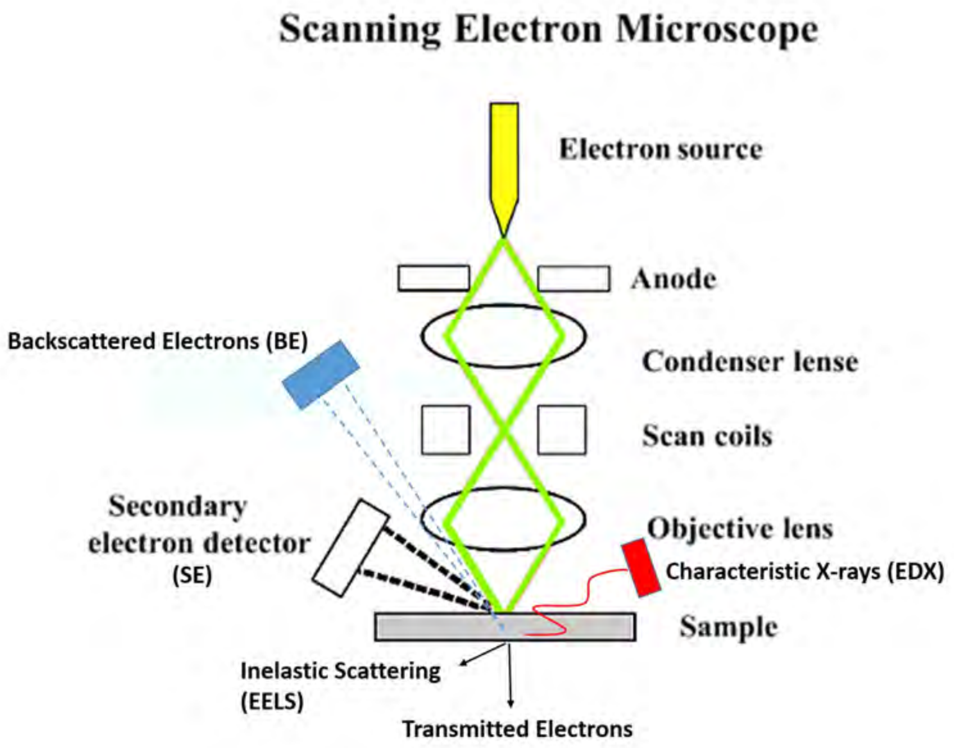

**Fig. 3.10:** Scanning electron microscope operational scheme: elastic scattering electrons give topological information, while the inelastic scatterings produces low energy electrons and/or X-rays. Each different type of electron is recorded with a different detector. Adapted from: *ThermoFisher Scientific/blog/microscopy/SEM working principles*

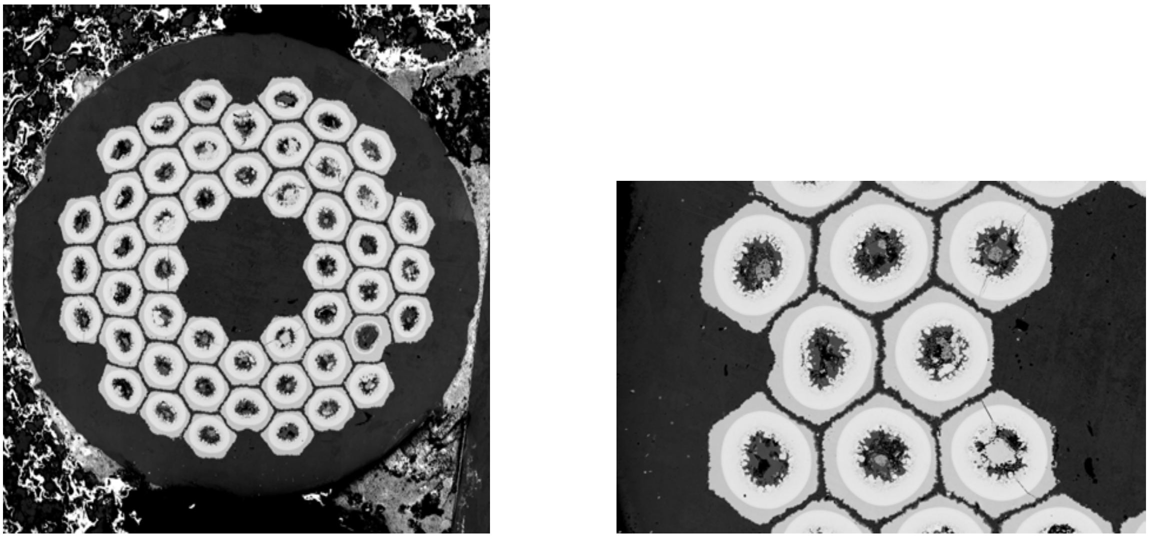

**Fig. 3.11:** Example of sample cross section images with the BSE detector in imaging mode.

For cross-section images (both transversal and longitudinal) the samples are embedded and polished as described in Subsection 2.2.3. The specimen are then placed in the SEM chamber, which is then pumped down below $1 \cdot 10^{-4}$ mbar. The settings used for running the SEM for imaging are summarized in Table 3.3.

**Tab. 3.3:** SEM experimental parameters used for cross-sectional imaging.

| Parameter | Experimental setting |
|---|---|
| Accelerating voltage | 10 kV |
| Working distance | 8-9 mm |
| Spot size | 4-6 nm |
| sample tilt | 0° |

### 3.3.2 EDX

An important option of the SEM is the Energy Dispersive X-ray (EDX) detector, which uses the characteristic X-rays emitted by each element in the sample bulk (Fig. 3.10) in order to provide an elemental analysis.

As already mentioned, the $Nb_3Sn$ phase formation is always subject to gradients in the elemental composition, as a result of the diffusion process occurring during the heat treatment. These differences, one of which is the Sn content "$\beta$" variation ($\Delta\beta$) along the diffusion direction, can easily affect the superconducting properties.

As already illustrated in Chapter 1, the A15 phase of interest exists with Sn content $0.18 < \beta < 0.255$: a small variation within this range can modify the electron-phonon coupling [139], resulting e.g. in a $\Delta T_c(\beta)$ [43, 66]. Another example is the presence of ternary alloys or selected impurities/inclusions, substituting to Sn or Nb in the lattice so modifying the normal state resistivity just above $T_c(\rho_n)$, resulting for example in a $\Delta H_{c2}(\beta)$ ([188]).

The relation between the Sn content/ternary additions/lattice parameter variations has been

studied through the last decades ([40, 124, 139]), making phase composition studies unavoidable for guaranteeing the wire quality and the achievement of the best performance.
For this reason, EDX was used as being tailored for heavy elements investigation: first for measuring the Sn content over the radial diffusion path (as it is the case in Fig. 3.12b) and secondarily on the lamellae prepared for particle size/density measurements, as it will best described in Subsection 3.5.8.

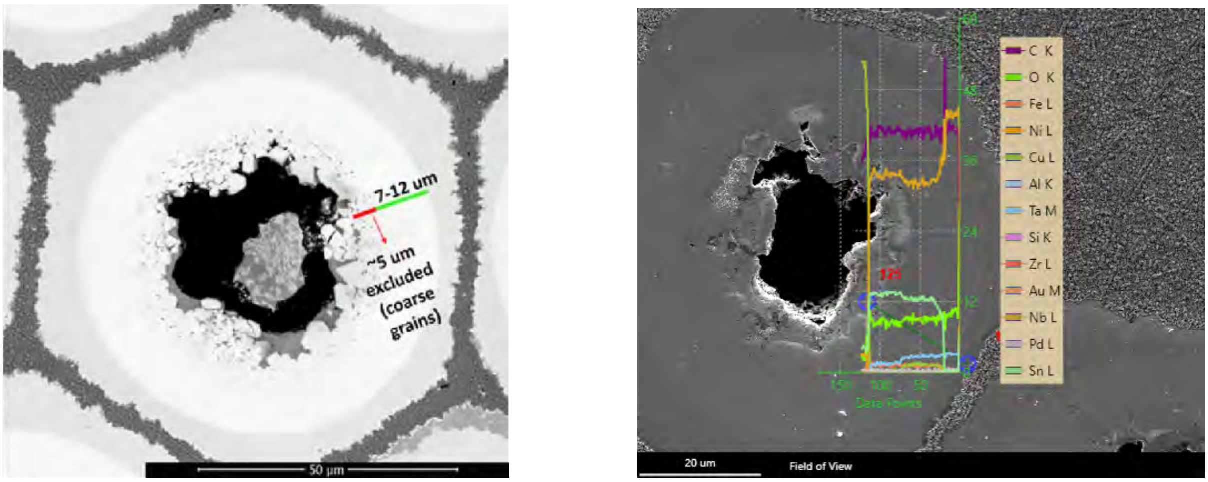

**(a)** **(b)** EDX scan

**Fig. 3.12:** (a) Range used for EDX line scans: the first 5 $\mu$m are excluded in order to avoid measuring on the coarse grain region; (b) EDX line scan measurement as it looks on the dedicated software (*EDAX* from *AMETEK*®)

EDX measurements were performed only on few samples representatives of the recipes, always starting from a good quality picture taken with SEM imaging mode (same sample preparation as for from SEM). The electron beam then scans the filament from its inner core (Sn + Cu) along the cross sectional radial direction toward the outer border (Nb barrier), showing the X-rays emitted point-by-point on a color bar. The experimental settings used for these measurements are summarized in Table 3.4.

**Tab. 3.4:** EDX experimental parameters for phase composition analysis

| Parameter | Experimental setting |
|---|---|
| Accelerating voltage | 15 kV |
| Working distance | 8-9 mm |
| Resolution | 0.3 $\mu$m |
| Dwell time/point | 6 s |

With the listed parameters, a typical line scan performed over the A15 width is composed of approximately 40 points. A spectrum is collected per each measurement point, which is

interpreted by the analysis software as it is explained in Subsection 3.5.6. Two measurements per filament and at least 3 filaments per sample (one per each concentric filament's corona) were investigated.
The results and their validity are discussed in Sections 4.1 and 4.3.

### 3.3.3 STEM and TKD

Scanning transmission electron microscopy (STEM) and transmission Kikuchi diffraction (TKD) are techniques also deployed in this study: the first for analysing the nano-precipitates size (from now on called only "PS") and density (from now on called only "PD"); the last for analysing the grains size (from now on called only "GS"). Even though sample preparation and imaging where not undertaken by the author, some experimental details about these two techniques are needed to understand the analyses widely discussed in Section 3.5 and Section 4.1. The samples were prepared and imaged at the Universitäre Service-Einrichtung für Transmissionselektronenmikroskopie (USTEM) by Sabine Schwarz at the TU Wien.
STEM is an operating mode of the transmission electron microscope (TEM). This device is similar to SEM (which gives 3D image of the sample's surface), but based on recording the transmitted electrons rather than the scattered ones, resulting in 2D projected images of the sample inner structure. The key differences between SEM and STEM/TEM are here summarized:

- Beam acceleration voltages: SEM uses lower voltages, up to 30 kV, while TEM can reach 300 kV;
- Magnification: SEM magnifies a feature 1-2 million times, while TEM up to 50 millions;
- Maximum field of view (FOV) and optimal resolution: TEM allows to image very small parts of the sample, with an optimal spatial resolution <50 pm; SEM can frame larger spots, but with a lower optimal resolution (0.5 nm);
- Sample preparation: TEM requires <150 nm thick samples (also called "lamellae") for the samples to be electron transparent, while SEM has no thickness limits;

The last point of this list is the key reason for STEM/TEM to be operated by trained users only, especially for the case of APC-$Nb_3Sn$ samples. Production of a lamella from these specimen needs a combination of focused ion beam (FIB) and ion milling, resulting in a high risk of lamellae breakage mostly at the very final steps of thickness refinement [155].
STEM is essentially the same mode as standard TEM, but with reversed optics (if one ignores inelastic scattering). Magnetic lenses are disposed in such a way that the beam is finely focused and scans the sample area in a raster pattern as it happens with SEM imaging, while the image is generated by transmitted electrons. In fact, while in TEM parallel electron beams are directly focused to the sample surface, in STEM the beam comes first at a large angle and then is converged into a focal point. Fig. 3.13 shows the beam-focusing difference between the two devices.

Depending on the selected camera length, two detectors were used:

- High-angle annular dark field (HAADF): the camera has a length between 80 mm and 200 mm, matching the HAADF conditions. The contrast stems from Rutherford scattering of the electrons and different Z number of the elements (also called "Z-scattering") ;
- Annular bright field (ABF): the camera has a length of L=680 mm and small collection angles (only the outer annulus of the bright-field disk is used). The signal comes from Bragg scattering, so giving unique contrast effects (useful mainly when the investigated specimen does not differ significantly in Z from the surrounding matrix);

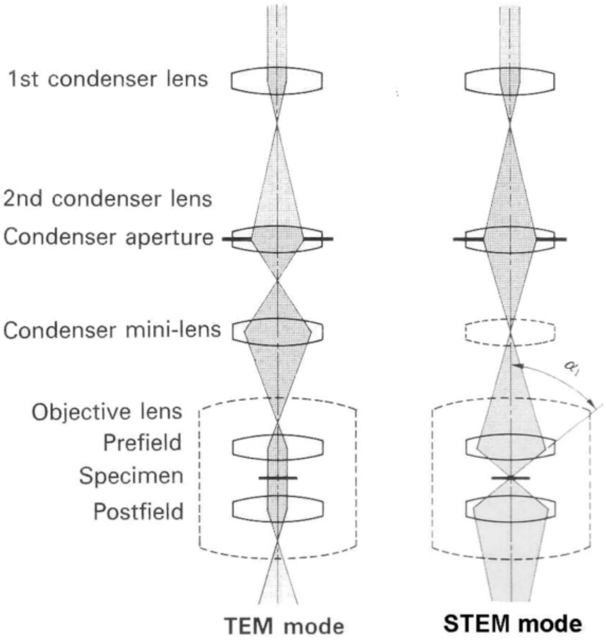

**Fig. 3.13:** Differences between TEM and STEM operating layouts: in STEM the beam is focused through the last lenses before hitting the sample.
Credits:*numis.northwestern.edu*

From these specifications come the advantages of using STEM over TEM, since HAADF is very effective for Z-contrast imaging, having a very low diffraction contrast. Moreover, STEM also allows to couple imaging with EELS/EDX in order to have spatial maps of the information one is looking at. This turns out to be fundamental if one wants to measure the lamellae's thickness, which is unavoidable for calculating PD.

As mentioned, TKD was used for measuring the grain size GS, together with the grains orientation and aspect ratios.
This technique, also known as "t-EBSD", represents the "transmission mode" variant of the electron backscatter diffraction (EBSD). TKD is not the most widely-used technique for determining grain sizes: widely adopted is the so called "fractured sample imaging", where standard EBSD is used for imaging wire samples literally fractured along their radial direction. The grain size is there determined by drawing lines across the grains and counting the number of intersections, with the clear disadvantage of not accounting for the grain shape and eventual overlapping grains in the measured volume.

Differently from STEM, TKD measurements can be performed both with SEM and TEM devices. In fact, the samples need to be thinned as for the STEM measurements in order to be electron transparent, but the required electron beam voltage is way lower than TEM/STEM operational levels, so also SEM can be used. Another reason for refining the thickness of the lamellae is related to the grain size: in these samples, grains are expected not to exceed the 100 nm size threshold, so thicker samples would allow for imaging overlapping grains.

The EBSD camera of the SEM was indeed used for recording the electrons diffracted by the samples' crystal planes. The specimen is only slightly tilted (less than standard EBSD), resulting in smaller diffraction volume/beam diameter which grantees higher spatial resolution compared to EBSD.
Another important advantage over EBSD is the automatic grain size calculation based on the amount of points (and their distance) measured per each grain, allowing also to track their shape and orientation as it will be discussed in Section 4.1. The main experimental settings used for TKD measurements are summarized in Table 3.5.

**Tab. 3.5:** TKD experimental parameters for grain size analysis

| Parameter | Experimental setting |
|---|---|
| Accelerating voltage | 20-25 kV |
| Working distance | 4-5 mm |
| Specimen tilt angle | -30° to -20° |
| Sample thickness | 40-100 nm |
| Step size | 10-20 nm (hexagonal grid) |

## 3.4 Scanning Hall Probe Microscopy

The main disadvantage of the magnetometry devices listed before is their signal coming from the whole sample volume.
Whatever magnetic induction gradient within the volume is impossible to resolve, be it related to microstructural heterogeneity, local damages or presence of different phases.
In this respect, scanning Hall probing provides an efficient solution for local investigations [22]. Hall sensors allow to directly measure the magnetic field and its spatial distribution, without any indirect calculation. Since it is possible to fabricate Hall-probes with active areas down to the nanometric level ([32]), it is intuitively possible to record micro to nano scaled maps of the magnetic field, to be related to several phenomena. For this reason, scanning Hall probing is also referred to be a "microscopy" technique, therefore the acronym SHPM ("scanning Hall probe microscopy") is widely adopted.
The device used in this work is a self-built assembly based on piezo-positioners operating in a helium flow cryostat, offering a scan range of 3 x 3 mm$^2$. The magnet has a maximum magnetic field of 8 T, allowing for a full magnetization of the samples in a wide temperature range (stable between 2.5 K and 150 K). A description of the set-up can be found in [96]. Fig. 3.14 shows the sample rod bottom, where the sample, the Hall probe, the actuators and the thermometer have place.

**Fig. 3.14:** SHPM at the Atominsitut, TU Wien. Placed in a non magnetic holder, the probe (tip of the black arrow) scans the sample placed below (white strip) on a rigid plate. The movement is controlled by piezo-actuators while the temperature is recorded (as close as possible) with a resistance thermometer placed on the left.
Credits: *Sigrid Holleis.*

During operations, the distance between the active area of the probe and the surface to be scanned should be kept as small as possible for investigating the smallest details; moreover, since the spatial resolution depends on the active area of the Hall probe, the latter should be selected as small as the resolving needs. The one here used has an active area of 400 x 400 nm$^2$, but the spatial resolution is limited to 1 x 1 $\mu$m$^2$ by the piezopositioners, which position is monitored by a resistive encoder [97].

In this work, after the sample were prepared following the procedure described in Subsection 2.2.3, two main type of Hall scans have been performed:

- Scans of the Meissner state of the wire sample;
- Scans of the remanent magnetization profile after full magnetization of the wire sample;

The first type of experiments allows to investigate the single filaments geometry over the wire radial direction and also the evolution of some superconducting parameters within the filament itself, as it is better explained in Subsection 3.5.7. The applied field is kept below the lower critical field $H_{c1}$ of the sample, so that the Meissner shielding of each filament is recorded in the experiment. By raising the temperature close to $T_c$, the shielding diminishes down to the point where the filament gets fully penetrated by the applied field.

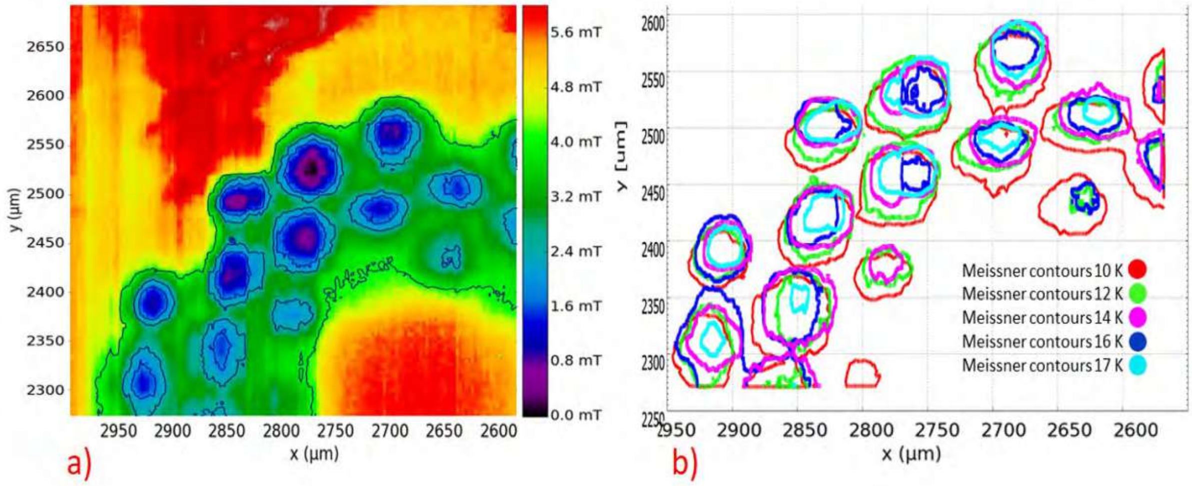

**Fig. 3.15:** **a)** SHPM Meissner-scan of a cross-section quadrant at 12 K and 5 mT ; **b)** Shielding contours evaluation for B=50%$B_{app}$: The A-15 Meissner-shielding radii shrink with increasing temperature.

Figure 3.15 a) presents such a scan at 12 K, where a field of 5 mT was applied in order to safely measure below $H_{c1}$: the shielding contours of the sub-elements are then evaluated where the measured field equals 50% of the applied field (in Fig. 3.15 b), demonstrating how the effective shielding changes with temperature. The drift to the right of the contours, visible in Fig. 3.15, is only apparent and due to an artefact of the resistive encoder (encoding of x and y positions change slightly with $\Delta T$).

In the same way, possible inhomogeneities in the filament diameters over the wires longitudinal cross section were investigated. These gradients can be due to problems during the drawing process or to non-uniform heat treatments, leading to deformations of the inner A15 hollow tube (also known as "sausaging" of the A15 phase). The latter can affect severely the superconducting performance (reduction of the effective current transport area), mainly present in the early prototype stage of the wire development. Fig. 3.16 shows a comparison of a SEM picture (left) with a Meissner state scan (right) taken with the SHPM from the same longitudinal cross section of a monofilamentary sample: the magnetic signal disappears in the shielded region, perfectly correlating to the deviations observable in the microstructure on the left.

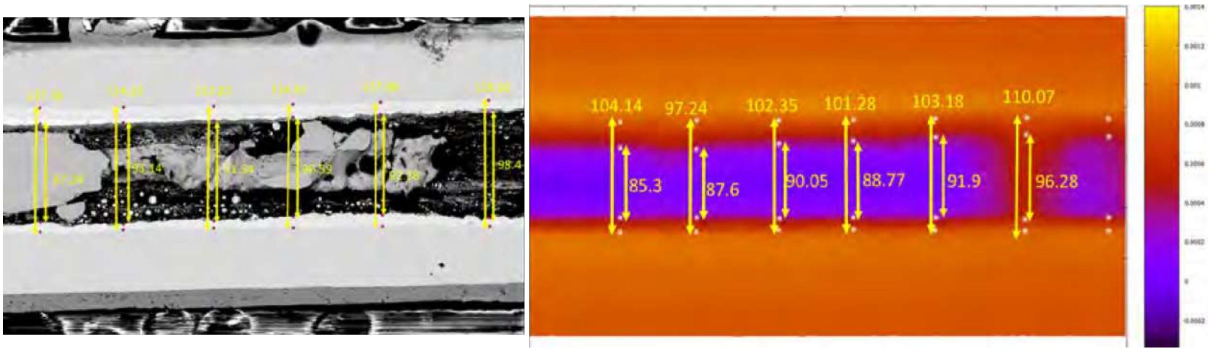

**Fig. 3.16:** Comparison between SEM (left) and SHPM (right) pictures of the same ≃ 400$\mu$m of sample length. The displayed values in yellow are expressed in $\mu$m.

The second type of measurements were used for investigating the local currents. By inverting the Biot-Savart law (the algorithm was devised in Ref. [50], from now on called only "inversion script"), it is possible to extract absolute values of the flowing currents from a really thin sample, needing the thickness to be negligible if compared to the other dimensions. This is the main reason for trying to polish the slices to be as thin as possible, as explained in Subsection 2.2.3: in order to produce valuable results, the inversion script needs the scanning step-size, the surface-probe distance and the sample thickness to be substantially comparable quantities.

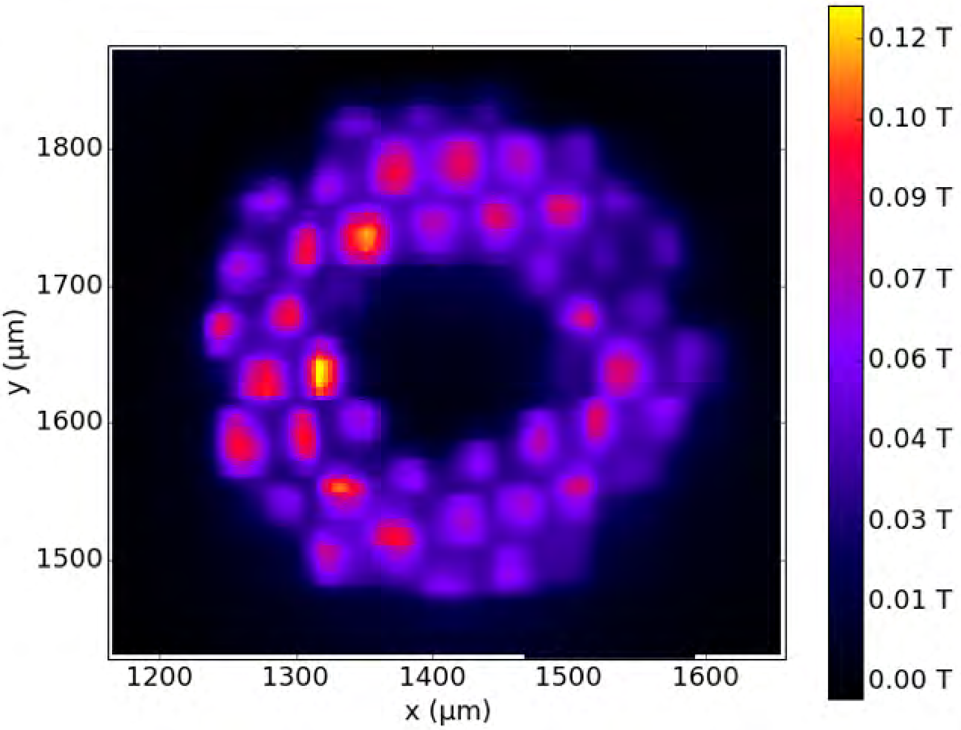

**Fig. 3.17:** Remanent magnetization profile recorded of the sample B-Zr2 at 10 K and zero field, after applying $H_a$=1 T. The sample is approximately 80 $\mu$m thick with the probe being $\simeq 6\mu$m above the scanned surface. The non-uniformity of the signal from the filaments indicates inter-filaments inhomogeneities of the superconducting properties.

The samples were fully magnetized with an applied field (according to the Bean model $H_a \geq 2H^*$) at a constant temperature, then the residual magnetization was measured with the Hall probe. An output of such an experiment is shown in Fig 3.17.
The evaluation methods used for analysing these experiments is discussed in Subsection 3.5.7.

## 3.5 Data Analysis

### 3.5.1 $J_c$ evaluation from m-H loops

As it is impossible to measure the critical current density of the sample by means of magnetometry, a model relating the irreversible magnetic moment of the sample to $J_c$ is used. Among the two main proposals in literature [183] and [17], the one of *Baumgartner et al.* was selected. The latter considers the wire's filaments to have all the same geometry (hollow cylinders) and each to contribute equally to the global magnetic signal. The layer $J_c$ - the current flowing only through the superconducting region of the wire - is derived as follows:

$$J_c = \frac{3}{4} \cdot \frac{m_{irr}}{NL(r_o^3 - r_i^3)} \tag{3.5}$$

where $L$ is the length of the sample perpendicular to the applied field and larger than $r_o$ and $r_i$, the outer and inner radii of the filament-representative hollow cylinder, respectively (already mentioned in Subsection 3.1.3). $N$ is the number of filaments in the wire sample and $m_{irr}$ is the irreversible magnetic moment as described in Eq. 3.1.
Very similar results are obtainable with the other listed method, this being a good feedback for the assumptions used in the selected model. From the calculated quantity in Eq. 3.5 it is also possible to calculate the current density averaged over the entire wire cross section $J_e$ ("*engineering* $J_c$") as :

$$J_e = J_c \cdot \frac{N(r_o^2 - r_i^2)}{R^2} \tag{3.6}$$

In general, if a transport or induced current is flowing in a sample, there will always be a magnetic field generated by it. The latter is called "self-field" $B_{sf}$ and it has to be taken in consideration when evaluating the magnetic moment as a function of an applied field. Indeed, a more accurate version of Eq. 3.1 is:

$$m_{irr}(H_a) = \frac{1}{2}(m_{dec}(H = H_a + B_{sf}/\mu_0) - m_{inc}(H = H_a - B_{sf}/\mu_0)) \tag{3.7}$$

By using the script described in [17] it is also possible to automatically correct for the self-field contribution, so computing the right magnetic moment at the right field as $m_{irr}(B)$. The single filament is divided into line elements carrying each part of the total $J_c$, then the generated magnetic field distribution is calculated. This is extended to the whole wire cross section by superposition of each filament contribution, coming up with an average value of $B_{sf}$ for the whole sample. The simulated small impact of the self field in multi-filamentary wires together with the intrinsic first-order correction in the calculation of Eq. 3.7 motivated the assumption of $B = B_a$ for all the analyses in this work.

### 3.5.2 $I_c$ from resistive measurements

The critical current $I_c$ from transport measurements is usually determined using the well known power law:

$$V = CI^n \tag{3.8}$$

which well describes the transition from the superconducting to a resistive state, as it is possible to see in Fig. 3.18. $I$ is the applied current, while $V$ is the measured voltage and $n$ the so called "$n$-value", being a transition index inversely related to the width of the $V$-$I$ transition. The constant $C$ does not represent a useful parameter while $n$ is considered a quality factor for wires and cables: a high $n$-value means a narrow transition to the resistive state, representing either a distribution in the elementary flux-pinning forces (intrinsic effects) or filaments heterogeneities along length/cross section (extrinsic effects) [71, 190].

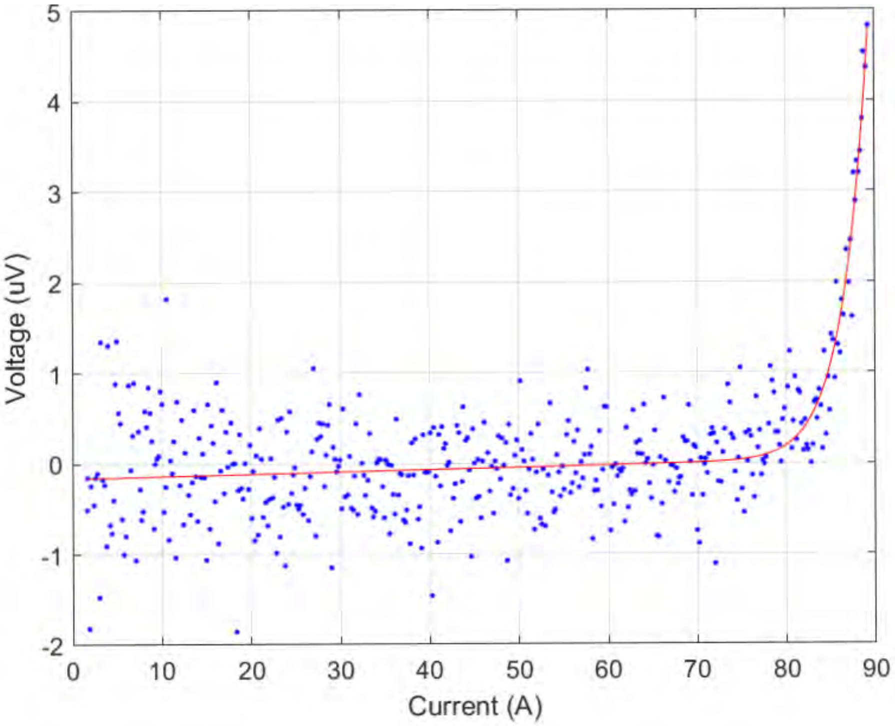

**Fig. 3.18:** I-V curve of sample T-Zr1-700x71 at 20 T measured at the NHMFL. The red solid line represents Eq. 3.8 fitting the experimental data (in blue).

The evaluation script here used identifies the measurement baseline, performs offset corrections, compute the logarithm of the data and fit a linear function to them (the power functions look linear in log-log plots). Finally, by looking at Eq. 3.9 (a more practical form of eq. 3.8), the critical current $I_c$ is obtained by calculating the intersection of the fit function with an electric field criterion for $E_c$ chosen by the user.

$$(E/E_c) = (I/I_c)^n \tag{3.9}$$

The latter is essential for identifying $I_c$, being selected according to the type of measured superconductor ([71]). In this case, both the $E_c$=1 $\mu$V/cm and $E_c$=0.1 $\mu$V/cm criteria were tried, thus evaluating always a double set of $I_c$ on a gauge length of 8 mm (Subsection 2.2.2), corresponding to voltage thresholds of 0.8 $\mu$V and 0.08 $\mu$V respectively.

### 3.5.3 H$_{c2}$ from resistive measurements

The upper critical field measurements taken at the NHMFL were recorded using the standard 4-points method, by raising the applied $H_a$ up to the field where the transition to normal state is completed. The evaluation procedure follows the fit function used in [75]:

$$\rho(\mu_0 H) = \rho_{base} + (\rho_{norm} + C\mu_0 H) \cdot \frac{exp\left[4e\left(\mu_0 H - \mu_0 H_{1/2}/\mu_0 H_w\right)\right]}{exp\left[4e\left(\mu_0 H - \mu_0 H_{1/2}/\mu_0 H_w\right)\right] + 1} \tag{3.10}$$

where $\rho_{base}$ is the resistivity in the superconducting state (0 Ohm) plus some offset (often present from measuring small induced voltage from the applied field ramp) and $\rho_{norm}$ is the resistivity at the end of the transition. $H_{1/2}$ is the applied magnetic field value at half the transition height and and $H_w$ is the transition width; $C$ is a constant in a linear term that describes the magneto-resistance; the tangent hyperbolic functions ratio describe the measured transition. This fitting function yields very good fits to the experimental data, as it is possible to see in Fig. 3.19.

The upper critical field $H_{c2}$ is then chosen from one of the highlighted points of the fit as in Fig. 3.19 (three points, namely $B_{c2-10}$, $B_{c2-50}$ and $B_{c2-90}$ were automatically recorded by the evaluation script per each measured sample).

The upper critical field measurement taken at the Atominstitut were, as explained in Section 3.2, bonded by the 17 T maximum applicable field. For this reason the evaluation procedure differed from the just listed, this time following the method in [16]. Three linear fits are computed: $f_1(T)$ fits the transition, $f_2(T)$ the superconducting region and $f_3(T)$ the normal conducting one. The point where $f_1(T)$ crosses $f_2(T)$ and $f_3(T)$ are calculated for obtaining $T_1$ and $T_2$ (transition start and end). Finally the $B_{c2}(T)$ curve is built using 3.11, where $B_a$ is the applied field.

$$B_{c2}\left(\frac{T_1 + T_2}{2}\right) = B_a \tag{3.11}$$

### 3.5.4 $B_{irr}$ from SQUID magnetometry

$B_{irr}$ of each sample in this study was investigated also from $m$-$H$ loops. SQUID magnetometry was used, allowing for applying field up to 7 T as mentioned in Section 3.1. This field cap constrained the measurements to be valuable only at relatively high temperatures (from 10 K on), since extrapolating $B_{irr}$ would result in unreliable values at lower temperatures [170]. Two different methods, described in the following sections, were used to evaluate the field $B_{irr}$ of the samples at specific temperatures:

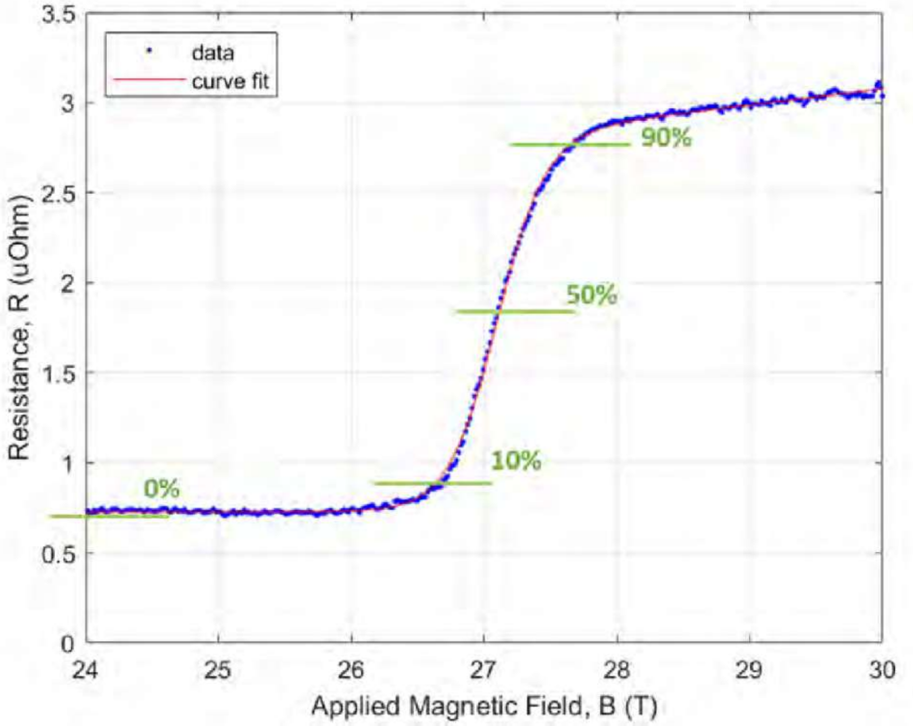

**Fig. 3.19:** R-H curve of a T-Zr2-700x69 sample taken in a 31 T cryostat. The red solid line represents Eq. 3.10 fitting the experimental data (in blue). The horizontal lines indicate the most common evaluation points at 0, 10, 50 and 90 % of the transition to the normal state.

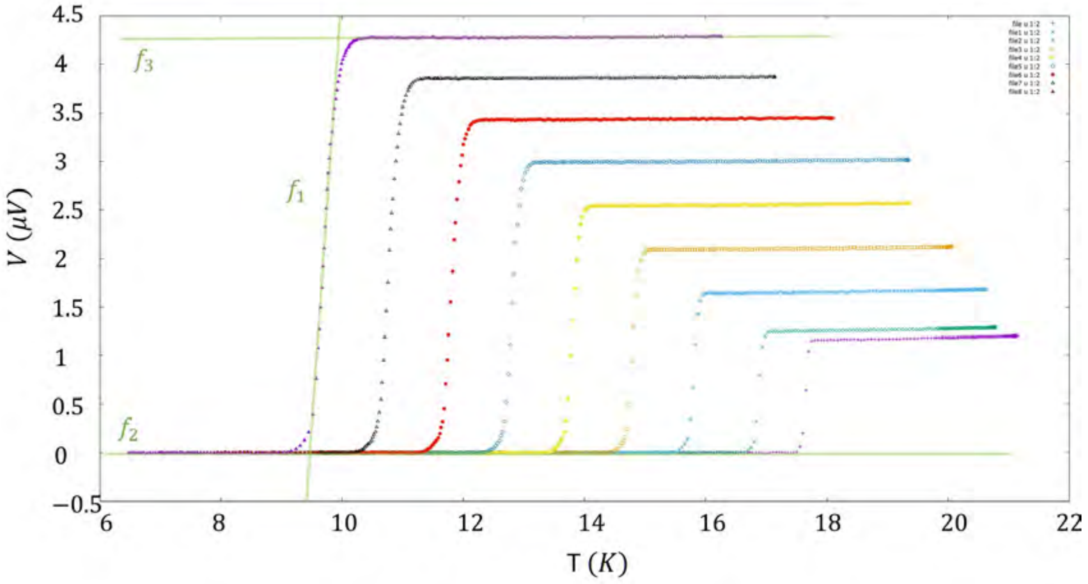

**Fig. 3.20:** V-T curves of sample B-Zr1 taken in the 17 T cryostat at the Atominstitut. Different colors represent the applied magnetic field for each measurement; the solid green lines are the fitting functions $f_1(T)$, $f_2(T)$ and $f_3(T)$ used on the 15 T dataset for identifying the transition temperatures of each measurement.

- Evaluation from SQUID $m$-$H$ loops;
- Kramer extrapolation

The first method is directly connected to the observed end of the induced transport currents, therefore closer to the definition of "irreversibility field" $B_{irr}$ than $B_{c2}$. The second one is instead a long-time used extrapolation method for predicting $J_c$ or $B_{irr}$ when the experimental possibilities do not allow for direct measurements [110]. Only recently, the latter started to lose credibility due to always richer and heterogeneous manufacturing of $Nb_3Sn$ compounds (ternary/quaternary starting alloys, presence of inclusions, oxide powders, etc.) [188].
The results from both procedures are discussed and compared here following.

#### 3.5.4.1 Evaluation from *m*-*H* loops

$Nb_3Sn$ superconductors are always found to lose their capacity to carry super-currents at a field that is smaller than $B_{c2}$, also called $B_{irr}$.
The difference between the two entities was first observed in a LaBa-Cu oxide by Muller, Takashige, and Bednorz [142] they showed that in this material there exists a large temperature region below the mean-field critical-magnetic-field line $H_{c2}$(T) where the motion of magnetic flux lines is reversible.
If the difference between $B_{irr}$ and $B_{c2}$ is quite consistent in HTS [151, 173], for $Nb_3Sn$ $B_{irr}$ is usually 0.8-0.9 $B_{c2}$: this gap was first noticed by Suenaga et al. [179], who attributed it to the threshold of thermally activated flux line jumping, as it is for high temperature superconductors. Only later, it was found that in wire samples this $B_{irr}/B_{c2}$ difference is mostly caused by the inhomogeneity of the A15 layer [34, 77]. It corresponds to a transformation of the vortex lattice: at a given temperature, for fields below $H_{irr}$, the vortices are pinned and above move freely. Consequently, there is no hysteresis in the magnetization and electrical resistivity appears. For this reason, $B_{irr}$ will be used as the field at which $J_c$ vanishes in the following discussions.

At high temperatures (e.g. 15K) $B_{irr}$ should be in the magnetic field range of the SQUID-magnetometer. The irreversibility field is reached when the hysteresis loop of the magnetic moment goes to zero or that the moments measured in raising ($m_+$) and decreasing ($m_-$) applied field are the same.
By deploying a fine step size of 0.05 T or 0.1 T in the higher field range (from 4 to 7 T), it is possible to fit the SQUID data: a spline fitting curve is used, which is a piecewise polynomial function. The number of spline knots is determined by the amount of measured points: the evaluation script automatically selects the fitting parameters in order to fit all points. When the net difference between the two branches is $\leq 2 \cdot 10^-9$ Am$^2$, the script considers this point to be the value of $B_{irr}$.

Figure 3.21 illustrates the experimental points of the magnetic moment of a T-Zr1 sample at a temperature of 15 K and the fitted curves connecting these points. The intersection is at 5.23 T, corresponding to $B_{irr}$.

As long as there is an intersection of the fitted curves in the magnetic field range of the SQUID, this method can be used to provide accurate results for the irreversible field. At lower temperatures (e.g. 10 K) other methods have to be used to identify the $B_{irr}$ value.

#### 3.5.4.2 Kramer extrapolation

At low temperatures the irreversible field value exceeds the maximal possible magnetic field of the SQUID magnetometer, therefore $B_{irr}$ cannot be measured directly. If evaluating within 17-10

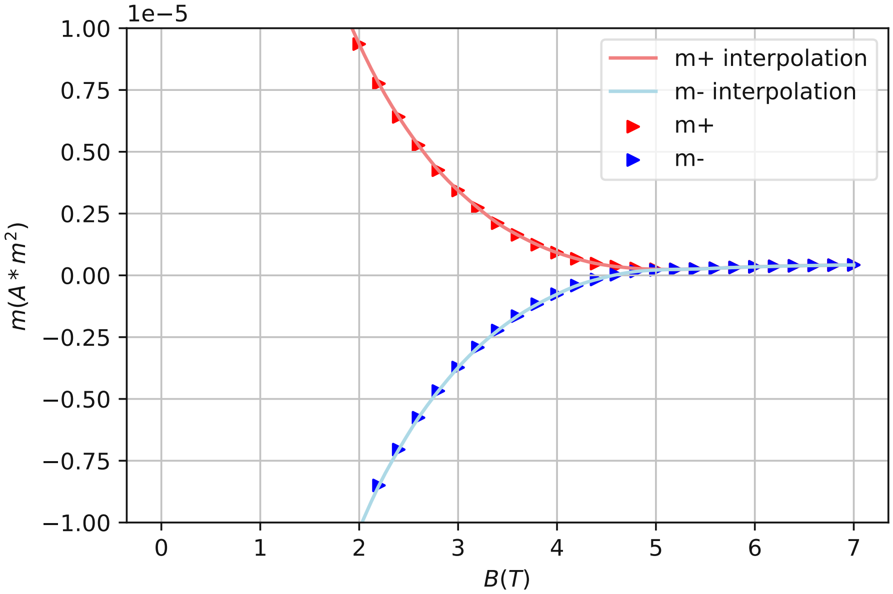

**Fig. 3.21:** Experimental points of a m-H loop from a T-Zr1 sample recorded at 15 K: the moments recorded in raising ($m_+$) and decreasing ($m_-$) are displayed in red and blue, respectively. The interpolating curve is also shown.

K, a "short range" (0.5 to 9 T) extrapolation is enough for identifying $B_{irr}$, so endorsing the validity of the Kramer method (see [188]).
The Kramer function $Kr$(B) is a model of the flux pinning force $\mathrm{F_p}$, defined as

$$Kr(B) = J_c^{0.5} B^{0.25} \tag{3.12}$$

Where $Kr(B)$ is the so called "Kramer function", proportional to (1-$b$) (where $b$=$B/B_{irr}$ is the so called "reduced field"). The irreversibility field can be now found as a solution to the equation $Kr(B_K) = 0$, where $B_{irr}$ is approximated as the Kramer field $\mathrm{B_K}$ [170]. To determine the zero point of this function, a linear regression of the Kramer function to the field axis is used.

In Figure 3.22 the Kramer extrapolation for a T-Zr1 sample, the same sample type as in the previous section, is shown at two different temperatures. The linear regression for 15 K is done between 2 T and 4 T and for 10 K between 3 and 6.6 T. These magnetic field ranges have been chosen, because of the good linear behaviour of the Kramer function in this sections.

Between $T_c$ and 14 K both the above discussed methods provide results for the irreversibility field and can be therefore compared. $B_{irr}$ from the Kramer extrapolation is constantly smaller than the evaluated value from the m-H loops by an average difference of about 0.2 T, diverging from this trend only on few outliers.
The results of these evaluations and their placement in the pinning models are presented in Section 4.1 and Section 4.2.

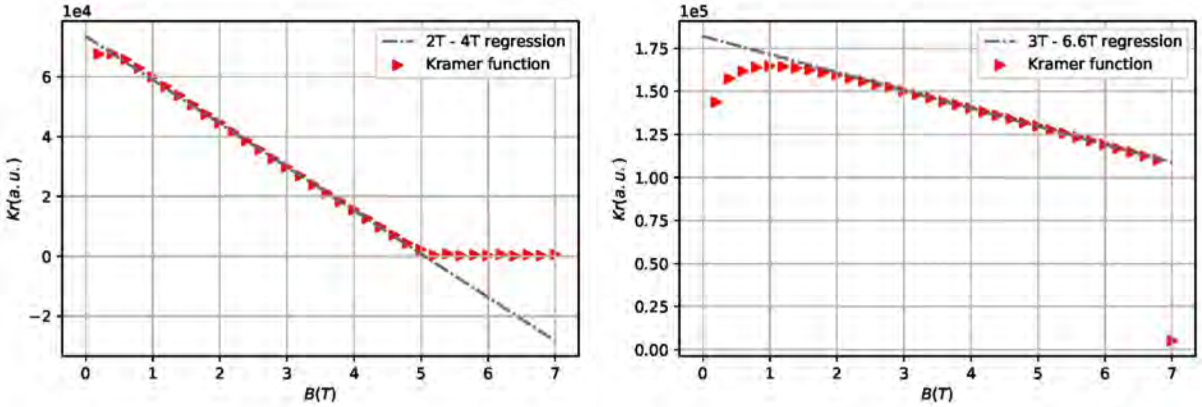

**Fig. 3.22:** Kramer extrapolation points and linear regression lines for 15K (a) and 10K (b) of a T-Zr1 sample.

### 3.5.5 $T_c$ and $T_c$-distributions from AC susceptibility

The critical temperature $T_c$ as well as the transition width $\Delta T_c$ were assessed from AC susceptibility measurements by using a similar fitting method to the one deployed for the $H_{c2}$ evaluation from the 17 T cryostat measurements. As explained in Subsection 3.1.2, in PIT samples one finds fine-grains FG and coarse-grains CG to have different $T_c$. For this reason, since the current transport properties are dominated by the FG population, the focus was on assessing only their $T_c$.
The used script first normalizes the measured $m'$ to its minimum, then looks for peaks in $m''$. Differently from the other $Nb_3Sn$ manufacturing technologies, in PIT wires two peaks in $m''$ are detected: the first indicates the transition of the fine grains, the second (0.5 K to 1 K above the first) of the coarse grains. As it is shown in Fig.3.4, the in-phase magnetic moment $m'$ results in a two-humps curve, with the $m''$ peaks corresponding to the points of max slope of $m'$. Three linear functions are then fitting the curve as netter showed in Fig.3.23: the transition point between FG and CG is the "cap value" of $m'$, identified as being the point where $m'$=constant. Finally, the border temperatures $T_1$ and $T_2$ are calculated.

From these values, the critical temperature is defined as follows:

$$T_c = \frac{T_2 - T_1}{2} \tag{3.13}$$

with the transition width being

$$\Delta T_c = T_2 - T_1 \tag{3.14}$$

AC susceptibility curves were also used for evaluating how $T_c$ is distributed within a filament itself. The critical temperature is not constant along the A15 radial direction, therefore it is more correct to talk about $T_c$ distribution rather than a single $T_c$ value (which is nevertheless used as a representative for practical reasons).
Evaluating this feature is possible for the reason why a magnetic field applied parallel to the wire

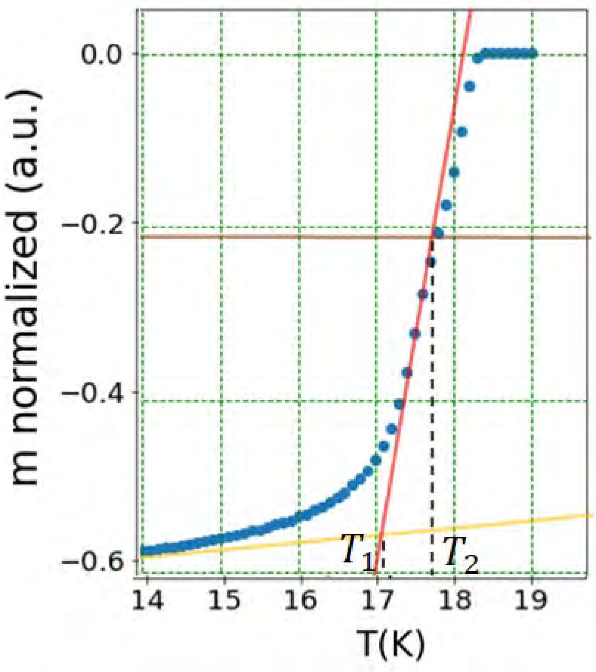

**Fig. 3.23:** Zoom of Fig.3.4 illustrating in detail the $T_c$ evaluation method: the critical temperature is evaluated between $T_1$ and $T_2$ since the focus in on the fine grain population only.

can penetrate a sub-element from the barrier towards the core, thus allowing to probe the radial $T_c$ distribution [93]. This method is now well established [14, 92] and was used also in this work: all sub-elements are assumed to be identical parallel tubes with same geometry, composition and radial Sn gradient (with the highest value on the inside). In fact, as mentioned in Subsection 3.3.2, Sn gradients from the filament core to the outer A15 border reflect as $\Delta T_c$, considering the latter to be a particularly stoichiometric-sensitive parameter for this material [65, 78].
If the assumptions before listed are valid, the script divides the filament in a number $k$ of shells assigning each an initial $T_c$ value. For each shell, it calculates the magnetic penetration depth based on the assigned $T_c$ as follows:

$$\lambda(t) = \lambda(0)\frac{1}{\sqrt{(1-t^4)}}, \qquad t = \frac{T}{T_c} \tag{3.15}$$

which is the two-fluid model expression for the temperature dependence, where the zero-temperature penetration depth $\lambda(0)$ was chosen to be 124 nm according to [77].
Calculating $\lambda$ allows the magnetic field inside the filaments to be computed based on its exponential decay as:

$$H(x) = H(0)e^{-x/\lambda} \quad \longrightarrow \quad H_k = H_{k-1}e^{-d/\lambda} \tag{3.16}$$

where $d$ is the shell thickness, and $H_k$ is the magnetic field at the $\mathrm{k^{th}}$ shell. The current I is then evaluated from Maxwell's equation $\nabla \times H = j$ by integrating over the cross section perpendicular to $j$.
Having I of each simulated shell allows to finally compute the total magnetic moment of the $i^{th}$ filament $m_i$ as a summation of each filament's shell $m_i = \pi \sum_{k=i+1}^{N} r_k^2 I_k$.
If the latter does not match the experimental moment $m_{exp}/N$ (where $N$ is the number of filaments in the sample), $T_c$ of each shell is adjusted until finally $m \equiv m_{exp}/N$.

An example of output of this evaluation is shown in Fig. 3.24: the position of the shell along the radius is displayed in terms of relative position between the Sn-Cu core and the Nb barrier. Each shell has its own $T_c$(r) value, eventually reflecting a Sn content value.

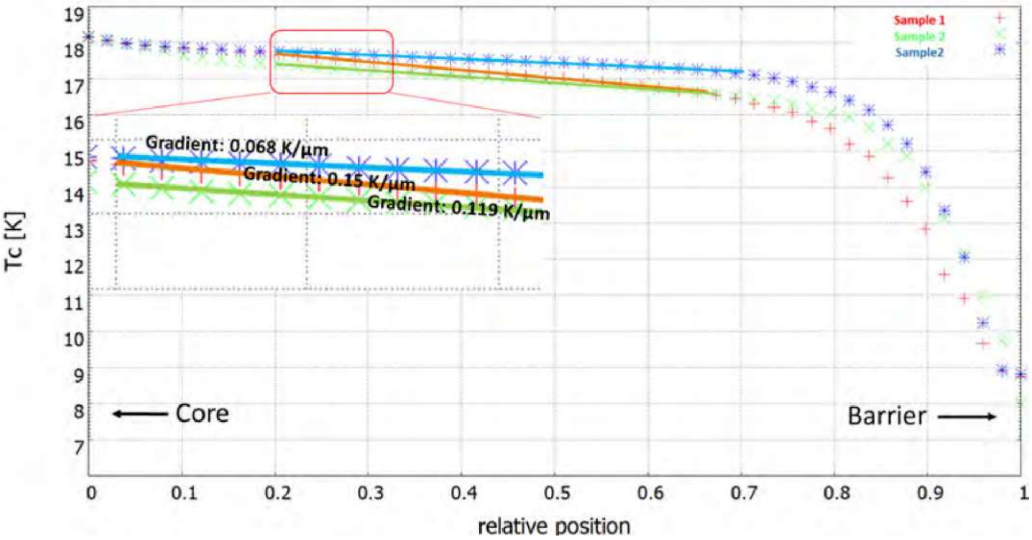

**Fig. 3.24:** Critical temperature distribution of two T-Zr1 and one T-Hf1 samples. $T_c$ clearly decays by approaching the Nb-barrier side, following the direction of solid state diffusion occurred during the heat treatment. Sn gradients along this direction are a strong correlation factor.

The latter is in fact strongly indicated to be the main responsible for the distributed $T_c$ over the A15 cross section, being the latter often correlated with microstructural investigations to $T_c$ (e.g. EDX line scans) [93, 94]. The evaluation script here described can also convert the obtained $T_c$(r) results into Sn content $\beta$ by means of the empirical model proposed by *Godeke* [76]:

$$T_c(\beta) = \frac{T_c^{min} - T_c^{MAX}}{1 + e^{(\beta - 0.22)/0.009}} + T_c^{MAX} \tag{3.17}$$

where $\mathrm{T}_c^{MAX} = 18.3$ K, the highest recorded value for $\mathrm{Nb_3Sn}$ [90]. Equation 3.17 represents a Boltzmann sigmoidal function fitting the datasets of *Devantay et al.* [40], where the minimum atomic Sn content for a stable A15 phase is 17%, corresponding to $\mathrm{T}_c^{min} = 6.09$ K.
Since this model was proposed for binary samples, it was needed to modify the parameters by

taking into account how Ta modifies $T_c$ in the ternary samples. The latter have all 4 at.% Ta content alloyed in the starting alloy, resulting into approximately 3 at.% into the A15 phase (also called "phase content") after the HT [180]. At this level, Ta is expected to slightly increase $T_c$. Therefore, more appropriate parameters were obtained after adding 0.2 K to each calculated $T_c(\beta)$ value, so fixing $T_c^{MAX} = 18.5$ K to ensure a reasonable value at the phase boundary ($T_c(\beta = 25.5) = 18.25$ K) and obtaining by substitution $T_c^{min} = 6.29$ K, this increase being the mid-value between the reported data in [90] and [14].
The results and comparisons of this technique with EDX are presented in Chapter 4, Sections 4.1 and 4.2.

### 3.5.6 EDX analysis

As mentioned in the previous Subsections, compositional variations in the A15 lattice affect deeply the superconducting properties of the phase: atomic Sn content $\beta$ is only one among the other variables, e.g. the lattice parameter (a), the long range order (LRO) or the normal state resistivity just above $T_c(\rho_n)$. Changes in composition ($\Delta\beta$) are described by *Godeke* [77], who summarizes their impacts on $T_c$ and $H_{c2}$ respectively over decades of experimental and modelling work from different research groups, as it shown in Fig. 3.25.

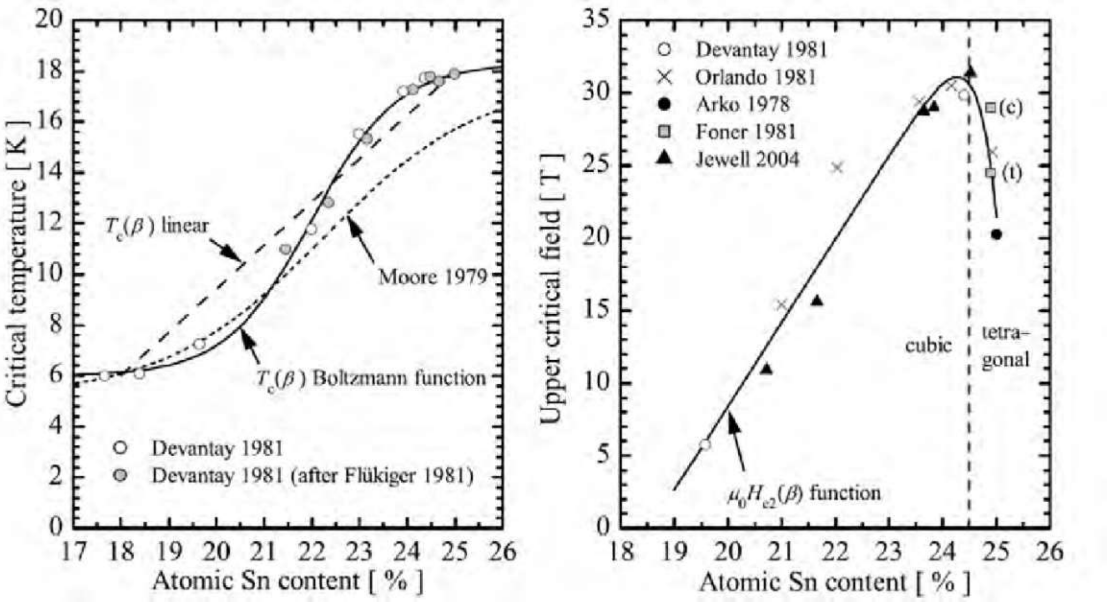

**Fig. 3.25:** on the left: collection of results from *Devantay et al.* as in [40]; on the right: results collected by *Flükiger* and others after him [4, 40, 146].
The plotted functions summarize most of the available results in literature.
Credits *A. Godeke, PhD Thesis.*

Equation 3.17 is represented by the solid black line on the left plot of Fig. 3.17, while the following equation for $B_{c2}(\beta)$ represents the black line shown on the right plot:

$$\mu_0 H_{c2}(\beta) = -10^{-30} exp\left(\frac{\beta}{0.00348}\right) + 577\beta - 107 \tag{3.18}$$

These empirical formulations are mostly deduced from EDX measurements, the latter being still a valuable experimental technique for correlating the performance of a $Nb_3Sn$ sample with, for example, its manufacturing parameters [76]. Since the compositional gradients mostly occur because of the diffusive process inherent in any manufacturing, EDX results coupled with $T_c$ measurements of *ad hoc* prepared samples constitute the most of the available literature, being for the manufacturer a "quality map" for assessing e.g. the progresses in optimization of a new prototype wire.

For the purpose of this work, besides pure reporting of the APC-$Nb_3Sn$ manufacturing technology advancement, EDX is used for assessing the impact of compositional gradients on the flux pinning.

The analysis of the EDX measurements starts from the spectrum interpretation. The latter is composed of:

- X-rays continuum: inelastic scattering of the primary beam electrons, where the latter lose energy without producing ionization of atoms in the sample;
- Characteristic X-rays: inelastic scattering between electron beam and inner shell electrons, resulting in electron ejections from the atom with formation of characteristic X-rays;

Only peaks which are statistically significant were considered for elemental identification: the minimum peak size should be 3 times the standard deviation of the background at the peak position [79].

By using the analysis software *Elemental Analytical Microscopy Texture (TEAM)* from *EDAX™*, one begins the qualitative analysis with the most intense line towards the high-energy region of the spectrum, where the lines within a "family" are well separated. As an example: if the analysed peak is above 3.5 keV, this must be originated either by a K or L shell electron (the most inner ones).

The peaks locations are then compared to the "KLM markers" (the known positions of $\alpha$, $\beta$ and $\gamma$ energy peaks of the shells K, L and M of an atom): if the chosen line does not correspond to e.g. a K line, then an L series is tried. If the same line is identified as being the L$\alpha$, several other lines both above and below the L$\alpha$ should be present and correspond uniquely to the investigated element.

This process continues from high to low energies: when all high-energy lines and low-energy L and M lines are identified, light elements spotting can be attempted: resolving those peaks is not always easy and will not be here discussed since the most of the investigated elements are considered to be heavy elements.

A spectrum recorded with EDX is shown in Fig. 3.26a: the user selects the elements to be investigated and only the related peaks are shown. Nb and Sn peaks emerge out of the continuum as being forming the A15 phase. This is clear from 3.26b, where the scanned elements are expressed in weight % and atomic %.

Also the Ta content was investigated, since its content is an important parameter as discussed in Subsection 3.5.5.

For extracting the single element compositions (as it is the case for Sn), the total atomic content of the elements Nb, Sn and Cu as well as Ta was normalized to 100% and the fractions of the

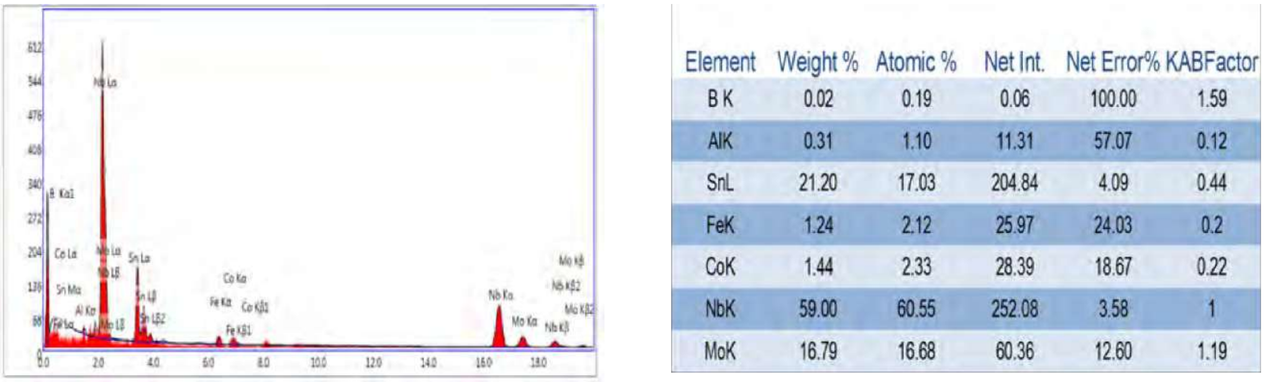

| Element | Weight % | Atomic % | Net Int. | Net Error% | KABFactor |
|---|---|---|---|---|---|
| B K | 0.02 | 0.19 | 0.06 | 100.00 | 1.59 |
| AlK | 0.31 | 1.10 | 11.31 | 57.07 | 0.12 |
| SnL | 21.20 | 17.03 | 204.84 | 4.09 | 0.44 |
| FeK | 1.24 | 2.12 | 25.97 | 24.03 | 0.2 |
| CoK | 1.44 | 2.33 | 28.39 | 18.67 | 0.22 |
| NbK | 59.00 | 60.55 | 252.08 | 3.58 | 1 |
| MoK | 16.79 | 16.68 | 60.36 | 12.60 | 1.19 |

(a) (b)

**Fig. 3.26:** (a): Spectrum of an EDX line scan performed along the A15 width; (b) output of the analysis for the selected elements.

atomic contents were calculated. In this way, Sn-content plots were produced for the measured samples, as it presented in Fig. 3.27. The scanned width is approximately 9 $\mu$m along the A15 radial direction, normalized to 1. The uncertainty is expressed through the blue 1$\sigma$ region, confirming one more time the limited accuracy of the EDX quantification [143]. The red solid line represents the fit over the linear region, so defining a gradient (expressed in at.%/$\mu$m).
In PIT samples (as the ones studied in this Thesis) a two-fold gradient is usually visible , being the first (higher amount of Sn) closer to the core representing the coarse grains $\Delta\beta$ and the second (lower amount of Sn) representing the fine grains $\Delta\beta$. The latter is usually the value used in literature for representing/comparing the homogeneity level of a specimen, being the current transport properties ruled by the fine grained population only .

The results and their impact on the pinning potential of the samples - ultimately, Sn gradients $\Delta\beta$ affect the critical current density as $J_c(\beta)$ - are discussed in Chapter 4.

### 3.5.7 Scanning Hall probe microscopy

As explained in Section 3.4, two types of measurements were done using the SHPM.
The first ones are Meissner scans, in which the Meissner shielding effect is used for the following investigations :

a) Filament geometry uniformity over the wire transversal and longitudinal cross sections: reproducibility of the filaments geometry and check for mechanical integrity as a base measurement to assess the wire quality;

b) Evaluation of the critical temperature distribution within the filament, to be correlated with the same experiment from SQUID (bulk) magnetometry and composition analysis from EDX.

For the case a), the layout uniformity was assessed by visually evaluating the contours of the shielded regions and eventually comparing them with BSE images from SEM, as also for the longitudinal scans in Fig. 3.16.
Each filament scanned looks like the one in Figure 3.28: the field is 0 in the inner region, while outside the filament the applied field $H = H_a$ is recorded. A Sn leakage or micro fractures of

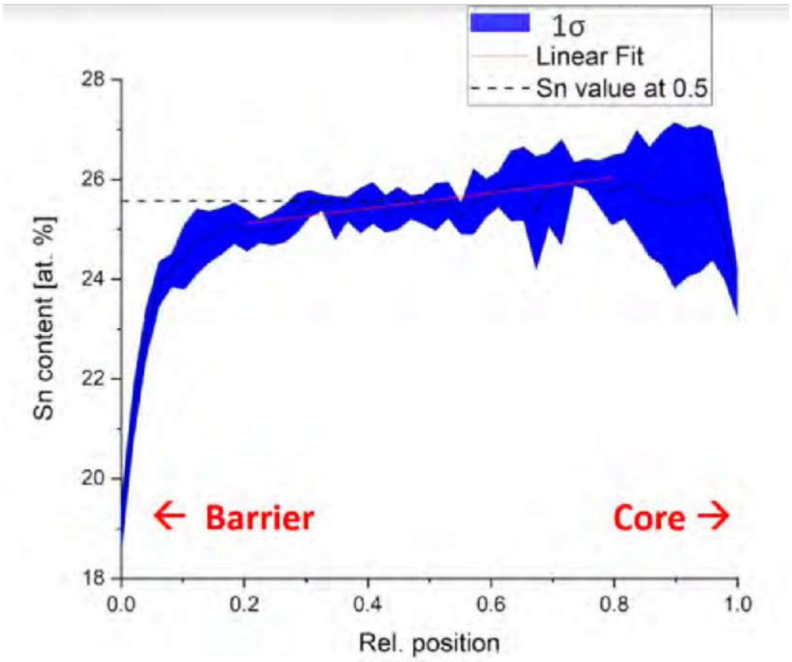

**Fig. 3.27:** Sn compositional gradient vs position along the A15 width : the red solid line is the linear fit applied in the mid-range "plateauing region". The half-value of this transition is indicated with the dashed black line, while the uncertainty ($1\sigma$) is displayed in blue.

the filament would manifest as a penetration of the field into the shielded volume, resulting in lighter coloured areas in the scans.

For the case b), the evaluation of the shielding contours is performed at different temperatures and used to evaluate the critical temperature distribution of the filament.
Differently from AC susceptibility, this time the information is local (subelement-per-subelement) as it visible from Fig. 3.15. The evaluation of the shielding radii(T) does not need an iterative simulation as for the AC-susceptibility case: the single contour plots are used to obtain the average radii of the shielded regions (assuming circular geometry) and then converted to relative positions between the inner and outer radii of the A15.
On the other hand, performing such an experiment is much more difficult and one can safely evaluate its output only thanks to an optimal sample preparation: this is the only way to resolve meaningful differences in the recorded field profile, excluding experimental artefacts coming from tilts of the specimen. Figure 3.28 presents such a scan at 10 K, 16 K and 17 K, where a field of 5 mT was applied in order to safely measure below $H_{c1}$: the shielding contours of the sub-elements are then evaluated where the measured field equals 80 %, 50 % and 35% of the applied field, demonstrating how the effective shielding changes with temperature. Figure 3.29 presents how the processed data look like when evaluated at 50% of field penetration.

The second and last type of measurements were the remanent magnetization scans, from which it is in principle possible to extract information about local currents. As explained in Section 3.4,

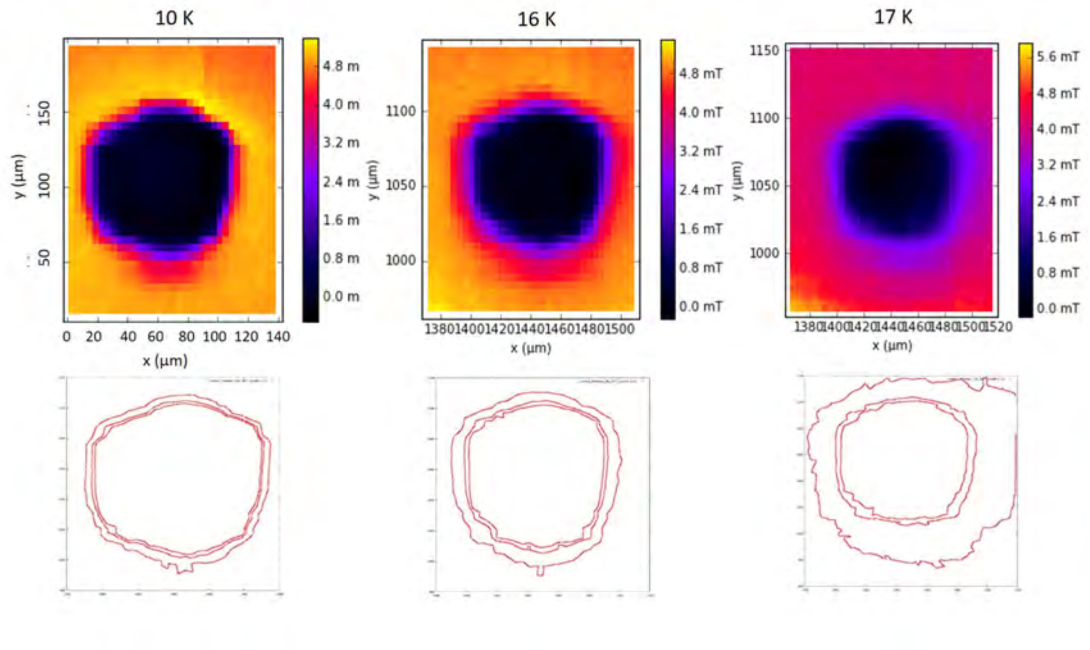

**Fig. 3.28:** Meissner scans of a single filament of sample B-Zr2 at 10 K, 16 K and 17 K and $\mu_0 H_a$=5 mT. The dark core represents the absence of field due to the Meissner shielding, getting closer to the surrounding applied field as temperature increases. Below each scan, the shielding contours are evaluated at a field $B$ equals 80 %, 50 % and 35% of the applied field (from the inner to the outer contours, respectively).

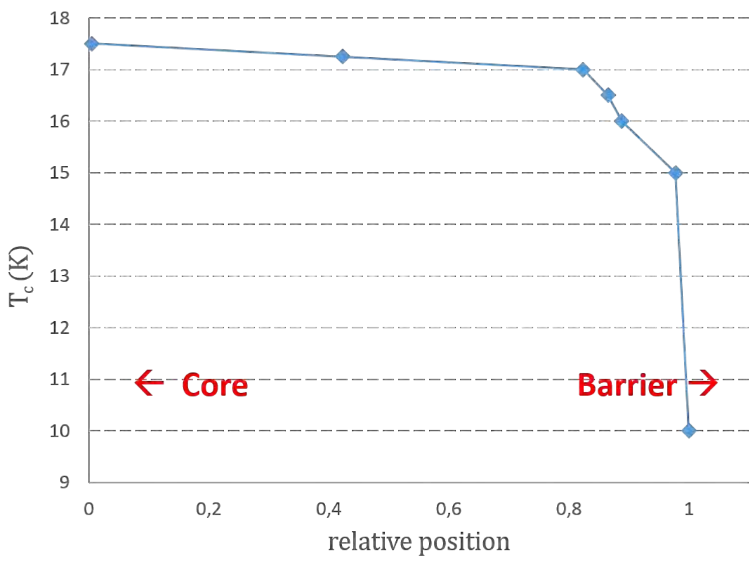

**Fig. 3.29:** $T_c$ distribution plot of sample T-Zr1-700x71 from SHPM Meissner-scans: the shielding radii recorded at B = 5 mT at different temperatures are converted in relative position (x-axis) and associated to the measured temperature.

the sample is fully magnetized at a specific temperature, then it is scanned in self-field. There is an established literature on how algorithms successfully evaluate two-dimensional (2D) current distributions from the sample's self field [82, 144, 153, 199], but for bulk superconductors it is still difficult to assess the quality of such an analysis, as explained in [50].

The samples should be prepared to be as thin as possible, as already mentioned in 3.4. For this reason, this type of analysis was conducted only on few samples where the preparation procedure was extremely successful (sample thickness $< 30$ $\mu$m). In this work, the algorithm proposed by Hengstberger ([100]) was used for producing the local $J_c$ plots.

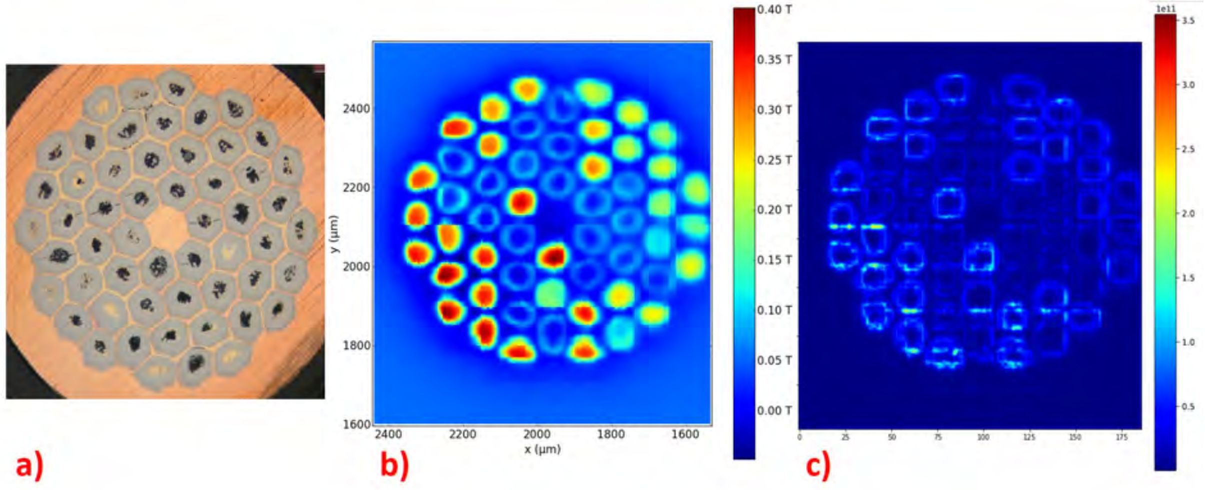

**Fig. 3.30:** a) Optical-microscopy picture of a $\simeq$15 $\mu$m thick sample prepared for the inversion analysis; b) Remanent magnetization profile after applying 2 T on the same sample at 4.2 K (field applied at 6.2 K, then removed and sample cooled to 4.2 K); c) Local critical currents after using the inversion algorithm (the values are expressed in A/m$^2$).

Fig. 3.30 presents the path to a good quality derivation of the critical currents by using the inversion algorithm. The sample (a) is thin enough ($\sim$ 15 $\mu$m) for being comparable to the other two parameters: probing distance ($\sim$ 4 $\mu$m) and probing step size ($\sim$ 5 $\mu$m).

The magnetization profile in self field and the local currents are shown in Fig. 3.30 b) and 3.30 3.30 c) respectively.

The validity of these analyses and how they correlate/complement with the EDX evaluations (Meissner shieldings) and with SQUID magnetometry ($J_c$ from remanent magnetization profiles) is discussed in the Chapter 4.

### 3.5.8 STEM analysis

As discussed in Subsection 3.5.8, several analyses were carried out from measurements taken with the scanning transmission electron microscopy (STEM) mode of TEM.

The advantage of using this mode instead of standard TEM is the opportunity to record signals that cannot be spatially correlated in TEM, including characteristic X-rays (for nano-EDX) or electron energy loss (for EELS). The latter is particularly relevant as being an effective method for extracting sample thickness information, indispensable for calculating the inclusion density in a given measuring volume.

Three type of measurements were analysed:

1. STEM high-angle annular dark field (HAADF) images for high Z-contrast precipitates identification;
2. STEM annular bright-field (ABF) images for high diffraction contrast;
3. EELS measurement in different lamella's locations for determination of the average sample thickness;

Eventually also EDX was performed on the lamellae on their edges, with the aim of keeping track of the sample orientation (what is oriented towards the filament core and vice versa).
The evaluation of the precipitates size relies on the fact that $ZrO_2$ precipitates appear brighter than the $Nb_3Sn$ matrix under diffraction contrast and dark under Z-contrast due to a lower atomic number of 18.67 (if compared to the 43.25 of the $Nb_3Sn$). In the $HfO_2$ case instead, the average atomic number is 29.33 and therefore closer to that of $Nb_3Sn$, leading to a weaker contrast between these phases so to a more difficult analysis.
The STEM scans were analysed by the author using the software *Digital Micrograph®* as a part of the *Gatan Microscopy Suite Software*. The latter allows to easily post-process the images (contrast/brightness/$\gamma$) and to annotate (length/orientation) the inclusions present in the image. The precipitates were identified based on the following characteristics:

- Grayscale: $ZrO_2$ inclusions range from RGB(0,0,0) (black) to RGB(105,105,105) ("dimgray") while the $HfO_2$ inclusions shine on the other side of greys' scale, from RGB(128,128,128) to RGB(220,220,220) ("gainsboro");
- Shape: $ZrO_2$ particles always show a circular or elliptical 2-dimensional contour, as it was assessed by *Pfeiffer* by means of high-resolution transmission electron microscopy (HRTEM) [155]. If a more complex geometry is analysed, this is most probably a *cluster* of inclusions or is not a precipitate; $HfO_2$ ones have instead polygonal borders, often arranging themselves as hexagons or octagons;
- Size: both $ZrO_2$ and $HfO_2$ are known so far to nucleate via internal oxidation in particles no bigger than 30 nm and no smaller than 0.8 nm ([155, 211]), so these thresholds are applied for particle detection. This avoids to take into account eventually similar defects as the ones from ion milling and/or impurities deposited on the lamellae;

In the case of ABF-recorded images, the diffraction contrast makes all the precipitates looking much brighter than the HAADF case, being that a key feature for analysing some samples with $HfO_2$ inclusions, where the difference in atomic number with the surrounding matrix is smaller. The grey-scale criterion is therefore scaled to lighter colors (higher RGB values).

Based on the listed criteria, the images with highest magnification and best quality were analysed. An example is shown in Fig. 3.31, where two 230x230 nm images of samples with $ZrO_2$ (a) and with $HfO_2$ (b) inclusions are compared: the particles are tracked with red lines along their longest direction and their size is automatically recorded as a diameter.
Discovering of "hidden" particles is possible only by tuning the brightness/contrast/$\gamma$ settings in the processing phase, so selectively illuminating areas where the counting elements would not stand out. Image (a) shows smaller elements with a higher density than in image (b), where the inclusions look also bigger and more frequently concentrated in clusters (2/3/4 inclusions packed together).
Three to five images were analysed per each lamella/sample, keeping consistency on investigating the same areas among the samples (within the A15 width) for the analysis. This is better

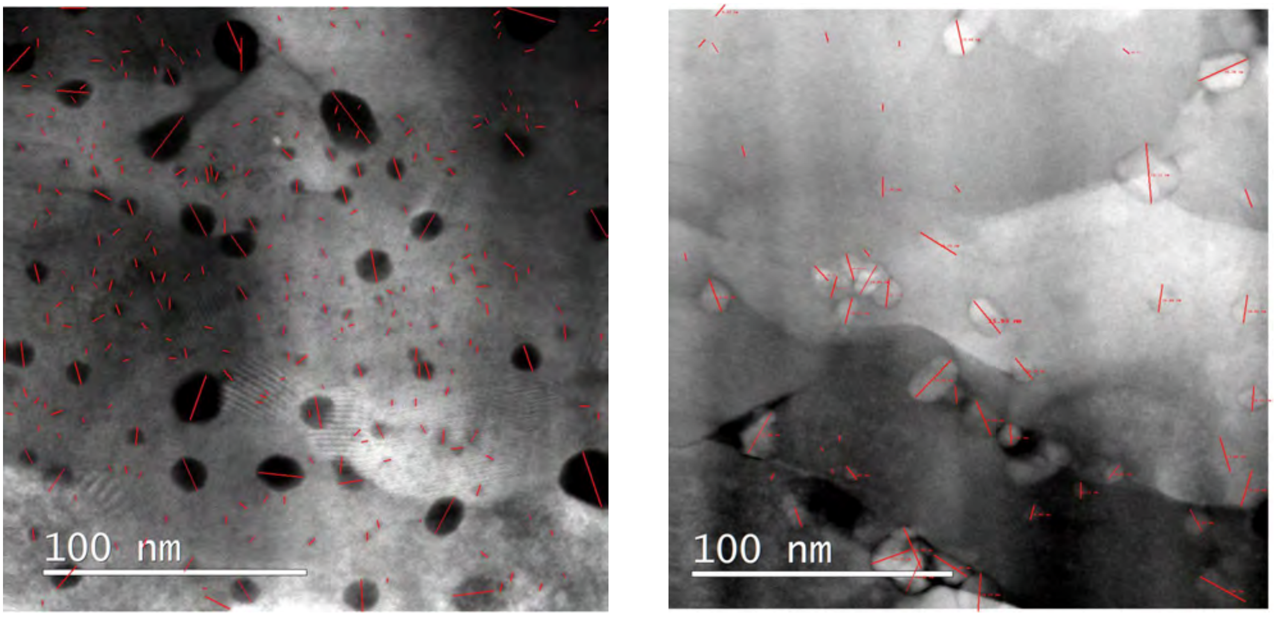

**(a)** **(b)**

**Fig. 3.31:** Two scans taken with STEM at x450.000 magnification. Red solid lines are used for tracking the particle length along the longest direction.
(a) the darker spots are $ZrO_2$ inclusions in the A15 matrix; (b) the lighter spots are $HfO_2$ inclusions, often grouped in clusters.

explained in Fig. 3.32, where the typical three spots from where the pictures are analysed are displayed on a lamella (close to Sn core, center, close to Nb barrier). It is clear that the darkest spots are preferred over the surroundings, since a picture taken in these areas come from thinner regions, where each feature sharply stands out.
If good quality pictures were obtainable, the central area ("Area 2" in Fig. 3.32) was usually the one used for representing the final statistics, since it is far enough from the CG region and a good representative of the average grain size of the sample [211].

Figure 3.32 also shows the EDX line-scans results along the lamella's edges, indicating the Sn-core side to be on the left and the Nb barrier on the right.
As mentioned before, additional data analyses were conducted on the spectra obtained from EELS on several spots of the lamellae: for the volume calculation one needs to know the volume where a certain amount of particles is tracked, therefore the missing information is the lamellae thickness. EELS data consist of energy loss spectral information from the sample (spectroscopy) or images that have contrast created by the energy loss properties of the distribution of material in the sample (energy-filtered TEM).

By using EELS measurements, one profits from the energy-loss profile of the recorded electrons in order to get a "travel length" of the transmitted particle, to be translated in nm. This quantification is possible within the *Digital Micrograph®* software, which process the Zero-loss peak (ZLP) and the total spectrum intensity by using the Kramers-Kronig absolute ratio method [129].
Figure 3.33 presents the spots where the EELS analysis is performed on the "AREA 2" of Fig. 3.32. The parameters for converting the ZLP information (3.33b) to sample thickness are the

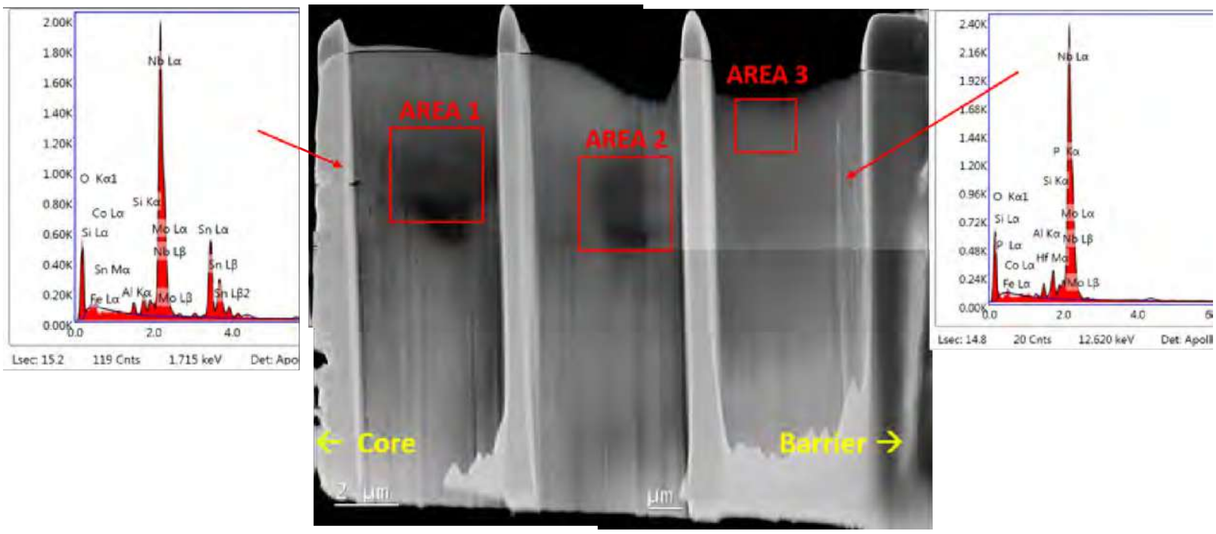

**Fig. 3.32:** Collage-image taken with TEM of a lamella from a T-Zr1 sample : the red squares show the areas were high-magnification pictures where taken from, while the EDX scans on the edges keep track the lamella orientation. The pictures magnification is x450.000, the beam accelerating voltage 200 kV and the image size 230x230 nm.

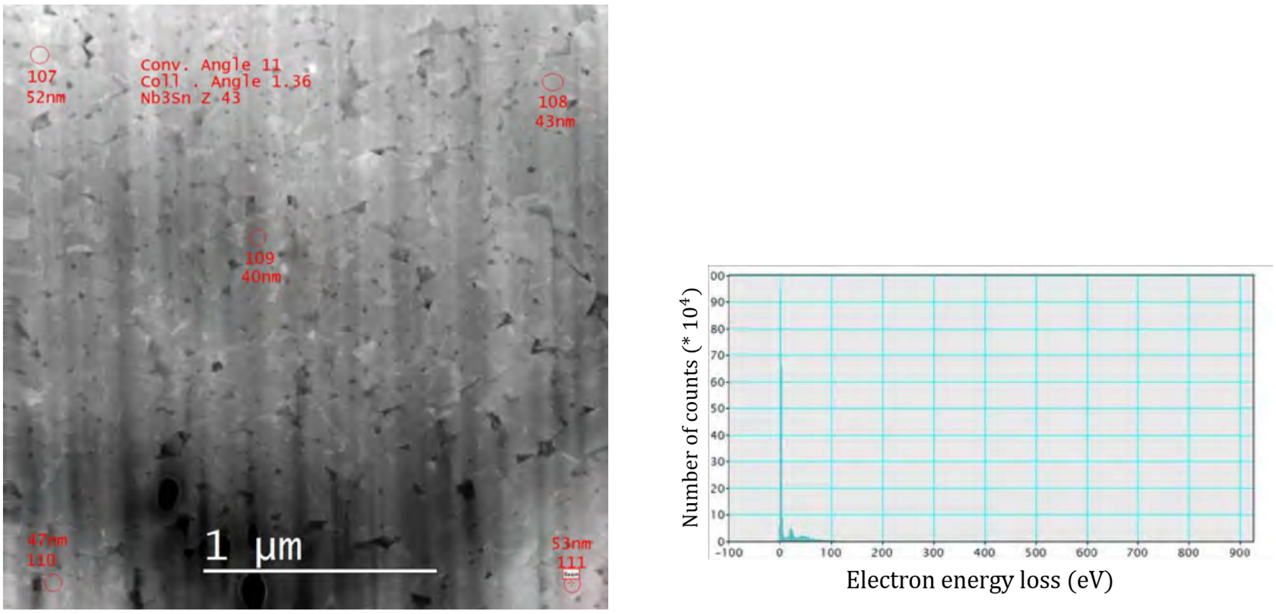

(a) (b)

**Fig. 3.33:** a) Spots of "AREA 2" (Fig.3.32) used for EELS quantification; b) transmitted electron energy loss spectrum at the spot 107.

convergence and collision angles, together with the specimen atomic number. The first two are set to 1.36 mrad and 11 mrad respectively, while the $Nb_3Sn$ atomic number is 43.
Similarly to EELS thickness calculations, also energy filtered transmission electron microscopy (EFTEM) was deployed for the same purpose. This was done to check the quality of the EELS-driven numbers and also for increasing the statistics of counts. EFTEM works basically as HRTEM imaging (lenses are used to magnify and focus the electron beam after it has passed through the specimen) but here an "energy filter" takes place between the specimen and the detector. Some of the electrons will lose energy when they interact with the specimen, therefore the energy filter is used to select for image formation only the electrons that have a defined energy spread. EELS and EFTEM substantially differs in how the scattered electrons are used. EFTEM forms images (and electron diffraction patterns) using the scattered electrons while EELS is the analysis of the energy loss spectrum itself.

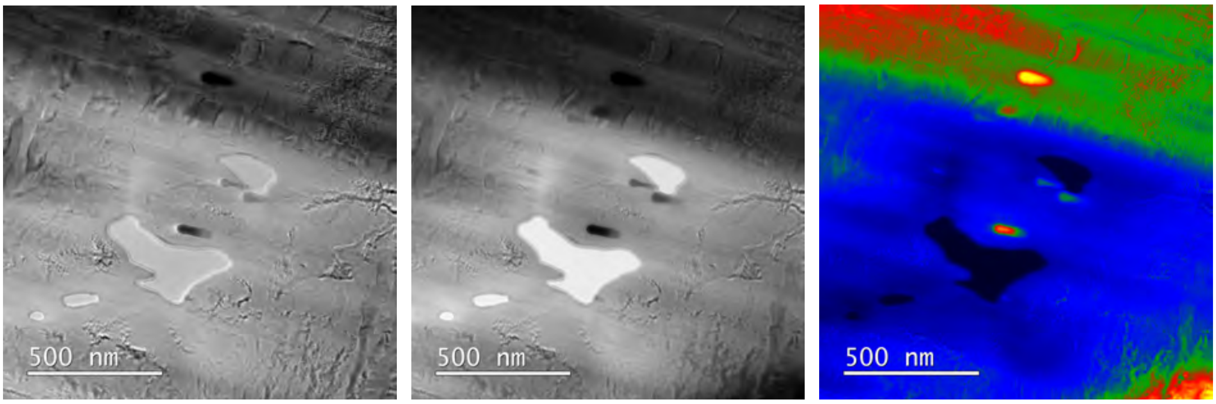

**Fig. 3.34:** Illustration of various images

In Fig. 3.34 a EFTEM thickness map from sample T-Hf2 is shown: from the original TEM unfiltered image, the energy filter is applied and the thickness map os recorded. The darker spots are the thinner ones (an ad-hoc spot with two holes in the thin lamella has been chosen to show the total black spots - no thickness - in the EFTEM map) while the warmer ones are the thickest. These analyses were used to produce statistics on the precipitate size and the precipitate density, aiming to extract a single representative value per sample of both quantities.

The first approach was to calculate the median value and the absolute deviation for each analysed image, since it is considered the most meaningful measure of central tendency [122]. Three to five median values per sample were therefore obtained, from which the net average was calculated. In order to define a procedure for analysing repetitively the data, different distribution fits were tried, being the log-normal distribution the overall best fitting to each dataset. This is clearly visible in Fig. 3.35, where four datasets from 230x230nm images on the same lamella are displayed.
The particle size is expressed by its diameter (nm), as it is shown in Fig. 3.35b: here the bin size is set to 1.5 nm, even though the statistics displayed is built over the raw data. Defining a single distribution fit which well suits the statistics for each sample is useful for immediately identifying the data outliers, always affecting otherwise the final representatives. It is therefore interesting to see a good agreement between the average of the medians and the mean values extracted from the log-normal applied fits.
As a final result of these analyses, the particle densities PD were calculated by using the counted

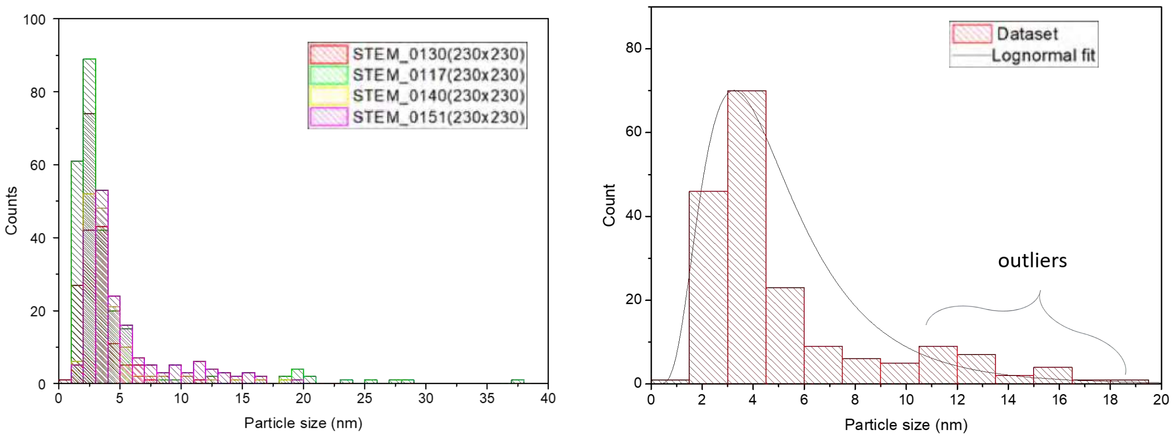

**(a)** **(b)**

**Fig. 3.35:** Particle size statistics of a T-Zr2 sample. (a) four lamellae statistics of the same sample; (b) applied distribution fit (lognormal) on the dataset: identification of the outliers.

particles and the volumes information.

The results and their effect on the superconducting properties as well as their impact on the pinning models are discussed in Sections 4.1, 4.3 and 4.2.

### 3.5.9 TKD analysis

As explained in Section 3.3, TKD maps were recorded by using the EBSD camera of SEM for the assessment of the samples grain sizes.

Recording of the TKD maps was done at USTEM, TU Wien. The methodes used for analysing the diffraction patterns and the size allocations can be found in [155]. Only grains and pixels clearly identifiable with high image quality IQ and confidence index were taken into account for the statistics. The IQ is a metric describing the quality of a diffraction pattern [181]: an IQ map is constructed by mapping the IQ value measured for each diffraction pattern obtained during an EBSD scan to a gray scale.

As it is shown in Fig. 3.36, the areas not considered for the final statistics are identifiable as white spots. The latter are points from which the diffraction pattern was not exhaustively collected, mainly because of small impurities or image re-construction problems. These not being related to any size-driven measuring issue, allowing to consider these missing points to not interfere with the global statistics.

The diameter of a grain was calculated (hexagonal grid) by determining its area and then assuming the grain is a circle of the same area. It was found that the TKD lower detection limit for a reliable identification of a single grain was 29 nm. This means that any grain smaller than this diameter threshold was not accounted, being most probably included in the calculation of a a bigger grain if the neighbouring grains have the same small size.

This experimental limit would potentially result in a significant source of error. Nevertheless, it has been confirmed from other studies - on the very same or similar samples, conducted also with different experimental techniques (e.g. SEM fractured-samples imaging)- that there are few

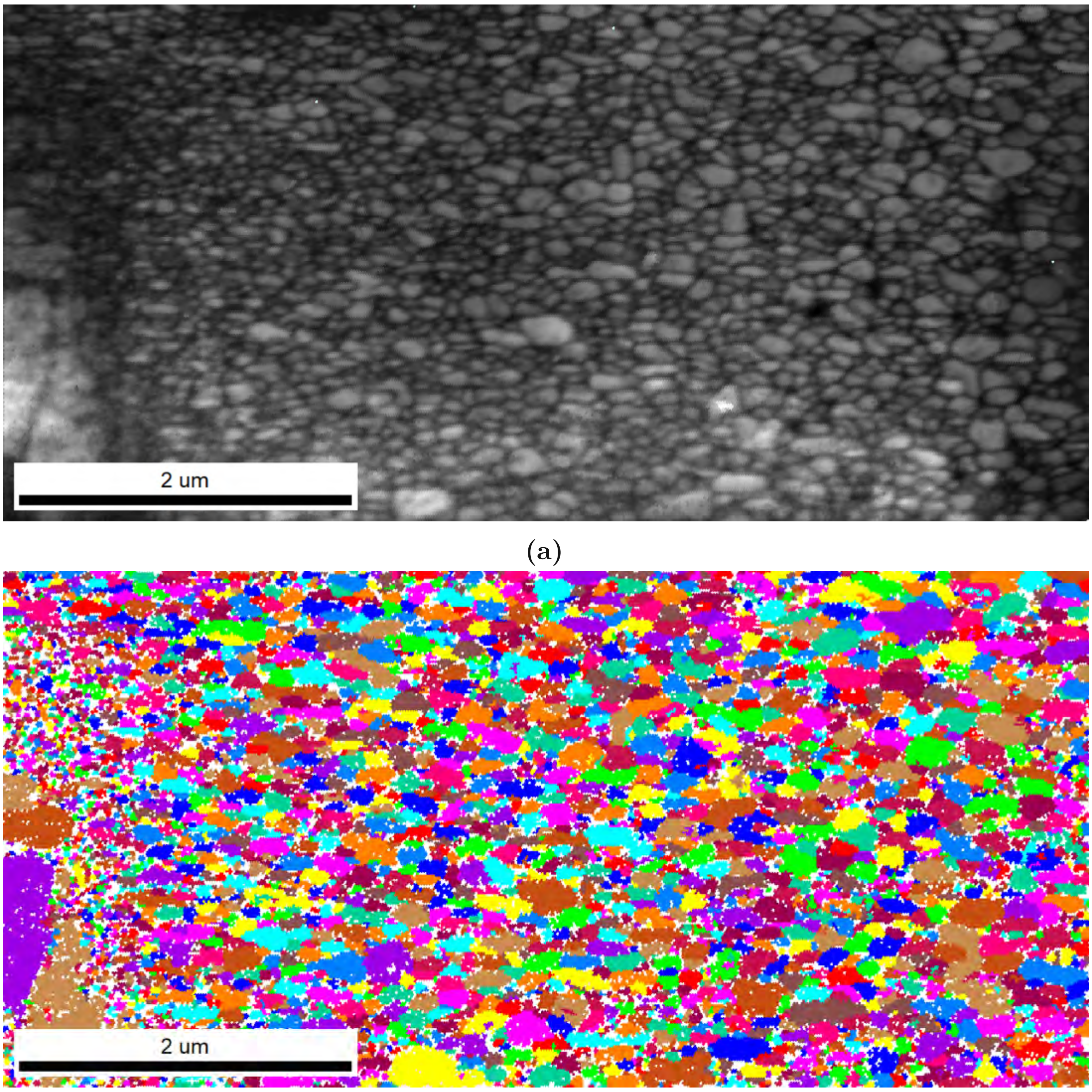

(a)

(b)

**Fig. 3.36:** TKD map acquisition of a $\simeq 7\mu$m wide lamella, therefore spanning over almost the whole FG region. The signal coming from the white spots is not considered into the statistics.

or no grains found to be smaller than the 29 nm limit [5, 209, 212]

The statistics were produced following the procedure explained in Subsection 3.5.8, identifying the log-normal and/or the half normal distributions (in a most generic terms, low $k$ and $\theta$ "gamma" distributions [105, 204]) to best fit almost all the acquired statistics.
The results of these analyses are discussed in Chapter 4 (Sec. 4.1 and 4.2), where the grain sizes play an important role as being $J_c$ historically $\propto \frac{1}{GS}$ (cf. Sec. 1.4) and of course in the understanding of the APC-$Nb_3Sn$ mixed pinning scenario.

# Chapter 4

# Results

The results obtained from the measurements as described in Chapter 3 and analysed as in Section 3.5 are shown and discussed in the following chapter.
The main results of the systematic study are reported in Section 4.1, while the possible correlations between them are investigated and their potential impact on the flux pinning discussed in Sec.4.2. In Section 4.3, some modelling of the flux pinning involved in these specimens is presented, involving the main microstructural data and A15 inhomogeneities. Finally, in Section 4.4 the main conclusions of this work are presented.

## 4.1 Systematic study

Grouped by recipe (initial alloy and powder composition), the main superconducting properties together with the main microstructural features of each APC-sample as a function of eat treatment temperature are shown in this Section.
The critical current densities obtained by means of SQUID magnetometry (cf. Sec. 3.1) and - where obtainable - the high-field $J_c$ were analysed using the evaluation method described in Subsection 3.5.1. The results, obtained also by using the method presented in Subsection 3.1.3 are discussed in Subsection 4.1.1.
Along this path, $B_{c2}$ and $B_{irr}$ at 10 K, 12 K and 15 K and, where available, at 4.2 K are presented in Subsection 4.1.2. Results obtained by STEM-TKD as described in Subsection 3.3.3 and analysed as in Subsection 3.5.9 are discussed in Subsection 4.1.3. Finally, precipitates size and densities, obtained with STEM and EELS/EFTEM as explained in Subsection 3.5.8, are presented in Subsection 4.1.4.

### 4.1.1 $J_c$ and $F_p$

The plots in this Section show $F_p$(B) (as being $J_c$ x B, cf. Eq. 1.9), at 4.2 K, 10 K, 12 K and 15 K for every recipe as summarized in Table 2.2. The same evaluations were done also at 5, 6, 7, 8, 9, 11, 13 and 14 K, not reported in this work only because not being further discussed in terms of flux pinning.

As mentioned in Subsection 3.1.3, it was fundamentally important to assess the A15 contours for the evaluation of magnetometry layer-$J_c$, in terms of $r_{in}$ and $r_{out}$ of the superconducting hollow tube (cf. Eq. 3.5). This turned to be even more fundamental when calculating layer-$J_c$ from transport current measurements, as being:

$$J_c = \frac{I_c}{A_{eff} \cdot N} \tag{4.1}$$

To quantify the impact of possible wrong radii calculated by eye (microscope pictures), it is possible to extend the assumptions made for magnetometry also to equation 4.1 (all filaments behaving as identical hollow cylinders): in this way, since the filaments cross-sections is never a perfect corona, we can intend $A_{eff}$ to be the area of an equivalent disc of inner and outer radii $r_i$ and $r_o$, respectively:

$$A_{eff} = \pi(r_o^2 - r_i^2) \tag{4.2}$$

The impact on magnetometry and transport measurements can be now estimated by looking at the example depicted in Fig. 4.1 (from one of the T-Zr1 samples).
For this filament, the high level of contrast between the phases (and the round-shape of the filament cross-section) allows easily to identify the outer radius $r_o$, described by the green solid line in Fig. 4.1. As an example, three radii could be arbitrarily chosen (a,b and c), all of them within the plausible range of choices as they are between the Sn-Cu centre and the outer border of the gloomy CG-region in the SEM-image ($\Delta r_i = 4.3$ $\mu$m). The impact on the current evaluation is different for the two experimental methods: for magnetometry, choosing $r_i$ to be 21.6 $\mu$m (case a) leads to a layer $J_c(r_a = 21.6$ $\mu$m$) = 0.76 J_c(r_c = 25.9$ $\mu$m$)$. This gap increases when calculating $J_c$ from transport: the currents calculated in case a) are 72% of the ones in case c).

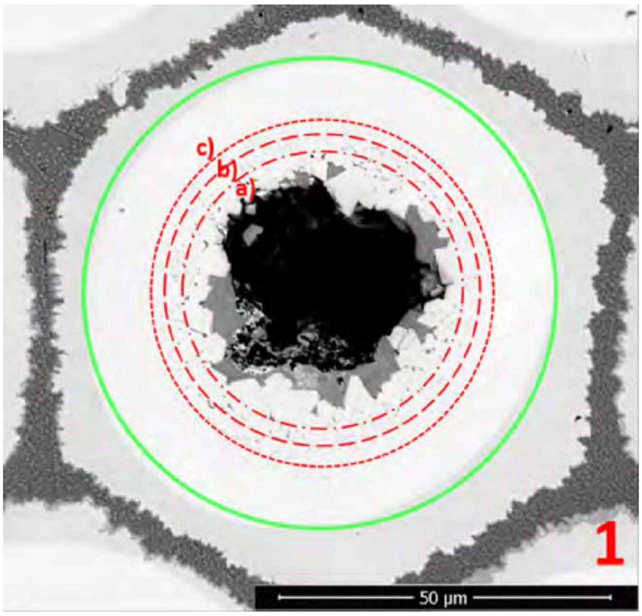

**Fig. 4.1:** SEM image of a T-Zr1 filament: three possible choices for $\mathrm{r_i}$, where a) corresponds to 21.6 $\mu$m, b) to 23.5 $\mu$m and c) to 25.9 $\mu$m.
Published by *Ortino et al., IEEE 2021* [149]

Considering the magnetic moment for a hollow cylinder of radii $r_o$ and $r_i$ and length $L$

$$m = \int_{r_i}^{r_o} JL\pi r^2 dr = \frac{\pi J_c L}{3}(r_o^3 - r_i^3) \tag{4.3}$$

we first focus on the initial slope of $m_+$ vs $H$. Since the measured $m$ refers to the signal coming from all the filaments $N$ in the wire, all the experimental magnetic moments have to be divided by this number.
By looking at Fig. 4.3 a) it is possible to define the radius where the flux penetration is completed

$$r_f = r_o - \frac{\Delta H_n}{J_c} \tag{4.4}$$

where $\Delta H_n/J_c$ is the slope of the flux front. Combining (4.4) with (4.3), together with identifying $r_i$=$r_f$ (inner radius of the flux front), this yields to

$$m_+ = -\pi N J_c L \left( r_o^2 \frac{\Delta H_n}{J_c} - r_o \left(\frac{\Delta H_n}{J_c}\right)^2 + \frac{1}{3}\left(\frac{\Delta H_n}{J_c}\right)^3 \right) \tag{4.5}$$

From (4.5) we can derive $dm/dH$ by only concentrating on the initial slope of the magnetization

$$\frac{dm_+}{dH_n} = -\pi N r_o^2 L \tag{4.6}$$

This last formula allows to directly calculate $\mathrm{r_o}$ from our measured $\mathrm{m_+}$, by evaluating $dm/dH$ within $\Delta H \leq 7{\cdot}10^4$ A/m (in our case, between 6.5 T and 6.58 T).

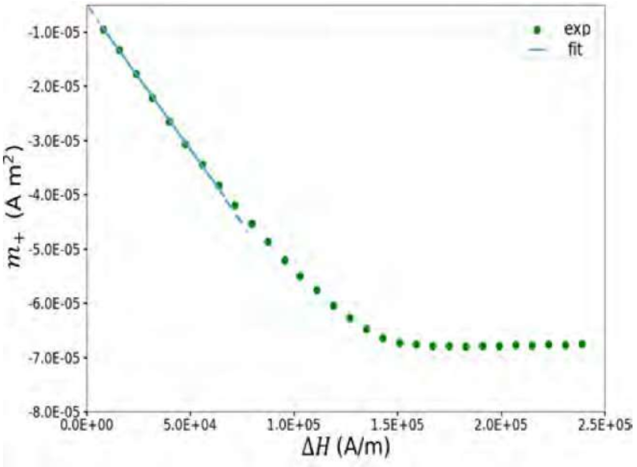

**Fig. 4.2:** Magnetic moment in increasing field: $dm_+/dH_n$ is evaluated within $7 \cdot 10^4$ A/m (0.08 T) before it saturates.
Published by *Ortino et al., IEEE 2021* [149]

The calculation gives $r_o$=34.6 $\mu$m, which is as expected really close to what is directly observable from Fig. 4.1. This derivation is very reliable, since the initial slope of the magnetization curve directly reflects the shielded volume. It is often used to determine or confirm the volume of superconducting samples.
We now focus on $m_{rem}$ to extract $r_i$ [160]. Looking at Fig. 4.3b, it is possible to define the

remanent magnetic moment which is measured after removing $\Delta H_n$. To get to this quantity we subtract $2m(\Delta H/2)$ (dashed orange areas in Fig.4.3 b) from the magnetic moment $m_+$ (full triangle area, Fig 4.3 a). This means:

$$\begin{aligned} m_{rem} &= m_+(\Delta H_n) - 2m_+\left(\frac{\Delta H_n}{2}\right) \\ &= \pi N J_c L\left(\frac{r_o}{2}\left(\frac{\Delta H_n}{J_c}\right)^2 - \frac{1}{4}\left(\frac{\Delta H_n}{J_c}\right)^3\right) \\ &= \pi N L\left(\frac{r_o}{2J_c}\Delta H_n^2 - \frac{1}{4J_c^2}\Delta H_n^3\right) \end{aligned} \tag{4.7}$$

Eq. (4.7) can be extended to calculate the points above $\sim 6.7$ T, where $m_+$ saturates because $r_o - r_i \leq \Delta H/J_c$. By defining $\Delta H_{sat}$ as the field at which the saturation occurs, this means:

$$m_{sat} = m_+\left(r_o - r_i = \frac{\Delta H_{sat}}{J_c}\right) \tag{4.8}$$

where $r_i$ is the inner radius of the sub-element, and

$$m_{rem}(\Delta H_n \geq \Delta H_{sat}) = m_{sat} - 2m_+\left(\frac{\Delta H_n}{2}\right) \tag{4.9}$$

By sticking to the experimental $m_{sat}$, we can now calculate $J_c$ as a function of $r_i$ by using (4.3) and the experimental value of the saturation moment $m_{sat-exp}$. The latter is here the most relevant experimental parameter, as being generally used for evaluating $J_c$ from magnetization measurements.

This condition for m allows us to calculate $J_c$ as being $3m_{sat-exp}/\pi L(r_o^3 - r_i^3)$.

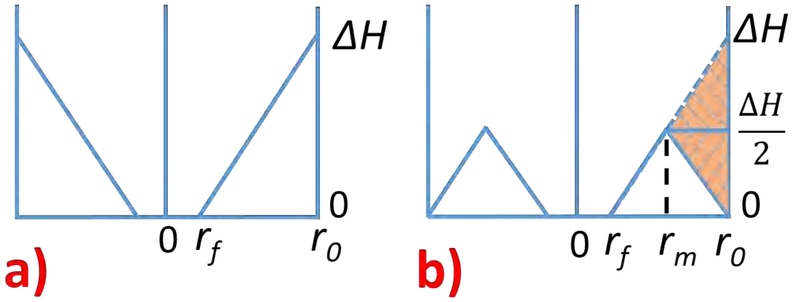

**Fig. 4.3:** Bean model for a cylinder in an applied field $\Delta H_n$ (a) and the remanent field at 0 T(b).
Published by *Ortino et al., IEEE 2021* [149]

The best fit for the function gives $r_i = 24\ \mu$m, which is exactly between the proposed radii b) and c) in Fig. 4.1. The resulting value for $J_c$ is $1.42 \cdot 10^{10}$ A/m$^2$. This current should not be confused with the longitudinal current induced when the sample is placed orthogonal to the applied magnetic field. The latter is in fact the usually reported $J_c$ of a sample, as being the useful parameter for technical applications. The difference between these two currents is not necessarily negligible (e.g. cracks, texture [168]): in our case the longitudinal current density was found to be $1.81 \cdot 10^{10}$ A/m$^2$, thus being $\sim 24\%$ higher than the azimuthal current density at this field and temperature. By using this geometry and Eq. 3.5, the calculated $J_c$ is consistent with literature data [209, 212]. Moreover, these radii are in agreement with the eye-evaluated ones and with independent SEM measurements [206].

The entire procedure also shows good stability.

Comparing the entire theoretical and experimental behaviour of the magnetization process enables an estimation of the reliability of the assumptions in terms of geometry and homogeneity. Fig. 4.4 demonstrates that the agreement is excellent up to about $1.5\Delta H_{sat}$ but saturation is delayed because of the variation of sub-element geometry. The most massive sub-elements need a higher field to saturate. It is evident that one can derive only representative values for the best description of the hysteretic magnetization, which is exploited by magnetic $J_c$ measurements as well. Therefore, this method represents the most consistent way of choosing the simplified geometry for magnetic $J_c$ measurements.

On the other hand, no clear signs of A15 inhomogeneities can be observed in Fig. 4.4, which should manifest themselves also by deviations at small fields, if arising from compositional gradients [15]. The best fitting $r_i$ is quite sensitive to the input data, as demonstrated in Fig. 4.4 by the solid line. A change of $r_i$ by only 1 $\mu$m results in a dramatic deterioration of the theoretical description (dashed lines).

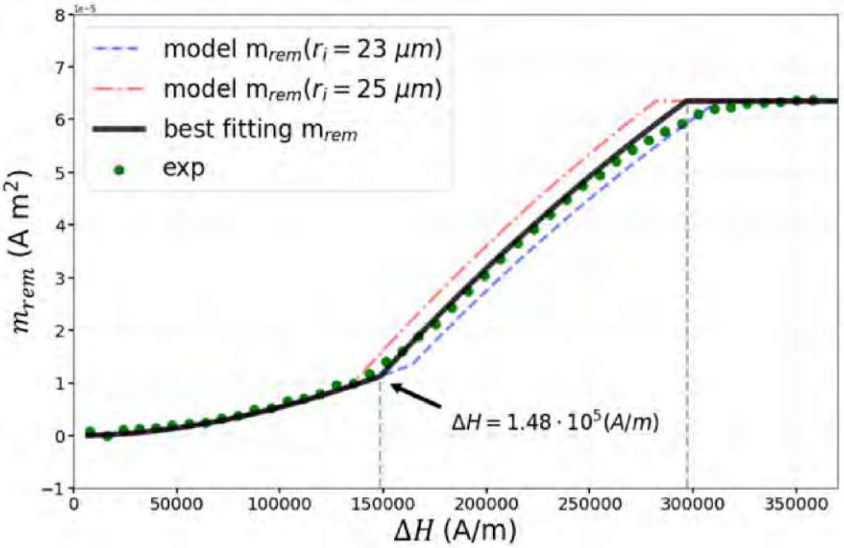

**Fig. 4.4:** Experimental and modelled remanent magnetic moment: the green dots are the experimental values; the solid black line represents the best fit to the data, while the red dashed and blue dash-dotted trends are the simulated behaviour for (4.7) accounting for a slightly longer and shorter $r_i$, respectively.
Published by *Ortino et al., IEEE 2021* [149]

Profiting from the just elucidated method, $F_p$(B) of each sample was evaluated, using the procedure described in Subsection 3.5.1 (Figures 4.5 - 4.10). The two multi-filamentary binary

samples are shown together, even though their starting Nb/Sn/Cu precursors ratios are not exactly the same (therefore they are not the very same recipe).
The error bars are not displayed, since the standard deviation $\sigma_{J_c}$ calculated from SQUID magnetometry was always at least 3 order of magnitude smaller than $J_c$.

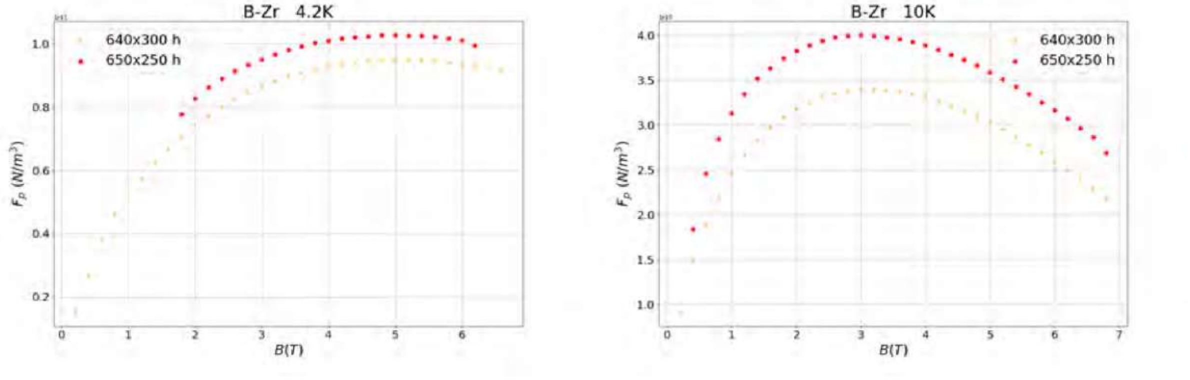

(a) 4.2 K (b) 10 K

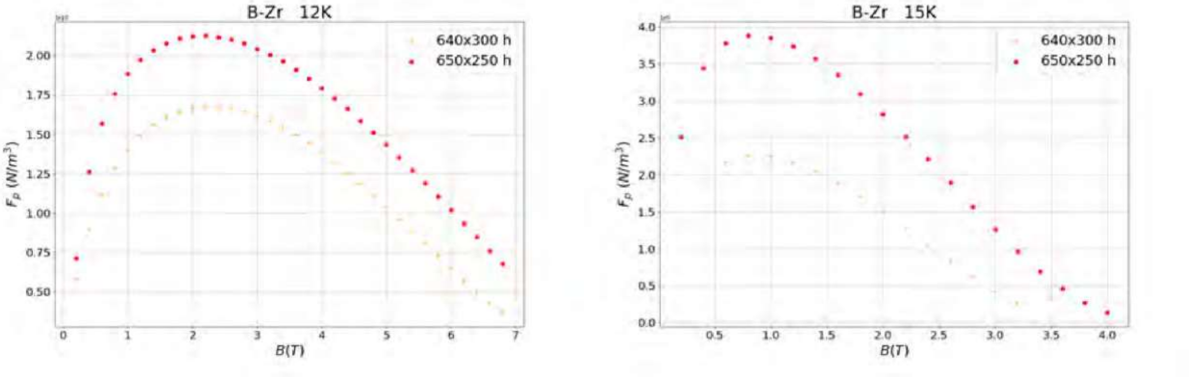

(c) 12 K (d) 15 K

**Fig. 4.5:** Pinning force $F_p$(B) values for the recipes B-Zr1 and B-Zr2 at 4.2 K, 10 K ,12 K and 15 K.

A summary of the maximum values of the pinning force $F_{p\text{-}max}$ at 4.2 K is shown for each sample in Fig.4.11.

In Fig. 4.11, also the commercial reference sample ("PIT-R") is shown, while only the binary sample reacted at 650°C is displayed (640°C as heat treatment temperature resulted often in low quality ternary wires, therefore was excluded from this master-plot).
From Fig. 4.11, two conclusions appear to be more solid than any other:

- No-APC recipes (PIT-R, T-Hf3) show consistent and significant lower values than APC samples;
- Zr-doped samples show relatively higher values;

As will be discussed in Subsec. 4.1.3 and 4.1.4, the reasons explaining the first point are to be tracked in the grain size and presence of precipitates found in APC samples.

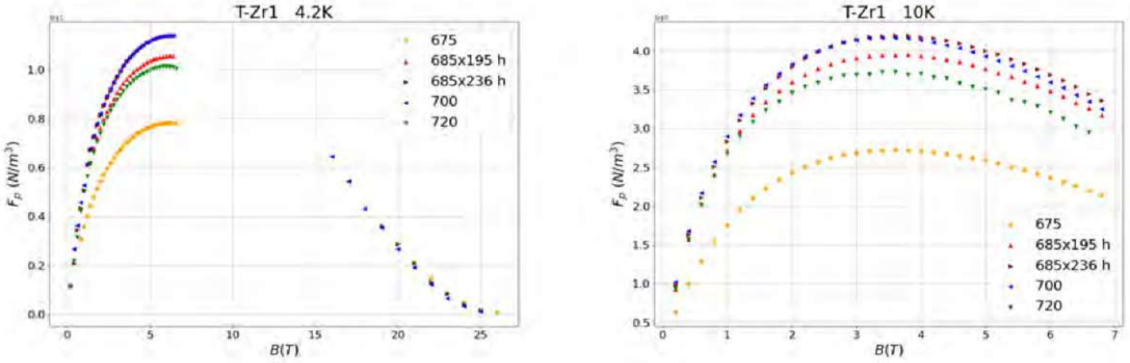

**(a)** 4.2 K **(b)** 10 K

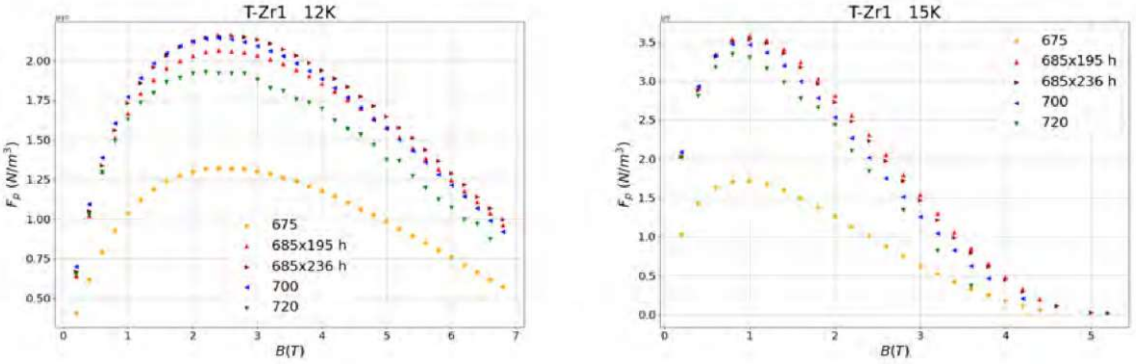

**(c)** 12 K **(d)** 15 K

**Fig. 4.6:** Pinning force $F_p$(B) values for the recipe T-Zr1 at 4.2 K, 10 K ,12 K and 15 K.

While this is not surprising, the second evidence is not immediately understandable and seems rather to be due to manufacturing optimization reasons: maximum pinning force $F_{p\text{-}max}$ values of Hf samples are in fact similar to those of Zr if the dopant concentration in the starting alloy is lower (e.g. T-Hf3), being it a consequence of the more recent deployment of this element addition.

In terms of $J_c$, it is interesting to evaluate how these samples behave towards the FCC-goal at 16 T.
It is still quite difficult to directly measure transport currents at 16 T (at 4.2 K), since these specimens even now suffer from thermal stability problems, which are usually related to the Cu/non Cu ratio in the recipes, the total amount of filaments - which re-distribute local Joule-heating over the cross section - and the purity of the Cu layer at the end of the reaction.
The latter is probably considered the most sensitive point, being in fact standardized (by the International Electrotechnical Commission - IEC - under the code 'IEC 61788-11' in 2003) by measuring the residual resistivity ratio (RRR), the ratio between the resistance at room temperature to that just above the superconducting transition. According to [77], ternary PIT wires are designed to hold very good (high) RRRs, therefore the hh-FCC specification of RRR≥ 150 can be faced at subsequent stages of the wire development process. For this reason, evaluating $J_c$ at 16 T was for this work possible only by interpolating between low-field points (magnetometry)

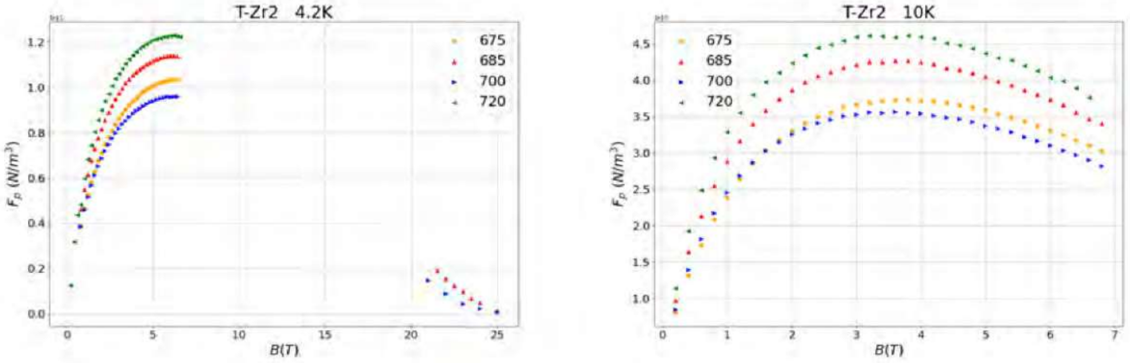

**(a)** 4.2 K **(b)** 10 K

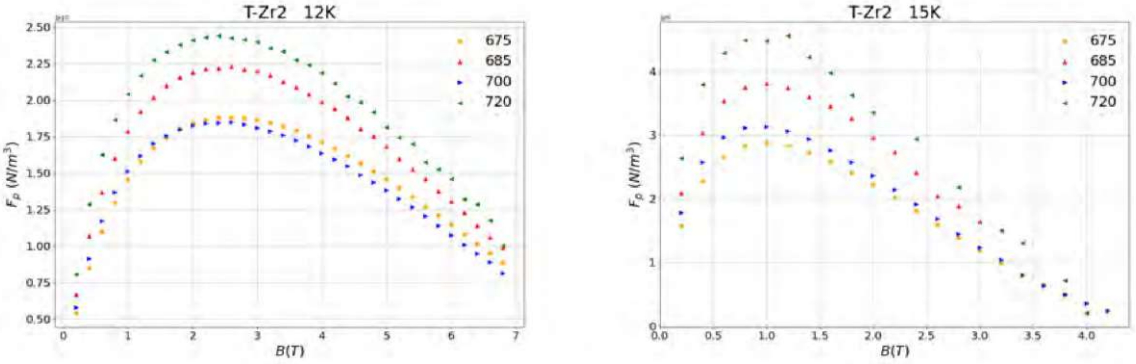

**(c)** 12 K **(d)** 15 K

**Fig. 4.7:** Pinning force $F_p$(B) values for the recipe T-Zr2 at 4.2 K, 10 K ,12 K and 15 K.

and high-field ones (transport current), as it is depicted in Fig. 4.12.

Here $J_c$ is expressed as "non-Cu $J_c$" (cf. 1.1.2), which in the APC wires is between 30-35% lower than the layer-$J_c$. Two binaries, two first generation and one newer Zr-doped samples are compared with a commercial reference. The high-field points of T-Zr2-720 were not measured but only projected by always holding the same +11% difference with T-Zr1-685 from the low-field values. It is clearly visible how the specification at 16 T is approached and even surpassed by the newest sample, being it a great result for this technology as already published [148].
Moreover, a lowering of the low field (1-7 T) $J_c$ compared to the binary generation is evident in the T-Zr1-675 sample (zoom inset). Even if the other ternary-APCs cannot be directly compared with the two studied binaries (different precursors ratios and different HT), each of the former shows consistently lower low-field $J_c$ performance juxtaposed to the latter.
This should be beneficial for the wire development, since magnetization is the driving force for low-field flux jumps and field errors in magnets [196, 210]. These field errors in the magnet aperture are in fact caused by shielding currents induced in the superconducting filaments during the accelerator field-ramps, eventually degrading the accelerator performance in particular at low fields. This is usually the case at the injection level [136]: decreasing the low field $J_c$ should improve low-field stability and help in suppressing these field errors.

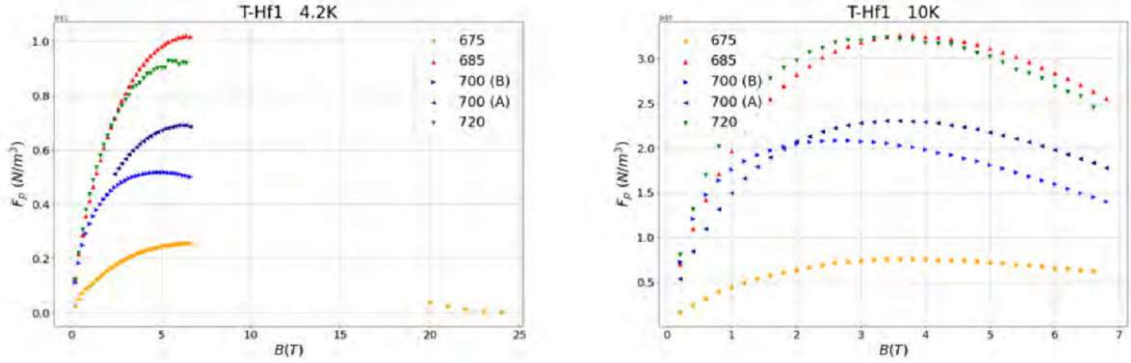

**(a)** 4.2 K **(b)** 10 K

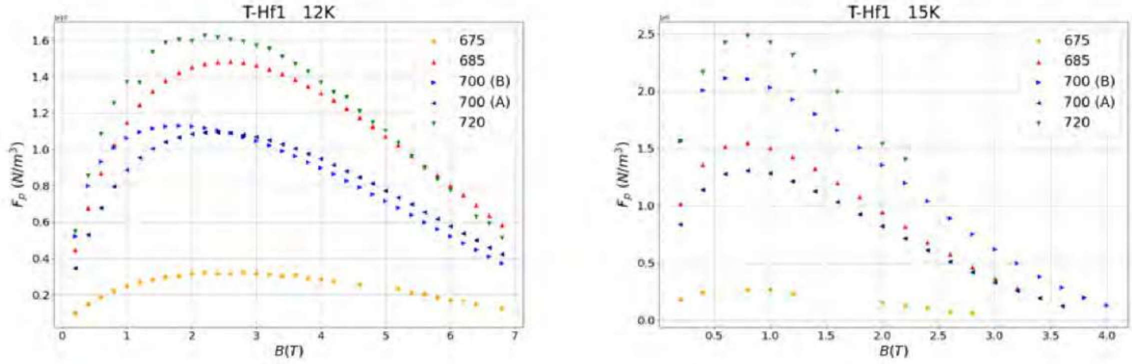

**(c)** 12 K **(d)** 15 K

**Fig. 4.8:** Pinning force $F_p$(B) values for the recipe T-Hf1 at 4.2 K, 10 K ,12 K and 15 K.

No clear indications of a correlation with HT temperature is visible from these analyses.
It is well known that in standard PIT manufacturing there are optima for the reaction temperatures, ensuring a complete Sn diffusion and the best grain refinement. Still, this does not appear the case for this systematic set of samples, whose HT settings are nevertheless not to be considered as randomly selected. Both temperatures and reaction times were already tailored for guaranteeing good quality wires, showing high inter-granular connectivity, comparable levels of compositional gradients (as it is discussed in Sec. 4.3), no drawing-related cracks nor longitudinal inhomogeneities. Only the T-Hf2-675 sample can be considered somehow showing an under-performing behaviour, resulting in a gap in terms of $F_{p\text{-}max}$ of at least -50% if compared with the other samples of the same recipe.

### 4.1.2 $B_{c2}$ and $B_{irr}$

$B_{irr}$ values are here reported for each specimen at 4.2 K (when available), 10 K, 12 K and 15 K. At 4.2 K, $B_{irr}$ is directly extracted from the resistivity versus field (R-B) curves, evaluated using a criterion of 1% of the normal-state resistivity (cf. Sec. 3.5.3).

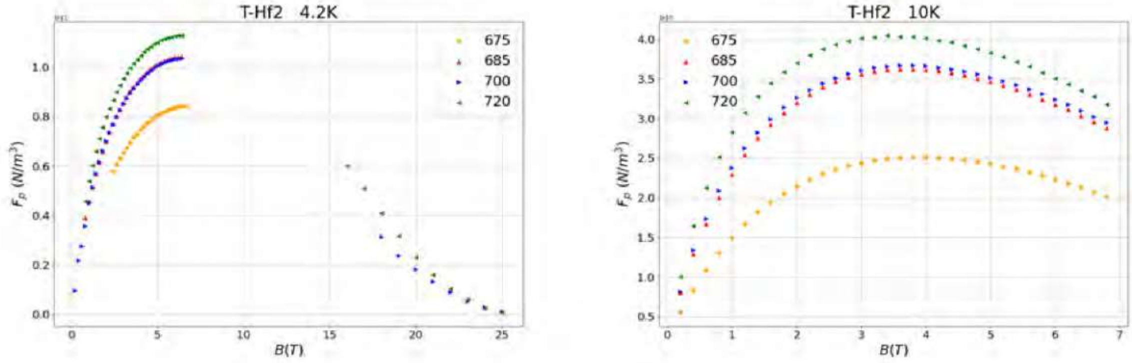

**(a)** 4.2 K **(b)** 10 K

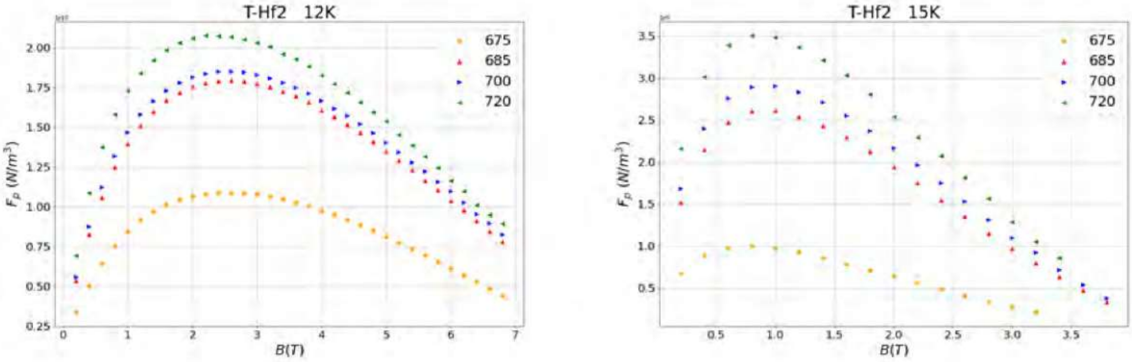

**(c)** 12 K **(d)** 15 K

**Fig. 4.9:** Pinning force $F_p$(B) values for the recipe T-Hf2 at 4.2 K, 10 K ,12 K and 15 K.

At 15 K, $B_{irr}$ is directly evaluated from m-H loops as described in module 3.5.4.1 and at 10 K and 12 K by means of a "short-range" Kramer extrapolation, as described in module 3.5.4.2.

At 4.2 K also $B_{c2}$ values were measured (evaluated using a criterion of 90% of the normal-state resistivity). They are reported in Sec. 4.2, since the difference between the two fields - $B_{irr}$ and $B_{c2}$- is modelled by including the critical temperature distribution along the superconducting layer.

The first clear feature is the great $B_{irr}$ enhancement obtained from the binary to the Ta-doped samples (up to +25%), which is visible from Fig.4.13a. If this last effect is quite expectable and well known in literature (e.g. [188]), the small gap between $B_{irr}$ of no-APC sample (T-Hf3) and its APC verions (T-Hf1) is harder to fully understand. This difference (from ≈ same value to + ≈ 20%), could be due to Kramer extrapolation inaccuracies at 10 and 12 K, as well as "sample-to-sample" statistical fluctuations. In fact, the only available value from R-B measurements for the T-Hf3 (no-APC) recipe comes from a wire reacted at 650°C, which is not directly comparable with $B_{irr}$ values from T-Hf1 (APC) samples reacted at higher temperatures. Nevertheless, this effect seems to decrease with increasing HT temperatures, eventually vanishing at 720°C. The reasons behind a possible true impact of the presence of $HfO_2$ nanoparticles on $B_{irr}$ (rather than a large amount of pure Hf dissolved in the A15 matrix) deserves an ad-hoc study, so far not present in literature.

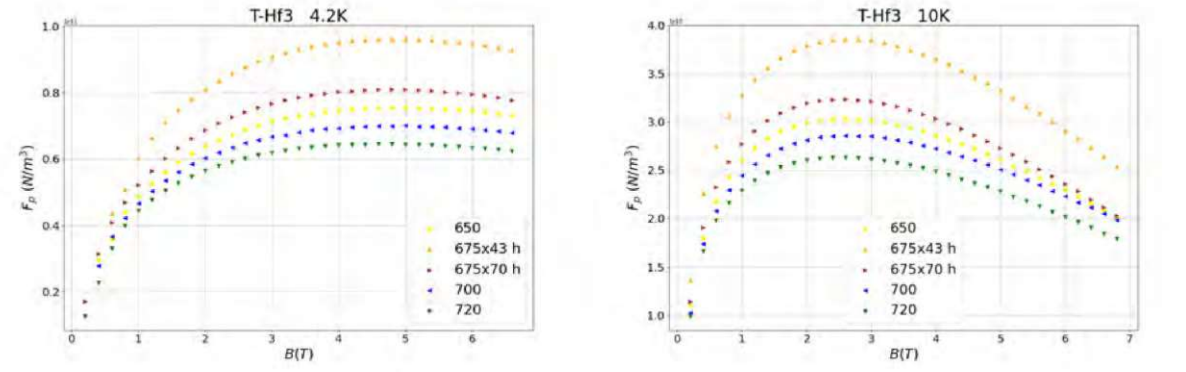

**(a)** 4.2 K **(b)** 10 K

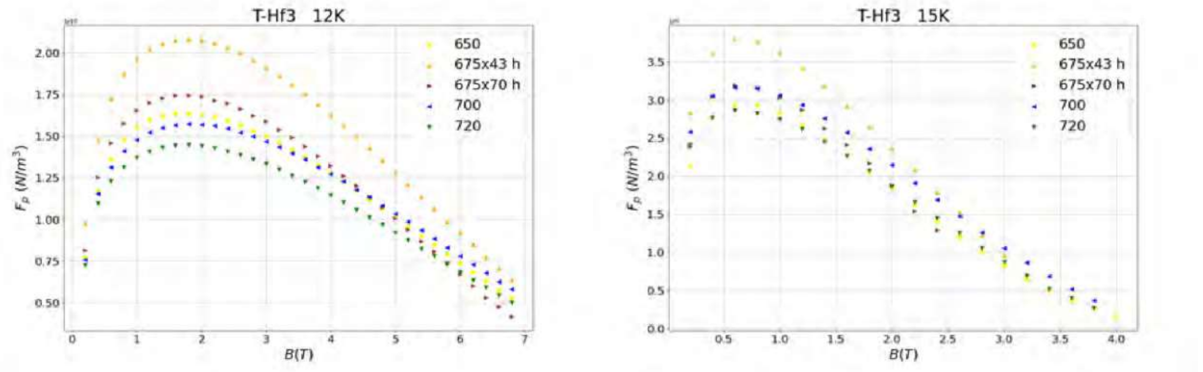

**(c)** 12 K **(d)** 15 K

**Fig. 4.10:** Pinning force $F_p$(B) values for the recipe T-Hf3 at 4.2 K, 10 K ,12 K and 15 K.

Also the reduced fields b=B/$B_{irr}$ (cf. Sec.1.4) were calculated. In particular, the values of $b_{peak}$=$B_{peak}/B_{irr}$ - where $B_{peak}$ is the field at which $F_{p\text{-}max}$ is measured- are reported in Fig. 4.14 ( in Sec.1.4 they are refereed as $h_{peak}$, being A/m less practical units for picturing the operational-field conditions than T).

The $b_{peak}$ values are significant since they help on identifying the relevant pinning mechanism. The reduced field at which *f(b)* reaches its maximum is given by:

$$b_{peak} = \frac{p}{p+q} \tag{4.10}$$

which is =0.2 for pure GB-pinning or =0.33 for pure PP-pinning (cf. Fig. 1.24).
In the measured samples, values of $b_{peak}$≃0.2 are shown in fact for PIT-R and T-Hf3, where no precipitates are expected. Higher values have been instead measured for the APC-rich recipes, with a maximum of 0.25 registered at 4.2 K in a T-Hf1 sample. These values are consistent with the hypothesis of strongly mixed pinning mechanism, as well as it expected the observable decreasing of $b_{peak}$ with raising experimental temperature (Fig. 4.15).

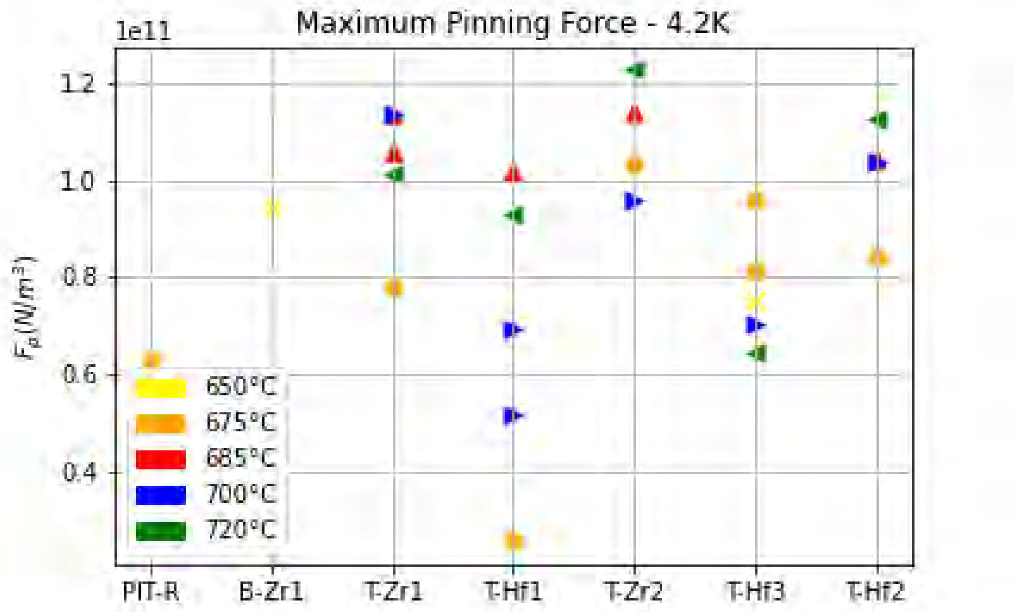

**Fig. 4.11:** Maximum pinning force $F_{p\text{-}max}$ values at 4.2 K for each sample of the systematic study. For each reaction temperature a different color and marker shape is used.

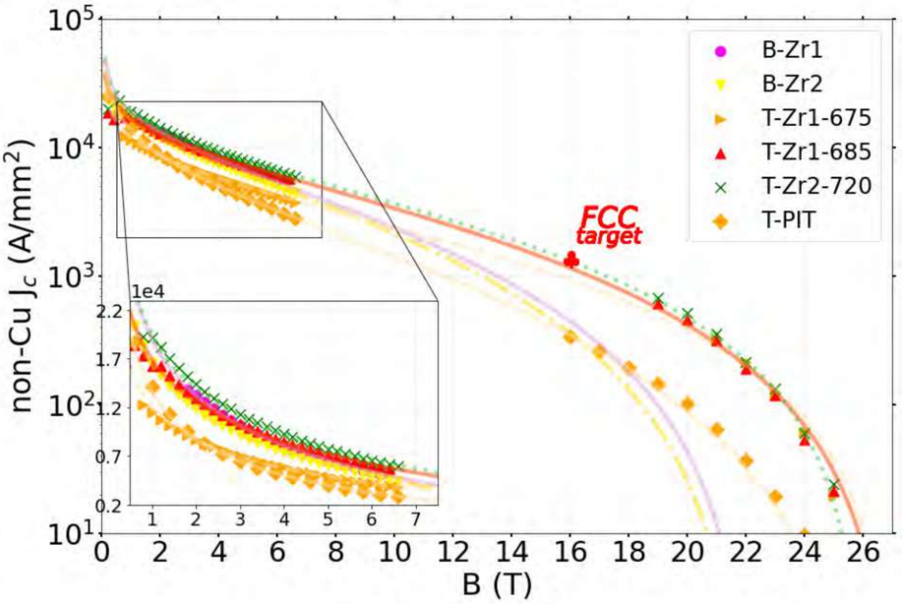

**Fig. 4.12:** Non-Cu $J_c$(B) values for two B-Zr, two T-Zr1, one T-Zr2 and a reference PIT samples. For each sample, $B_{irr}$ was known and some samples have also high-field data. A zoom inset shows the low-field $J_c$.
Published by *Ortino et al., SUST 2021* [148]

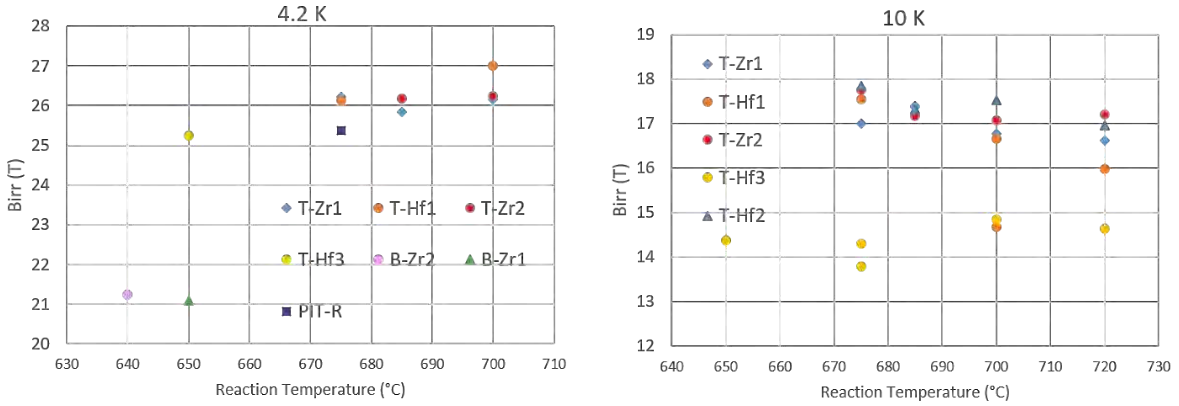

(a) 4.2 K (b) 10 K

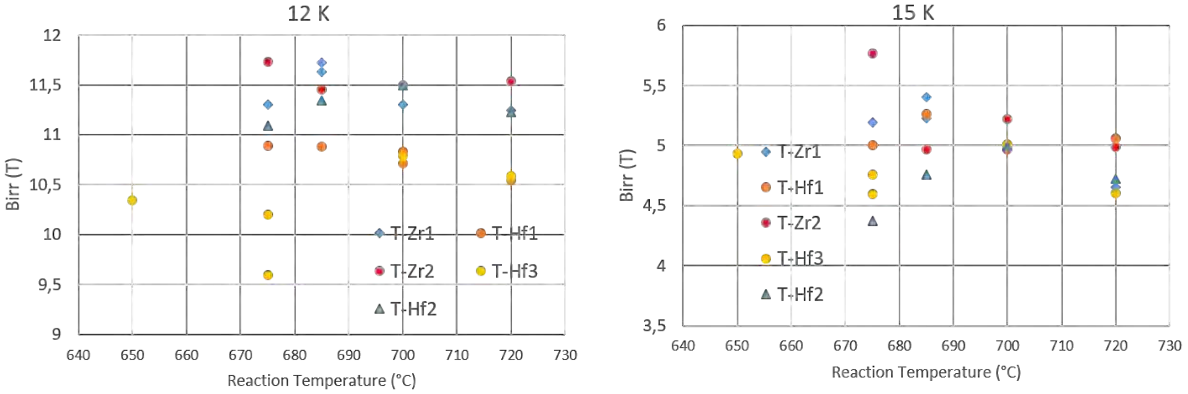

(c) 12 K (d) 15 K

**Fig. 4.13:** Irreversibility field $B_{irr}$ of each recipe at 4.2 K (R-B measurements), 10 K, 12 K and 15 K (magnetometry).

Along the cross-section in fact, as the operational temperature increases (in Fig 4.14b, 4.14c and 4.14d) some of the A15 spots could already have approached their $T_c$, differently from their neighbouring spots. They can contribute to current transport only at low fields. The overall $J_c/F_p$ is deeply affected by these local "weak points" - caused e.g. by Sn gradients - resulting in $F_{p\text{-}max}$ eventually manifesting at lower $B_{peak}$ (if compared with $B_{irr}$ at the experimental temperature) than those at lower experimental temperatures. This is better explained by Fig. 4.15, where the decreasing of $b_{peak}$ (averaged for each recipe) with increasing measuring temperature is clearly visible.

The role of $B_{irr}$ compared to $B_{c2}$, as well as the possible correlation of $b_{peak}$ with the precipitates size/density is discussed in Section 4.3.

### 4.1.3 Grain Size

Evaluation of grain sizes was done by SEM-TKD analyses as elucidated in 3.5.9. The acquisition of TKD images was provided by Andreas Stieger-Thirsfeld at USTEM (TU Wien, AT). Mapping of grains and production of statistics were provided by the latter together with the author. Three macro-areas per sample where investigated, covering as much as possible all the A15 width.

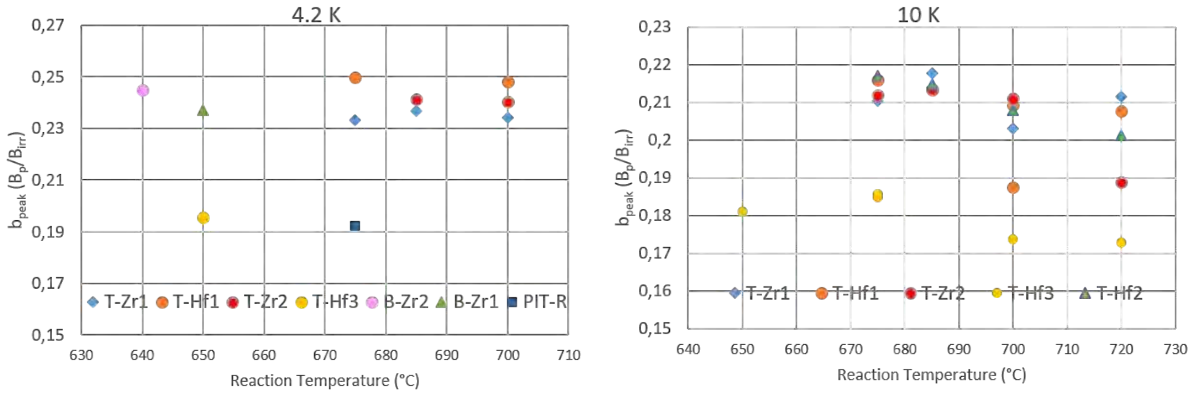

**(a)** 4.2 K **(b)** 10 K

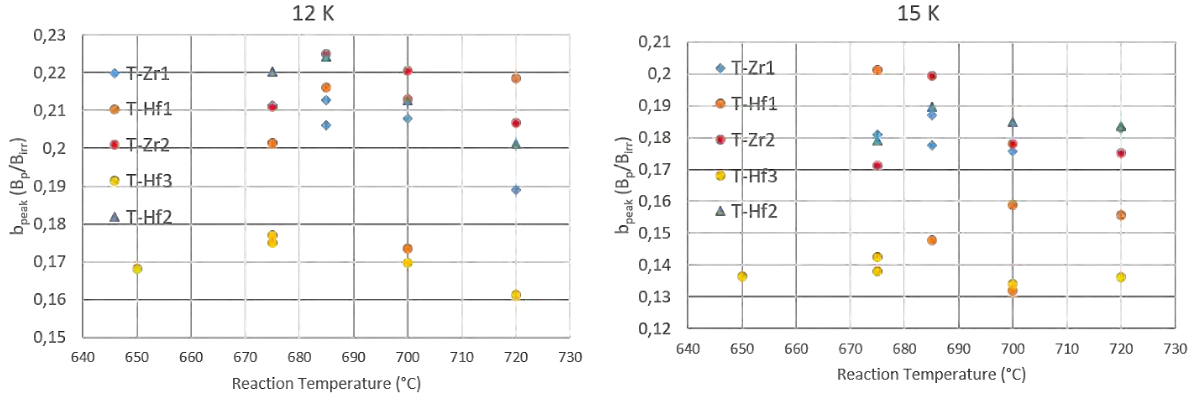

**(c)** 12 K **(d)** 15 K

**Fig. 4.14:** Reduced field $b_{peak} = B_p/B_{irr}$ calculated at the field $B_p$ where $F_p$ peaks for each sample and each recipe ($F_{p\text{-}max}$). From top left, clockwise: evaluation at 4.2 K, 10 K, 15 K, 12 K.

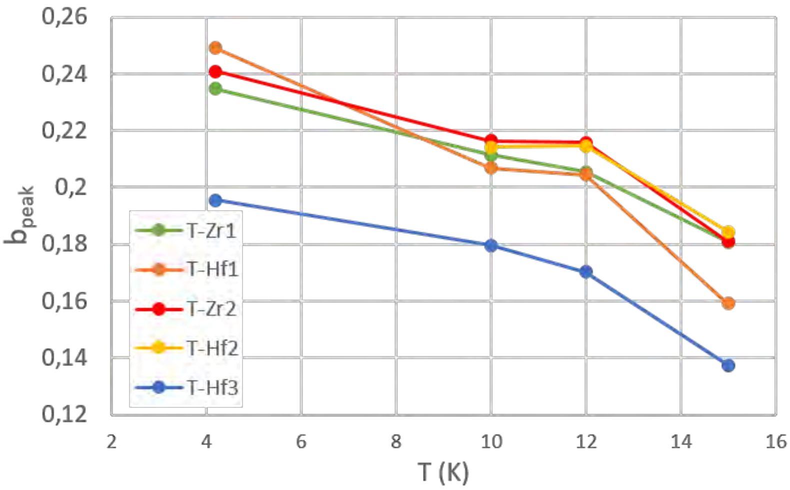

**Fig. 4.15:** Lowering of $b_{peak}$ with increasing measuring temperature for each recipe.

This allowed to get - considering the limits of this technique - the best comprehensive overview of how size and morphology of the grains change form the inner boundary of the superconducting layer (CG region) to the outer contour of the A15 (end of FG refion), where the grains get particularly elongated. This is immediately understandable, for example, by looking at Fig. 4.16

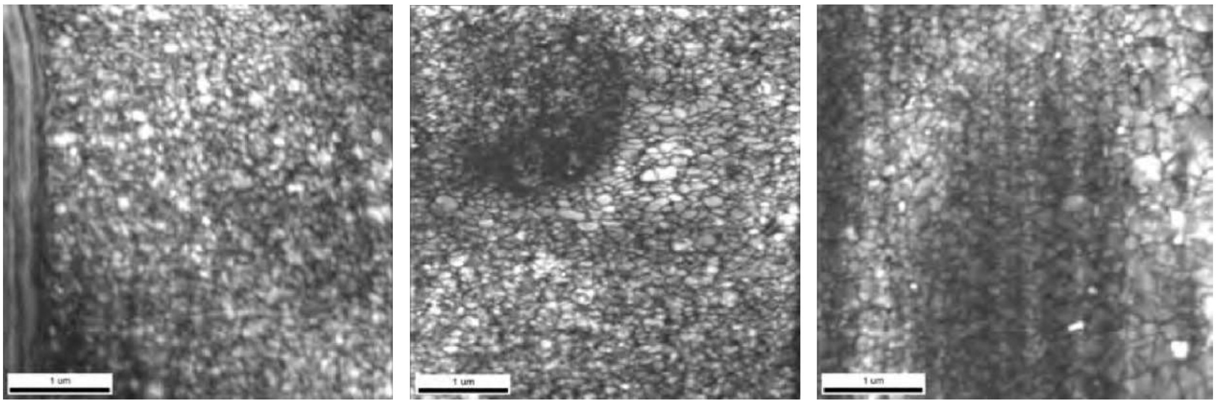

**(a)** TKD images

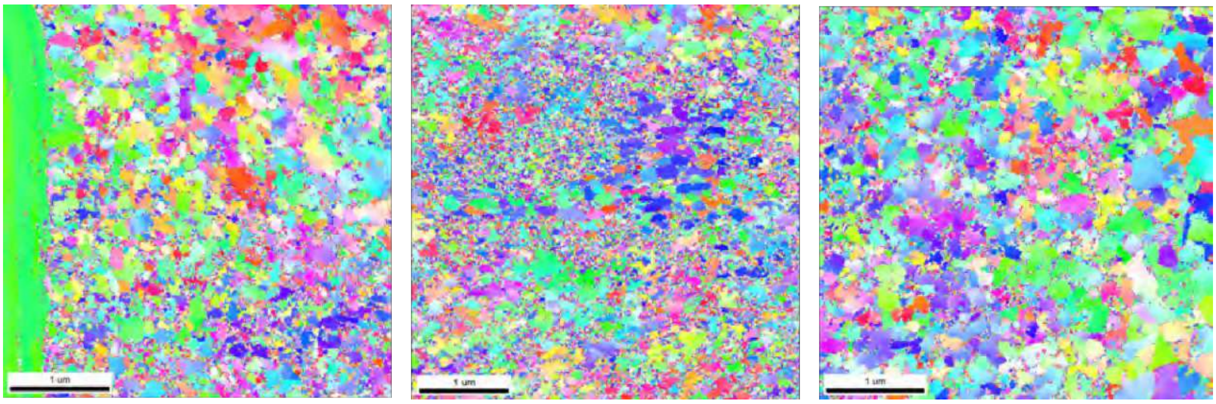

**(b)** TKD mapping

**Fig. 4.16:** SEM-TKD images and grains-mapping, evaluated as in Subsec. 3.5.9, of a T-Zr1 sample. Three images are stitched together to recreate the ≈ 13 $\mu$m long width. On the left, the end of the FG region, on the right the beginning of the CG region.

In these pictures, a total length of about 12 $\mu$m was covered (such a uniform quality of the analysis is possible only by refining each lamella down to comparable thicknesses, typically 40-80 nm).

Following the method in [155], both the number fraction NF and area fraction AF statistics describing grains of a certain diameter were calculated. The former gives the absolute portion of the grains with a specific size in the measured picture area, while the latter tells us the relative portion of area occupied by those grains.

From both AF and NF statistics, the mean value is taken as being the representative GS. Consequently, for each sample a set of three AF-GS and three NF-GS were evaluated. The ultimate AF-GS and NF-GS is finally calculated as the average between these 3 entries, respectively. If the A15 is particularly homogeneous, the two GS extracted from AF and NF statistics should be really close, whereas a inhomogeneous layer will result in a large gap between the two representatives.

In Fig. 4.17 both NF and AF representatives for each recipe are plotted, together with their variation (bars) over the A15 radius.

Since the critical current density is mainly determined by the GB density in the FG region, it was decided not take into account grains bigger than 400 nm in diameter, considered not to actively participate to current transport [214, 216]. For the same reason, the area fraction statistics should give a more accurate portrait of the flux pinning potential of a certain sample: it gives information about the true relevant sample area contributing to current transport.
Correlations and flux pinning modelling are usually based on single representative numbers of these heterogeneous distributions (especially for PIT wires), typically summarized in the so called "grain size" GS of a sample. Unifying and generally accepting one of the two statistics as being the most representative is actually one of the main problems in the community, often preventing from meaningfully compare the microstructure of samples produced from different manufacturing technologies and/or in different ages.
This problem and its impact on the flux pinning modelling will be further discussed in Sec. 4.3.

The first evidence from the plot in Fig. 4.17 is the grain refinement obtained in the APC wires if compared to the commercial PIT reference. Even if reacted at different temperatures than the PIT-R sample, the binary APCs already show a refinement of $\approx 10\%$, which is similar to the refinement observed in the T-Hf3 sample (no APC but Hf alloyed).

The really striking achievement is what the ternaries show, as having been optimized in terms (at least) of heat treatment/precursors ratios.
The average NF-GS among all the ternary APC recipes is 68.6 nm, while the AF-GS is 125 nm. The gap between these two numbers probably reflect the increased inhomogeneities of these recipes, being it a natural consequence of the presence of Ta. The best result is achieved in the T-Hf2, with a NF-GS (averaged among the heat treatment temperatures) of 63 nm and the best result of 56 nm found for the sample reacted at 720 °C. This recipe has a lower initial content of alloyed Hf, which can be the true key behind this great result.
What is instead somehow surprising is the relatively absence of correlation with the heat treatment temperatures. It is known in literature that PIT wires are quite sensitive to variations in the reaction temperature [165], but this does not seem to be the case for the APCs in this work.
This is nevertheless consistent with the $F_p$(B) results showed in the previous Section, and comparisons with the AF-GS and NF-GS are presented in Sec. 4.2, where correlations are clearly shown.

### 4.1.4 Precipitates size and density

The correct assessment of the particle size PS and particle density PD, representatives of the precipitates found in the APC wires, was the most time-consuming and difficult part of this work. The main issues of these evaluations were:

- Borderline experimental possibilities of STEM imaging: only perfect thinning of the lamellae (ideally no thicker than 30 nm) allows to magnify and resolve (low or null electron scattering) nanoparticles smaller than 2 nm. This is not always reproducible and often preparation of a new lamella is required (thin lamellae are very fragile and risk to easily break);

- Lack of literature data regarding the size and morphology of these inclusions in multi-filamentary wires. To date in fact, there is a very limited understanding on how $ZrO_2$ and $HfO_2$ particles look like and distribute over the A15. This is troublesome if one has

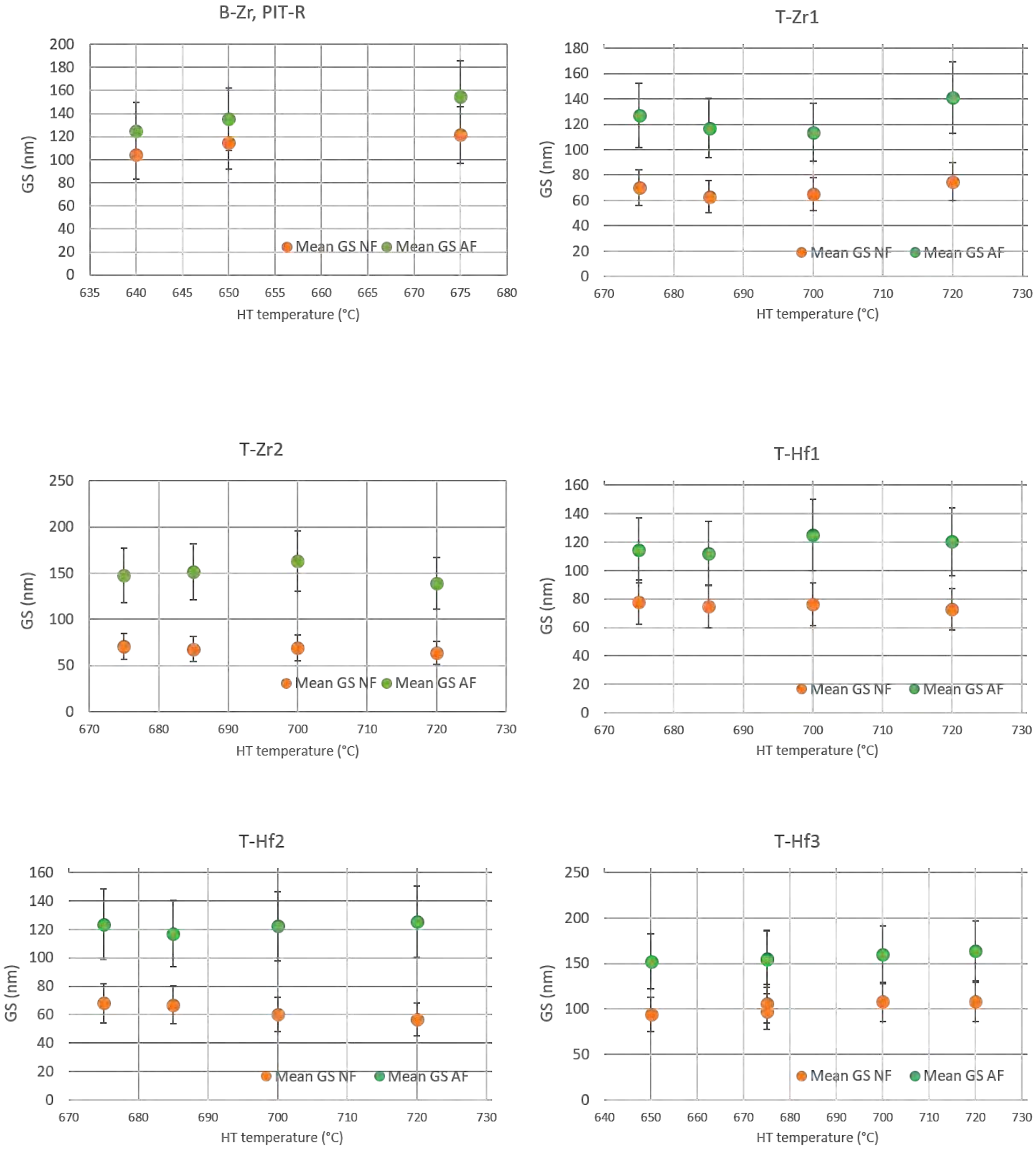

**Fig. 4.17:** Area fraction (AF) and number fraction (NF) statistics representatives grain size GS (nm) measured with SEM-TKD for each recipe. The bars reflect the variation along the radius of the filament.

to address a very small feature: is it a nanoparticle? Is it an impurity (e.g. dust, ion implantations)? Is it elemental Zr/Hf?;

- Long evaluation time for "by-eye" tracking of particles and problems on defining the evaluation criteria for a supervised machine learning algorithm;

- Checking of the amount of Zr/Hf present - respectively - in $ZrO_2$ /$HfO_2$ particles from final PD results with the initial amount of alloyed precursors shows not negligible inconsistencies. This eventually turned out to be an issue also by using other experimental techniques (e.g. atom probe tomography [189]). Where is the remaining Zr/Hf? Did we look at the right features so far?

The second and fourth point are strictly connected. In Fig. 4.19 this problem is well depicted in a sample from T-Zr2 recipe.
From a x160.000 magnified STEM picture, the black small spots - between and within the grains - seem to be zirconia ($ZrO_2$ ) precipitates, with sizes ranging between 3.5 and $\approx$ 19 nm. On some of these bigger spots in fact, it is also possible to perform EDX, with long acquisition times in order to get the clearest indication of the Zr/O ratios and confirm the features to be for real $ZrO_2$ particles.
By further magnifying to x320.000 times (picture below), these features get clearer, revealing their preference on occupying the so called "double" or "triple points", where in other words two or three grain edges/boundaries meet on a single point.
Though, also smaller details start now to appear. Smaller particles, lighter-coloured than their big darker siblings, each surrounded by a contrasting contour (smaller versions, also in shape, of the bigger clearly distinguishable features just elucidated, as in Fig. 4.18).

These subtle difference clearly emerges from the bottom picture, where a further magnification to x1.300.000 (to be considered the experimental limit for this technique) reveals even better a vast scenario of smaller features, typically in the 0.3-4 nm range. The latter are everywhere, and only few of them are tracked with red lines in the picture. They are findable even and often *especially* inside the bigger darker objects: in the bottom picture, one can count at least 15 smaller features into a 5 nm "large" one. The eventuality that those big features do only *appear* so, being them an image reconstruction artefact or only few outliers in a wide scenario of smaller features, has to be considered.
In the first place, it was decided to account only for the "clearly distinguishable" features, as they appear from the x320.000 times magnified picture in Fig. 4.19. The results for particle density and size are plotted for the four ternary recipes in Figures 4.20, 4.21, 4.22, 4.23.

For the particle density PD, the uncertainty comes from the thickness evaluation method used for assessing the lamellae volumes: it was in fact found that there is often a difference of (max) 20% between EELS and EFTEM thickness calculations (cf. Subsec. 3.5.8).
In the T-Hf3 samples no precipitates were found, this being consistent with the expectations since there is no oxygen powder in the starting recipe.
In the first Zr-doped recipe (T-Zr1) the particle density increases with increasing reaction temperature (+35% from 675°C to 720°C) while the particle size does not vary accordingly, not deviating from the 4-5.5 nm range. A clear trend is instead visible in the newer (more optimized) version of this recipe (T-Zr2), where for higher reaction temperatures we see lower PD (-55% from 675°C to 720°C) and increasing mean PS , with a minimum of 3 nm at 675°C corresponding to the highest density value among the measured samples (70.000/$\mu m^3$).
In the T-Hf1 recipe (with Hf content of 1 at.%) it appears again a correlation with HT temperature for the particle density, whereas particle sizes appear to be slightly changing (with the

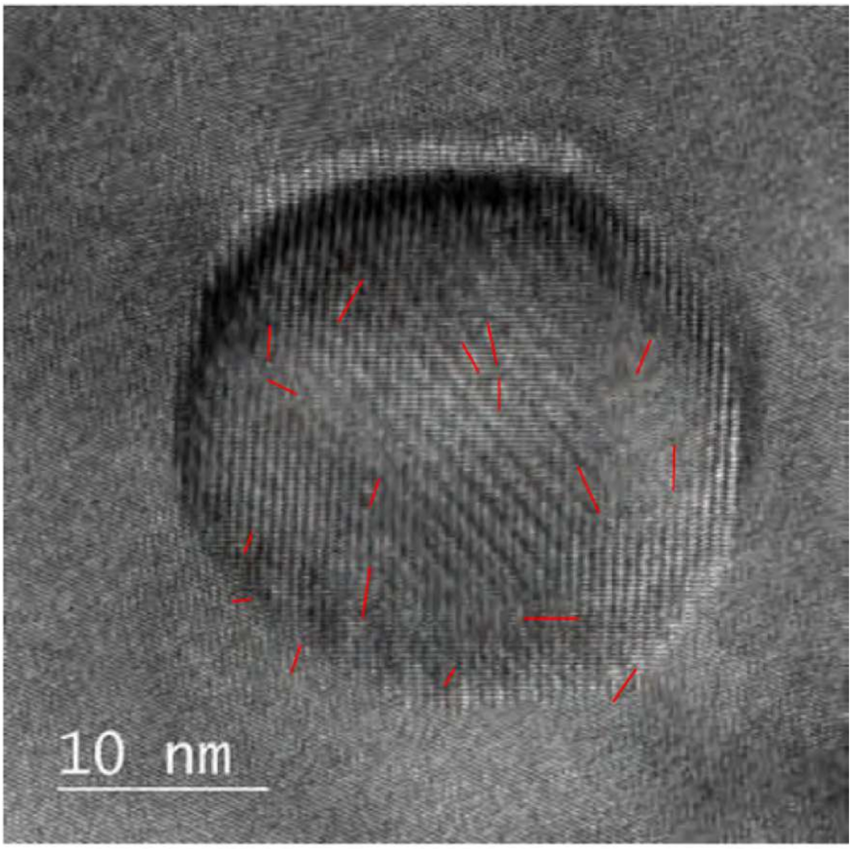

**Fig. 4.18:** High resolution TEM (HRTEM) image of a $ZrO_2$ precipitate. Within the clearly distinguishable ≈16 nm large feature, few smaller ones are tracked with red lines.

exception of T=685°C, where the largest mean PS was calculated).
Finally, in the reduced-Hf recipe (T-Hf2), the PD counts get drastically lowered (almost an order of magnitude), revealing a monotonic growing trend both for PS and PD with increasing HT temperature.

For the binary APC samples, particle density and size were calculated by Pfeiffer [155] following the same procedure, resulting for the sample B-Zr1 in a mean PS of 8.7 nm and PD of 9454 $1/\mu m^3$; for the sample B-Zr2, the mean PS was found to be 11.8 nm and PD to be 2480 $1/\mu m^3$. These last numbers suggest a lower pinning contribution at high-fields for the binary APCs if compared to the ternaries, considering the point-particle pinning to exploit better its potential at higher reduced fields b. Moreover, such large PS and low particle densities in the binaries appear consistent if compared with the average ternaries PS and PD, resembling the same total volumes tracked also in the ternaries, where the total amount of Zr alloyed in the starting recipe is the same (1 at.%).
Starting from this last consideration, a counter-check on the quantity of moles of Zr/Hf found from particle tracking compared with the initial moles of alloyed Zr/Hf was done.
Let's therefore consider a STEM picture, being it a segment of the lamella. The moles-check can be summarized as follows:

1. The picture volume is known, as we have its x/y sizes and z from EELS/EFTEM;

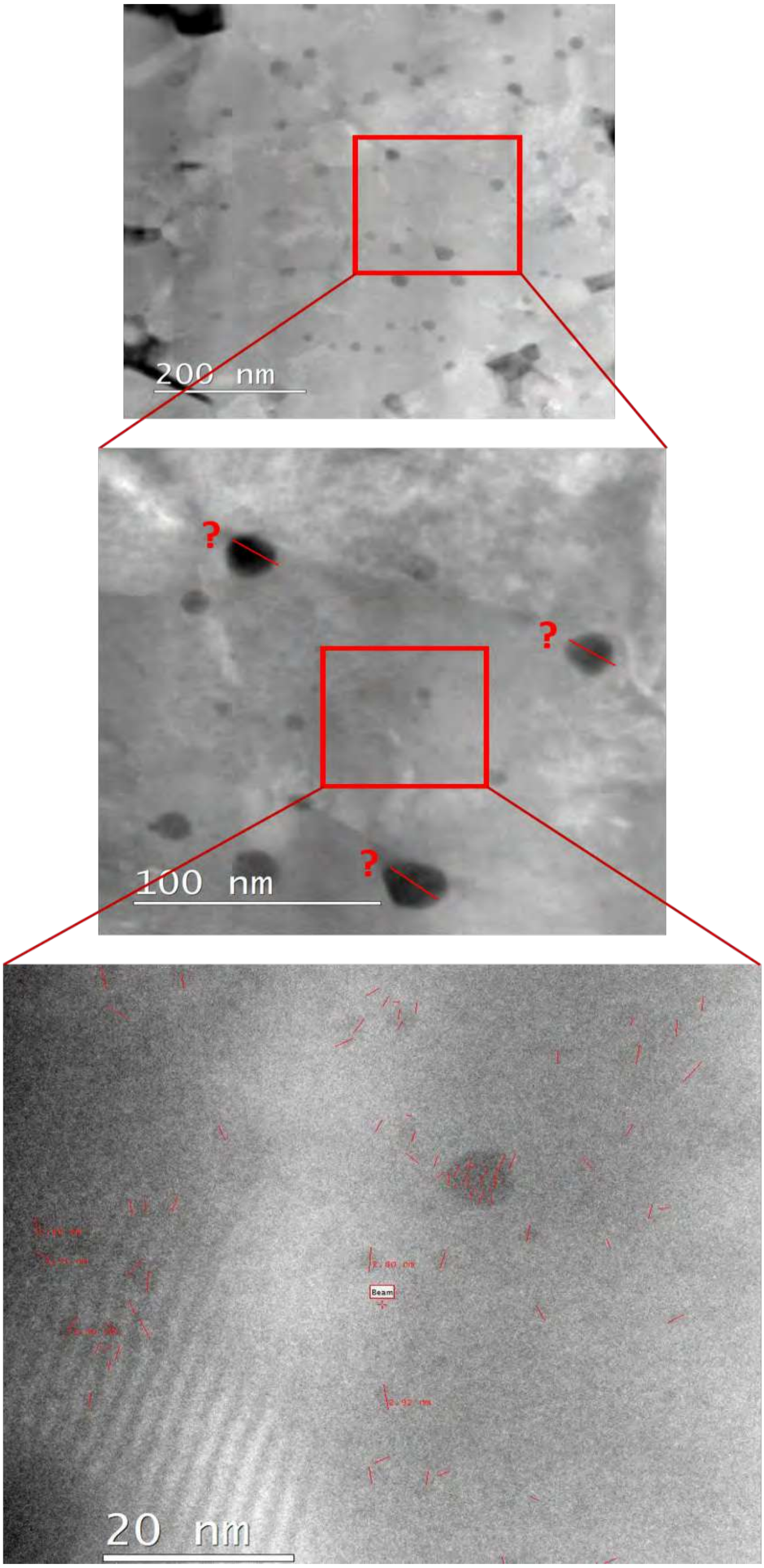

**Fig. 4.19:** A T-Zr2 STEM image further magnified. Pictures from top to bottom: 650 nm x 650 nm , 230 nm x 230 nm and 79 nm x 79 nm. By looking at the first two only few features appear clear; a deep look reveals smaller details.

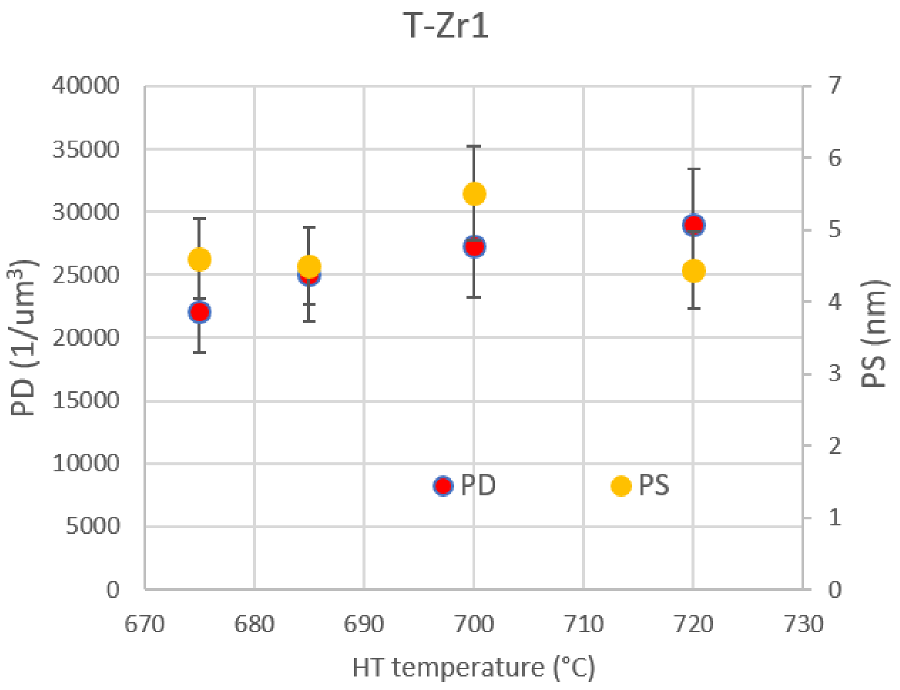

**Fig. 4.20:** Mean particle size PS (nm) and density PD ($1/\mu m^3$) for the recipe T-Zr11, plotted with standard deviations in red and yellow, respectively.

2. We assume the precipitates to have a spherical shape, so that we can easily calculate the volume of any single particle tracked (the diameters are tracked);
3. The densities of $ZrO_2$ and $HfO_2$ are known: $5.68{\cdot}10^6$ ($g/m^3$) and $9{,}68{\cdot}10^6$ ($g/m^3$), respectively [156]. Through them and the before mentioned volume of the found specimens, it is possible to calculate the total weight of the found $ZrO_2$ /$HfO_2$ present in the picture;
4. Since the molar masses of $ZrO_2$ /$HfO_2$ are known (123.218 g/mol and 210.49 g/mol, respectively), it is possible to calculate the number of moles of pure Zr/Hf in the respective compounds;
5. $Nb_3Sn$ volume is calculated from the total picture volume minus the total $ZrO_2$ or $HfO_2$ volume as at point 2);
6. Using the same procedure of points 3) and 4) - $Nb_3Sn$ density=$8.69{\cdot}10^6$ ($g/m^3$) and molar mass= 397.4 (g/mol) - the moles of Nb in $Nb_3Sn$ are calculated.
7. As the initial content of Zr or Hf in the starting Nb alloy is known (1 at.% or 0.7 at.%), we can now calculate it (in moles) and compare to the number of moles found from point 4).

This procedure was deployed for each specimen, as being a first - not aiming to be necessarily 100% exact - prediction of the expected amount of features observed with STEM, resulting in a "should be/found" series or ratios.
The very first indication of good STEM tracking/counting results from the fact that this ratios never goes below 1 for any of the samples measured, meaning that no features that weren't precipitates were accounted.

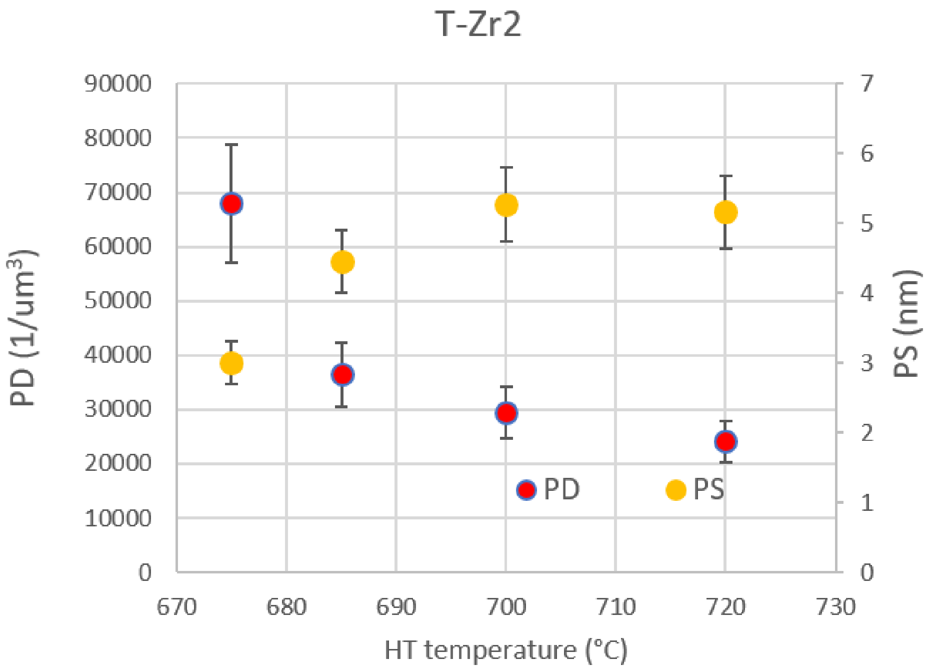

**Fig. 4.21:** Mean particle size PS (nm) and density PD (1/$\mu$m$^3$) for the recipe T-Zr2, plotted with standard deviations in red and yellow, respectively.

Still, for all the samples, these ratios are never exactly 1, but always quite higher. In Tab 4.1 these ratios are reported for each specimen:

**Tab. 4.1:** "Should be/found" number of moles of Zr or Hf for each measured ternary-APC sample

| Sample | 675(°C) | 685 (°C) | 700 (°C) | 720 (°C) |
|---|---|---|---|---|
| T-Zr1 | 2.12 | 2.91 | 4.5 | 1.73 |
| T-Hf1 | 3.22 | 2.3 | 2.57 | 2.33 |
| T-Zr2 | 3.71 | 1.66 | 1.57 | 2.02 |
| T-Hf2 | 1.33 | 3.44 | 3.9 | 4.45 |

The clear evidence from these counts is that numbers do not add up. Where is the remaining amount of Zr/Hf?
Motivated by this question, an even wider tracking of *"any feature"* found in the A15 matrix, as discussed before and depicted in 4.19 (bottom) was conducted. Any small feature ($\geq$ 500 counts per 230 nm x 230 nm picture) was accounted, resulting in remarkably smaller mean PS and higher PD.
The results of these analyses are plotted in Fig. 4.24 these results are plotted per each recipe.

The trends/correlation with HT temperatures are very similar to those showed before (referred as "clearly distinguishable features", while these lasts were referred as "any feature").
Mean particle sizes are now in the order of 2 nm (showing an overall reduction of about 50-70%

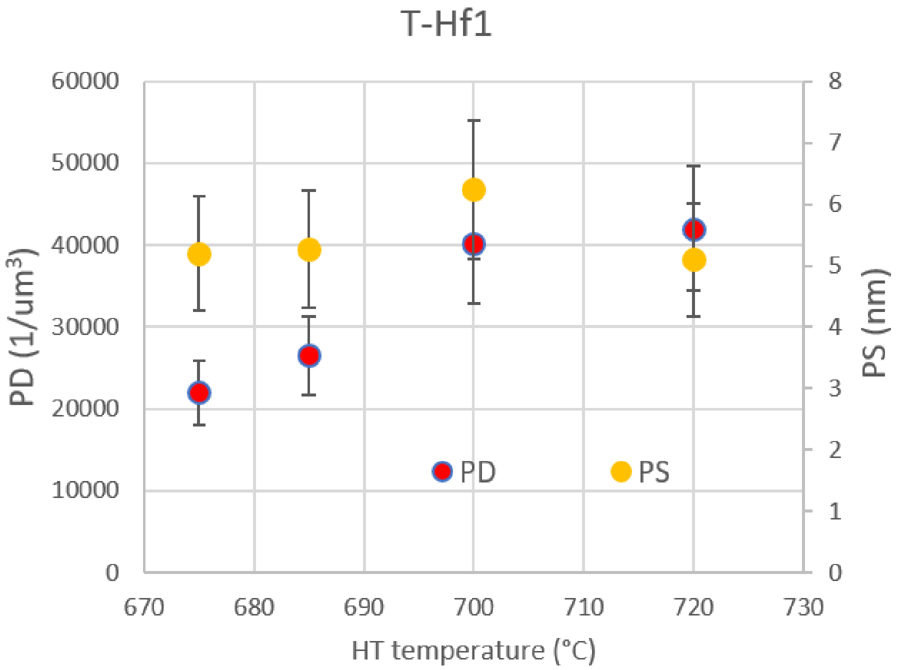

**Fig. 4.22:** Mean particle size PS (nm) and density PD ($1/\mu m^3$) for the recipe T-Hf1, plotted with standard deviations in red and yellow, respectively.

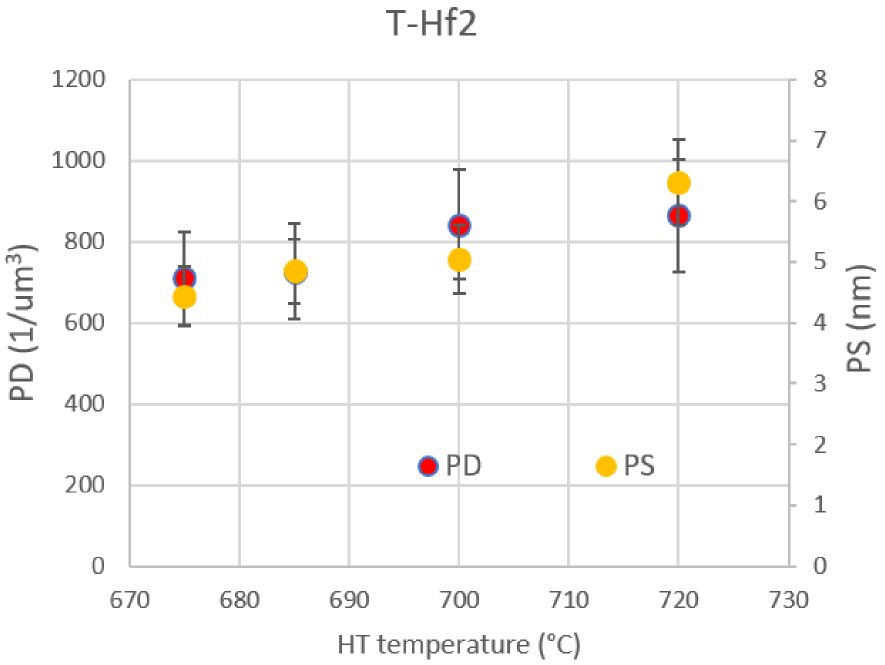

**Fig. 4.23:** Mean particle size PS (nm) and density PD ($1/\mu m^3$) for the recipe T-Hf2, plotted with standard deviations in red and yellow, respectively.

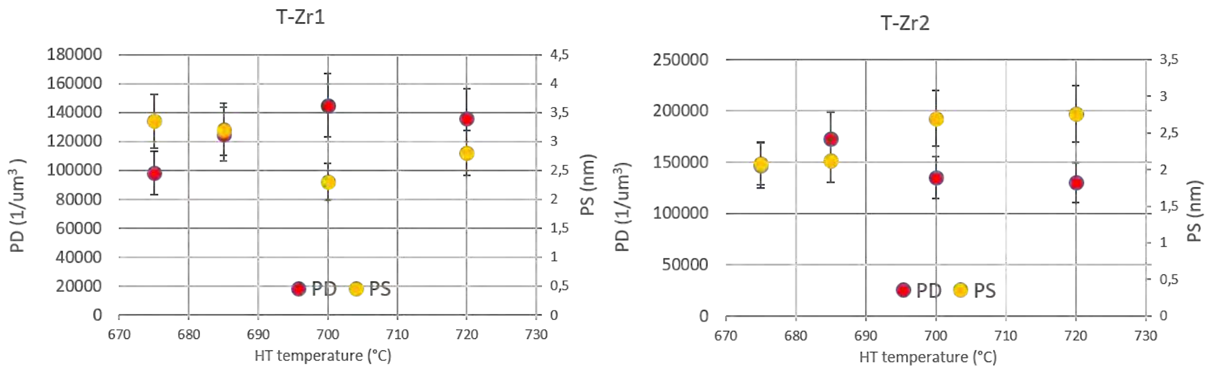

**(a)** 4.2 K **(b)** 10 K

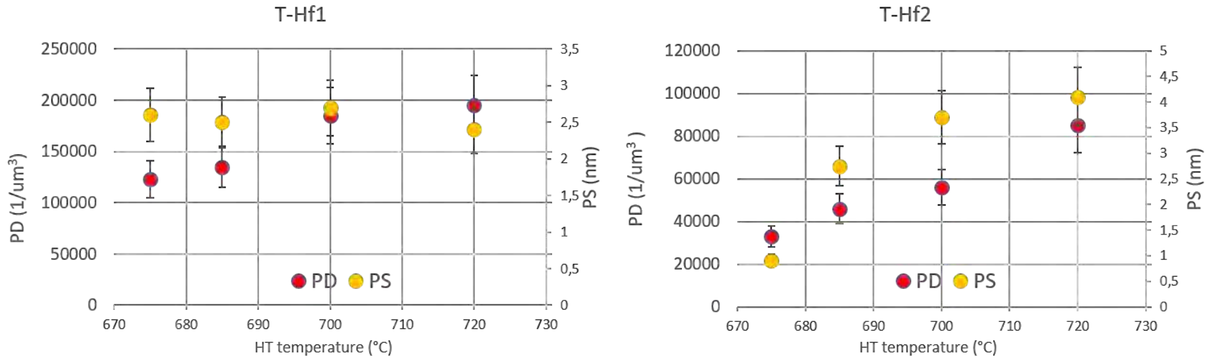

**(c)** 12 K **(d)** 15 K

**Fig. 4.24:** Particle size PS (in yellow), particle density PD (in red) as for the "any features" case. Data are plotted with standard deviations for each recipe.

from the first analysis) and at the same time the calculated densities doubled/tripled accordingly.

Still, also in this case, it does not add up. It is clear already by eye that a vast population of those small features can simply not be accounted in a "by-eye" procedure (the example of Fig. 4.18 is particularly eloquent on this respect) therefore the should be/found ratios eventually even increased. The latter are reported in Tab. 4.2.

Recent studies by Tarantini et al. on $HfO_2$ samples [189] (as well manufactured by Hyper Tech Inc. and reacted at Fermilab) demonstrated the precipitates to have very similar shapes and size if compared with the clearly distinguishable" features as they are here analysed and plotted in Figures 4.20, 4.21, 4.22, 4.23.
Their investigation revealed very similar if not the same PD numbers (1000 to 100.000 $1/\mu m^3$), as well as comparable mean PS (4-9 nm). Moreover, their analyses revealed a vast amount of smaller features very similar to those discussed as being everywhere tracked within the second ("any feature") type os STEM investigation.
Elemental Hf particles (as for the Hf-doped recipes) were indeed found to be dispersed everywhere in the A15 after reaction, which let us think about a possible explanation to the problem of addressing raised in this Chapter. The reason why all this Hf did not fully react with O so resulting in $HfO_2$ is not clear though: insufficient O? O-diffusion problems (something impeding

**Tab. 4.2:** "Should be/found" number of moles of Zr or Hf for each measured ternary-APC sample in the "any-feature" case.

| Sample | 675(°C) | 685 (°C) | 700 (°C) | 720 (°C) |
|---|---|---|---|---|
| T-Zr1 | 4.85 | 5.91 | 8.5 | 4.8 |
| T-Hf1 | 6 | 4.3 | 4.67 | 5.64 |
| T-Zr2 | 6.71 | 9 | 2.57 | 4.02 |
| T-Hf2 | 11 | 10,02 | 4.39 | 4.05 |

its path through the A15 towards the most peripheral areas? Temperature homogeneity during HT processes?

As for the first question, it was ensured the oxygen to be always sufficient for a complete internal oxidation for each ternary sample [206]. As for the second query, a defined limit of completely reacted $ZrO_2$ /$HfO_2$ particles should be observable if the O path is slowed down or even stopped within the A15 matrix.

This is not the case, since a homogeneous presence of the oxides, always carrying similar mean PS/PD, is observable throughout the whole A15 length, in all the examined recipes. This is visible at a first glance already from Fig. 3.32 and clearly observable from the series of pictures contained in Fig. 4.25.

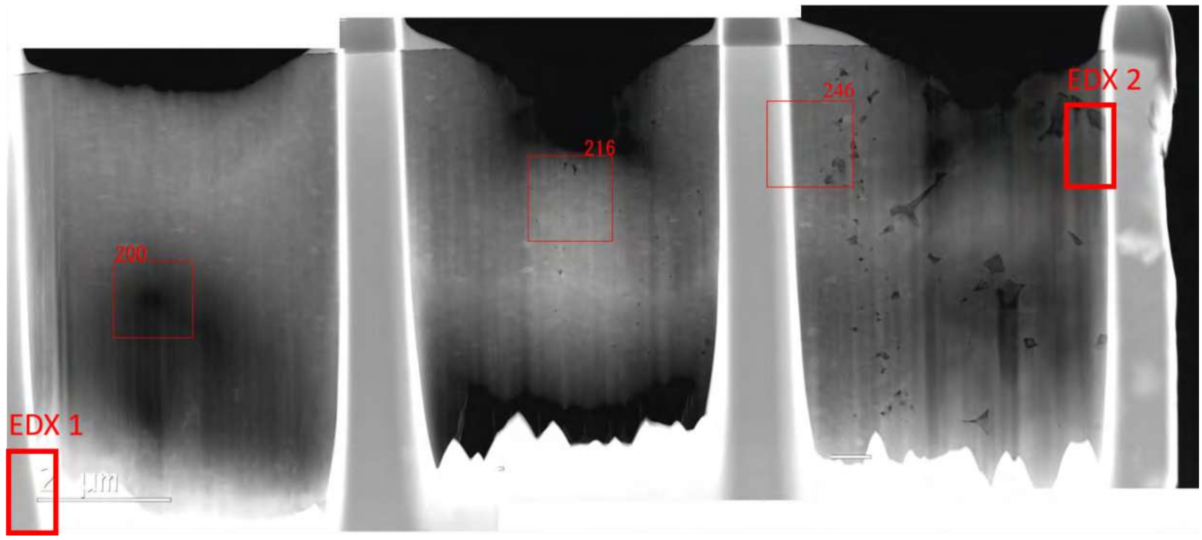

**Fig. 4.25:** STEM collage-pictures of a lamella from T-Zr2-685 sample, covering the entire width of the A15. In red, the further magnified spots and EDX measurements spots are underlined.

In these figures, the sample T-Zr2-685 is taken as an example. The further magnified areas are taken in spots 200 (end of A15, Cu direction), 216 (A15 centre), 246 (CG region, core direction) in Fig. 4.26, 4.27 and 4.28), with the darker and lighter areas meaning a thinner or thicker lamella's region, respectively. The layout direction is recorded by means of EDX as it is visible from Fig. 4.29: in this way, tracking of the evolution of size and density of the precipitates is possible.

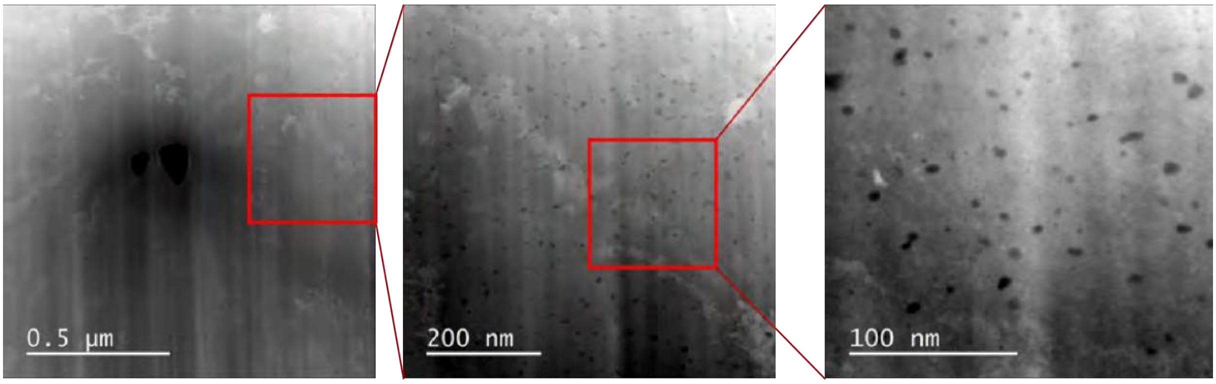

**Fig. 4.26:** Spot 200 from Fig. 4.25: further magnifications to x50.000, x160.000 and x320.000 times. The mean PS is here 4.4 nm

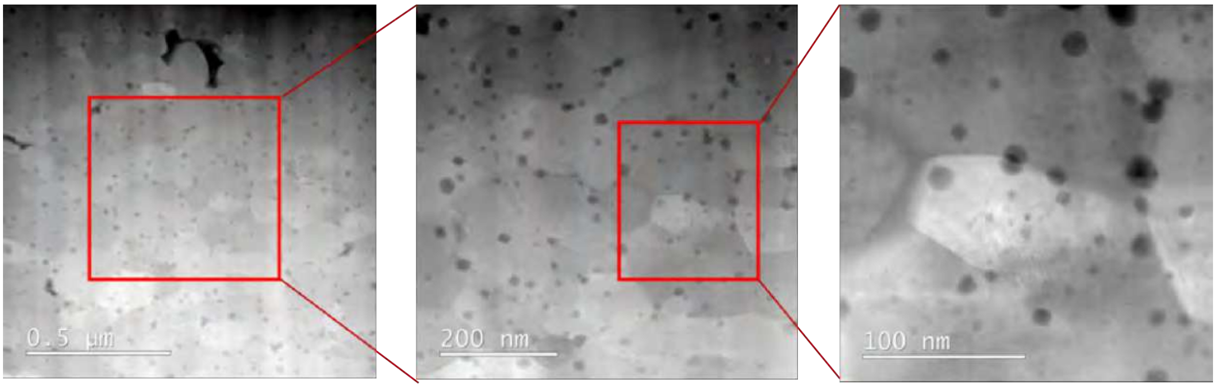

**Fig. 4.27:** Spot 216 from Fig. 4.25: further magnifications to x50.000, x160.000 and x320.000 times. The mean PS in this picture is 7.1 nm

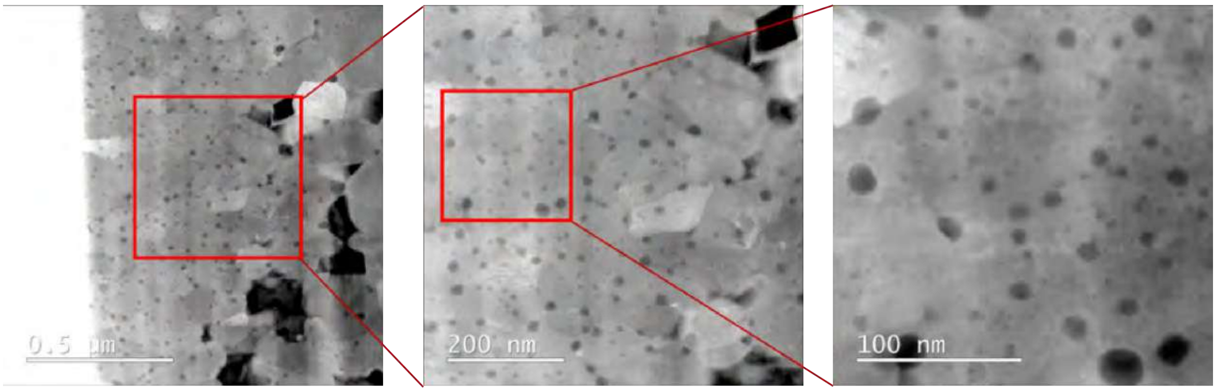

**Fig. 4.28:** Spot 246 from Fig. 4.25: further magnifications to x50.000, x160.000 and x320.000 times. The mean PS is here 5.8 nm.

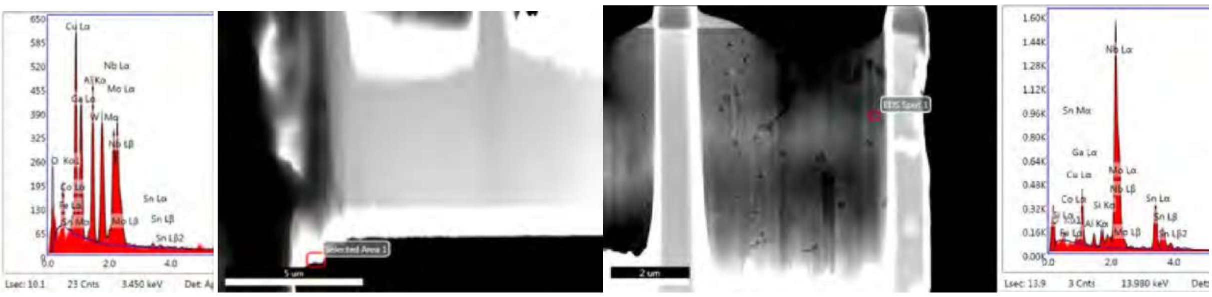

**(a)** Spot "EDX1" from Fig. 4.25 with EDX elemental chart.

**(b)** Spot "EDX2" from Fig. 4.25 with EDX elemental chart.

**Fig. 4.29:** Particle size PS (in yellow), particle density PD (in red) as dor the "any features" case. Data are plotted with standard deviations for each recipe.

Each spot is further magnified down to x320.000 times (230 nm x 230 nm pictures, as the rightmost ones of each picture). A slightly different size/density is observable among the three spots (with a maximum ΔPS of about 60%), resulting in a ± 20% from the CG to FG side (along ≈ 10 $\mu$m). Though $ZrO_2$ particles are present ecerywhere, up to the end of the A15 (Fig. 4.26) meaning that the oxygen is able to oxidise particles extensively throughout the entire A15 width.

In the end, while the question to the presence of pure elemental Hf/Zr around is not yet answered, a clear distinction between the two populations - Hf and $HfO_2$ / Zr and $ZrO_2$ particles- should shed light on the amount of unoxidized material, eventually confirming the metallic nature of the smallest particles (Hf).
With EDX, it is in fact extremely difficult to make this separation clear, as this technique is not suited for quantitative analyses with light elements as O [121] and anyway already beyond its spatial resolution physical limit, which cannot be lower than 15 nanometers as estimated with Monte-Carlo simulations [145].
In terms of pinning, it is important to account Hf and Zr (metals) not to have the same properties if compared to their oxides, as it is explained in [42, 88, 110, 154, 158, 166, 205].

The impact of this last important difference and of PS and PD on the pinning models is discussed in Sec. 4.3, while the correlations with the other properties so far elucidated are treated in the next Section.

## 4.2 Correlations and Pinning

In this section the main properties as they are shown in the previous section are compared trying to unveil possible correlations. Moreover, their potential impact on the flux pinning is discussed.

### 4.2.1 Correlations

In Fig. 4.30 a series of master plots is displayed, where NF-GS, AF-GS and the maximum values of the pinning forces at 5 K $F_{p\text{-}max}(5\text{K})$ are shown together for each sample.

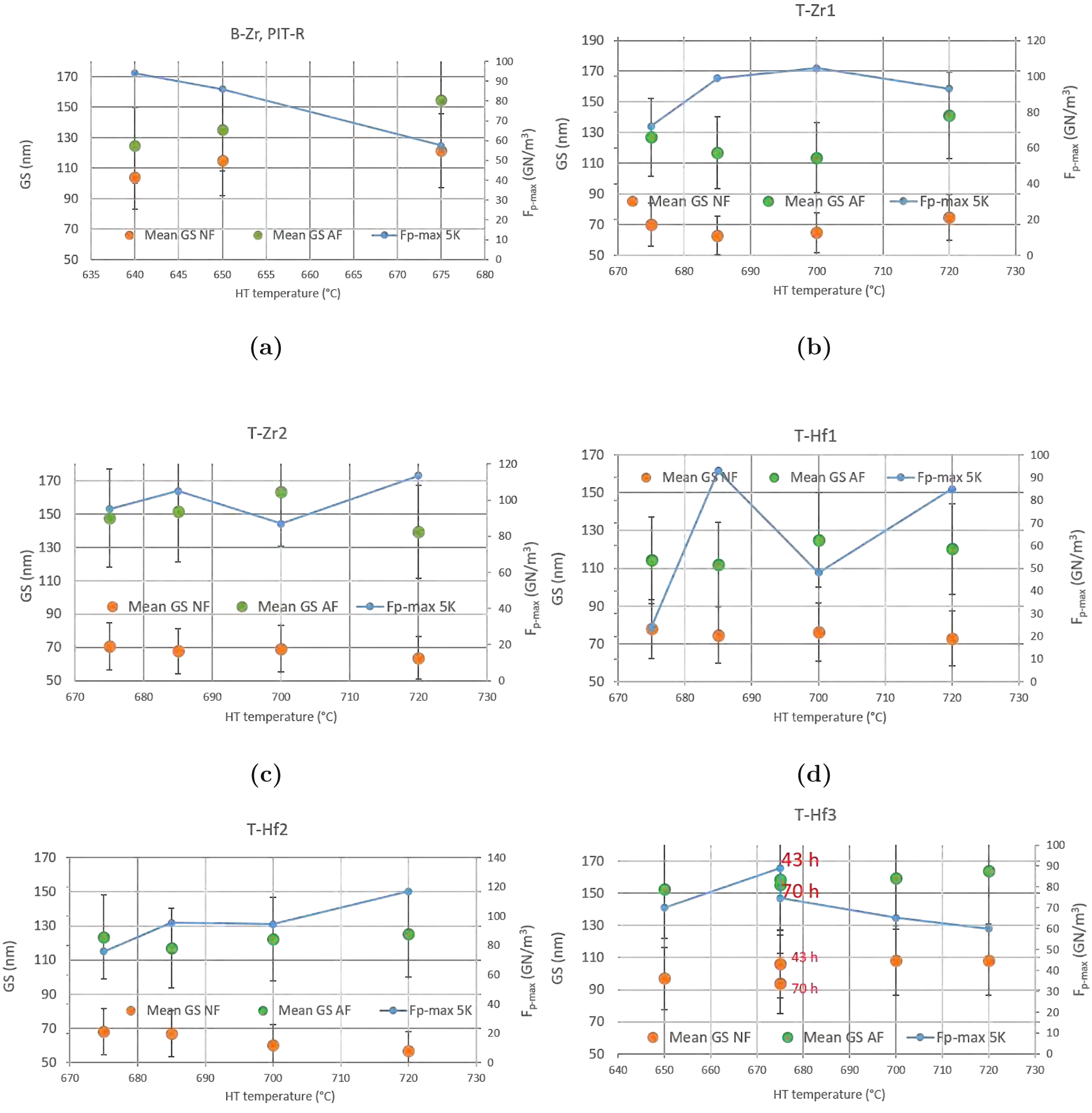

(a) (b)

(c) (d)

(e) (f)

**Fig. 4.30:** Area fraction AF grain size (in green), number fraction NF grains size (in orange) and maximum pinning force $F_{p\text{-}max}$ (in blue) at 5 K compared for each recipe. The bars reflect the variation along the radius of the filament.

A reasonably good overall agreement with the known relation $J_c \propto 1/\text{GS}$ is visible through all the recipes, with the only exception of the recipe T-Hf2 where this is better made clear for the NF-GS statistics only. This general understanding was already summarized in Fig. 1.18, which is replotted here in Fig. 4.31 by adding five recipes of the examined wires - 2 Zr-ternaries, 2 Hf-ternaries and a Zr-binary APC - to the layer-$F_p$ extrpolation.

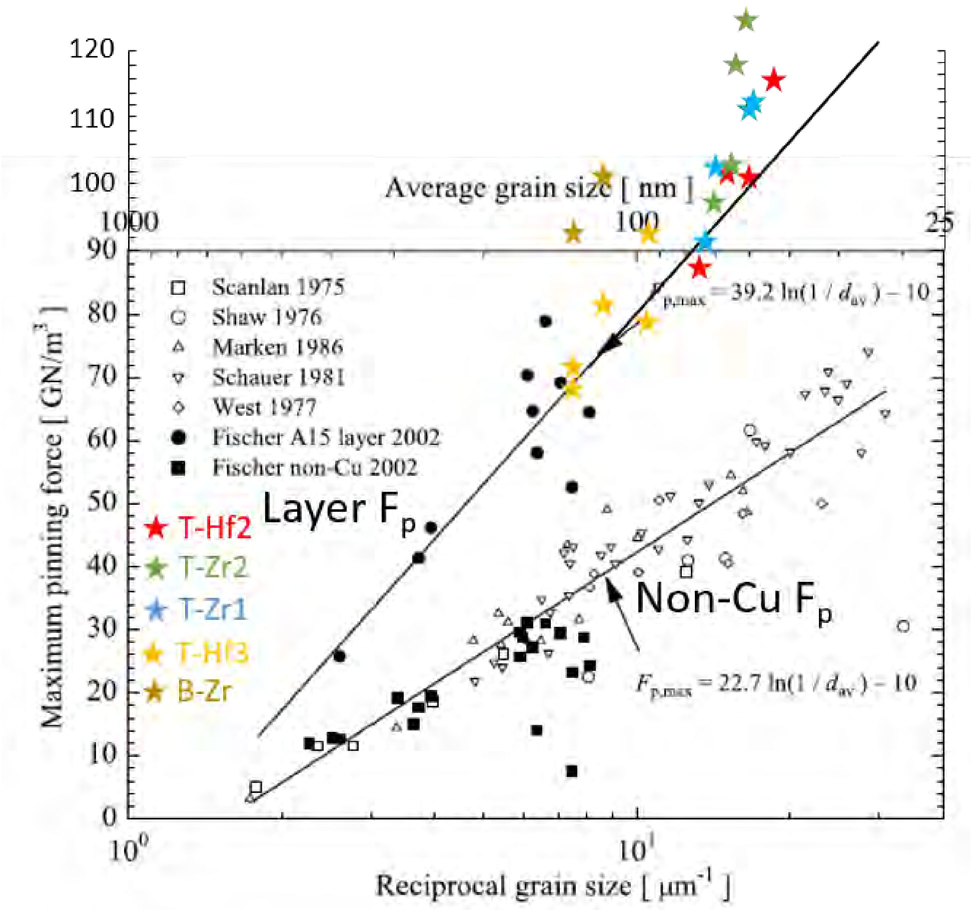

**Fig. 4.31:** Collection of maximum pinning force values at 4.2 K vs reciprocal NF grain size GS, enriched with some of the findings of this study.
Adapted from the original plot by: *C.M. Fischer, University of Wisconsin-Madison 2002*

From Fig. 4.31 it is clearly visible how the T-Hf3 recipe (in yellow, no-APC) well fits with the long series of different samples analysed through decades (binaries and ternaries), collected on the same trend-line for the layer pinning force maximum values as for "conventional" core-surface (grain-boundary, GB) pinning.
At the same time, also the APC-ternaries do agree with this trend, eventually extending the validity of the findings/extrapolations by Fischer to consistently lower GS values for multi-filamentary wires (GS vs $F_{p\text{-}max}$ data are now covering down to half-grain size the last entry in the plot).
Some of the best samples (e.g. T-Zr2) do show 10-20 % higher values than predicted, being this probably an indication of the point particle PP additional pinning contribution. This is clearly visible also by looking at the behaviour of the two binaries (in gold, B-Zr), which as well differ for ≈ +20% from the prediction.

It is interesting to notice that the absence of correlation between HT temperature and GS/$F_{p\text{-}max}$ does not reflect on the reciprocal proportionality between GS and $F_{p\text{-}max}$.
In fact, net of sample-to-sample fluctuations and/or uncertainties, a consistent alternation of "smaller grain - higher $F_{p\text{-}max}$"/"bigger grain - lower $F_{p\text{-}max}$ is visible from Fig. 4.30, especially clear in the B-Zr (Fig. 4.30a), T-Zr1 (Fig.4.30b), T-Zr2 (Fig. 4.30c) and T-Hf3 (Fig. 4.30f) recipes. Observing the GS correlating with $F_{p\text{-}max}$ is a strong indication of leading pinning mechanism (at least within the 0-7 T range, where $F_{p\text{-}max}$ is detected): this is further confirmed in Sec. 4.2, where the absolute contribution of GB- and PP- pinning mechanisms are addressed.

Also interesting is to observe how the GS correlates with the precipitates density PD - calculated as for the "clearly-distinguishable features" case - for most of the samples.
In Fig. 4.32 these comparisons are shown taking the example of number fraction calculated grain size (NF GS).

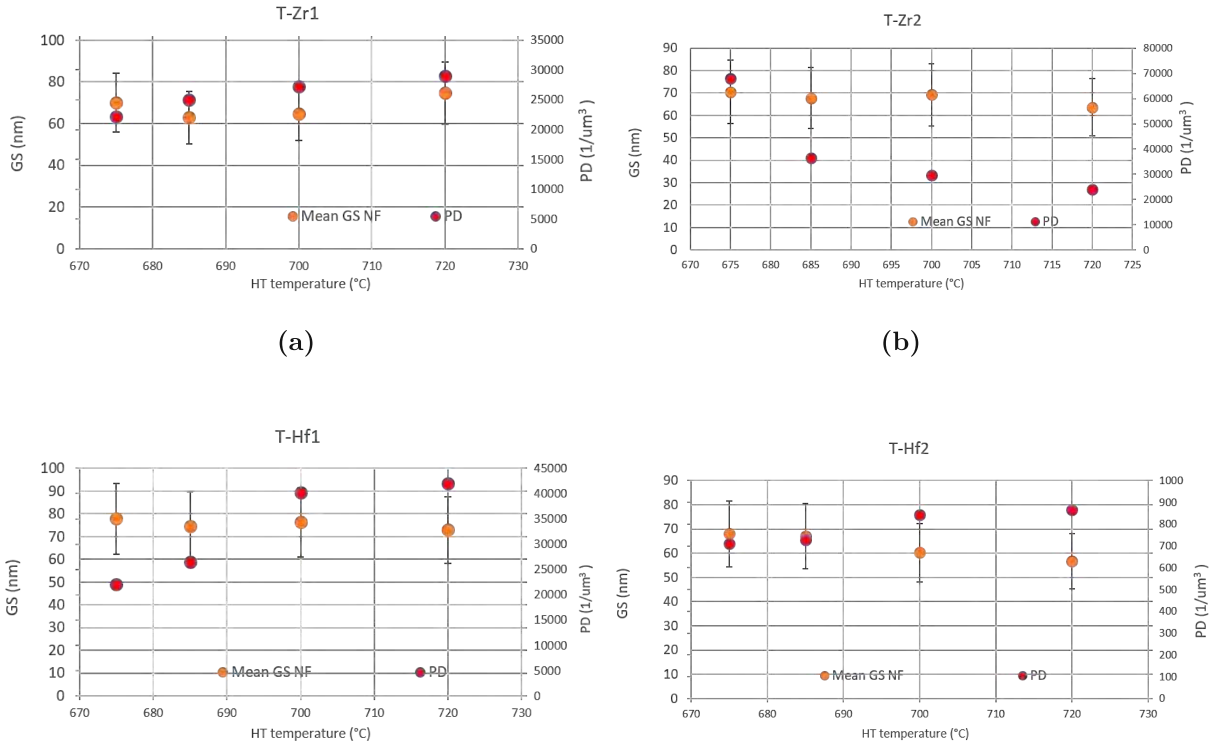

(a) (b)

(c) (d)

**Fig. 4.32:** Number-faction NF grain size GS (orange) and particle density PD (in red) compared for each APC-recipe. The bars reflect the variation along the radius of the filament.

From these plots, a possible indication of decreasing grain size with increasing precipitate density is observable in the Hf-samples. This would be the most expectable behaviour in these strands, since the grain refinement has already shown to be driven by the amount of oxidized elements forming in the matrix [27, 28, 215].
At the same time, to an increasing or lowering PD corresponds a slight increase or decrease of GS in the Zr-based recipes, respectively. Here the trends are less evident than those shown by Hf-based recipes, but can nevertheless be indicative of a different formation/refinement of the precipitates as based on their nucleation properties. At 675°C for example, $ZrO_2$ particles have just a faintly lower standard formation energy (-917 kJ/mol of $O_2$) than $HfO_2$ (-930 kJ/mol),

likely to result in slightly smaller particles and probably higher densities PD, as suggested also in [211].

The impact of such a difference can be sensed also by evaluating the gap in size between mean PS for T-Zr1 and T-Hf1 samples. These recipes are in fact the only ones here comparable on this respect, as they have a very similar initial alloy-structure with same amount of solute element (1 at.%). This is displayed in Fig. 4.33.

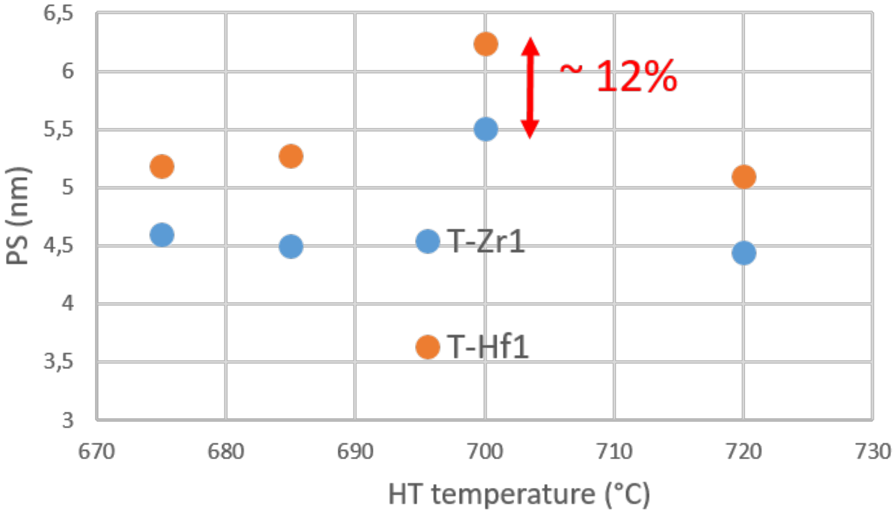

**Fig. 4.33:** Particle size PS (nm) for the T-Zr1 and T-Hf1 recipes. An almost costant gap, between 9% and 12% is visible throughout each representative sample.

This plot shows the PS being in the Hf samples between ≈9 and 12% higher than in the zr samples, which does not experience a reduction nor a boost through the different reaction temperatures.

Another indication of how PP-pinning is weighing in the mixed pinning scenario of these strands can be indirectly sensed by comparing $b_{peak}$ with the values of particle density PD. A good correlation (and high $b_{peak}$ values) would reflect a strong influence on the PP mechanism.

This does not appear the case by analysing Fig. 4.34: here $b_{peak}$ at 4.2 K (when available) and $b_{peak}$ at 10 K are plotted - together with PD - vs reaction time for each APC recipe. An increasing PD corresponds often to a stable, if not decreasing $b_{peak}$.

The latter can be a good indication that, despite all, GB mechanism is still the leading flux pinning mechanism in these superconductors. This evidence needs further analysis, which is provided in Sec. 4.3: in fact, even though the GB "character" seems to prevail in terms of overall highest total $F_p$ contribution, it will be shown that at the operational fields (12 T Hi-Lumi FCC, 16 T hh-FCC) the PP mechanism absolute contributions take over. This is quite remarkable, since rather than just increasing the maximum values at low b, the goal for these strands is to *right-shift* their potential towards higher b.

This could be explained as the rate - and therefore the weight on flux pinning - of formation of (actively pinning) precipitates is slower than the simultaneous grain refinement undergoing in these samples.

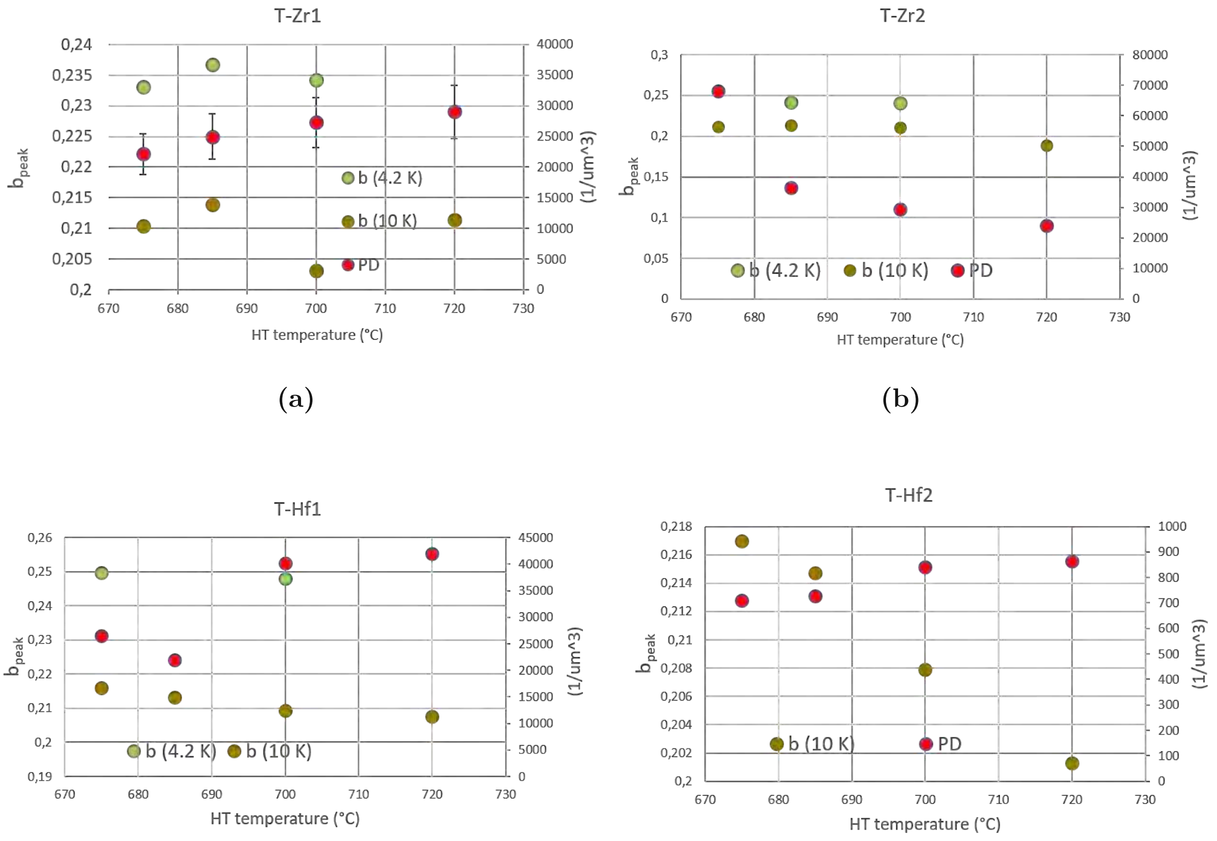

(a) (b)

(c) (d)

**Fig. 4.34:** $b_{peak}$ and particle density PD (in red) compared for each APC-recipe.

### 4.2.2 APC-pinning

Now I would like to discuss the impact of the nanoparticles on pinning as they have been tracked and classified in Sec.4.1.
It is fundamental to remember, as explained by Campbell and Evetts in [30], that the vortex (fluxon) substructure consists essentially of a central cylindrical core region where the superconducting order parameter $\psi$ rises from zero to unity over a distance of the order of $\xi$, and a larger region, again cylindrical, in which circulates the supercurrent vortex necessary to generate just one quantum of flux. For isolated flux lines, the current vortexes are of radii given by $\lambda$.
The two authors also classified what can be considered an effective "flux point-shaped pinner". Indeed, it looks very unlike for any feature having a size PS not comparable to the coherence length $\xi$ to be considered retaining individually any fluxon. The interaction core has the size of $\approx \xi$, being the latter also a function of temperature. The functional dependency $\xi(T)$ is here not deepened as its impact in $Nb_3Sn$ is considered to be minor and not affecting - if not even reinforcing - the forthcoming discussion.

If we consider the small features as tracked and depicted in Fig 4.24 and their eventual projection as depicted in Tab. 4.2, it is therefore difficult to still consider them as core-point pinners.
For each recipe we would observe an average PS of less/much less than 3.5 nm. The latter has to be considered even lower than what calculated in this scenario, as being the smallest features (0.3-0.7 nm) extremely difficult to be accounted by human eye from STEM/HRTEM pictures.

On the other side, $\xi$ is about 3.6 nm at zero temperature (Tab. 1.2) and eventually slightly larger at increasing temperatures. Therefore, it has to be concluded that these landscape of small features should be "invisible" to fluxons as for core interaction, eventually participating to the overall pinning with a different type of mechanism.

If we assume these small features to be pure metals, Dew-Hughes collection of facts indicates them to be good candidates for producing $\Delta\kappa$ pinning. Indeed, if non superconducting metallic particles have a diameter $\leq$ than $\xi$, the proximity effect "will induce them to become superconducting, and their presence can be regarded as producing a change in $\kappa$" [43].
By becoming superconducting, APC are transformed into internal defects of the superconducting phases [39]. Addition of metallic APC in $Nb_3Sn$ wires has been reported also by Tachikawa with Germaium [186] and more recently by Rodrigues with Cu(Sn) nanometric APCs [158].
A significant involvement of "$\Delta\kappa$" pinning mechanism, as expressed in Tab. 1.4 in equation 8, would exhibit as a second local maximum in $F_p$(B), peaking at $b_{peak}$=0.67 [205]. An evidence of a second peak, which would be at a field between 17 and 18 T according to all the measured $B_{irr}$, was not directly observable through the $F_p$ measurements presented in this work. Below 18 T, most of the strands start easily to get thermally unstable, therefore transport current measurements are difficult or not reliable. The only one proof of such a lack of a second peak - which would be eventually beneficial as it shifts the flux retaining potential to higher fields - is observable in the sample T-Hf2-720, which was tested down to 16 T as it is shown in Fig. 4.9a. The absence of $b_{peak}$=0.67 in this specimen motivated therefore the conclusion that this pinning mechanism is not relevant in these samples.

Likewise, a "magnetic" interaction is not possible because the "wavelength" of the microstructure - represented by PS and $l$ - is too small compared to the magnetic penetration depth $\lambda$. In fact, this does not allow the induction B to adjust everywhere to its equilibrium value, thus creating a Bean-Livingston barrier to flux motion at the interface between pin and matrix which would be the cause of pinning [29].

For commodity of the reader and since they will be used for modelling of $F_p$(B) in the next Section, the particle size PS and density PD values as from the "clearly distinguishable case" are here summarized in Tables 4.3 4.4, respectively.

**Tab. 4.3:** Particle size PS (nm) representative values as from the "clearly distinguishable case" in Subsec. 4.1.4. These values are used in Sec. 4.3.

| Sample | 675(°C) | 685 (°C) | 700 (°C) | 720 (°C) |
|---|---|---|---|---|
| T-Zr1 | 4.6 | 4.5 | 5.51 | 4.44 |
| T-Hf1 | 5.19 | 5.27 | 6.24 | 5.1 |
| T-Zr2 | 3.05 | 4.45 | 5.27 | 5.16 |
| T-Hf2 | 4.37 | 4.76 | 4.99 | 4.73 |

As a final remark, it should be noted that both in [158, 186] and more recently in [5] a grain refinement in APC-$Nb_3Sn$ with no oxygen was observed. This is somehow the case also for the T-Hf3 recipe, were Hf is alloyed but no oxidation is provided. In these samples, the mean GS is

**Tab. 4.4:** Particle density PD ($10^{22}/m^3$) representative values as from the "clearly distinguishable case" in Subsec. 4.1.4. These values are used in Sec. 4.3.

| Sample | 675(°C) | 685 (°C) | 700 (°C) | 720 (°C) |
|---|---|---|---|---|
| T-Zr1 | 2.26 | 2.55 | 2.73 | 2.90 |
| T-Hf1 | 2.25 | 2.65 | 4.01 | 4.20 |
| T-Zr2 | 6.80 | 3.64 | 2.95 | 2.41 |
| T-Hf2 | 0.071 | 0.073 | 0.084 | 0.087 |

lowered by at least 20% if compared to the reference PIT-R sample (also ternary).
The mechanism involved in this smaller formation of grains while a vast amount of nanometric-dispersed metals is included in the matrix is not here further discussed, being it eventually part of a future investigation.

## 4.3 Pinning Models

In this section several aspects of the flux pinning involved in the studied specimens are discussed.

So far, compositional gradients in the A15 have been included only to some extend in modelling of the pinning forces (e.g. [15, 16, 187]). It is in fact known by now that critical temperature distributions $T_c$(r), as often being related with Sn gradients, do affect the other superconducting properties as well as the models predicting them. What we measure e.g. by current transport measurements as being the representative - macroscopic - $J_c$ is actually resulting from a more complex distributions of $J_c$(r).
The upper critical field $H_{c2}$ is affected by local variations in $T_c$, correlating e.g. with Sn content $\beta$ as it is shown in eq. 3.18. As for any formulation of the pinning force $F_p$(B) as in Tab.1.4 and, in our specific case eq.1.16, the impact of $H_{c2}$(T) on the overall strength of pinning has to be taken into account, especially in highly doped superconductors where several substitutions (of ternary/quaternary elements) to the occupancy sites are made (both to Nb and Sn, as recently demonstrated in [95]).

In particular, a literature gap is present to date regarding critical temperature distributions and/or A15 inhomogeneities affecting $F_p$(B) for the APC-Nb$_3$Sn multi-filamentary manufacturing technology.
For this reason, an analysis was conducted in this Thesis on five samples, namely B-Zr1, B-Zr2, T-Zr1-675, T-Zr1-685 and PIT-R. The non-Cu $J_c$ of these samples is displayed in Fig. 4.12. For fitting of low-to-high field $J_c$ data, the following equation was used:

$$F_p^{fit}(B) = C \cdot \left(\frac{B}{B_{c2}}\right)^p \cdot \left(1 - \frac{B}{B_{c2}}\right)^q \tag{4.11}$$

, not meaning to be representative of any of the involved pinning mechanisms but only for interpolating realistic values in the mid-field range. In eq. 4.11 the parameters C, p and q were left as free parameters and summarized in Tab. 4.5. In the latter, also $B_{c2}$ and $T_c$ values of the specimens are displayed. The first are measured as explained in Subsec. 3.5.3 and identified at $\rho$=0.9$\rho_{normal\ state}$. Extrapolation to 4.2 K of $B_{c2}$ is provided by using the following fit to the Werthamer–Helfand–Hohenberg (WHH) temperature dependence [98, 99, 198]:

$$\begin{aligned} WHH(t) &= 1 - t - C_1(1-t)^2 - C_2(1-t)^4, \\ B_{c2}(t) &= B_{c2}(0) \cdot \left(\frac{WHH(t)}{WHH(0)}\right) \end{aligned} \tag{4.12}$$

where C$_1$ and C$_2$ were set to 0.153 and 0.152 respectively, as these values were found to be a good approximation of the WHH dirty limit temperature dependence [12]. $T_c$ values are instead evaluated as explained in Subsec. 3.5.5.

**Tab. 4.5:** $B_{c2}$, $T_c$ and non-Cu $J_c$ fit parameters
Published by *Ortino et al., SUST 2021* [148]

| Type | $B_{c2}$(4.2 K) (T) | $T_c$ (K) | C (GN/m$^3$) | p | q |
|---|---|---|---|---|---|
| B-Zr1 | 22.1 | 17.31 | 161 | 0.70 | 2.43 |
| B-Zr2 | 22.3 | 17.28 | 145 | 0.63 | 2.19 |
| T-Zr1-675 | 27.0 | 17.46 | 153 | 0.71 | 2.36 |
| T-Zr2-685 | 27.1 | 17.63 | 167 | 0.63 | 1.97 |
| PIT-R | 26.5 | 17.66 | 82.5 | 0.51 | 2.63 |

A deeper evaluation of the radial evolution of $T_c$ was conducted by means of AC-susceptibility, EDX and and Scanning Hall Probe methods following the procedures explained in Subsection 3.5.5, Subsection 3.5.6 and Subsection 3.5.7, respectively.

Such an analysis can be seen in Fig. 4.35, where the critical temperature distributions $T_c$(r) are shown as a function of the relative position between the coarse grain region (close to the Sn-core) and the external Nb-barrier. The shown data are resulting from AC-susceptibility, while SHPM measurements (the latter provides less data point than the former), between which the relative difference was always less than 4%. All specimens show an approximately linear decrease in $T_c$ for 0.2$\leq r \leq$0.75 - where a linear fit is applied - before reaching a fall-off close to the barrier.

The gradients stay in the range of usual PIT strands (around 0.1 K/$\mu$m), with the best result achieved with the B-Zr1 wire. This is an indication that the oxygen diffusion (therefore the precipitates formation) does not interfere with the standard sequence of the phases formation, during the heat treatment, in the PIT-APC technology.

These results from magnetometry were cross-checked by comparing to results from SEM EDX, whose results from EDX are summarized in Fig. 4.36.

$T_c$(r) values were converted into Sn content $\beta$ by using the model proposed by Godeke as in eq. 3.17. The adjustments provided to this formulation - extending its validity also to ternary specimens - $T_c^{MAX} = 18.5$ K , $T_c(\beta = 25.5) = 18.25$ K, $T_c^{min} = 6.29$ K - are in good agreement

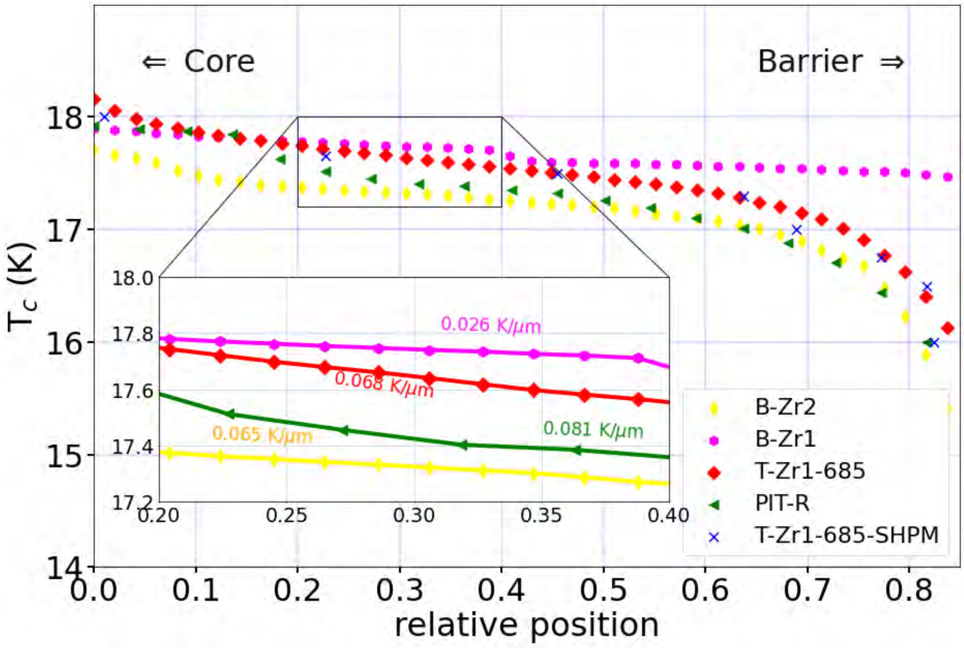

**Fig. 4.35:** $T_c$(r) distributions from AC-susceptibility for two binary APC, one ternary APC and one commercial ternary-PIT wire. SHPM data are shown for the sample T-Zr1-685, being in good agreement with AC susceptibility. Data are shown as a function of the relative position between the Sn-core and external Nb-barrier (this width varied on average between 10-12 $\mu$m between the samples).
Published by *Ortino et al., SUST 2021* [148]

with the values observed in $T_c$ and measurements on the examined ternary samples.
Table 4.6 demonstrates that the results from EDX are in a general agreement with the magnetometry data, confirming that Ta additions in APCs do not worsen the phase homogeneity more than what we observe in commercial Ta-doped PIT wires. Moreover, recent works based on EDS measurements [209] show that internally-oxidized $Nb_3Sn$ has indeed higher Sn at.% than standard non-oxidized $Nb_3Sn$, which is consistent with the findings in this thesis.
The codes MAG and EDX stay for "magnetometry" and "Energy dispersive x-rays spectroscopy" respectively. The effects of the composition gradients were included in the calculation of the

**Tab. 4.6:** Maximum Sn content and concentration gradients of three selected samples.
Published by *Ortino et al., SUST 2021* [148]

| Sample | $\beta_{max}$ [at.%] | Sn gradient-MAG [at.%/$\mu$m] | Sn gradient-EDS [at.%/$\mu$m] |
|---|---|---|---|
| B-Zr1 | 24.4 | 0.075 | 0.07 |
| T-Zr1-685 | 25.1 | 0.105 | 0.11 |
| PIT-R | 24.5 | 0.095 | 0.10 |

weights of the pinning mechanisms involved at 4.2 K,.
To do so, the algorithm proposed by Baumgartner in [15] was used, focusing on the samples

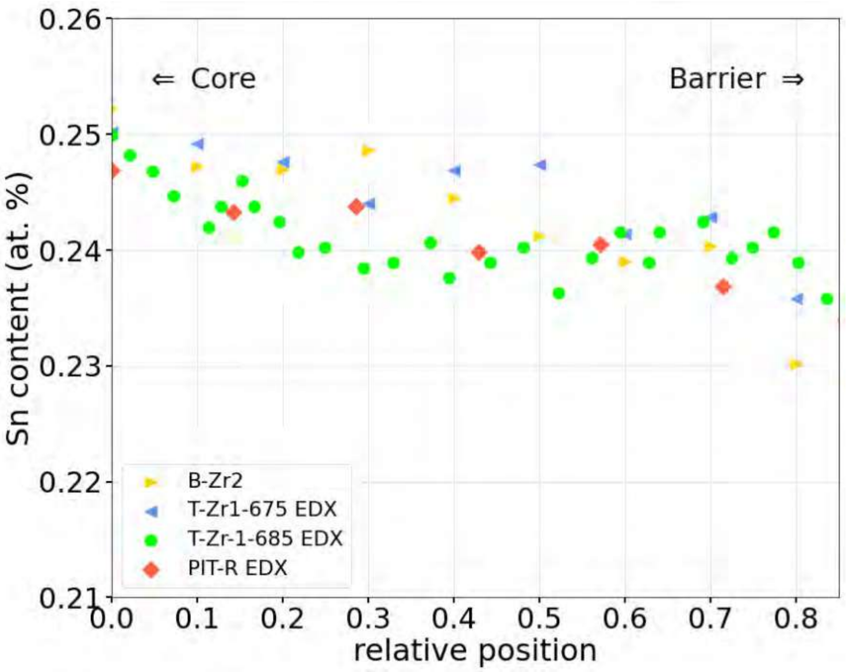

**Fig. 4.36:** Sn gradients from EDX measurements for two binary APC, one ternary APC and one commercial ternary-PIT wire. Data are shown as a function of the relative position between the Sn-core and external Nb-barrier.

B-Zr1 and T-Zr-685. In these simulations, the assumptions are the same as explained in Subsec. 3.5.5: all sub-elements assumed to be identical parallel tubes with same geometry, composition and radial Sn gradient (with the highest value on the inside).

The filaments are divided into concentric shells, assigning values for the Sn content to each of them. These profiles were taken from the experimental $\beta$ as outputs of the magnetometry measurements, represented by $\beta_{max}$ - the maximum Sn content in the filament - and the concentration gradient $\Delta\beta$ of the linear-fit region.

The binary B-Zr1 has $\beta_{max}$= 24.45 and $\Delta\beta$=0.6 at%, corresponding to a gradient of 0.075 at%/$\mu$m in the linear region (4.6); the ternary has instead $\beta_{max}$= 25.1 at% and $\Delta\beta$=0.8 at%, corresponding to a gradient of 0.11 at.%/$\mu$m in the linear region. T$_c(\beta)$ and B$_{c2}(\beta)$ of each shell are then calculated based on their Sn content $\beta$ as described in equations 3.17 and 4.12.

In this way, a "map" of local $B_{c2}$ and $T_c$ values is ascribed to each shell.

$J_c$(T, B) of each current carrying element is then computed based on its $T_c(\beta)$ and $B_{c2}(\beta)$ using the Unified Scaling Law (USL) [51–53], where the strain and temperature dependences were omitted since their influence on the pinning scaling behaviour were beyond the scope of this work:

$$F_p(b) = F_{p-max} f(b) \tag{4.13}$$

where $F_{p\text{-}max}$ is the maximum volume pinning force (peak of $F_p$(B,T)). Equation 4.13 is used for simulating the pinning forces in pure GB and PP scenarios, separately. For this purpose, the field dependence $f(b)$ was modelled as follows:

$$\begin{aligned} f(b) &= 3.49\ b^{p_1}(1-b)^{q_1} \qquad (GB) \\ f(b) &= 6.75\ b^{p_2}(1-b)^{q_2} \qquad (PP) \end{aligned} \tag{4.14}$$

where $b = B/B_{c2}(\beta)$, $p_1$=0.5, $p_2$=1 and $q_1$=$q_2$=2.
Once obtained the critical current of each shell, the final $J_c$values are computed ("$J_c^{GB}$" for GB and "$J_c^{PP}$" for PP mechanisms, independently), as they would be measured in the respective experiment: for simulations of transport measurements by summing the currents in all elements and dividing by the filament cross section; for magnetometry, the magnetic moment generated by shells currents in increasing and in decreasing applied field is computed, then $J_c$ is obtained from the resulting irreversible moment. The two simulations give similar results, so only magnetometry-based simulations are used for the following.
The simulated $J_c^{GB}$ and $J_c^{PP}$ profiles are then multiplied with B and fitted with equation 4.11 to extract the proper pinning exponents ($p_1$*,$q_1$*, $p_2$*, $q_2$*). The results of this fitting procedure are summarized in Table 4.7.
Finally, the experimental pinning forces are fitted as follows:

$$F_p^{exp}(B) = F_{p-max}^{fit} \cdot \left( C_1\ N_{GB}\ \left(\frac{B}{B_{c2}}\right)^{p_1*} \left(1-\frac{B}{B_{c2}}\right)^{q_1*} + (1-C_1)\ N_{PP}\ \left(\frac{B}{B_{c2}}\right)^{p_2*} \left(1-\frac{B}{B_{c2}}\right)^{q_2*} \right) \tag{4.15}$$

where $F_{p-max}^{fit}$ and $C_1$ are left as free parameters.
The exponents $p_1$*,$q_1$*, $p_2$*, $q_2$* reflect the values predicted by Dew-Hughes corrected for the influence of the observed Sn gradients. In the main brackets, the left term refers to the grain-boundary (GB) pinning contribution, and the right one to the point-pinning (PP) mechanism. The pre-factors $N_{GB}$ and $N_{PP}$ are used for normalizing the peak in the field dependencies to one. The output of such a fitting procedure is shown in Figure 4.37.

Here "bin" refers to the binary B-Zr1, "ter" to the T-Zr1-685 wire, "exp" to the experimental points, "fit" to the applied fit and "homog" to the simulated ternary wire neglecting radial inhomogeneities. Moreover, the grain-boundary (GB) and point-pinning (PP) curves (as components of the total $F_p$(B)) are shown individually for both wires.

The input and output parameters used in this fitting procedure are listed in Table 4.7.
The GB and PP "factors" are referring to $C_1$ and (1-$C_1$) in equation 4.15, representing how much the respective pinning character is contributing to the fitted $F_p$(B). In particular, a focus was on the evaluation of the absolute $F_p$ at specific fields, 12 and 16 T, namely the operational points of the HiLuminosity-LHC and FCC-hh dipole magnets (vertical lines in Figure 4.37). Here, the dashed and dotted lines represent the single $F_p$(B) of GB and PP pinning mechanisms in both samples. At 12 T, the binary wire has a $F_p$(B) of 5.74x$10^{10}$(N/$m^3$), split in a 60%-40% contribution of GB- and PP-pinning.
These numbers change in T-Zr1-685, showing a lower participation of the precipitates below ≃10 T, after which the PP contribution takes over. The weight of the PP mechanism increases indeed more at 16 T: B-Zr1 shows 53.6% of GB and 46.4% of PP-pinning, while T-Zr1-685 exceeds the 50-50 scenario (43.7% GB and 56.3% PP-pinning).

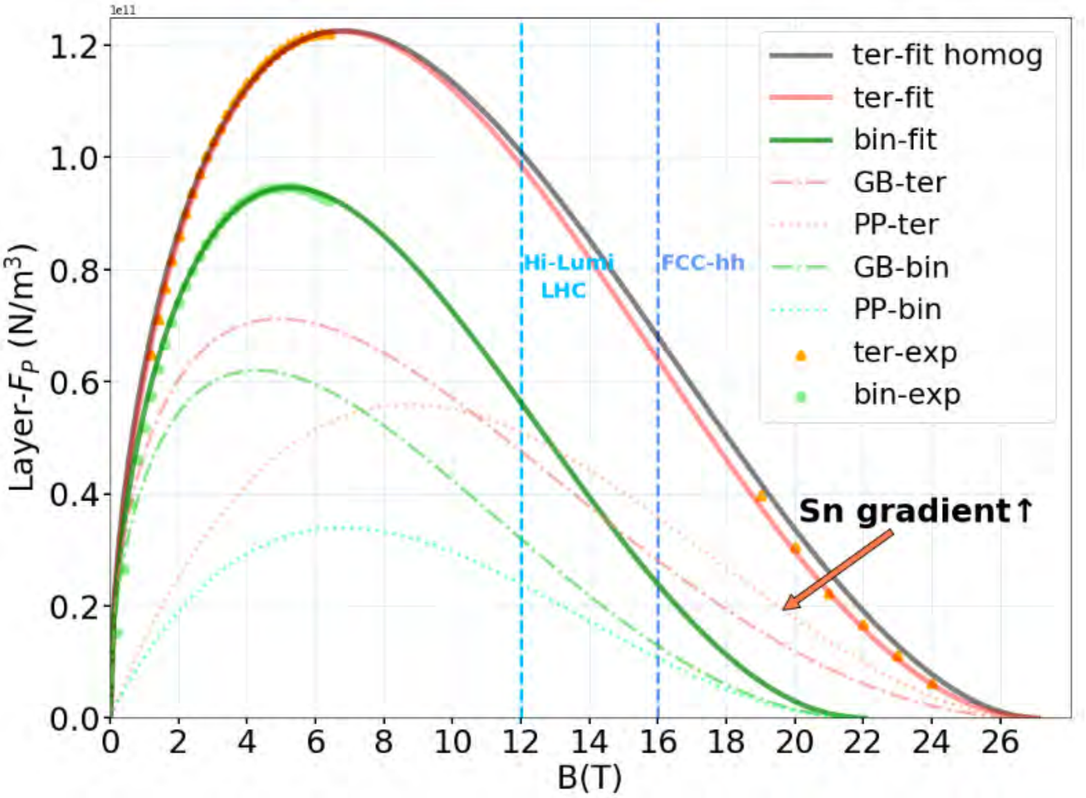

**Fig. 4.37:** Layer-$F_p$(B) at 4.2K as an output of the simulated $J_c$ accounting for the experimental Sn gradient in both generations of APC wires ("ter" stays for ternary T-Zr1-685 and "bin" for binary B-Zr1). The weights of the two pinning contributions were obtained by fitting the experimental data (dots).
Published by *Ortino et al., SUST 2021* [148]

As a further conclusion, a reliable allocation of these percentages requires the specific (experimental) Sn concentration gradient and can't be univocally determined otherwise. In fact, by looking at the black solid line "ter-fit homog" in Figure 4.37, it seems clear that it is impossible to get a perfect fit if one neglects inhomogeneities. This curve represents the fit to the experimental data of the T-Zr1-685 wire without including Sn composition gradients: experimental $F_p$(B) are simply fitted via Equation 4.14. In this case, the currents in the high-field region (from 10 T on) are clearly overestimated, most probably due to a decrease of the exponent q from the real case as already shown in [15]. The weights (so the absolute values) of the single pinning mechanisms involved change by including Sn concentration gradients that are strictly necessary to get valuable estimations of the pinning forces above 10 T.

This modelling motivated a further attempt of identifying the main key parameters within the Dew-Huges formulations (Tab. 1.4) able to depict at best the flux pinning in the APCs.
As for convenience, the simplest summation between GB-pinning and PP-pinning is here repeated from eq.1.16 by also adding the afore-omitted pinning-efficiencies terms for both mechanisms: $\eta_{GB}$ and $\eta_{PP}$, respectively defined for GB pinning and PP pinning.

**Tab. 4.7:** Parameters of the fitting procedure.
Published by *Ortino et al., SUST 2021* [148]

| Sample | B-Zr1 | T-Zr1-685 |
|---|---|---|
| $p_1$*, $q_1$* (GB) | 0.49;2.07 | 0.48 ; 2.16 |
| $p_2$*, $q_2$* (GB) | 0.95;2.13 | 0.98 ; 2.06 |
| $F_{p-max}^{fit}$(N/m$^3$) | 9.7x10$^{10}$ | 1.27x10$^{11}$ |
| GB-factor ($C_1$) [%] | 65 | 56 |
| PP-factor (1-$C_1$)[%] | 35 | 44 |
| b (HiLumi-LHC) | 0.543 | 0.44 |
| b (FCC-hh) | 0.724 | 0.588 |
| $F_p^{GB}$(HiLumi-LHC) [N/m$^3$] | 3.2x10$^{10}$ | 4.76x10$^{10}$ |
| $F_p^{PP}$(HiLumi-LHC) [N/m$^3$] | 2.54x10$^{10}$ | 5.09x10$^{10}$ |
| $F_p^{GB}$(FCC-hh) [N/m$^3$] | 1.35x10$^{10}$ | 2.85x10$^{10}$ |
| $F_p^{PP}$(FCC-hh) [N/m$^3$] | 1.15x10$^{10}$ | 3.58x10$^{10}$ |

$$F_p(H) = \eta_{GB}\frac{\mu_0 S_v H_{c2}^2 h^{1/2}(1-h)^2}{4\kappa^2} + \eta_{PP}\frac{\mu_0 V_f H_{c2}^2 h(1-h)^2}{4.64\ PS\ \kappa^2} \tag{4.16}$$

It is now possible to discuss, as a first point, the historic role of $H_{c2}$ in Dew Hughes modelling of $F_p$(B).
Is it correct to still consider $H_{c2}$ as being the field at which the very last fluxon gets unpinned? The - undesired - ambiguity is raised by the same Dew-Hughes in his 1974 paper, where it is said that "$F_p$(B) must return to zero at B=$\mu_0 H_{c2}$ where, by definition, $J_c$=0".
We now know, after the discovery of HTSs in late '80s, that there is a clear and - sometimes- huge difference between the field at which $J_c$=0 and $H_{c2}$ [131]. Nowadays it is also widely accepted that an irreversibility field $B_{irr}$ exists below the line of the upper critical field $B_{c2}$ and that $J_c$ disappears at or just above $B_{irr}$, which is 0.85$B_{c2}$ or more, in metallic superconductors [179]. The difference was indeed made clear by experiments on HTS, where it is now established that the difference between these two field lines can even be several tens of Teslas.
In our case, by comparing the values in the first column of Tab. 4.5 with Fig. 4.13a, it appears clear how the gap between $B_{c2}$ and $B_{irr}$ can vary between 0.7 and more than 1 T, as for example the T-Zr1-685 sample where this gap is ≈1.25.
In light of the above elucidated modelling of the inhomogeneities, it is legit to think that this gap - at least for A15 superconductors - can be due to compositional variations and that can be modelled, as proposed in this thesis. By using $B_{irr}$ in place of $B_{c2}$, a very good agreement is indeed obtained with the experimental data in Fig. 4.37, perfectly interpolating the high-field $J_c$ values of the T-Zr1 sample. The same was used for for fitting all the remaining specimens, by using eq. 4.16, as it is visible in Figures. 4.41 and 4.42.

Before discussing the other aspects of eq. 4.16, it is useful to stress out some of the limits of these formulations for APC-Nb$_3$Sn, as they do not match with the experimental data.
As explained in Sec. 1.4, equation 4.16 is a simple summation of equation 5 and 7 from Tab. 1.4 (right column). In the left term (equation 5) we have $S_v = 1/\mathrm{GS}$, being it the total grain boundary area per unit volume involved into the pinning process, while $\kappa$ is the Ginzburg-Landau parameter.
The right term (equation 7) refers to the "core-point pinning" mechanism, occurring when the defect or precipitate dimensions are in all directions less than the inter flux line spacing, showing $b_{peak} = 0.33$. $V_f = (PS/l)^3$ is the fraction of the precipitates which are actively pinning in a rigid lattice, where PS is the precipitate size (referred as $a$ in Sec. 1.4) and $l$ is the average distance between the precipitates.

Considering $l$ to be $\simeq (PD)^{-1/3}$ - where PD is the precipitates density - and $\kappa = H_{c2}/\sqrt{2}H_c$ - with $H_c$ assumed to be constant for simplicity - as proposed in [128], the following ratios can be obtained by dividing the two terms (or by dividing eq. 5 and 7 form Tab. 1.4):

$$\frac{F_{p-max}^{GB-TER}}{F_{p-max}^{GB-BIN}} \simeq \frac{GS^{BIN}}{GS^{TER}} \cdot \frac{f_p^{GB-TER}(b_{peak})}{f_p^{GB-BIN}(b_{peak})} \tag{4.17}$$

$$\frac{F_{p-max}^{PP-TER}}{F_{p-max}^{PP-BIN}} \simeq \left(\frac{PS^{TER}}{PS^{BIN}}\right)^2 \cdot \frac{PD^{TER}}{PD^{BIN}} \cdot \frac{f_p^{PP-TER}(b_{peak})}{f_p^{PP-BIN}(b_{peak})} \tag{4.18}$$

where $F_{p\text{-}max}$ refers to the maximum value of $F_p$(B), "TER" to the ternary T-Zr1-685 and "BIN" to the binary B-Zr1 sample. From equations 4.17 and 4.18 we can see that GS and PD have a linear impact on how $F_p$(B) scales between the two generations, while it is quadratic for PS. If a direct summation of GB and PP mechanisms was valid, the change in these properties from the binary to the ternary generation should lead to what is depicted in Figure 4.38. In fact, by varying $H_{c2}$, $S_v$ and $V_f$ as experimentally reported, the model foresees a twofold relevant increase, with a $F_{p-max}^{GB} \simeq 60\%$ higher and a $F_{p-max}^{PP} \simeq 300\%$ higher in the ternary than in the binary case.

This result is in contrast with the experimental evidence as it is clear from figure 4.14a, where this two-fold increase in $F_{p\text{-}max}$ is not visible ($\mathrm{F}_{p-max}^{-TER}=$ is only 20% higher than $\mathrm{F}_{p-max}^{-BIN}$). However, several pronounced shifts of $b_{peak}$ toward the predicted 0.265 are observable in other samples from plot 4.14a, with the highest value being $\approx 0.25$ measured in the T-Hf1-675 wire: the experimentally measured value could be reduced by the A-15 inhomogeneities which cause $b_{peak}$ to be shifted to lower values [15].
These last evidences, even though strongly indicating the precipitates to act as point-pinners according to the Dew Hughes theory, still leave the suspicion of some sacrifice of a pinning mechanism in favour of the other one.

The comparisons with experimental data provided by 60s-70s papers [20, 56, 110] did not reveal how accurate - quantitatively - were these collections of predicting formulae (as in Tab. 1.4, the authors rather assessed how f(b) was reflecting - quite well indeed - the expected behaviour

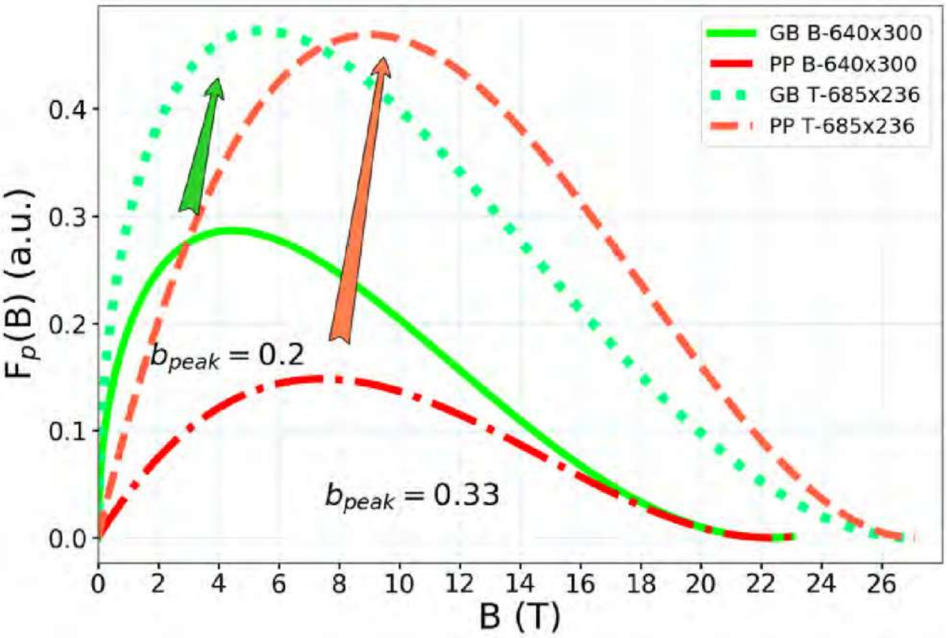

**Fig. 4.38:** $F_p$(B) increase according to Dew Hughes theory from binary to ternary generation, where $F_p^{GB}$(B) is in green (GB=grain boundary pinning) and $F_p^{PP}$(B) (PP=point-particle pinning) in red. $H_{c2}$, $S_v$ and $V_f$ are the experimental values.
Published by *Ortino et al., SUST 2021* [148]

of samples with known microstructure).
Sticking for example to the case of constant maximum pinning efficiencies $\eta_{GB}$=1/ $\eta_{PP}$=1 [42], the simple summation as in Eq. 4.16 clearly does not fit any of the experimental set of data. By using AF-GS and NF-GS, $F_{p\text{-}max}$ predicted values are found to be ≈ 2 to 4 times higher, respectively, than the experimentally measured. This is shown in Figures 4.39 and 4.40 for the T-Zr2-700 sample, the latter being particularly interesting as it shows a remarkable difference between NF-GS and AF-GS, as in Fig. 4.24c.

Since the $F_{p\text{-}max}$ gap is larger by using NF-GS, the grain size in $S_v$ looks to be better described by the AF-statistic representative GS, while the point-particle size PS and density PD are definitely better represented by the "clearly distinguishable features" case (much lower PS/higher PD as in the "any feature" case completely overestimated $F_p$(B) ).

Some assumptions and/or replacements to eq. 4.16 were made:

- The experimentally measured $H_{irr}$ in place of $H_{c2}$, for the reasons above discussed. This also introduces- to some extend - the influence of compositional gradients along the filament radius;
- $V_f = (PS/l)^n$ with n=3 is kept at a first glance: this circumstance would reflect a completely rigid FLL according to Dew Hughes. This should not be the real picture, as the fluxons have some degree of elasticity and are expected to eventually bend over several pinning centres [25];

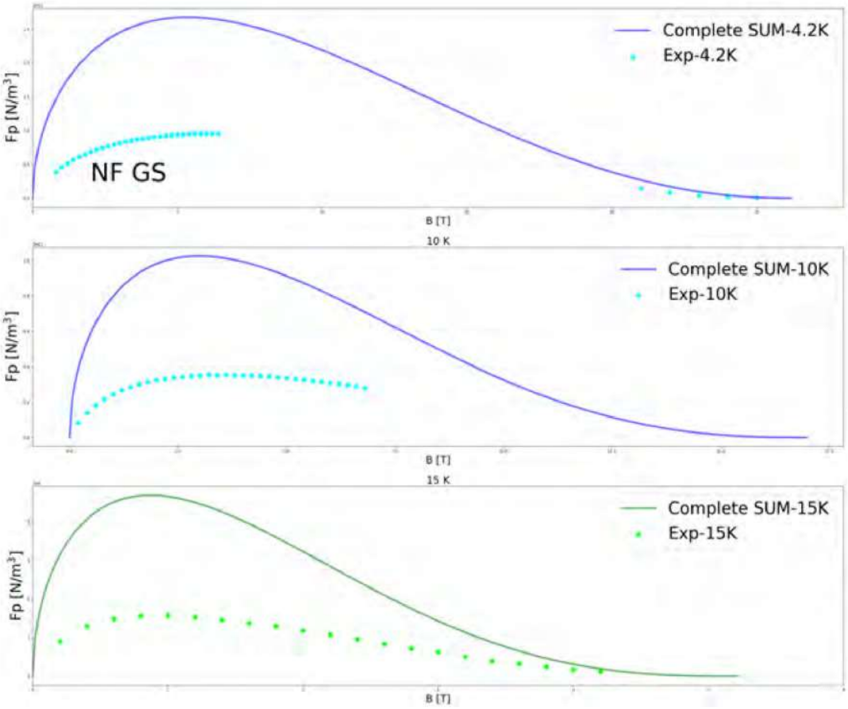

**Fig. 4.39:** Layer-$F_p$(B) experimental dataset for the sample T-Zr2-700 at 4.2K, 10 K and 15 K fitted with eq. 4.16. $S_v$=1/NF-GS, $\eta_{GB}$ and $\eta_{PP}$ are left =1.

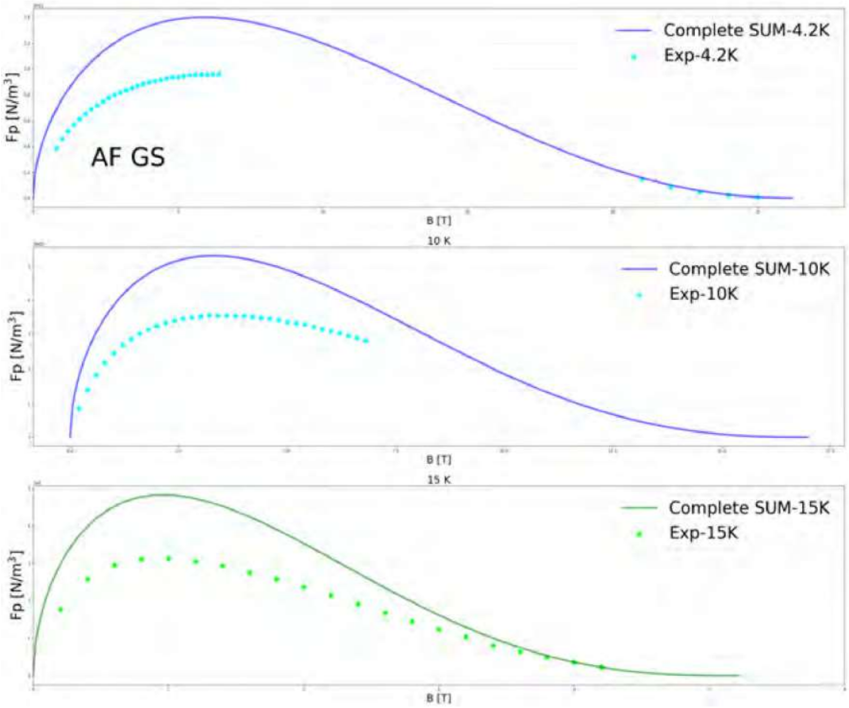

**Fig. 4.40:** Layer-$F_p$(B) experimental dataset for the sample T-Zr2-700 at 4.2K, 10 K and 15 K fitted with eq. 4.16. $S_v$=1/AF-GS, $\eta_{GB}$ and $\eta_{PP}$ are left =1.

Some additional fitting attempts are shown in Figures 4.41 and 4.42, for the T-Zr1-700 and T-Zr2-700 samples, respectively.

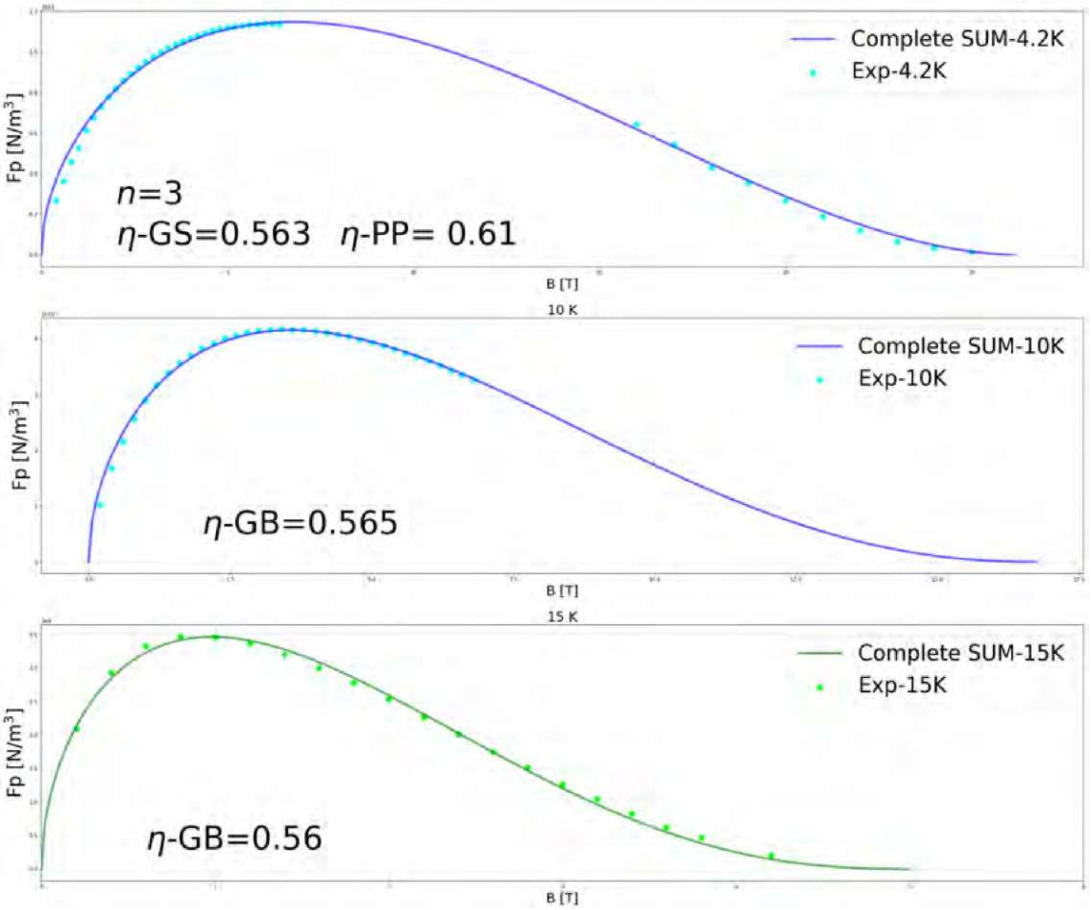

**Fig. 4.41:** Layer-$F_p$(B) experimental dataset for the sample T-Zr1-700 at 4.2K, 10 K and 15 K fitted with eq. 4.16. $\eta_{GB}$ and $\eta_{PP}$ are left as a free parameter.

In these plots, $F_p$(B) experimental data are fitted at 4.2 K, 10 K and 15 K for the T-Zr1-700 and T-Zr2-700 samples, taken as examples.

The grain-boundary and point-pinning efficiencies $\eta_{GB}$ and $\eta_{PP}$, as introduced in Sec. 1.4, were now left as free parameters. All the other parameters come instead from the just described choices among the experimental data (when available, at 4.2 K as well).

In these plots, two similar samples (both T-Zr1 and T-Zr2 are ternary Zr-doped recipes with only different Nb/Sn/Cu ratios), reacted at the same temperature (and almost same timing, 69 hours vs 71 hours) are compared. PS and PD are indeed very similar: 5.55-5.27 nm (PS) and 2.8-2.95 $10^{22}$ 1/m$^3$ (PD), respectively.

The $\eta_{GB}$ values from fit stabilize around 0.4-0.6 for each sample, eventually slightly decreasing by fitting at higher temperatures (as it is visible from 4.2 K to 15 K in Figures 4.41 and 4.42). Assigning a satisfactory meaning to $\eta_{GB}$ is not easy, since separating its weight from the rigidity degree of the lattice is at this stage not possible, nor it is possible to define if a pinning-degradation term - e.g. as possible result of a "too dense" microstructure - is somehow hidden behind it.

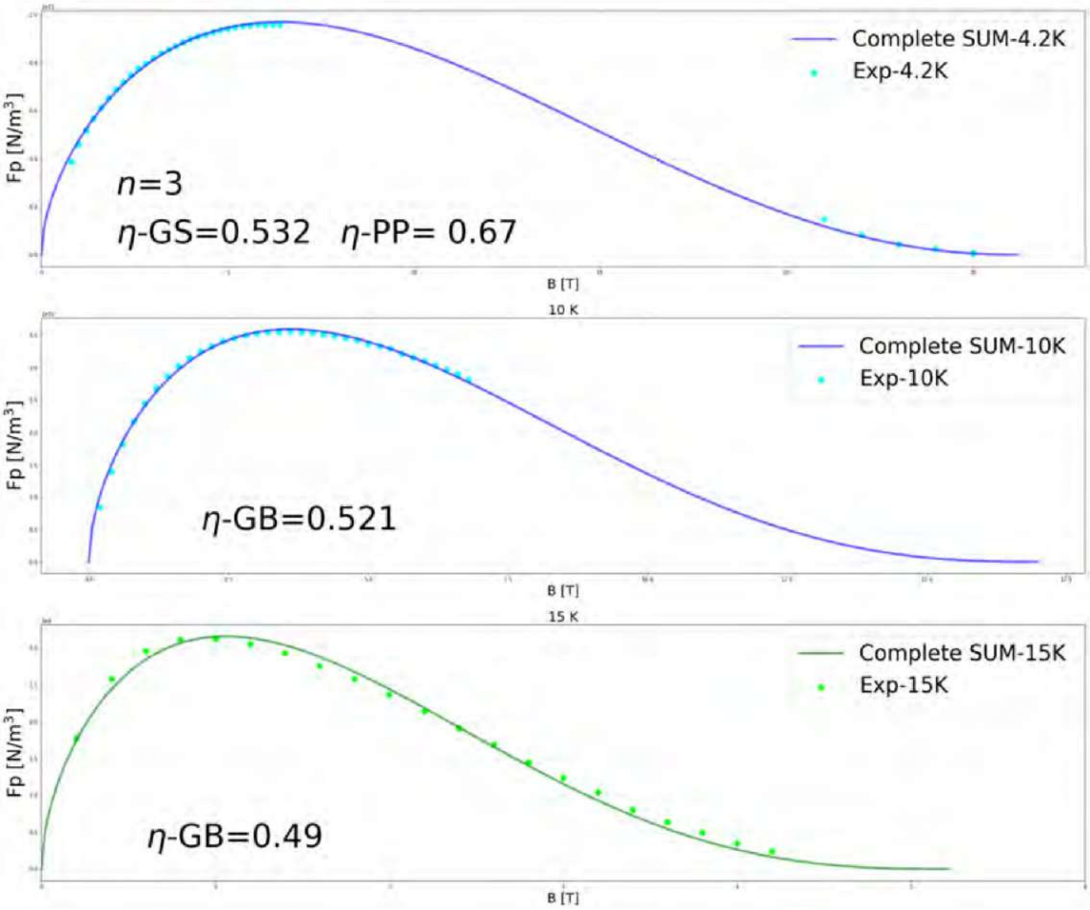

**Fig. 4.42:** Layer-$F_p$(B) experimental dataset for the sample T-Zr2-700 at 4.2K, 10 K and 15 K fitted with eq. 4.16. $\eta_{GB}$ and $\eta_{PP}$ are left as a free parameter.

Contrarily to $\eta_{GB}$, $\eta_{PP}$ showed a much lower impact as on the absolute values of $F_{p\text{-}max}$. Likewise Fig. 4.41 and 4.42, several fits were produced with $\eta_{PP}$ as a free parameter, eventually finding a trend depending on the size of the precipitates PS rather than their density PD. In fact, by still keeping the exponent $n$=3 (in $V_f = (PS/l)^n$), the majority of the fits resulted in relatively low-impact $\eta_{PP}$ (between unity and 0.7), whose weight on $F_p$(B) is more reflecting at higher fields than $\eta_{GB}$. These results were changing with increasing PS, eventually resulting in higher-impacting $\eta_{PP}$ (0.6-0.3).
Fig. 4.43 shows the collection of $\eta_{PP}$ vs PS values as a result of the fits provided above, over 14 samples (including the two binary APC).

$\eta_{PP}$ dependency to any of the other terms in Eq. 4.16 appears less evident, as e.g it seems to be less correlated with the particle density PD. This conclusion is driven by the fact that, as for the samples analysed in this work, to a smaller representative PS it was not always corresponding a higher PD, and viceversa (cf. Figures 4.20, 4.21, 4.22, 4.23). Some of the samples within the 3.5-4.5 nm size-range in Fig. 4.43 have in fact similar PD values as the ones with higher PS (but lower efficiency). In Fig. 4.43 the interpolating equation is displayed as well. The latter has the form of $\eta_{PP}\simeq$3.6 over PS, where the term at numerator (nm) extremely resembles the size of the coherence length $\xi$. Further investigations on different type of point-pinners are needed in order to confirm/deny the above expressed formulation, but still the opportunity of such a simple hy-

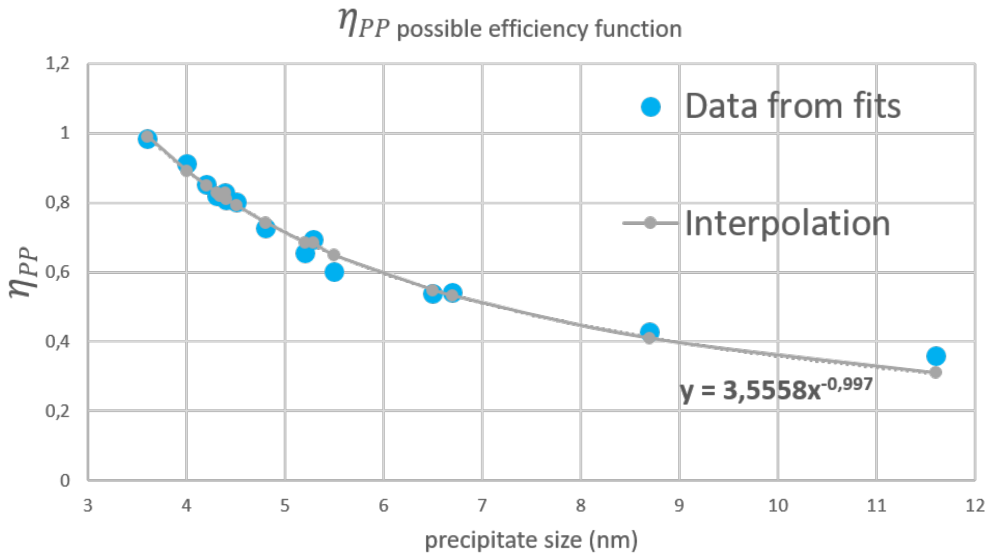

**Fig. 4.43:** $\eta_{PP}$ values as an output of the fits provided with Eq. 4.16. The values are interpolated with a hyperbolic function, displayed on the chart.

perbolic dependency with the mean PS remains charming and surely interesting for further studies.

A possible interpretation of $\eta_{PP}$ is here proposed. If we keep assuming for simplicity the point-pinners to be small spheres of diameter=PS, when a fluxon is pinned in its core by them (core dimension $\simeq \xi$) it is possible to depict three type of scenarios as in Fig. 4.44.

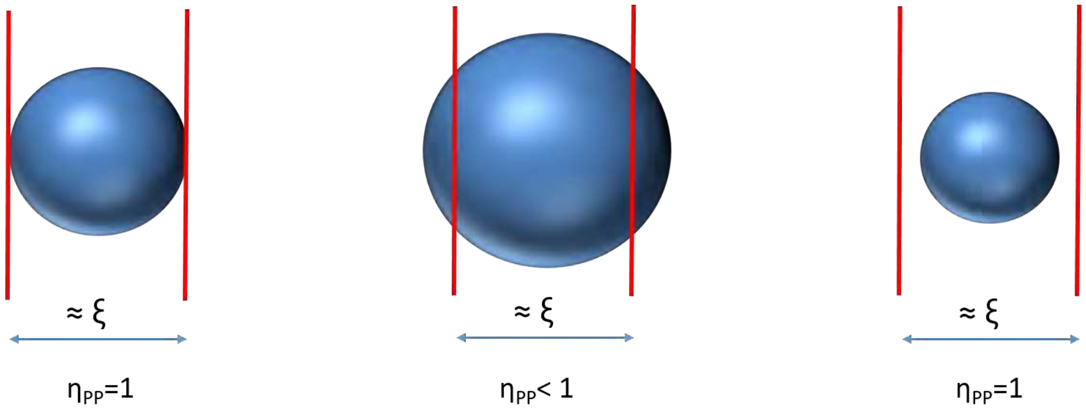

**Fig. 4.44:** Possible interpretation of $\eta_{PP}$ mechanism with varying PS of the precipitates. The fluxon core-size is displayed, together with the efficiency value associated.

The latter shows the precipitate to possibly have PS (diameter) larger, lower or of the same size of the fluxon core. The core-interacting length scales with the diameter, being it maximized when the core size exactly matches the precipitate size (PS=$\xi$, leftmost picture). In the same way, if PS exceeds the core size, some of the potential pinning surface - so the pinning potential - related with the precipitate is not deployed, meaning a lowering of the pinning efficiency.

To some extend, this would mean that a PS optimum could be found towards point-particle PP pinning full exploitability. By impacting on $\eta_{PP}$, the biggest precipitates could be as unexploitable as the very small ones (PS$\ll \xi$) - as elucidated in Sec. 4.2. Finally, if PS is $< \xi$, again the $\eta_{PP}$=1 scenario has to be considered, as the point-pinner should not retain the flux line any differently from what we saw if PS $\simeq \xi$.
This evaluations came by keeping $n$=3 in $V_f = (PS/l)^n$, with varying $\eta_{PP}$. In this respect, it should be noted that the just discussed fitting results (and interpretation) can be due to variations of the elasticity conditions of the lattice rather than a PP pinning efficiency. As being field independent, the product $V_f = (PS/l)^n \cdot \eta_{PP}$ is in fact a constant.
By fixing n to subsequently lower values, $\eta_{PP}$ was found to be plateauing to a constant $\eta_{PP}$=0.92 value for each PS starting from n=2.125. This could be the indication of an overall representative degree of elasticity, being the latter eventually driven than the presence of APC rather than the coexisting refinement of grains.
Considering also this reason, assigning a satisfactory meaning to $\eta_{GB}$ is not easy and will not here further investigated.

## 4.4 Conclusions and outlook

In this Section a summary of the results and the outlook on possible future studies pointing towards a better (possibly full) understanding of the physics ruling the APC-Nb$_3$Sn conductors is presented. The first is provided in Subsection 4.4.1 while the last in Subsection 4.4.2.

### 4.4.1 Summary

Several results have been obtained in this work, all related to - or motivated by - the study of the new APC-Nb$_3$Sn technology. In the following list the main ones are enumerated.

- A magnetic method is proposed for assessing the cross section of the effectively current-carrying elements of a filamentary-structured technical superconductor, when SEM evaluations are not sufficiently reliable (cf. Subsection 3.1.3 and Sec. 4.1). Specifically, this solution is suited for Nb$_3$Sn multi-filamentary wires, where the contours of the fine-grained A15 region are not clear and applicable to all types of wires whose filaments or sub-elements can be modelled as tubes. The proposed sequence allows to determine the outer and inner radii of the equivalent circular area (cross section) of the current carrying elements, simultaneously. The procedure is quite sensitive to changes in geometry and results in the most consistent values for magnetic $J_c$ measurements. A further advantage is the possibility of deriving the representative A15 geometry for the entire volume of sample not only for one or a few cross sections investigated by SEM.
  The method may hence be also useful for transport measurements allowing magnetometry to valuably support electron microscopy although the evaluation of resistive measurements does not rely on simplified assumptions about the geometry.

- Profiting also from this method, a complete overview of the $J_c$ performance of 5 different ternary recipes (with Hf or Zr as solute element) of APC-Nb$_3$Sn multifilamentary wires, reacted at different temperatures/times, is presented in Section 4.1.1 and now available in literature;

- A complete overview of $B_{irr}$ as directly recorded at 15 K from m-H loops and as a result of short-range Kramer extrapolations at 10 K and 12 K is presented in 4.1.2. Some $B_{irr}$ and $B_{c2}$ values are instead available from resistive measurements at 4.2 K. Very high $B_{c2}/B_{irr}$ values are recorded, being higher (3-14%) than the commercial ternary PIT reference values. Moreover, the Ta-alloying impact on this technology is assessed in terms of $B_{c2}$, resulting from a clear gain (up to +25%) compared with the binary (no Ta) APC-samples.

- A systematic overview of the representative grain size GS of each specimen by means of transmission Kikuchi diffraction TKD is given in Subsection 4.1.3.
  The evolution of the grain size and morphology along the A15 width is tracked and both number-fraction NF and area-fraction AF statistics are presented.
  It is found that the grain size is refined in the oxidized specimen with negligible differences between Zr-doped and Hf-doped specimen, whereas is remarkable the refinement compared to the no-oxides samples.

- The same samples were analysed by means of STEM and EELS/EFTEM for assessing the mean particle size PS and density PD as it is shown in Subsection 4.1.4. Two different type of evaluations were provided: the first, referred as "clearly distinguishable" case, is proposed as for recording 2-18 nm large particles which where confirmed to be either $ZrO_2$ or $HfO_2$ precipitates for the respective Zr- or Hf- alloyed recipes; the second analyses, referred as the "any feature" case, accounted instead for all the smaller features - 0.3-4.3 nm - identified in further magnified pictures to be everywhere in the A15 matrix, on which elemental analysis by means of EDX is not possible.
  As for their role in flux pinning (cf. Sec. 4.2) and for comparison with different type of experiments in literature, the first analysis is considered to be the most realistic one.

- A good agreement with literature data between the samples representative NF-GS is observable (cf.4.2). The maximum pinning force values $F_{p\text{-}max}$ a 4.2 K well correlate with 1/GS. In the strongly APC-dense samples, higher $F_{p\text{-}max}$ values are observed, as a possible consequence of the additional point-pinning contribution.

- Decreasing grain size GS with increasing precipitates density PD is observable in Hf-doped samples, while this trend appears to be slightly inverted in Zr-doped strands. Moreover, a consistent increase of the particle size PS is visible in the Hf-samples compared to the Zr ones at each reaction temperature (9-12% larger PS).

- Ta additions are shown to be affecting the superconducting properties of the samples by analysing their radial homogeneity and comparing these results to the binary generation and the commercial ternary reference wire. Critical temperature distributions $T_c$(r) are recorded and compared by means of AC susceptibility/SHPM/EDX (cf. Subsections 3.5.5, 3.5.6, 3.5.7 and Section 4.3). In the best performing ternaries, it was found that Ta worsen the phase homogeneity even less than what we observe in no-APC PIT samples.

- The effects of Sn concentration gradients on the evaluation of the pinning force at 4.2 K were assessed between binary and ternary APC-wires generations (cf. Sec. 4.3): the pinning mechanisms involved were derived by fitting the experimental $F_p$(B) values and taking the experimentally observed Sn gradients into account. Absolute values of the single mechanisms at specific fields were calculated, showing that point-particle PP pinning is clearly playing a role, taking over the GB-pinning contribution at 16 T in the ternary sample. Moreover, the importance of including Sn gradients in $F_p$(B) evaluations becomes evident. If they are not accounted for, a low quality fit results at high-fields and erroneous weights are ascribed to the involved pinning mechanisms.

- Further modelling by using net-summation of Dew-Hughes $F_p$(B) set of equations for core-GB and core-PP pinning interactions is provided at 4.2 K, 10 K and 15 K for each sample (cf. Sec. 4.3), where the GB-pinning efficiency $\eta_{GB}$ and PP-pinning efficiency $\eta_{PP}$ were first left as free parameters. It is found that there is a gap between the predicted $F_{p\text{-}max}$ and the experimental values, being modelled by means of $\eta_{GB}$ and/or the fluxons lattice elasticity, the latter being described by the exponent $n$ of the PP-pinning volume fraction $V_f = (PS/l)^n$.
- Finally, a possible formulation and interpretation of $\eta_{PP}$, according to the fitting-results, is presented. It was found that this pinning efficiency decreases hyperbolically with the pinning-particle size. At the same time, the alternative modelling possibility of the fluxons lattice elasticity is discussed.

### 4.4.2 Outlook

Despite the vast amount of data collected in this work, the author still believes that several confirmations, even better if provided by different/not-here-deployed experimental techniques, are needed to further confirm the findings presented in this systematic. New or hidden correlations need to be definitely unveiled and further conclusions to be drawn.

A first - absolutely necessary - condition is for the research to be supervised, from the precursors stage to the microstructural data analysis, by the very same researcher/s. This is extremely important as, at least, for understanding and keeping track of the most influencing parameters of the heat treatment on the reacted specimens. It was e.g. for the author not possible to weigh the impact of a different reaction temperature or precursors ratio at the same reaction time and/or vice-versa.

As the manufacturing develops, newer optimized version of the APC-strands will be available for testing (e.g. >200 filaments strands), therefore further conclusions upon the applicability of these conductors can be made. On this respect, when times are mature, it will be absolutely interesting to definitely deny (or confirm) experimentally the presence of a second $b_{peak}$ in the APC f(b) functions resulting from any eventual $\Delta\kappa$ pinning contribution (cf. Sec. 4.2).

The latter, and more in general the understanding of the proper pinning summation and the identification of the active pinning mechanisms deserves further study. Once experimentally addressed the precipitates and their role (atom probe tomography and X-rays surface analysis are suggested techniques), processing of large data amounts seems likely to be better provided nowadays by machine learning algorithms, which can truly be the solution to the long-standing summation problem.
The latter can also be an efficient and time-saving system for STEM particle-tracking, and a project for realizing such an algorithm in this respect has been already began by the author.

Finally, improving the knowledge on how the compositional gradients relate with the superconducting properties at a local level deserves clearly a further deepening. Especially in such complex structures as the APC strands, understanding how Zr and Hf influence the binary/ternary diagrams of $Nb_3Sn$ would be as important as difficult.
A dedicated set of samples prepared with known percentages of increasing additives - both Ta/Ti and Zr/Hf - followed by dedicated $J_c/B_{irr}/T_c$ measurements would be as challenging as fundamental, not only for the APC-wire development, but for whoever working with $Nb_3Sn$.

# Bibliography

[1] A. A. Abrikosov. “On the magnetic properties of superconductors of the second group”. In: *Sov. Phys. JETP* 5 (1957), pp. 1174–1182.

[2] P. B. Allen and R. Dynes. “Transition temperature of strong-coupled superconductors reanalyzed”. In: *Physical Review B* 12.3 (1975), p. 905.

[3] I. Anzel, R. Rudolf, L. Gusel, A. Kneissl, and L. Kosec. “Dispersion strengthening of copper by internal oxidation of rapidly solidified Cu-RE alloys. Part 2. Experimental study of internal oxidation”. In: *Zeitschrift für Metallkunde* 94 (2003).

[4] A. Arko, D. Lowndes, F. Muller, L. Roeland, J. Wolfrat, A. Van Kessel, H. Myron, F. Mueller, and G. Webb. “de Haas-van Alphen Effect in the High-T c A 15 Superconductors Nb 3 Sn and V 3 Si”. In: *Physical Review Letters* 40.24 (1978), p. 1590.

[5] S. Balachandran, C. Tarantini, P. J. Lee, F. Kametani, Y. Su, B. Waker, W. L. Starch, and D. Larbalestier. “Beneficial influence of Hf and Zr additions to Nb4at% Ta on the vortex pinning of Nb3Sn with and without an O source”. In: *Superconductor Science and Technology* 32 (2019), p. 044006.

[6] A. Ballarino. “Current leads for the LHC magnet system”. In: *IEEE transactions on applied superconductivity* 12.1 (2002), pp. 1275–1280.

[7] A. Ballarino et al. “Prospects for the use of HTS in high field magnets for future accelerator facilities”. In: *CERN Document Server* (2014), pp. 11–11.

[8] A. Ballarino and L. Bottura. “Targets for R&D on Nb 3 Sn conductor for high energy physics”. In: *IEEE Transactions on applied superconductivity* 25.3 (2015), pp. 1–6.

[9] A. Ballarino, S. C. Hopkins, B. Bordini, D. Richter, D. Tommasini, L. Bottura, M. Benedikt, M. Sugano, T. Ogitsu, S. Kawashima, et al. “The CERN FCC conductor development program: a worldwide effort for the future generation of high-field magnets”. In: *IEEE Transactions on Applied Superconductivity* 29.5 (2019), pp. 1–9.

[10] J. Bardeen, L. N. Cooper, and J. R. Schrieffer. “Theory of superconductivity”. In: *Physical review* 108.5 (1957), p. 1175.

[11] E. Barzi and A. V. Zlobin. “Nb3Sn Wires and Cables for High-Field Accelerator Magnets”. In: *Nb3Sn Accelerator Magnets* (2019), p. 23.

[12] T. Baumgartner, M. Eisterer, H. W. Weber, R. Flükiger, C. Scheuerlein, and L. Bottura. “Effects of neutron irradiation on pinning force scaling in state-of-the-art Nb3Sn wires”. In: *Superconductor Science and Technology* 27.1 (Nov. 2013), p. 015005. DOI: `10.1088/0953-2048/27/1/015005`.

[13] T. Baumgartner, M. Eisterer, H. Weber, R. Flükiger, C. Scheuerlein, and L. Bottura. “Performance boost in industrial multifilamentary Nb 3 Sn wires due to radiation induced pinning centers”. In: *Scientific reports* 5.1 (2015), pp. 1–7.

[14] T. Baumgartner, J. Hecher, J. Bernardi, S. Pfeiffer, C. Senatore, and M. Eisterer. “Assessing composition gradients in multifilamentary superconductors by means of magnetometry methods”. In: *Superconductor Science and Technology* 30.1 (2016), p. 014011.

[15] T. Baumgartner, S. Pfeiffer, J. Bernardi, A. Ballarino, and M. Eisterer. “Effects of inhomogeneities on pinning force scaling in Nb3Sn wires”. In: *Superconductor Science and Technology* 31.8 (June 2018), p. 084002.

[16] T. Baumgartner. “Effects of fast neutron irradiation on critical currents and intrinsic properties of state-of-the-art Nb3Sn”. English. PhD thesis. TU Wien, 2013.

[17] T. Baumgartner, M. Eisterer, H. W. Weber, R. Fluekiger, B. Bordini, L. Bottura, and C. Scheuerlein. “Evaluation of the Critical Current Density of Multifilamentary Nb3Sn Wires From Magnetization Measurements”. In: *IEEE Transactions on Applied Superconductivity* 22.3 (2012).

[18] M. Beasley. “A History of Superconductivity”. In: *Advances in Superconductivity.* Springer, 1989, pp. 3–15.

[19] J. G. Bednorz and K. A. Müller. “Possible high T c superconductivity in the Ba- La- Cu-O system”. In: *Zeitschrift für Physik B Condensed Matter* 64.2 (1986), pp. 189–193.

[20] M. Benz. “Mechanical and Electrical Properties of Diffusion-Processed Nb3Sn-Copper-Stainless Steel Composite Conductors”. In: *Journal of Applied Physics* 39.6 (1968), pp. 2533–2537.

[21] R. Blaschke, J. Ashkenazi, O. Pictet, D. Koelling, A. van Kessel, and F. Muller. “The influence of band structure on the electromagnetic properties of superconducting Nb and Nb3Sn”. In: *Journal of Physics F: Metal Physics* 14.1 (1984), p. 175.

[22] G. Boero, M. Demierre, P.-. Besse, and R. Popovic. “Micro-Hall devices: performance, technologies and applications”. In: *Sensors and Actuators A: Physical* 106.1 (2003). Proceedings of the 4th European Magnetic Sensors and Actuators Conference, pp. 314–320. ISSN: 0924-4247. DOI: `https://doi.org/10.1016/S0924-4247(03)00192-4`. URL: `https://www.sciencedirect.com/science/article/pii/S0924424703001924`.

[23] B. Boren. “X-ray investigation of alloys of silicon with chromium, manganese, cobalt and nickel”. In: *Arkiv för Kemi, Mineralogi och Geologi* 11 (1933), pp. 2–10.

[24] S. Bose. “Plancks Gesetz und Lichtquantenhypothese”. In: (1924).

[25] E. Brandt. “Elastic and plastic properties of the flux-line lattice in type-II superconductors”. In: *Physical Review B* 34.9 (1986), p. 6514.

[26] G. E. Brock. *Metallurgy of Advanced Electronic Materials: Proceedings of a Technical Conference.* Vol. 19. Interscience Publishers, 1963.

[27] C. Buehler, B. Sailer, M. Wanior, V. Abaecherli, M. Thoener, K. Schlenga, S. Kauffmann-Weiss, J. Hänisch, M. Heilmaier, and B. Holzapfel. “Challenges and perspectives of the phase formation of internally oxidized PIT-Type Nb 3 Sn conductors”. In: *IEEE Transactions on Applied Superconductivity* 30.4 (2020), pp. 1–5.

[28] F. Buta, M. Bonura, D. Matera, G. Bovone, A. Ballarino, S. Hopkins, B. Bordini, X. Chaud, and C. Senatore. “Very high upper critical fields and enhanced critical current densities in Nb3Sn superconductors based on Nb–Ta–Zr alloys and internal oxidation”. In: *Journal of Physics: Materials* 4.2 (2021), p. 025003.

[29] A. M. Campbell, J. E. Evetts, and D. Dew-Hughes. “Pinning of Flux Vortices in Type II Superconductors”. In: *The Philosophical Magazine: A Journal of Theoretical Experimental and Applied Physics* 18.152 (1968), pp. 313–343.

[30] A. Campbell and J. Evetts. “Flux vortices and transport currents in type II superconductors”. In: *Advances in Physics* 21.90 (1972), pp. 199–428.

[31] F. collaboration et al. “FCC-hh: The hadron collider: Future circular collider conceptual design report volume 3”. In: *European Physical Journal: Special Topics* 228.4 (2019), pp. 755–1107.

[32] D. Collomb, P. Li, and S. Bending. “Nanoscale graphene Hall sensors for high-resolution ambient magnetic imaging”. In: *Sci Rep* 9.14424 (2019). DOI: `https://doi.org/10.1038/s41598-019-50823-8`.

[33] L. Cooley and I. Pong. “Cost drivers for very high energy pp collider magnet conductors”. In: *FCC Week* (2016).

[34] L. D. Cooley, C. M. Fischer, P. J. Lee, and D. C. Larbalestier. “Simulations of the effects of tin composition gradients on the superconducting properties of Nb 3 Sn conductors”. In: *Journal of applied physics* 96.4 (2004), pp. 2122–2130.

[35] L. N. Cooper. “Bound electron pairs in a degenerate Fermi gas”. In: *Physical Review* 104.4 (1956), p. 1189.

[36] P. Dahl, G. Morgan, and W. Sampson. “Loss measurements on twisted multifilamentary superconducting wires”. In: *Journal of Applied Physics* 40.5 (1969), pp. 2083–2085.

[37] B. S. Deaver Jr and W. M. Fairbank. “Experimental evidence for quantized flux in superconducting cylinders”. In: *Physical Review Letters* 7.2 (1961), p. 43.

[38] R. DeHoff. *Thermodynamics in materials science*. CRC Press, 2006.

[39] G. Deutscher and P. G. de Gennes. “Proximity effects”. In: *pp 1005-34 of Superconductivity. Vols. 1 and 2. Parks, R. D. (ed.). New York, Marcel Dekker, Inc., 1969.* (Oct. 1969).

[40] H. Devantay, J. Jorda, M. Decroux, J.Muller, and R. Flükiger. “The physical and structural properties of superconducting A15-type Nb-Sn alloys”. In: *Journal of Materials Science* 16.8 (1981), pp. 2145–2153. DOI: `10.1007/BF00542375`.

[41] A. Devred. *Practical low-temperature superconductors for electromagnets*. CERN-2004-006. CERN, 2004.

[42] D. Dew-Hughes. “Flux pinning mechanisms in type II superconductors”. In: *The Philosophical Magazine: A Journal of Theoretical Experimental and Applied Physics* 30.2 (1974), pp. 293–305. DOI: `10.1080/14786439808206556`.

[43] D. Dew-Hughes. “Superconducting A-15 compounds: A review”. In: *Cryogenics* 15.8 (1975), pp. 435–454.

[44] M. Di Castro, D. Sernelius, L. Bottura, L. Deniau, N. Sammut, S. Sanfilippo, and W. Venturini Delsolaro. “Parametric field modeling for the lhc main magnets in operating conditions”. In: *2007 IEEE Particle Accelerator Conference (PAC)*. 2007, pp. 1586–1588. DOI: `10.1109/PAC.2007.4440831`.

[45] D. R. Dietderich and R. M. Scanlan. “Nb/sub 3/Sn artificial pinning microstructures”. In: *IEEE transactions on applied superconductivity* 7.2 (1997), pp. 1201–1204.

[46] D. Dietderich, M. Kelman, J. Litty, and R. Scanlan. “High Critical Current Densities in Nb 3 Sn Films with Engineered Microstructures—Artificial Pinning Microstructures”. In: *Advances in Cryogenic Engineering Materials*. Springer, 1998, pp. 951–958.

[47] R. Doll and M. Näbauer. “Experimental proof of magnetic flux quantization in a superconducting ring”. In: *Physical Review Letters* 7.2 (1961), p. 51.

[48] G. Domokos. “Fermilab: Physics, the frontier, and megascience”. In: *American Journal of Physics* 77.7 (2009), pp. 671–672.

[49] A. Einstein. “Quantentheorie des einatomigen idealen Gases”. In: *Kgl. Preuss. Akad. Wiss Sitz.* 261 (1924).

[50] M. Eisterer. “The significance of solutions of the inverse Biot–Savart problem in thick superconductors”. In: *Superconductor Science and Technology* 18.2 (2004), S58–S62. DOI: `10.1088/0953-2048/18/2/013`.

[51] J. W. Ekin. “Unified scaling law for flux pinning in practical superconductors: I. Separability postulate, raw scaling data and parameterization at moderate strains”. In: *Superconductor Science and Technology* 23.8 (July 2010), p. 083001. DOI: `10.1088/0953-2048/23/8/083001`.

[52] J. W. Ekin, N. Cheggour, L. Goodrich, and J. Splett. “Unified Scaling Law for flux pinning in practical superconductors: III. Minimum datasets, core parameters, and application of the Extrapolative Scaling Expression”. In: *Superconductor Science and Technology* 30.3 (Feb. 2017), p. 033005. DOI: `10.1088/1361-6668/30/3/033005`.

[53] J. W. Ekin, N. Cheggour, L. Goodrich, J. Splett, B. Bordini, and D. Richter. “Unified Scaling Law for flux pinning in practical superconductors: II. Parameter testing, scaling constants, and the Extrapolative Scaling Expression”. In: *Superconductor Science and Technology* 29.12 (Nov. 2016), p. 123002. DOI: `10.1088/0953-2048/29/12/123002`.

[54] J. Elen and C. van Beijnen. “van der Klein”. In: *IEEE Trans. Mag. MAG-13* 470 (1977).

[55] G. Eliashberg. “Interactions between electrons and lattice vibrations in a superconductor”. In: *Sov. Phys. JETP* 11.3 (1960), pp. 696–702.

[56] R. E. Enstrom, J. Hanak, J. Appert, and K. Strater. “Effect of Impurity Gas Additions on the Superconducting Critical Current of Vapor-Deposited Nb3Sn”. In: *Journal of The Electrochemical Society* 119.6 (1972), p. 743.

[57] C. of the European Commission. “The European Strategy for Particle Physics Update 2013”. In: *European Strategy Session of Council, Brussels, Germany CERN-Council-S/106* (2013).

[58] L. Fang, L. Feng, G. Huixian, C. Chao, L. Bo, W. Yu, and L. Huajun. “Comparison and analysis of twist pitch length test methods for ITER Nb3Sn and NbTi strands”. In: *Rare Metal Materials and Engineering* 44.9 (2015), pp. 2095–2099.

[59] P. Farmer. *DTN Retail Fertilizer Trends.* 2021. URL: `https://www.dtnpf.com/agriculture/web/ag/crops/article/2021/04/14/nitrogen-prices-continue-climb-price`.

[60] M. Field et al. “Optimizing conductors for high field applications”. In: *IEEE Transactions on Applied Superconductivty* 24 (2014), p. 6001105.

[61] W. Fietz and W. Webb. “Hysteresis in superconducting alloys—temperature and field dependence of dislocation pinning in niobium alloys”. In: *Physical Review* 178.2 (1969), p. 657.

[62] R. Flükiger. “Martensitic transformations and their effects on superconductivity in A15 superconductors”. In: *Le Journal de Physique Colloques* 43.C4 (1982), pp. C4–357.

[63] R. Flükiger, C. Senatore, M. Cesaretti, F. Buta, D. Uglietti, and B. Seeber. “Optimization of Nb3Sn and MgB2 wires”. In: *Superconductor Science and Technology* 21.5 (2008), p. 054015.

[64] R. Flükiger, W. Specking, M. Klemm, and S. Gauss. “Composite core Nb3Sn wires: preparation and characterization”. In: *IEEE transactions on magnetics* 25.2 (1989), pp. 2192–2199.

[65] R. Flükiger, D. Uglietti, C. Senatore, and F. Buta. “Microstructure, composition and critical current density of superconducting Nb3Sn wires”. In: *Cryogenics* 48.7 (2008). Special Issue: Low-Tc Superconducting Materials, pp. 293–307. ISSN: 0011-2275. DOI: `https://doi.org/10.1016/j.cryogenics.2008.05.005`.

[66] R. Flükiger. *Atomic ordering, phase stability and superconductivity in bulk and filamentary A15 type compounds.* Tech. rep. Kernforschungszentrum Karlsruhe GmbH (Germany, 1987.

[67] S. Foner and E. McNiff Jr. “Upper critical fields of cubic and tetragonal single crystal and polycrystalline Nb3Sn in DC fields to 30 tesla”. In: *Solid State Communications* 39.9 (1981), pp. 959–964.

[68] J. D. Galambos and Y. K. M. Peng. “Comparison of Nb3Sn and NbTi superconductor magnet ITER devices”. In: 15.2 (Jan. 1989). ISSN: 0748-1896.

[69] J. Garai. “Physics behind the Debye temperature”. In: *arXiv preprint physics/0703001* (2007).

[70] A. Ghosh, K. Robins, and W. Sampson. “Magnetization measurements on multifilamentary Nb 3 Sn and NbTi conductors”. In: *IEEE transactions on magnetics* 21.2 (1985), pp. 328–331.

[71] A. K. Ghosh. “V–I transition and n-value of multifilamentary LTS and HTS wires and cables”. In: *Physica C: Superconductivity* 401.1 (2004). Proceedings of the International Cryogenic Materials Conference: Topical Conference on the Voltage-Current Relation in Technical Superconductors, pp. 15–21. ISSN: 0921-4534. DOI: `https://doi.org/10.1016/j.physc.2003.09.006`. URL: `https://www.sciencedirect.com/science/article/pii/S0921453403014709`.

[72] M. Giampietro. *Exchanging knowledge with industry on superconducting tech.* Tech. rep. 2012.

[73] I. Giaver. *Electron tunneling and superconductivity. Nobel Lectures Physics. 1971–80.* 1973.

[74] A. Godeke, D. Cheng, D. Dietderich, P. Ferracin, S. Prestemon, G. Sabbi, and R. Scanlan. “Limits of NbTi and Nb3Sn, and Development of wind and react Bi–2212 High Field Accelerator Magnets”. In: *IEEE transactions on applied superconductivity* 17.2 (2007), pp. 1149–1152.

[75] A. Godeke, M. C. Jewell, C. M. Fischer, A. A. Squitieri, P. J. Lee, and D. C. Larbalestier. “The upper critical field of filamentary Nb 3 Sn conductors”. In: *Journal of applied physics* 97.9 (2005), p. 093909.

[76] A. Godeke. “A reviewof the properties of Nb3Sn and their variation with A15 composition, morphology and strain state”. In: *Superconductor Science and Technology* 19 (2006), R68–R80.

[77] A. Godeke. “Performance boundaries in Nb3Sn superconductors”. Undefined. PhD thesis. Netherlands: University of Twente, July 2005. ISBN: 9789036522243.

[78] A. Godeke, A. den Ouden, A. Nijhuis, and H. ten Kate. “State of the art powder-in-tube niobium–tin superconductors”. In: *Cryogenics* 48.7 (2008). Special Issue: Low-Tc Superconducting Materials, pp. 308–316. ISSN: 0011-2275. DOI: `https://doi.org/10.1016/j.cryogenics.2008.04.003`. URL: `https://www.sciencedirect.com/science/article/pii/S0011227508000519`.

[79] J. Goldstein. In: *Scanning Electron Microscopy and X-Ray Microanalysis*. Ed. by J. Goldstein. Boston, MA: Springer, 1992. Chap. Qualitative X-Ray Analysis.

[80] L. P. Gor'kov. "Microscopic derivation of the Ginzburg-Landau equations in the theory of superconductivity". In: *Sov. Phys. JETP* 9.6 (1959), pp. 1364–1367.

[81] L. Gor'Kov. "Theory of superconducting alloys in a strong magnetic field near the critical temperature". In: *Soviet Physics JETP* 10 (1960), p. 998.

[82] P. Grant, M. Denhoff, W. Xing, P. Brown, S. Govorkov, J. Irwin, B. Heinrich, H. Zhou, A. Fife, and A. Cragg. "Determination of current and flux distribution in squares of thin-film high-temperature superconductors". In: *Physica C: Superconductivity* 229.3-4 (1994), pp. 289–300.

[83] C. S. Group et al. "CEPC conceptual design report: Volume 1-accelerator". In: *arXiv preprint arXiv:1809.00285* (2018).

[84] V. Guritanu, W. Goldacker, F. Bouquet, Y. Wang, R. Lortz, G. Goll, and A. Junod. "Specific heat of Nb 3 Sn: The case for a second energy gap". In: *Physical Review B* 70.18 (2004), p. 184526.

[85] M. Haas, L. Mongeard, L. Ulrici, L. D'Aloia, A. Cherrey, R. Galler, and M. Benedikt. "Applicability of excavated rock material: A European technical review implying opportunities for future tunnelling projects". In: *Journal of Cleaner Production* (2021), p. 128049.

[86] S. Hahn, K. Kim, K. Kim, X. Hu, T. Painter, I. Dixon, S. Kim, K. R. Bhattarai, S. Noguchi, J. Jaroszynski, et al. "45.5-tesla direct-current magnetic field generated with a high-temperature superconducting magnet". In: *Nature* 570.7762 (2019), pp. 496–499.

[87] Y.-L. Hai, N. Lu, H.-L. Tian, M.-J. Jiang, W. Yang, W.-J. Li, X.-W. Yan, C. Zhang, X.-J. Chen, and G.-H. Zhong. "Cage Structure and Near Room-Temperature Superconductivity in TbH n (n= 1–12)". In: *The Journal of Physical Chemistry C* 125.6 (2021), pp. 3640–3649.

[88] R. G. Hampshire and M. T. Taylor. "Critical supercurrents and the pinning of vortices in commercial Ng-60 at% Ti". In: *Journal of Physics F: Metal Physics* 2.1 (Jan. 1972), pp. 89–106. DOI: `10.1088/0305-4608/2/1/015`.

[89] J. Hanak and R. Enstrom. "Proceedings of the 10th International Conference on Low Temperature Physics". In: 178 (1966).

[90] J. Hanak, K. Strater, and G. Cullen. "Preparation and properties of vapor-deposited niobium stannide". In: *RCA (Radio Corporation of America) Review (US)* 25 (1964).

[91] H. Hartmann, F. Ebert, and O. Bretschneider. "Elektrolysen in Phosphatschmelzen. I. Die elektrolytische Gewinnung von $\alpha$-und $\beta$-Wolfram". In: *Zeitschrift für anorganische und allgemeine Chemie* 198.1 (1931), pp. 116–140.

[92] C. D. Hawes, P. J. Lee, and D. C. Larbalestier. "Measurements of the microstructural, microchemical and transition temperature gradients of A15 layers in a high-performance Nb3Sn powder-in-tube superconducting strand". In: *Superconductor Science and Technology* 19.3 (2006), S27–S37. DOI: `10.1088/0953-2048/19/3/004`. URL: `https://doi.org/10.1088/0953-2048/19/3/004`.

[93] C. D. Hawes, P. J. Lee, and D. C. Larbalestier. "Measurement of the critical temperature transition and composition gradient in powder-in-tube Nb/sub 3/Sn composite wire". In: *IEEE Transactions on Applied Superconductivity* 10.1 (2000), pp. 988–991. DOI: `10.1109/77.828397`.

[94] C. D. Hawes. *Investigations of the inhomogeneity of a powder-in-tube Nb3Sn conductor.* University of Wisconsin–Madison, 2002.

[95] S. M. Heald, C. Tarantini, P. J. Lee, M. D. Brown, Z. Sung, A. K. Ghosh, and D. C. Larbalestier. “Evidence from EXAFS for different Ta/Ti site occupancy in high critical current density Nb 3 Sn superconductor wires”. In: *Scientific reports* 8.1 (2018), pp. 1–9.

[96] J. Hecher, T. Baumgartner, J. Weiss, C. Tarantini, A. Yamamoto, J. Jiang, E. Hellstrom, D. Larbalestier, and M. Eisterer. “Small grains: a key to high-field applications of granular Ba-122 superconductors?” In: *Superconductor Science and Technology* 29.2 (2015), p. 025004.

[97] J. Hecher, S. Ishida, D. Song, H. Ogino, A. Iyo, H. Eisaki, M. Nakajima, D. Kagerbauer, and M. Eisterer. “Direct observation of in-plane anisotropy of the superconducting critical current density in Ba (Fe 1- x Co x) 2 As 2 crystals”. In: *Physical Review B* 97.1 (2018), p. 014511.

[98] E. Helfand and N. R. Werthamer. “Temperature and Purity Dependence of the Superconducting Critical Field, $H_{c2}$”. In: *Phys. Rev. Lett.* 13 (23 Dec. 1964), pp. 686–688. DOI: `10.1103/PhysRevLett.13.686`.

[99] E. Helfand and N. R. Werthamer. “Temperature and Purity Dependence of the Superconducting Critical Field, $H_{c2}$. II”. In: *Phys. Rev.* 147 (1 July 1966), pp. 288–294. DOI: `10.1103/PhysRev.147.288`.

[100] F. Hengstberger, M. Eisterer, M. Zehetmayer, and H. Weber. “Assessing the spatial and field dependence of the critical current density in YBCO bulk superconductors by scanning Hall probes”. In: *Superconductor Science and Technology* 22.2 (2009), p. 025011.

[101] S. C. Hopkins, A. Baskys, B. Bordini, J. Fleiter, and A. Ballarino. “Design, Performance and Cabling Analysis of Nb3Sn Wires for the FCC Study”. In: *Journal of Physics: Conference Series*. Vol. 1559. 1. IOP Publishing. 2020, p. 012026.

[102] C.-M. Horejs and G. Pacchioni. “CERN’s next big thing”. In: *Nature Reviews Physics* 1.1 (2019), pp. 2–4.

[103] J. Hulm and R. Blaugher. “Superconducting solid solution alloys of the transition elements”. In: *Physical Review* 123.5 (1961), p. 1569.

[104] R. Jaklevic, J. Lambe, A. Silver, and J. Mercereau. “Quantum interference effects in Josephson tunneling”. In: *Physical Review Letters* 12.7 (1964), p. 159.

[105] M. Jambunathan. “Some properties of beta and gamma distributions”. In: *The annals of mathematical statistics* (1954), pp. 401–405.

[106] M. Jewell, A. Godeke, P. Lee, and D. Larbalestier. “The Upper Critical Field of Stoichiometric and Off-Stoichiometric Bulk, Binary Nb3Sn”. In: *AIP Conference Proceedings*. Vol. 711. 1. American Institute of Physics. 2004, pp. 474–484.

[107] H. Kamerlingh Onnes. “The superconductivity of mercury”. In: *Comm. Phys. Lab. Univ. Leiden* 122 (1911), pp. 122–124.

[108] C. Kittel. “Introduction to solid state physics. john wiley&amp; sons”. In: *Inc., New York* (2004).

[109] D. Kramer. “Helium shortage has ended, at least for now”. In: *Physics Today* 5 (2020).

[110] E. J. Kramer. “Scaling laws for flux pinning in hard superconductors”. In: *Journal of Applied Physics* 44.3 (1973), pp. 1360–1370. DOI: `10.1063/1.1662353`.

[111] J. Kunzler. “Superconducting materials and high magnetic fields”. In: *Proceedings of the Seventh Conference on Magnetism and Magnetic Materials*. Springer. 1962, pp. 1042–1048.

[112] J. E. Kunzler, E. Buehler, F. Hsu, and J. H. Wernick. "Superconductivity in Nb3Sn at high current density in a magnetic field of 88 kgauss". In: *Physical review letters* 6.3 (1961), p. 89.

[113] K. Kwasnitza. "Flux jumps in composite superconductors in a time dependent magnetic field". In: *Cryogenics* 13.3 (1973), pp. 169–174.

[114] R. Labusch. "Elastic constants of the fluxoid lattice near the upper critical field". In: *physica status solidi (b)* 32.1 (1969), pp. 439–442.

[115] R. Labusch and R. Schwarz. *Movement of dislocations through a random array of weak obstacles of finite width.* Tech. rep. Argonne National Lab., Ill.(USA), 1976.

[116] J. Lambe, A. Silver, J. Mercereau, and R. Jaklevic. "Microwave observation of quantum interference effects in superconductors". In: *Phys. Letters* 11 (1964).

[117] L. D. Landau and V. L. Ginzburg. "On the theory of superconductivity". In: *Zh. Eksp. Teor. Fiz.* 20 (1950), p. 1064.

[118] J. D. Larson III, R. Mitchell, J. A. Good, and J. Lopez. "AC Loss in NbsSn Superconducting Cable-Mechanisms and Measurement". In: *A/M Lab., Longview, WA, USA, HPL-95-119* (1995).

[119] J. Lee and C. Scott. "Work in the UK on filamentary A15 conductor development". In: *Filamentary A15 Superconductors.* Springer, 1980, pp. 35–45.

[120] P. J. Lee and D. C. Larbalestier. "Microstructural factors important for the development of high critical current density Nb3Sn strand". In: *Cryogenics* 48.7-8 (2008), pp. 283–292.

[121] Z. Leijten, M. Wirix, M. Strauss, J. Plitzko, G. de With, and H. Friedrich. "Low-dose (S)TEM elemental analysis of water and oxygen uptake in beam sensitive materials". In: *Ultramicroscopy* 208 (2020), p. 112855. ISSN: 0304-3991.

[122] C. Leys, C. Ley, O. Klein, P. Bernard, and L. Licata. "Detecting outliers: Do not use standard deviation around the mean, use absolute deviation around the median". In: *Journal of Experimental Social Psychology* 49.4 (2013), pp. 764–766. ISSN: 0022-1031. DOI: `https://doi.org/10.1016/j.jesp.2013.03.013`. URL: `https://www.sciencedirect.com/science/article/pii/S0022103113000668`.

[123] S. Li, Y. Chang, Y. Wang, Q. Xu, and B. Ge. "A review of sample thickness effects on high-resolution transmission electron microscopy imaging". In: *Micron* 130 (2020), p. 102813. ISSN: 0968-4328. DOI: `https://doi.org/10.1016/j.micron.2019.102813`. URL: `https://www.sciencedirect.com/science/article/pii/S0968432819303257`.

[124] Y. Li and Y. Gao. "GLAG theory for superconducting property variations with A15 composition in Nb 3 Sn wires". In: *Scientific reports* 7.1 (2017), pp. 1–13.

[125] S. Lindau, N. Magnusson, and H. Taxt. "A method to estimate the necessary twist pitch in multi-filamentary superconductors". In: *Journal of Physics: Conference Series.* Vol. 507. 2. IOP Publishing. 2014, p. 022016.

[126] F. London and H. London. "The electromagnetic equations of the supraconductor". In: *Proceedings of the Royal Society of London. Series A-Mathematical and Physical Sciences* 149.866 (1935), pp. 71–88.

[127] E. Lynton and W. McLean. "Type II superconductors". In: *Advances in Electronics and Electron Physics.* Vol. 23. Elsevier, 1967, pp. 1–37.

[128] K. Maki. "The magnetic properties of superconducting alloys. II". In: *Physics Physique Fizika* 1 (2 Sept. 1964), pp. 127–143. DOI: `10.1103/PhysicsPhysiqueFizika.1.127`.

[129] T. Malis, S. Cheng, and R. Egerton. “EELS log-ratio technique for specimen-thickness measurement in the TEM”. In: *Journal of electron microscopy technique* 8.2 (1988), pp. 193–200.

[130] W. Markiewicz, E. Mains, R. Vankeuren, R. Wilcox, C. Rosner, H. Inoue, C. Hayashi, and K. Tachikawa. “A 17.5 Tesla superconducting concentric Nb3Sn and V3Ga magnet system”. In: *IEEE Transactions on Magnetics* 13.1 (1977), pp. 35–37. DOI: `10.1109/TMAG.1977.1059431`.

[131] K. Matsumoto and P. Mele. “Artificial pinning center technology to enhance vortex pinning in YBCO coated conductors”. In: *Superconductor Science and Technology* 23.1 (2009), p. 014001.

[132] B. T. Matthias, T. H. Geballe, S. Geller, and E. Corenzwit. “Superconductivity of $\mathrm{Nb_3Sn}$”. In: *Phys. Rev.* 95 (6 Sept. 1954), pp. 1435–1435.

[133] E. Maxwell. “Isotope effect in the superconductivity of mercury”. In: *Physical Review* 78.4 (1950), p. 477.

[134] W. Meissner and R. Ochsenfeld. “Ein neuer effekt bei eintritt der supraleitfähigkeit”. In: *Naturwissenschaften* 21.44 (1933), pp. 787–788.

[135] Z. Melhem. “How to build a super-magnet”. In: *Physics World* 31.8 (2018).

[136] K. H. Mess, P. Schmüser, and S. Wolff. *Superconducting Accelerator Magnets*. Singapore: World Scientific, 1996.

[137] R. Mints and A. Rakhmanov. “The flux jump and critical state stability in superconductors”. In: *Journal of Physics D: Applied Physics* 8.15 (1975), p. 1769.

[138] A. Molodyk, S. Samoilenkov, A. Markelov, P. Degtyarenko, S. Lee, V. Petrykin, M. Gaifullin, A. Mankevich, A. Vavilov, B. Sorbom, et al. “Development and large volume production of extremely high current density YBa 2 Cu 3 O 7 superconducting wires for fusion”. In: *Scientific reports* 11.1 (2021), pp. 1–11.

[139] D. F. Moore, R. B. Zubeck, J. M. Rowell, and M. R. Beasley. “Energy gaps of the $A-15$ superconductors $Nb_3Sn$Sn, $V_3Si$, and $Nb_3G$ e measured by tunneling”. In: *Phys. Rev. B* 20 (7 1979), pp. 2721–2738. DOI: `10.1103/PhysRevB.20.2721`.

[140] A. Moros, M. Ortino, S. Löffler, M. Alekseev, A. Tsapleva, P. Lukyanov, I. M. Abdyukhanov, V. Pantsyrny, S. C. Hopkins, M. Eisterer, et al. “Nb 3 Sn Wires for the Future Circular Collider at CERN: Microstructural Investigation of Different Wire Layouts”. In: *IEEE Transactions on Applied Superconductivity* 31.5 (2021), pp. 1–5.

[141] L. Motowidlo, P. Lee, and D. Larbalestier. “The Effect of Second Phase Additions on the Microstructure and Bulk Pinning Force in Nb3Sn PIT Wire”. In: *IEEE transactions on applied superconductivity* 19.3 (2009), pp. 2568–2572.

[142] K. Müller, M. Takashige, and J. Bednorz. “Flux trapping and superconductive glass state in La 2 CuO 4- y: Ba”. In: *Physical review letters* 58.11 (1987), p. 1143.

[143] D. E. Newbury* and N. W. Ritchie. “Is scanning electron microscopy/energy dispersive X-ray spectrometry (SEM/EDS) quantitative?” In: *Scanning* 35.3 (2013), pp. 141–168.

[144] H. Niculescu, A. Saenz, M. Khankhasayev, and P. Gielisse. “Self-field measurements and current distribution in ceramic superconductors”. In: *Physica C: Superconductivity* 261.1-2 (1996), pp. 12–20.

[145] C. Notthoff, M. Winterer, A. Beckel, M. Geller, and J. Heindl. "Spatial high resolution energy dispersive X-ray spectroscopy on thin lamellas". In: *Ultramicroscopy* 129 (2013), pp. 30–35.

[146] T. Orlando, J. Alexander, S. Bending, J. Kwo, S. Poon, R. Hammond, M. Beasley, E. McNiff, and S. Foner. "The role of disorder in maximizing the upper critical field in the Nb-Sn system". In: *IEEE Transactions on Magnetics* 17.1 (1981), pp. 368–369.

[147] T. Orlando, E. McNiff Jr, S. Foner, and M. Beasley. "Critical fields, Pauli paramagnetic limiting, and material parameters of Nb3Sn and V3Si". In: *Physical Review B* 19.9 (1979), p. 4545.

[148] M. Ortino, S. Pfeiffer, T. Baumgartner, M. Sumption, J. Bernardi, X. Xu, and M. Eisterer. "Evolution of the superconducting properties from binary to ternary APC-Nb3Sn wires". In: *Superconductor Science and Technology* 34.3 (2021), p. 035028.

[149] M. Ortino and M. Eisterer. "Identification of the A15 Contours in Multifilamentary Nb3Sn Wires by Means of a Magnetic Method". In: *IEEE Transactions on Applied Superconductivity* 31.5 (2021), pp. 1–4.

[150] J. A. Osborne, J. Stanyard, L. Ariza, and W. Dellapiazza. "Tunnelling Studies for CERN's Future Circular Collider". In: *6th TLEP WS*. 2020.

[151] A. V. Pan, I. Golovchanskiy, and S. Fedoseev. "Critical current density: Measurements vs. reality". In: *EPL (Europhysics Letters)* 103.1 (2013), p. 17006.

[152] J. Parrell et al. "High Field Nb3Sn conductor development at Oxford Superconductor Technology". In: *IEEE Transactions on Applied Superconductivty* (2003).

[153] A. Pashitski, A. Gurevich, A. Polyanskii, D. Larbalestier, A. Goyal, E. Specht, D. Kroeger, J. DeLuca, and J. Tkaczyk. "Reconstruction of current flow and imaging of current-limiting defects in polycrystalline superconducting films". In: *Science* 275.5298 (1997), pp. 367–369.

[154] J. Petermann. "Ausscheidungen und Flußverankerung in einer supraleitenden PbNa-Legierung/Precipitates and Flux Line Pinning in a Superconducting Pb-Na Alloy". In: *International Journal of Materials Research* 61.10 (1970), pp. 724–733.

[155] S. Pfeiffer. "The microstructure of Nb3Sn superconductors for the Future Circular Collider project and its impact on the performance". PhD thesis. Wien, 2020.

[156] M. Project. URL: `https://materialsproject.org/materials/`.

[157] E. Ravaioli, G. Ambrosio, B. Auchmann, P. Ferracin, M. Maciejewski, F. Rodriguez-Mateos, G. Sabbi, E. Todesco, and A. P. Verweij. "Quench Protection System Optimization for the High Luminosity LHC Nb $_3$Sn Quadrupoles". In: *IEEE Transactions on Applied Superconductivity* 27.4 (2017), pp. 1–7. DOI: `10.1109/TASC.2016.2634003`.

[158] D. Rodrigues, L. Da Silva, C. Rodrigues, N. Oliveira, and C. Bormio-Nunes. "Optimization of Heat Treatment Profiles Applied to Nanometric-Scale Nb3Sn Wires With Cu-Sn Artificial Pinning Centers". In: *IEEE transactions on applied superconductivity* 21.3 (2010), pp. 3150–3153.

[159] H. Rogalla and P. H. Kes. *100 years of superconductivity*. Taylor & Francis, 2011.

[160] R. W. Rollins, H. Küpfer, and W. Gey. "Magnetic field profiles in type-II superconductors with pinning using a new ac technique". In: *Journal of Applied Physics* 45.12 (1974), pp. 5392–5398.

[161] A. Roovers, A. Van Pelt, and L. Van De Klundert. “AC losses in a prototype NbTi cable for the LHC dipole magnets”. In: *Advances in Cryogenic Engineering Materials*. Springer, 1990, pp. 183–190.

[162] L. Rossi. “Superconductivity and the LHC: the early days”. In: *CERN Cour. N* 519 (2011), pp. 21–27.

[163] L. Rossi. “The LHC main dipoles and quadrupoles toward series production”. In: *IEEE transactions on applied superconductivity* 13.2 (2003), pp. 1221–1228.

[164] L. E. Rumaner, M. G. Benz, and E. Hall. “The role of oxygen and zirconium in the formation and growth of Nb3Sn grains”. In: *Metallurgical and Materials Transactions.* 25 (1994), p. 213.

[165] C. Sanabria. “A new understanding of the heat treatment of Nb-Sn superconducting wires”. PhD thesis. The Florida State University, 2017.

[166] R. Scanlan, W. Fietz, and E. Koch. “Flux pinning centers in superconducting Nb3Sn”. In: *Journal of Applied Physics* 46.5 (1975), pp. 2244–2249.

[167] W. Schauer and W. Schelb. “Improvement of Nb 3 Sn high field critical current by a two-stage reaction”. In: *IEEE Transactions on Magnetics* 17.1 (1981), pp. 374–377.

[168] C. Scheuerlein, M. D. Michiel, F. Buta, B. Seeber, C. Senatore, R. Flükiger, T. Siegrist, T. Besara, J. Kadar, B. Bordini, A. Ballarino, and L. Bottura. In: 27.4 (Mar. 2014), p. 044021. DOI: `10.1088/0953-2048/27/4/044021`.

[169] J. Schultz. “The medium temperature superconductor (MTS) design philosophy”. In: *IEEE Transactions on Applied Superconductivity* 13.2 (2003), pp. 1604–1607. DOI: `10.1109/TASC.2003.812803`.

[170] C. Segal, C. Barth, I. Falorio, A. C. Zurita, A. Ballarino, X. Chaud, C. Tarantini, P. J. Lee, and D. C. Larbalestier. “Evidence of Kramer extrapolation inaccuracy for predicting high field Nb3Sn properties”. In: *Journal of Physics: Conference Series*. Vol. 1559. 1. IOP Publishing. 2020, p. 012062.

[171] C. Segal, C. Tarantini, P. Lee, and D. Larbalestier. “Improvement of small to large grain A15 ratio in Nb 3 Sn PIT wires by inverted multistage heat treatments”. In: *IOP Conference Series: Materials Science and Engineering* 279 (Dec. 2017), p. 012019. DOI: `10.1088/1757-899X/279/1/012019`.

[172] P. Seidel. *Applied superconductivity: handbook on devices and applications*. John Wiley & Sons, 2015.

[173] C. Senatore, R. Flükiger, M. Cantoni, G. Wu, R. Liu, and X. Chen. “Upper critical fields well above 100 T for the superconductor SmFeAsO 0.85 F 0.15 with T c= 46 K”. In: *Physical Review B* 78.5 (2008), p. 054514.

[174] B. J. Shaw. “Grain size and film thickness of Nb3Sn formed by solid-state diffusion in the range 650–800° C”. In: *Journal of Applied Physics* 47.5 (1976), pp. 2143–2145.

[175] E. Snider, N. Dasenbrock-Gammon, R. McBride, M. Debessai, H. Vindana, K. Vencatasamy, K. V. Lawler, A. Salamat, and R. P. Dias. “Room-temperature superconductivity in a carbonaceous sulfur hydride”. In: *Nature* 586.7829 (2020), pp. 373–377.

[176] T. Spina, A. Ballarino, L. Bottura, C. Scheuerlein, and R. Flükiger. “Artificial Pinning in Nb3Sn Wires”. In: *EEE Transactions on Applied Superconductivity* 27,4 (2017), p. 395.

[177] T. Spina, A. Ballarino, L. Bottura, C. Scheuerlein, and R. Flukiger. “Artificial pinning in Nb 3 Sn wires”. In: *IEEE Transactions on Applied Superconductivity* 27.4 (2017), pp. 1–5.

[178] M. Statera, F. Alessandria, G. Bellomo, F. Broggi, L. Imeri, A. Leone, S. Mariotto, A. Paccalini, A. Pasini, D. Pedrini, M. Prioli, M. Sorbi, M. Todero, C. Uva, R. U. Valente, A. Musso, E. Todesco, M. Campaniello, M. Canetti, F. Gangini, P. Manini, C. Santini, and A. Zanichelli. “Optimization of the High Order Correctors for HL-LHC Toward the Series Production”. In: *IEEE Transactions on Applied Superconductivity* 31.5 (2021), pp. 1–5. DOI: `10.1109/TASC.2021.3070904`.

[179] M. Suenaga, A. Ghosh, Y. Xu, and D. Welch. “Irreversibility temperatures of nb 3 sn and nb-ti”. In: *Physical review letters* 66.13 (1991), p. 1777.

[180] M. Suenaga, D. Welch, R. Sabatini, O. Kammerer, and S. Okuda. “Superconducting critical temperatures, critical magnetic fields, lattice parameters, and chemical compositions of “bulk”pure and alloyed Nb3Sn produced by the bronze process”. In: *Journal of applied physics* 59.3 (1986), pp. 840–853.

[181] J. D. Sugar, J. T. McKeown, D. Banga, and J. R. Michael. “Comparison of Orientation Mapping in SEM and TEM”. In: *Microscopy and Microanalysis* 26.4 (2020), pp. 630–640.

[182] M. Sumption, S. Bhartiya, C. Kovacks, X. Peng, E. Gregory, M. Tomsic, and E. Collings. “Critical current density and stability of Tube Type Nb3Sn conductors”. In: *Cryogenics* 52.2-3 (2012), pp. 91–99.

[183] M. Sumption, E. Collings, and P. Barnes. “AC loss in striped (filamentary) YBCO coated conductors leading to designs for high frequencies and field-sweep amplitudes”. In: *Superconductor Science and Technology* 18.1 (2004), p. 122.

[184] M. Szleper. “The Higgs boson and the physics of $WW$ scattering before and after Higgs discovery”. In: *arXiv preprint arXiv:1412.8367* (2014).

[185] K. Tachikawa and Y. Iwasa. “Current capacities of superconducting V3Ga tapes in high magnetic fields”. In: *Applied Physics Letters* 16.6 (1970), pp. 230–231.

[186] K. Tachikawa, M. Terada, M. Endo, and Y. Miyamoto. “Bronze-processed Nb3Sn with addition of germanium to matrix”. In: *Cryogenics* 33.2 (1993), pp. 205–208.

[187] C. Tarantini, Z. Sung, P. Lee, A. Ghosh, and D. Larbalestier. “Significant enhancement of compositional and superconducting homogeneity in Ti rather than Ta-doped Nb3Sn”. In: *Applied Physics Letters* 108.4 (2016), p. 042603.

[188] C. Tarantini, S. Balachandran, S. M. Heald, P. J. Lee, N. Paudel, E. S. Choi, W. L. Starch, and D. C. Larbalestier. “Ta, Ti and Hf effects on Nb3Sn high-field performance: temperature-dependent dopant occupancy and failure of Kramer extrapolation”. In: *Superconductor Science and Technology* 32.12 (2019), p. 124003.

[189] C. Tarantini, F. Kametani, S. Balachandran, S. M. Heald, L. Wheatley, C. R. Grovenor, M. P. Moody, Y.-F. Su, P. J. Lee, and D. C. Larbalestier. “Origin of the enhanced Nb3Sn performance by combined Hf and Ta doping”. In: *Scientific reports* 11.1 (2021), pp. 1–8.

[190] D. M. J. Taylor and D. P. Hampshire. “Relationship between the n-value and critical current in Nb3Sn superconducting wires exhibiting intrinsic and extrinsic behaviour”. In: *Superconductor Science and Technology* 18.12 (2005), S297–S302. DOI: `10.1088/0953-2048/18/12/012`. URL: `https://doi.org/10.1088/0953-2048/18/12/012`.

[191] M. Tinkham. *Introduction to superconductivity*. Courier Corporation, 2004.

[192] E. Todesco, H. Allain, G. Ambrosio, F. Borgnolutti, F. Cerutti, D. Dietderich, L. S. Esposito, H. Felice, P. Ferracin, G. Sabbi, P. Wanderer, and R. Van Weelderen. "Design Studies for the Low-Beta Quadrupoles for the LHC Luminosity Upgrade". In: *IEEE Transactions on Applied Superconductivity* 23.3 (2013), pp. 4002405–4002405. DOI: `10.1109/TASC.2013.2248314`.

[193] D. Tommasini, B. Auchmann, H. Bajas, M. Bajko, A. Ballarino, G. Bellomo, M. Benedikt, S. I. Bermudez, B. Bordini, L. Bottura, et al. "The 16 T dipole development program for FCC". In: *IEEE transactions on applied superconductivity* 27.4 (2016), pp. 1–5.

[194] S. W. Van Sciver and K. R. Marken. "Superconducting magnets above 20 tesla". In: *Physics Today* 55.8 (2002), pp. 37–43.

[195] G. Volpini, F. Alessandria, G. Bellomo, F. Broggi, A. Paccalini, D. Pedrini, A. Leone, V. Marinozzi, M. Quadrio, M. Sorbi, et al. "Development of the superferric sextupole corrector magnet for the LHC luminosity upgrade". In: *IEEE Transactions on Applied Superconductivity* 26.4 (2016), pp. 1–4.

[196] X. Wang, G. Ambrosio, G. Chlachidze, E. Collings, D. Dietderich, J. Dimarco, H. Felice, A. Ghosh, A. Godeke, S. Gourlay, M. Marchevsky, S. Prestemon, G. Sabbi, M. Sumption, G. Velev, X. Xu, and A. Zlobin. "Validation of Finite-Element Models of Persistent-Current Effects in Nb3Sn Accelerator Magnets". In: *IEEE Transactions on Applied Superconductivity* 25 (June 2015), pp. 1–6. DOI: `10.1109/TASC.2014.2385932`.

[197] D. Welch. "An approximate closed-form expression for the electron-scattering-induced interaction between magnetic flux lines and grain boundaries". In: *IEEE Transactions on Magnetics* 21.2 (1985), pp. 827–830. DOI: `10.1109/TMAG.1985.1063714`.

[198] N. R. Werthamer, E. Helfand, and P. C. Hohenberg. "Temperature and Purity Dependence of the Superconducting Critical Field, $H_{c2}$. III. Electron Spin and Spin-Orbit Effects". In: *Phys. Rev.* 147 (1 July 1966), pp. 295–302. DOI: `10.1103/PhysRev.147.295`.

[199] R. J. Wijngaarden, H. Spoelder, R. Surdeanu, and R. Griessen. "Determination of two-dimensional current patterns in flat superconductors from magneto-optical measurements: An efficient inversion scheme". In: *Physical Review B* 54.9 (1996), p. 6742.

[200] R. Willens, T. Geballe, A. Gossard, J. Maita, A. Menth, G. Hull, and R. Soden. "Superconductivity of Nb3Al". In: *Solid State Communications* 7.11 (1969), pp. 837–841. ISSN: 0038-1098.

[201] M. N. Wilson. "100 years of superconductivity and 50 years of superconducting magnets". In: *IEEE transactions on applied superconductivity* 22.3 (2011), pp. 3800212–3800212.

[202] M. N. Wilson. "NbTi superconductors with low ac loss: A review". In: *Cryogenics* 48.7-8 (2008), pp. 381–395.

[203] M. N. Wilson. "Superconducting magnets". In: (1983).

[204] M. Wiper, D. R. Insua, and F. Ruggeri. "Mixtures of gamma distributions with applications". In: *Journal of computational and graphical statistics* 10 (2001), pp. 440–454.

[205] M. Witcomb and D. Dew-Hughes. "Superconductivity of heat-treated Nb-65 at.% Ti alloy". In: *Journal of Materials Science* 8.10 (1973), pp. 1383–1400.

[206] X. Xu. In: *private communication* (), data on which the evaluation in Ref. [205] was based, information on samples quality (Oxygey amount, draqing related issues, special recommendations for R–B measurements.

[207] X. Xu, M. Sumption, X. Peng, and E. Collings. “Refinement of Nb3Sn grain size by the generation of ZrO2 precipitates in Nb3Sn wires”. In: *Applied Physics Letters* 104.8 (2014), p. 082602.

[208] X. Xu, M. Sumption, S. Bhartiya, X. Peng, and E. Collings. “Critical current densities and microstructures in rod-in-tube and tube type Nb3Sn strands—present status and prospects for improvement”. In: *Superconductor Science and Technology* 26.7 (2013), p. 075015.

[209] X. Xu, M. Sumption, J. Lee, J. Rochester, and X. Peng. “Persistent compositions of non-stoichiometric compounds with low bulk diffusivity: A theory and application to Nb3Sn superconductors”. In: *Journal of Alloys and Compounds* 845 (2020), p. 156182.

[210] X. Xu, M. Majoros, M. D. Sumption, and E. W. Collings. “Persistent-Current Magnetization of $Nb_3Sn$ Strands: Influence of Applied Field Angle and Transport Current”. In: *IEEE Transactions on Applied Superconductivity* 25.3 (2015), pp. 1–4.

[211] X. Xu, X. Peng, J. Rochester, M. Sumption, J. Lee, G. Calderon Ortiz, and J. Hwang. “The strong influence of Ti, Zr, Hf solutes and their oxidation on microstructure and performance of Nb3Sn superconductors”. In: *Journal of Alloys and Compounds* 857 (2021), p. 158270. ISSN: 0925-8388. DOI: `https://doi.org/10.1016/j.jallcom.2020.158270`.

[212] X. Xu, J. Rochester, X. Peng, M. Sumption, and M. Tomsic. “Ternary Nb3Sn superconductors with artificial pinning centers and high upper critical fields”. In: *Superconductor Science and Technology* 32 (2019), 02LT01.

[213] X. Xu, M. Sumption, and X. Peng. “Internally Oxidized Nb 3 Sn Strands with Fine Grain Size and High Critical Current Density”. In: *Advanced Materials* 27 (2015), p. 1346.

[214] X. Xu. “A review and prospects for Nb3Sn superconductor development”. In: *Superconductor Science and Technology* 30.9 (2017), p. 093001.

[215] X. Xu, X. Peng, J. Rochester, J.-Y. Lee, and M. Sumption. “High critical current density in internally-oxidized Nb3Sn superconductors and its origin”. In: *Scripta Materialia* 186 (2020), pp. 317–320.

[216] X. Xu, X. Peng, M. Sumption, and E. Collings. “Recent progress in application of internal oxidation technique in Nb3Sn strands”. In: *IEEE Transactions on Applied Superconductivity* 27.4 (2016), pp. 1–5.

[217] X. Xu, M. Sumption, and E. Collings. “Influence of heat treatment temperature and Ti doping on low-field flux jumping and stability in (Nb-Ta)3Sn strands”. In: *Superconductor Science and Technology* 27 (Aug. 2014), p. 095009. DOI: `10.1088/0953-2048/27/9/095009`.

[218] K. Y. Y. Hashimoto and M. Tanaka. “ICEC-5”. In: 332. K. Mendelssohn Editor, 1974.

[219] W. E. Yetter and E. J. Kramer. “Flux pinning by thin planar defects”. In: *Journal of Materials Science* 17.10 (1982), pp. 2792–2800.

[220] B. Zeitlin, J. S. Marte, D. Ellis, M. Benz, and E. Gregory. “Results on Mono Element Internal Tin Nb3Sn Conductors (MEIT) With Nb7.5Ta and Nb(1Zr + Ox) Filaments”. In: *Advanced Cryogenic Engineering.* 50B (2005), p. 395.

[221] R. Zhou, S. Hong, W. Marancik, and B. Kear. “Artificial flux pinning in Nb and Nb3Sn superconductors”. In: *IEEE transactions on applied superconductivity* 3.1 (1993), pp. 986–989.

[222] F. Zimmermann. “Future colliders for particle physics—“Big and small””. In: *Nuclear Instruments and Methods in Physics Research Section A: Accelerators, Spectrometers, Detectors and Associated Equipment* 909 (2018), pp. 33–37.

[223] A. V. Zlobin, V. V. Kashikhin, and E. Barzi. “Effect of Flux Jumps in Superconductor on $Nb_3Sn$ Accelerator Magnet Performance”. In: *IEEE transactions on applied superconductivity* 16.2 (2006), pp. 1308–1311.